

Cellulosic Nanocomposites for Advanced Manufacturing

An Exploration of Advanced Materials in Electrospinning and Additive Manufacturing

by

Andrew Christopher Finkle

A thesis

presented to the University of Waterloo

in fulfilment of the

thesis requirement for the degree of

Doctor of Philosophy

in

Chemical Engineering (Nanotechnology)

Waterloo, Ontario, Canada, 2020

© Andrew Christopher Finkle 2020

Examining Committee Membership

The following served on the Examining Committee for this thesis. The decision of the Examining Committee is by majority vote.

External Examiner

Douglas J. Gardner, Ph.D.
Professor, University of Maine

Supervisors

Leonardo Simon, Ph.D.
Professor, University of Waterloo

Internal Members

Michael Tam, Ph.D.
Professor, University of Waterloo

Aiping Yu, Ph.D.
Associate Professor, University of Waterloo

Internal-External Member

Sheshakamal Jayaram, Ph.D.
Professor, University of Waterloo

Author's Declaration

I hereby declare that I am the sole author of this thesis. This is a true copy of the thesis, including any required final revisions, as accepted by my examiners.

I understand that my thesis may be made electronically available to the public.

Abstract

The effects of formulation and processing of thermoplastics and composites containing Nanocrystalline Cellulose (NCC) were explored and characterized for electrospinning and fused deposition modeling 3D printing advanced manufacturing techniques.

Through electrospinning, desirable outcome responses were optimized through design of experiments for electrospun fibers of 3 material systems by controlling up to four formulation and processing factors. Regression models were developed for fiber diameter, beading density, and bead diameter responses for each material system and improved with center point measurements where applicable. The three material systems include: NCC and polycarbonate (PC) in a mixture of tetrahydrofuran and dimethylformamide (THF:DMF), NCC and PC in chloroform, and NCC and polyamide-6,6 (PA 6,6) in formic acid.

For NCC and PC in THF:DMF, the inclusion of NCC tended to improve the spinnability of the system. Less beading, smaller fibers, and more pristine fibers were observed with the incorporation of 2-wt.% of NCC with PC. NCC surface modified with (2-dodecen-1-yl) succinic anhydride (cNCC) and PC in chloroform was the least ideal system tested, as it had a very narrow window of parameters to achieve desirable fibers. Concentrations of PC are required to be greater than 15-wt.% to achieve some fibers and this was improved through the addition of cNCC, but the resulting uniformity and repeatability of the chloroform solvent was not ideal for the current benchtop experimental setup. Modified cNCC and PA 6, 6 lead to the most desirable fibers, with 200 to 300 nm fiber diameters that can lead to desired nanoscale effects, like extremely high surface area and slip-flow filtration benefits. The cNCC and PA 6,6 system did not include any beading and produced a regression model for fiber diameter that has an R-squared fit of 0.999, making it excellent for producing desired fiber diameters.

Proof of concept application of electrospun fibers in transparent coatings with improved surface properties were presented and validated through microhardness and light transmittance testing.

Through fused deposition modeling thermoplastic starch-resin copolymer (TPS) and NCC reinforced TPS was explored. 3D printer filaments were designed and manufactured on a benchtop scale extruder as well as in a scale-up facility used for industrial production. ASTM specimens were 3D printed on the Makerbot Replicator 2X printer with Gcode and slicing parameters optimized for the new formulation. Mechanical properties were measured for impact, tensile, and flexural testing.

3D Printing slightly increased tensile and flexural modulus relative to injection molding techniques, while only slightly decreasing impact, flexural and tensile strength, suggesting that 3D printing may be a suitable replacement process for certain applications. The addition of NCC to TPS increased tensile and flexural modulus at 1, 3, and 5-wt.% loadings while the addition of NCC increased impact, tensile and flexural strength to a maximum at 3-wt.% loading. Scale-Up trials were successful at preparing NCC/TPS filaments for 3D printing, but in general, mechanical properties were at about 65-80% of the desktop filament extrusion.

Acknowledgements

I express my sincerest gratitude to Dr. Leonardo C. Simon and Dr. Richard Berry, my co-supervisors, for all their assistance, guidance and supervision through my graduate research.

I would like to thank Dr. Sheshakamal Jayaram, Dr. Michael Tam, and Dr. Aiping Yu, my thesis committee members at the University of Waterloo, for their time, dedication, and guidance through my comprehensive examination as well as the completion of my thesis.

I would also like to thank all of my friends and colleagues in my research group and engineering department. Most notably, I would like to acknowledge Dr. Charles dal Castel, Dr. Ryan Kim, and Chong Meng for all their valuable assistance through the lab experimentation and interpretation of results.

The hard work of University of Waterloo Nanotechnology Engineering co-op students Jeremy Vandenberg, AbdulAziz AlMutairi, Dan Pepler, Meagan Carno, Felicia Abbruzzese, Michael Shon, Tobi Ibikunle, Petar Tardovic, and Pablo Eder for their assistance in my thesis experimentation is also extremely appreciated.

I am also greatly thankful to Dr. Charles Mire and Amir Solowjeizcyk, my co-founders at Structur3d Inc. for taking on extra workload and their encouragement while I continued pursuit of higher education.

Special thanks is given to Celluforce Inc. and the kind support of their employees for donating cellulose research materials and exceptional technical support; PolyOne Inc. for donation of the molding grade polycarbonate; and also acknowledge financial support from the Natural Science and Engineering Council of Canada (NSERC Discovery Grant), Ontario Ministry of Research and Innovation (BioCar Initiative), as well as Dr. Ron Crotagino and the NSERC-AlboraNano program.

Dedication

I would like to dedicate this thesis to my family and most notably, my grandmother, Gwendolyn Joy Finkle, who celebrated her 87th year in 2019. Without you and Grandpa Don, none of this would be possible.

This is also dedicated to my loving parents, Christopher and Susan Finkle; my sister and brother-in-law, Julia and Mark Walker; and my brother, roommate, and lifetime friend, Adam Finkle. I thank you for all your love and support throughout this difficult stage of my life, I would never have accomplished this without you guys.

And finally, Christine van Beest, my sidekick, co-pilot, best friend, and love of my life. You are the inspiration that keeps me moving forward, even when the path is unclear – or does not yet exist.

I love you, all!

Table of Contents

Examining Committee Membership	ii
Author’s Declaration	iii
Abstract.....	iv
Acknowledgements	v
Dedication	vi
Table of Contents	vii
List of Figures.....	xi
List of Tables	xviii
Chapter 1. Introduction.....	1
1.1 – Background and Motivation.....	1
1.1.1 – Electrospinning.....	1
1.1.2 – 3D Printing (Fused Deposition Modeling).....	5
1.1.3 – Nanocomposites	8
1.1.4 – Nanocellulose Composites	8
1.1.5 – Nomenclature	9
1.2 – Thesis Objectives	10
1.2.1 – Electrospinning Objectives	11
1.2.2 – 3D Printing Objectives	11
1.3 – Thesis Layout	12
Chapter 2. Literature Review	15
2.1 – Electrospinning	15
2.1.1 – History of Electrospinning and Polymer Nanofibers	15
2.1.2 – Electrospinning of Polymer Nanofibers	16
2.1.3 – Electrospinning of Composite Nanofibers	22
2.1.4 – Parameters Affecting Nanofiber Electrospinning	26
2.1.5 – Performance of Composite Nanofiber Electrospinning	30
2.1.6 – Applications of Electrospun Nanofibers	33
2.2 – 3D Printing.....	35
2.2.1 – History of Fused Deposition Modelling.....	35
2.2.2 – 3D Printing of Thermoplastics	37
2.2.3 – 3D Printing of Nanocomposites	41
2.2.4 – Slicing and Print Processing Parameters.....	46
2.3 – Polymer Composites	49
2.3.1 – Nanocomposites	51
2.3.2 – Thermoplastic Matrices.....	53
2.3.3 – Cellulose Nanocrystal Reinforcements	53

Chapter 3. Preparation of Polycarbonate Nanofibers Containing Nanocrystalline Cellulose	57
3.1 - Introduction	57
Objective	58
3.2 – Materials	58
3.3 – Methods	59
3.4 – Results and Discussion	61
Chloroform	61
Dimethyl sulfoxide (DMSO)	62
Tetrahydrofuran (THF)	63
n,n-Dimethylformamide (DMF)	64
60:40 wt-% Tetrahydrofuran:n,n-Dimethylformamide (THF:DMF) mixture	65
Nanocrystalline cellulose (NCC) + (60:40) THF:DMF	66
3.5 – Conclusions	67
Chapter 4. Modeling Nanofibers of Polycarbonate Containing Nanocrystalline Cellulose Prepared by Electrospinning in Different Solvent Systems	68
4.1 – Introduction	68
Objective	68
4.2 – Materials	69
StarPlastic PC743R Polycarbonate	69
SABIC Lexan XL10 Polycarbonate	70
FP Innovations Ultra Nanocrystalline Cellulose	70
CelluForce Ultra Nanocrystalline Cellulose	71
CelluForce DDSA Modified Nanocrystalline Cellulose	71
Tetrahydrofuran	71
N,N-Dimethylformamide (DMF)	71
Chloroform	72
4.3 – Methods	72
4.1 – Design of Experiment Methodology	72
4.2 – Experimental Setup	80
4.4 – Results and Discussion	83
DOE#1 - 60:40 wt.-% Tetrahydrofuran:n,n-Dimethylformamide (THF:DMF) mixture	83
DOE#2 - Nanocrystalline Cellulose (NCC) + (60:40) THF:DMF	106
DOE#0 - Nanocrystalline Cellulose (NCC) + (60:40) THF:DMF (combining DOE#1 and DOE#2)	118
DOE#3 - Chloroform	122
DOE#4 - DDSA-modified Nanocrystalline Cellulose (cNCC) + Chloroform	133
4.5 – Conclusions	142
Novel Contributions	142
Challenges	143
Chapter 5. Modeling of Nanofibers of Polyamide-6,6 Containing DDSA Modified Nanocrystalline Cellulose Prepared by Electrospinning for Coating Applications	144
5.1 – Introduction	144

Objective	144
5.2 – Materials.....	145
Polyamide-6,6	145
StarPlastic PC743R Polycarbonate	145
CelluForce DDSA Modified Nanocrystalline Cellulose	145
CelluForce Ultra Nanocrystalline Cellulose.....	145
Formic Acid, 90%	145
5.3 – Methods	146
Polyamide-6,6 and 4 wt.-% cNCC in 90% Formic Acid 2 ³ Full Factorial Design of Experiments.	146
Experimental Setup	147
Surface Properties of Transparent Coatings using Electrospun PA 6,6 and PC Composite Fibers Including NCC	147
5.4 – Results and Discussion	152
2 ³ Full Factorial Design of Experiments for Fiber Diameter	152
Surface Properties of Transparent Coatings using Electrospun Composite Fibers.....	161
5.5 – Conclusions.....	167
Novel Contributions	167
Challenges	168
Chapter 6. Mechanical Characterization of 3D Printed Thermoplastic Starch-Resin Copolymer Nanocomposites Reinforced with Nanocrystalline Cellulose.....	169
6.1 – Introduction	169
Objective	169
6.2 – Materials.....	170
PSI Inc. Thermoplastic Starch-Resin Copolymer	170
CelluForce Ultra Nanocrystalline Cellulose.....	171
6.3 – Methods	171
Desktop Melt Compounding of TPS and NCC/TPS 3D Printing Filament	171
3D Printing	172
Scale Up Production of TPS Filament	173
6.4 – Results and Discussion	178
Melt Flow Index	178
Mechanical Properties.....	180
Comparison of TPS and NCC-TPS Bench and Scale-up Mechanical Properties	198
6.5 – Conclusions.....	201
Novel Contributions	201
Challenges	202
Chapter 7. Conclusions.....	203
7.1 – Summary of Electrospinning Results.....	205
7.2 – Inspiration for Continued Work.....	208
7.2.1 – Controlling Electrospinning Temperature.....	208
7.2.2 – Measuring Branching Density.....	209
7.2.3 – Measuring Porosity	210
7.2.4 – Mechanical Properties of Electrospun Fibers and Mats.....	210

7.2.5 – Measuring Nanofiber Crystallinity.....	211
References	212
Appendix A. Material Specification Sheets.....	226
Appendix B. Supplementary Electrospinning Results.....	229
B.1 – PC Electrospun Nanofibers in 60:40 (w/w) THF/DMF Solvent (DOE#1)	229
B.2 – 2 wt.-% NCC/PC Electrospun Nanofibers in 60:40 (w/w) THF/DMF Solvent (DOE#2) ...	235
B.3 – PC and 2 wt.-% NCC/PC Electrospun Nanofibers in 60:40 (w/w) THF/DMF Solvent (DOE#0).....	245
B.4 – PC Electrospun Nanofibers in Chloroform Solvent (DOE#3)	254
B.5 – 2 wt.-% cNCC/PC Electrospun Nanofibers in Chloroform Solvent (DOE#4)	266
B.6 – 4 wt.-% cNCC/PA 6,6 Electrospun Nanofibers in Formic Acid Solvent (DOE#5)	274
Appendix C. Supplementary 3D Printing Data	279

List of Figures

Figure 1.1 - Schematic diagram of typical electrospinning technique [3].....	2
Figure 1.2 - Typical morphology of electrospun polyamide-6 nanofibers observed with scanning electron microscope [4].....	3
Figure 1.3 – i) Annual patents published in electrospinning until 2008 and ii) nanofiber production industry market capitalization as of 2015 with forecasts through 2024 [5], [6].....	4
Figure 1.4 - Schematic diagrams of fused deposition modeling (FDM) of thermoplastics from the patent “Apparatus and method for creating three-dimensional objects” by S. Crump including an FDM i) 3D printer and ii) extrusion head [8]	5
Figure 1.5 – i) EY 3D printing and services industry market capitalization as of 2016 with forecasts through 2020 and ii) Wholers Associates’ annual industry report on additive manufacturing market capitalizations for equipment (purple) and materials (maroon) as of 2018, with projections [10], [11].....	7
Figure 2.1 - i) a schematic for the dry-skin model for puckering observed in PC; puckering observed for ii) chloroform and iii) THF and DMF (1:1) solvent systems; the internal rarified core showing iv) small bubbles in chloroform and v) a hollow core in THF and DMF; and crazing observed in chloroform similar to vi) bulk PC [16].....	18
Figure 2.2 - Bar graph showing bead density as a function of process voltage for a PC-CH electrospun fiber-mat [16].....	19
Figure 2.3 - Different types of collectors used in electrospinning [2].....	21
Figure 2.4 - Scale-up nanofiber production equipment: i) Elmarco’s NanoSpider and ii) FibeRio’s Cyclone [40], [41].....	22
Figure 2.5 - SEM images of A)PCL nanofibers with loadings of B) 2.5% CNX, C) 5% CNX, D) 7.5% CNX, E) 2.5% g-CNX and, F) 5% g-CNX [46].....	24
Figure 2.6 - i) DMTA results and ii) tensile test results for PCL(□) and 2.5%(□), 5%(Λ), and 7.5%(V) CNX-PCL [46]	25
Figure 2.7 - i) TEM micrographs of the in situ tensile testing of the individual nanofibers as well as ii) a schematic depicting the mechanical deformation process occurring in the composite fiber and iii) the strong stress overlapping zone in the core of the fiber [32]	26
Figure 2.8 - Visible representation of turbidity in nephelometric turbidity units (NTUs) for <0.1, 20, 200, 1000 and 4000 NTU [52].....	31
Figure 2.9 - i) Example of grid system used to choose measuring points as well as ii) measuring 379.9 nm PC nanofiber diameter using Image J image analysis software.....	32
Figure 2.10 - Examples of low (left) and high (right) concentration of bead density electrospun mats.....	33
Figure 2.11 - i) Filtration efficiency and ii) pressure drop of PC nanofiber filter in comparison with a polypropylene HEPA filter (PP) [66].....	35
Figure 2.12 - i) Adrian Bowyer and Vik Olliver, of the ii) RepRap movement, with the first parent and child Darwin FDM printers [73]	36

Figure 2.13 - Formulation and process factors in 3D printing that have an influence of the final part quality and performance [76].....	37
Figure 2.14 - 3.00 mm Thermoplastic filament spools typical of FDM processes.....	38
Figure 2.15 - Filastruder 1.0 bench-top 3D printer filament extruder [79].....	39
Figure 2.16 - i) Cartesian style Makerbot Replicator 2X and ii) Delta style SeeMeCNC Rostock Max v3.2 3D printers [80], [81].....	40
Figure 2.17 - a) LAYWOO-D3 40% wood-based composite for FDM and b) the tree ring effect observed [82]	42
Figure 2.18 -Cross sectional view of a 3D printed specimen identifying A) thermoplastic polymer chain entanglement and B) reinforcement dispersion therein, identifying how voids may be created [76].....	42
Figure 2.19 - i) diagram representing the typical hierarchical structure of an FDM assembled part and ii) microscope images of a fractured PLA FDM tensile specimen [92], [93].....	44
Figure 2.20 - 3D Printed smart ‘vessel’ and flex sensors fabricated using conductive nanoscale carbon black reinforced polycaprolactone (PCL) as conductive sensors [94].....	45
Figure 2.21 - 3D printed sample showing rectilinear fills with three different fill percentages [104]	48
Figure 2.22 - Simple diagram of a two-phase polymer composite material [18]	50
Figure 2.23 - i) Effect of the nano-scale on number of particles and surface area and ii) the interaction zone between the filler particle and matrix [110].....	52
Figure 2.24 - Effect of particle size and filler concentration on mechanical properties in polypropylene [110].....	53
Figure 3.1 – Schematic diagram of a typical vertical electrospinning apparatus.	59
Figure 3.2 – SEM micrographs of 15 wt-% PC nanofibers electrospun using chloroform. Fibers i) and ii) were electrospun using $V_{app} = 20$ kV and iii) using $V_{app} = 15$ kV over a gap distance of 15 cm.....	62
Figure 3.3 – SEM micrographs of 15 wt-% PC nanofibers electrospun using DMSO. Fibers i) were electrospun using $V_{app} = 5$ kV, ii) using $V_{app} = 15$ kV and iii) using $V_{app} = 20$ kV over a gap distance of 15 cm.	63
Figure 3.4 – SEM micrographs of 15 wt-% PC nanofibers electrospun using THF. Fibers i) were electrospun using $V_{app} = 20$ kV, ii) using $V_{app} = 25$ kV and iii) using $V_{app} = 25$ kV over a gap distance of 15 cm.	64
Figure 3.5 – SEM micrographs of 15 wt-% (98:2) PC/NCC spheres electrosprayed using DMF. Spheres i), ii), and iii) were sprayed using $V_{app} = 20$ kV over a gap distance of 15 cm.	65
Figure 3.6 – SEM micrographs of PC nanofibers electrospun using (60:40 wt-%) THF/DMF. Fibers i) were electrospun at 10 wt-% PC using $V_{app} = 10$ kV and ii) at 5 wt-% PC using $V_{app} = 15$ kV over a gap distance of 15 cm.....	66
Figure 3.7 – SEM micrographs of (5:95 wt-%) NCC-FP/PC nanofibers electrospun using (60:40 wt-%) THF/DMF. Fibers i) were electrospun using $V_{app} = 20$ kV, ii) using $V_{app} = 25$ kV, iii) using $V_{app} = 20$ kV, and iv) using $V_{app} = 20$ kV over a gap distance of 15 cm.....	67

Figure 4.1 - Repeating unit of BPA-phosgene polycarbonate	70
Figure 4.2 - Chemical structure of modifying agent (2-dodecen-1-yl) succinic anhydride (DDSA)	71
Figure 4.3 - The electrospinning apparatus used for the production of fibers in this study	81
Figure 4.4 - Working area of electrospinning equipment showing working (gap) distance, adjustable collector, and needle positioning	83
Figure 4.5 - Turbidity versus StarPlastic PC concentration in 60:40 (w/w) THF/DMF solvent for each run of DOE#1	87
Figure 4.6 - Viscosity versus StarPlastic PC concentration in 60:40 (w/w) THF/DMF solvent for each run of DOE#1	89
Figure 4.7 - Scanning electron micrographs of StarPlastic PC electrospun fibers for each run (i-xi) of DOE#1	91
Figure 4.8 - Cube plot of fitted means for the fiber diameter regression model for StarPlastic PC electrospun fibers in DOE#1	95
Figure 4.9 - Pareto chart (i) and normal plot (ii) of the standardized effects for the StarPlastic PC electrospun nanofiber diameter response of DOE#1	96
Figure 4.10 - Main (i) and interaction (ii) effects plots for the StarPlastic PC electrospun nanofiber diameter response in DOE#1	97
Figure 4.11 - Residual plots for the StarPlastic PC electrospun nanofiber diameter response in DOE#1	99
Figure 4.12 - Contour (i) and surface (ii) plots for the StarPlastic PC electrospun nanofiber diameter response in DOE#1	100
Figure 4.13 - Cube plot of fitted means for the bead density regression model for StarPlastic PC electrospun fibers in DOE#1	103
Figure 4.14 - Contour plots for the StarPlastic PC electrospun bead density response in DOE#1	103
Figure 4.15 - Cube plot of fitted means for the bead diameter regression model for StarPlastic PC electrospun fibers in DOE#1	105
Figure 4.16 - Contour plots for the StarPlastic PC electrospun bead diameter response in DOE#1	106
Figure 4.17 - Turbidity versus StarPlastic PC concentration in 60:40 (w/w) THF/DMF solvent with (DOE#2, grey) and without (DOE#1, black) 2-wt.-% NCC incorporation for all runs.....	109
Figure 4.18 - Viscosity versus StarPlastic PC concentration in 60:40 (w/w) THF/DMF solvent with (DOE#2, grey) and without (DOE#1, black) 2-wt.-% NCC incorporation for all runs.....	110
Figure 4.19 - Scanning electron micrographs of StarPlastic PC and 2 wt.-% NCC electrospun fibers for each run (i-xi) of DOE#2	112
Figure 4.20 - Contour plots for the StarPlastic PC and NCC electrospun fiber diameter response in DOE#2	115
Figure 4.21 - Contour plots for the StarPlastic PC and NCC electrospun bead density response in DOE#2	117

Figure 4.22 - Contour plots for the StarPlastic PC and PC/NCC electrospun fiber diameter response in DOE#0	121
Figure 4.23 - Contour plot for the StarPlastic PC and PC/NCC electrospun bead density response in DOE#0	122
Figure 4.24 - Turbidity versus PC concentration in chloroform solvent for StarPlastic (black) and Lexan (grey) PC for each run of DOE#3	125
Figure 4.25 - Viscosity versus PC concentration in chloroform solvent for StarPlastic (black) and Lexan (grey) PC for each run of DOE#3	126
Figure 4.26 - Scanning electron micrographs of StarPlastic and Lexan PC electrospun fibers for each run (i-xiv) of DOE#3	129
Figure 4.27 - Contour plots for the StarPlastic and Lexan PC electrospun fiber diameter response in DOE#3	131
Figure 4.28 - Turbidity versus StarPlastic PC concentration in chloroform solvent with (DOE#4, grey) and without (DOE#3, black) 2-wt.-% cNCC incorporation for all runs	136
Figure 4.29 - Viscosity versus StarPlastic PC concentration in chloroform solvent with (DOE#4, grey) and without (DOE#3, black) 2-wt.-% cNCC incorporation for all runs	137
Figure 4.30 - Scanning electron micrographs of StarPlastic and Lexan PC and cNCC electrospun fibers for each run (i-xi) of DOE#4	139
Figure 5.1 - Repeating unit of Polyamide-6,6.....	145
Figure 5.2 - Rotating drum collector built in-house for testing coating applications	149
Figure 5.3 - Schematic representation of the cross section profile of fiber deposition of transparent coatings made via rotating drum and compression techniques compared to a desired (ideal) profile	150
Figure 5.4 - i) A typical Vickers hardness tester, ii) schematic of the test parameters, and iii) a close-up image of the diamond indenter used to indent surface [165]	151
Figure 5.5 - Schematic representation of light path within a UV-Vis spectrometer apparatus [166]	152
Figure 5.6 - Turbidity versus PA 6,6 concentration in formic acid solvent for each run	155
Figure 5.7 - Viscosity versus PA 6,6 concentration in formic acid solvent for each run	156
Figure 5.8 - Scanning electron micrographs of PA 6,6 and cNCC electrospun fibers for each DOE run (i-xi)	158
Figure 5.9 - Contour plots for the PA 6,6 and cNCC electrospun fiber diameter response	161
Figure 5.10 - SEM images showing nanofiber morphology of tested material systems: i) PC, ii) NCC/PC, iii) PA 6,6, and iv) cNCC/PA 6,6	162
Figure 5.11 - Depiction of the two casting methods used for creating transparent coatings with improved surface properties, 1) Rotating Drum Technique, and 2) Compression Technique ...	163
Figure 5.12 - Coating specimen percent transmittance over the visible spectrum of wavelength	164
Figure 5.13 - Graph of Vickers Microhardness (HV) measurements for nanofiber coating samples	165

Figure 5.14 - Graph of Vickers Microhardness (HV) measurements for 2% PC/NCC coating samples for extended run rotating drum collection.....	166
Figure 5.15 - Visual representation of ideal, rotating drum (Method #1) and compression (Method #2) technique strengths (V) and weaknesses (X).....	167
Figure 6.1 - Compositional units of TPS i) amylopectin, iii) maleic anhydride (MAH), and iii) polybutyrate	171
Figure 6.2 - i) The Filastruder 3D printer filament extruder with ii) resulting 1.75 mm NCC-TPS composite filament.....	172
Figure 6.3 - i) ASTM D1708 microtensile testing specimens 3D printed with pure TPS and ASTM D256 (Impact) and ASTM D790 (Flexural) testing specimens 3D printed with ii) pure TPS and iii) 5% NCC-TPS	173
Figure 6.4 - i) commercial filament extruder at IPEG Conair North America equipped with a ii) Conair GRH-1.0 filament extrusion die and iii) HTMP multi-pass cooling and sizing tank [186]	174
Figure 6.5 - Control unit with measurement settings for Conair Filament Extrusion Line.....	177
Figure 6.6 - Melt Flow Index values for thermoplastic starch-resin co-polymer composites as a function of Nanocrystalline Cellulose additive.....	179
Figure 6.7 - Post-test ASTM D790 3D printed flexural testing specimens for a) pure TPS and b) 5% NCC-TPS.....	180
Figure 6.8 - ASTM D256 Izod Impact Strength measurements for TPS printed at varying layer heights and NCC loading.....	181
Figure 6.9 - Post break ASTM D256 Izod impact strength specimens for 300 μ m i) pure TPS, ii) 3% NCC-TPS, and iii) 5% NCC-TPS	182
Figure 6.10 - Depiction of air channels that can form inside specimens due to the 3D printing process in i) each TPS and NCC-TPS sample tested and ii) a schematic representation	182
Figure 6.11 - ASTM D1708 micro-tensile mechanical testing stress-strain curves for 3D printed 200 μ m TPS specimens.....	184
Figure 6.12 - ASTM D1708 micro-tensile mechanical testing stress-strain curves for 3D printed 300 μ m TPS specimens.....	185
Figure 6.13 - ASTM D1708 micro-tensile mechanical testing stress-strain curves for 3D printed 300 μ m 1% NCC-TPS specimens.....	186
Figure 6.14 - ASTM D1708 micro-tensile mechanical testing stress-strain curves for 3D printed 300 μ m 3% NCC-TPS specimens.....	187
Figure 6.15 - ASTM D1708 micro-tensile mechanical testing stress-strain curves for 3D printed 300 μ m 5% NCC-TPS specimens.....	188
Figure 6.16 - i) Post break ASTM D1708 micro-tensile testing specimens for 5% NCC-TPS including ii) close-up of cross-section	189
Figure 6.17 - ASTM D1708 micro-tensile mechanical testing stress-strain curves for 3D printed 300 μ m TPS specimens from scale up trial	190

Figure 6.18 - ASTM D790 flexural mechanical testing stress-strain curves for 3D printed 100 μm TPS specimens.....	191
Figure 6.19 - ASTM D790 flexural mechanical testing stress-strain curves for 3D printed 200 μm TPS specimens.....	192
Figure 6.20 - ASTM D790 flexural mechanical testing stress-strain curves for 3D printed 300 μm TPS specimens.....	193
Figure 6.21 - ASTM D790 flexural mechanical testing stress-strain curves for 3D printed 300 μm 1% NCC-TPS specimens.....	194
Figure 6.22 - ASTM D790 flexural mechanical testing stress-strain curves for 3D printed 300 μm 3% NCC-TPS specimens.....	195
Figure 6.23 - ASTM D790 flexural mechanical testing stress-strain curves for 3D printed 300 μm 5% NCC-TPS specimens.....	196
Figure 6.24 - ASTM D790 flexural mechanical testing stress-strain curves for single 3D printed 300 μm 20% NCC-TPS specimen.....	197
Figure 6.25 - ASTM D790 flexural mechanical testing stress-strain curves for 3D printed 300 μm 2% NCC-TPS specimens from scale up trial.....	198
Figure 6.26 - ASTM Tensile Modulus and Flexural Modulus measurements for TPS with varying 3D printed layer heights and NCC loading, as well as scale-up trials.....	199
Figure 6.27 - ASTM Tensile Strength and Flexural Strength measurements for TPS with varying 3D printed layer heights and NCC loading, as well as scale-up trials.....	200
Figure 6.28 - ASTM Impact Strength measurements for TPS with varying 3D printed layer heights and NCC loading, as well as scale-up trial.....	201
Figure 7.1 – Stanley hydraulic crimping attachment reduced by 3 lb. through generative design [189].....	205
Figure 7.2 - Schematic designs for proposed melt-vacuum electrospinner.....	208
Figure 7.3 - Examples of low (left) and high (right) concentration of branching density electrospun mats.....	210
Figure A.1 - Specification Sheet for StarPlastic Polycarbonate PC743R [131].....	226
Figure A.2 - Certificate of Analysis for Polycarbonate PC743R Batch 62896.....	227
Figure A.3 - Specification Sheet for Sabic Lexan XL10 Polycarbonate [146].....	228
Figure B.1 - Cube plot representation of the 3D space of DOE#1 defined by high and low factor levels.....	229
Figure B.2 - Minitab plot and chart outputs for DOE#1 – Bead Density.....	232
Figure B.3 - Minitab plot and chart outputs for DOE#1 – Bead Diameter.....	234
Figure B.4 - Cube plot representation of the 3D space of DOE#2 defined by high and low factor levels.....	235
Figure B.5 - Cube plot of fitted means for the fiber diameter regression model for StarPlastic PC and NCC electrospun fibers in DOE#2; i) without CtPt and ii) with CtPt inclusion.....	236
Figure B.6 - Cube plot of fitted means for the bead density regression model for StarPlastic PC and NCC electrospun fibers in DOE#2.....	237

Figure B.7 - Minitab plot and chart outputs for DOE#2 – Fiber Diameter	238
Figure B.8 - Minitab plot and chart outputs for DOE#2 – Fiber Diameter (including CtPt).....	240
Figure B.9 - Minitab plot and chart outputs for DOE#2 – Bead Density	242
Figure B.10 - Minitab plot and chart outputs for DOE#2 – Bead Diameter.....	244
Figure B.11 - Cube plot representation of the 3D space of DOE#0 defined by high and low factor levels	245
Figure B.12 - Cube plot of fitted means for the fiber diameter regression model for StarPlastic PC and PC/NCC electrospun fibers in DOE#0.....	247
Figure B.13 - Cube plot of fitted means for the bead density regression model for StarPlastic PC and PC/NCC electrospun fibers in DOE#0.....	247
Figure B.14 - Minitab plot and chart outputs for DOE#0 – Fiber Diameter	249
Figure B.15 - Minitab plot and chart outputs for DOE#0 – Bead Density	251
Figure B.16 - Minitab plot and chart output for DOE#0 – Bead Diameter	253
Figure B.17 - Cube plot representation of the 3D space of DOE#3 defined by high and low factor levels	254
Figure B.18 - Cube plot of fitted means for the fiber diameter regression model for StarPlastic and Lexan PC electrospun fibers in DOE#3; i) without CtPt and ii) with CtPt inclusion.....	256
Figure B.19 - Cube plot of fitted means for the bead density regression model for StarPlastic and Lexan PC electrospun fibers in DOE#3.....	257
Figure B.20 - Minitab plot and chart outputs for DOE#3 – Fiber Diameter	259
Figure B.21 - Minitab plot and chart outputs for DOE#3 – Fiber Diameter (including CtPt)....	261
Figure B.22 - Minitab plot and chart outputs for DOE#3 – Bead Density	263
Figure B.23 - Minitab plot and chart outputs for DOE#3 – Bead Diameter.....	265
Figure B.24 - Cube plot representation of the 3D space of DOE#4 defined by high and low factor levels	266
Figure B.25 - Cube plot of fitted means for the fiber diameter regression model for StarPlastic PC and cNCC electrospun fibers in DOE#4.....	267
Figure B.26 - Minitab plot and chart outputs for DOE#4 – Fiber Diameter	269
Figure B.27 - Minitab plot and chart outputs for DOE#4 – Bead Density	271
Figure B.28 - Minitab plot and chart outputs for DOE#4 – Bead Diameter.....	273
Figure B.29 - Cube plot representation of the 3D space of DOE#5 defined by high and low factor levels	274
Figure B.30 - Cube plot of fitted means for the fiber diameter regression model for PA 6,6 and cNCC electrospun fibers in DOE#5; i) without CtPt and ii) with CtPt inclusion.....	275
Figure B.31 - Minitab plot and chart outputs for DOE#5 – Fiber Diameter	276
Figure B.32 - Minitab plot and chart outputs for DOE#5 – Fiber Diameter (including CtPt)....	278

List of Tables

Table 2.1 - Diameters of electrospun, natural, and textile fibers [2]	15
Table 2.2 - Experimental process and formulation parameter constants for DOE#1	30
Table 2.3 - Comparison of the cellulosic dimensions of NCC and pulp [15].....	55
Table 2.4 - Potential applications for Nanocrystalline Cellulose [15].....	55
Table 3.1 – PC and NCC/PC electrospinning solutions process and formulation parameters.	60
Table 4.1 - Summary of factors, levels, and formulation parameters for each DOE#0 through DOE#5	69
Table 4.2 - 2^3 full factorial DOE#1, including the three different factors tested (coded a, b, c, and d*) with their low (-1), high (+1), and center point (0) values	73
Table 4.3 - Standard order of experiments for a 2^3 full factorial DOE including the treatment shorthand notation and coded factor levels; high (1), center (0), and low (-1).....	73
Table 4.4 - 2^3 full factorial DOE#1, including the three different factors tested (coded a, b, and c) with their low (-1), high (+1), and center point (0) values	74
Table 4.5 - Experimental process and formulation parameter constants for DOE#1	75
Table 4.6 - 2^3 full factorial DOE#2, including the three different factors tested (coded a, b, and c) with their low (-1), high (+1), and center point (0) values	75
Table 4.7 - Experimental process and formulation parameter constants for DOE#2	76
Table 4.8 - 2^4 full factorial DOE#0, including the four different factors tested (coded a, b, c, and d) with their low (-1) and high (+1) values.....	77
Table 4.9 - Experimental process and formulation parameter constants for DOE#0	77
Table 4.10 - 2^3 full factorial DOE#3, including the three different factors tested (coded a, b, and c) with their low (-1), high (+1), and center point (0) values	78
Table 4.11 - Experimental process and formulation parameter constants for DOE#3	78
Table 4.12 - 2^3 full factorial DOE#4, including the three different factors tested (coded a, b, and c) with their low (-1), high (+1), and center point (0) values	79
Table 4.13 - Experimental process and formulation parameter constants for DOE#4	80
Table 4.14 - DOE#1 target and actual concentration calculations for StarPlastic PC in 60:40 (w/w) THF/DMF for each 11 runs	85
Table 4.15 - Turbidity measurements for StarPlastic PC in 60:40 (w/w) THF/DMF solvent for each run of DOE#1	86
Table 4.16 - Viscosity measurements for StarPlastic PC in 60:40 (w/w) THF/DMF solvent for each run of DOE#1	88
Table 4.17 - Fiber diameter, standard deviation, and measurement counts for StarPlastic PC electrospun fibers made for each run of DOE#1	92
Table 4.18 - Bead density and measurement counts for StarPlastic PC electrospun fibers made for each run of DOE#1	102
Table 4.19 - Bead diameter, standard deviation, and measurement counts for StarPlastic PC electrospun fibers made for each run of DOE#1	104

Table 4.20 - DOE#2 target and actual concentration calculations for StarPlastic PC and NCC in 60:40 (w/w) THF/DMF for each 11 runs.....	107
Table 4.21 - Turbidity and viscosity measurements for StarPlastic PC and NCC in 60:40 (w/w) THF/DMF solvent for each run of DOE#2.....	108
Table 4.22 - Fiber diameter, standard deviation, and measurement counts for StarPlastic PC and 2% NCC electrospun fibers made for each run of DOE#2.....	113
Table 4.23 - Bead density and measurement counts for StarPlastic PC and NCC electrospun fibers made for each run of DOE#2.....	116
Table 4.24 - Bead diameter, standard deviation, and measurement counts for StarPlastic PC and NCC electrospun fibers made for each run of DOE#2.....	118
Table 4.25 - DOE#0 target and actual concentration calculations for StarPlastic PC and NCC in 60:40 (w/w) THF/DMF for each 16 runs.....	119
Table 4.26 - DOE#3 target and actual concentration measurements for StarPlastic and Lexan PC in chloroform for each 14 runs.....	123
Table 4.27 - Turbidity and viscosity measurements for StarPlastic and Lexan PC in chloroform for each run of DOE#3.....	124
Table 4.28 - Fiber diameter, standard deviation, and measurement counts for StarPlastic and Lexan PC electrospun fibers made for each run of DOE#3.....	129
Table 4.29 - Bead density and measurement counts for StarPlastic and Lexan PC electrospun fibers made for each run of DOE#3.....	132
Table 4.30 - Bead diameter, standard deviation, and measurement counts for StarPlastic and Lexan PC electrospun fibers made for each run of DOE#3.....	133
Table 4.31 - DOE#4 target and actual concentration calculations for StarPlastic PC and cNCC in chloroform for each 11 runs.....	134
Table 4.32 - Turbidity and viscosity measurements for StarPlastic PC and cNCC in chloroform for each run of DOE#4.....	135
Table 4.33 - Fiber diameter, standard deviation, and measurement counts for StarPlastic PC and cNCC electrospun fibers made for each run of DOE#4.....	140
Table 4.34 - Bead density and measurement counts for StarPlastic PC and cNCC electrospun fibers made for each run of DOE#4.....	141
Table 4.35 - Bead diameter, standard deviation, and measurement counts for StarPlastic PC and cNCC electrospun fibers made for each run of DOE#4.....	142
Table 5.1 - 2 ³ full factorial DOE including the three different factors tested (coded a, b, and c) with their low (-1), high (+1), and center point (0) values for PA-6,6-cNCC.....	146
Table 5.2 - Experimental process and formulation parameter constants for PA-6,6-cNCC electrospinning.....	147
Table 5.3 - Target and actual concentration calculations for PA 6,6 and cNCC in formic acid for each 11 runs.....	153
Table 5.4 - Turbidity and viscosity measurements for PA 6,6 and cNCC in formic acid for each run.....	154

Table 5.5 - Fiber diameter, standard deviation, and measurement counts for PA 6,6 and cNCC electrospun fibers made for each run of DOE	159
Table 5.6 - Measured fiber diameter for nanofiber material systems tested for coating applications	162
Table 5.7 - List of coating specimen percent transmittance at 545 nm wavelength.....	164
Table 5.8 - Vickers Microhardness (HV) measurements for nanofiber coating samples including standard deviation	165
Table 5.9 - Vickers Microhardness (HV) measurements for 2% PC/NCC coating samples including standard deviation for extended run rotating drum collection	166
Table 6.1 - Preliminary scale-up TPS filament extrusion temperature profiles and notes for successive trials to find ideal profile.....	175
Table 6.2 - Scale-up TPS and NCC/TPS filament extrusion temperature profiles, extruder RPM, and filament output rate for successive trials (spool number)	176
Table 6.3 - Melt Flow Index values for thermoplastic starch-resin co-polymer with Nanocrystalline Cellulose additives	178
Table 6.4 - Izod Impact Strength measurements for TPS printed at varying layer heights and NCC loading.....	181
Table 6.5 - Densities calculated for each 3D printed sample for TPS and NCC-TPS composites relative to injection molded pure TPS	183
Table 6.6 - ASTM D1708 micro-tensile mechanical testing measurements for 3D printed 200 μm TPS specimens	184
Table 6.7 - ASTM D1708 micro-tensile mechanical testing measurements for 3D printed 300 μm TPS specimens	185
Table 6.8 - ASTM D1708 micro-tensile mechanical testing measurements for 3D printed 300 μm 1% NCC-TPS specimens	186
Table 6.9 - ASTM D1708 micro-tensile mechanical testing measurements for 3D printed 300 μm 3% NCC-TPS specimens	187
Table 6.10 - ASTM D1708 micro-tensile mechanical testing measurements for 3D printed 300 μm 5% NCC-TPS specimens	188
Table 6.11 - ASTM D1708 micro-tensile mechanical testing measurements for 3D printed 300 μm TPS specimens from scale up trial.....	190
Table 6.12 - ASTM D790 flexural mechanical testing measurements for 3D printed 100 μm TPS specimens.....	191
Table 6.13 - ASTM D790 flexural mechanical testing measurements for 3D printed 200 μm TPS specimens.....	192
Table 6.14 - ASTM D790 flexural mechanical testing measurements for 3D printed 300 μm TPS specimens.....	193
Table 6.15 - ASTM D790 flexural mechanical testing measurements for 3D printed 300 μm 1% NCC-TPS specimens	194

Table 6.16 - ASTM D790 flexural mechanical testing measurements for 3D printed 300 μm 3% NCC-TPS specimens	195
Table 6.17 - ASTM D790 flexural mechanical testing measurements for 3D printed 300 μm 5% NCC-TPS specimens	196
Table 6.18 - ASTM D790 flexural mechanical testing measurements for single 3D printed 300 μm 20% NCC-TPS specimens	197
Table 6.19 - ASTM D790 flexural mechanical testing measurements for 3D printed 300 μm 2% NCC-TPS specimens from scale up trial	198
Table 7.1 - Summary of each of the responses of the six design of experiments including goodness-of-fit (R^2) and Lack of Fit (LoF) P-Values, $\alpha = 0.1$	206
Table B.1 - Target solution formulation masses for each run of DOE#1	229
Table B.2 - DOE#1 target and actual mass (m) measurements for StarPlastic PC in 60:40 (w/w) THF/DMF for each 11 runs	230
Table B.3 - Target solution formulation masses for each run of DOE#1	235
Table B.4 - DOE#2 target and actual mass measurements for StarPlastic PC and NCC in 60:40 (w/w) THF/DMF for each 11 runs.....	236
Table B.5 - Standard order of experiments for a 2^4 full factorial DOE including the treatment shorthand notation and coded factor levels; high (1) and low (-1).....	245
Table B.6 - Target solution formulation masses for each run of DOE#0	246
Table B.7 - Standard order of experiments for a 2^3 full factorial DOE including the treatment shorthand notation and coded factor levels; high (1), center (0), and low (-1) with one non-numeric (discrete) factor	254
Table B.8 - Target solution formulation masses for each run of DOE#3	255
Table B.9 - DOE#3 target and actual mass measurements for StarPlastic and Lexan PC in chloroform for each 14 runs.....	255
Table B.10 - Target solution formulation masses for each run of DOE#4.....	266
Table B.11 - DOE#4 target and actual mass measurements for StarPlastic PC and cNCC in chloroform for each 11 runs.....	267
Table B.12 - DOE#5 target and actual mass measurements for PA 6,6 and cNCC in formic acid for each 11 runs.....	274
Table C.1 - ASTM D256 Izod Impact results for 3D printed a) 200 μm TPS, b) 300 μm TPS, c) 300 μm 1% NCC-TPS, d) 300 μm 3% NCC-TPS, e)300 μm 5% NCC-TPS	279

Chapter 1. Introduction

1.1 – Background and Motivation

The primary motivation for this doctoral thesis is to explore advanced manufacturing techniques for the preparation of polymer nanocomposites with fiber-based morphologies. The techniques to be explored herein include electrospinning – a high-voltage process for the creation of nano-scale polymer fiber mats from solution – and fused filament fabrication (FFF), commercially trademarked fused deposition modeling (FDM), and more commonly referred to as 3D printing, which uses melt extrusion to build bottom-up an object of small micro-scale fibers layer-by-layer. Both of these techniques have been explored greatly in literature for many thermoplastic polymer systems, but not as thoroughly for various thermoplastic nanocomposite systems. A major focus of this thesis is to explore the effects that cellulose additives, specifically Nanocrystalline Cellulose (NCC) have on the formulation, processing, and resulting properties of electrospun fiber mats and 3D printed parts. The background and motivation for these two manufacturing processes and materials selections are described here in more detail.

1.1.1 – Electrospinning

For the past several decades, academia and industry have been pursuing the production of increasingly smaller diameter textile materials. DuPont spun the first sub-micron fibers, or nanofibers, in 1989. Since then, various methods have been explored to create these nano-scale non-woven mats including blow molding, melt-spinning, separation or extraction processes containing multiple phases, and electrospinning [1]. Electrospinning, although first patented in 1902 by J. F. Cooley, is proving itself to be one of the leading contenders in nanofiber textile production more recently. The main reason behind this includes the ability to fabricate sub-micron fibers of a wide range of materials including polymers, composites, semiconductors, metals, and ceramics. Electrospinning requires a high degree of formulation and process control allowing the tailoring of desired nanotextile morphologies and properties. This production technique has great potential for scale-up, with companies like NanoSys and Elmarco selling electrospinning equipment capable of high-throughput nanofiber synthesis. The applications for nanotextiles are broad and include filtration media, scaffolding for tissue growth, support for catalysts, composites, chemical sensors, and even electronics. [2]

Electrospinning is a technique to make micro and nano-scale fibers using a strong electric field to draw a polymer solution out of a fine tip. The electrospinning technique can be discussed easily using the schematic diagram in Figure 1.1. Electrospinning uses an applied voltage typically in the range of 5 to 30 kV to create an electric field and draws out very fine fibers from a liquid droplet. The droplet of polymer solution is formed at a charged syringe tip that is fed with a polymer solution via a syringe pump. A conical shape called the Taylor Cone is formed at the tip of the droplet attributable to the accumulation and repulsion of charges on the droplet surface. Small amounts of solution are pulled away from the droplet, as the surface tension is broken because of a force imbalance caused by the electric field. This forms a long fiber attributable to

polymer chain entanglement in the solution as it whips through the gap distance towards the grounded base collector; the area where the whipping of the electrospun jet occurs is termed the instability region. The fibers are gradually deposited on a collector several centimeters below the needle in a non-woven mat.

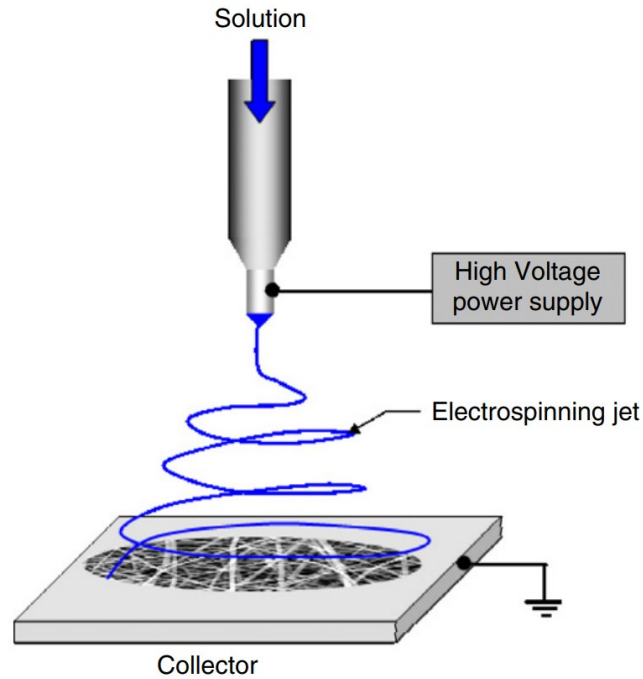


Figure 1.1 - Schematic diagram of typical electrospinning technique [3].

These fibers typically have a sub-micron diameter (<1000 nm) and can go as low as a few nanometers and have countless possible applications. Because of the benefits of the extremely high surface area to volume ratio on the nanoscale, electrospinning is opening a new manufacturing field, which hopes to find new applications for well-known polymer systems. Electrospinning is thus a relatively simple and low-cost method to achieve nano-scale fibers with desired properties in a non-woven mat. A scanning electron micrograph of a typical polyamide-6 nanofiber mat is presented in Figure 1.2.

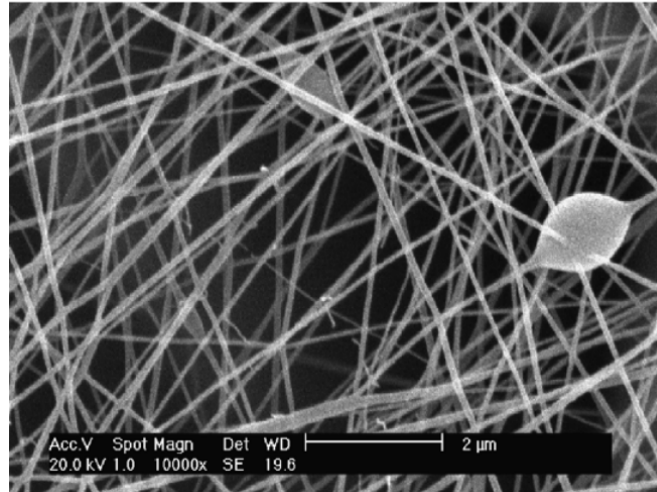


Figure 1.2 - Typical morphology of electrospun polyamide-6 nanofibers observed with scanning electron microscope [4].

The advantages of these nano non-woven mats over traditional textiles include the higher surface area to volume ratio, high porosity, surface functionalization, and great improvement in mechanical properties [5]. In the past two decades, the focus has shifted from the creation of these fibers to pursuing commercial applications (like catalysis and ultra-fine filtration); this is evident in Figure 1.3(i) which depicts a survey of electrospinning patents as of 2008 [5]. There is an obvious exponential increase after 2001 with nearly 44% of the awarded patents involving composite reinforcement and filtration and the remaining patents covering a broad spectrum of applications.

The market size of worldwide nanofiber production was approximately \$390.6M in 2015 up from about \$140M USD in 2011. The annual growth rate for nanofiber production by electrospinning is expected to be 25.3% between 2016 and 2024 [6], [7]. It is also interesting to note that cellulose nanofibers are expected to be the fastest growing segment of all nanofibers between 2016 and 2024 because of shifting consumer focus to sustainable materials, this is also expected to drive bio-based nanoparticle demand over the coming years. It is expected that the overall nanofiber production market will reach over \$550M by 2024 with polymer nanofibers taking up over half of the material of choice, this is represented in Figure 1.3(ii).

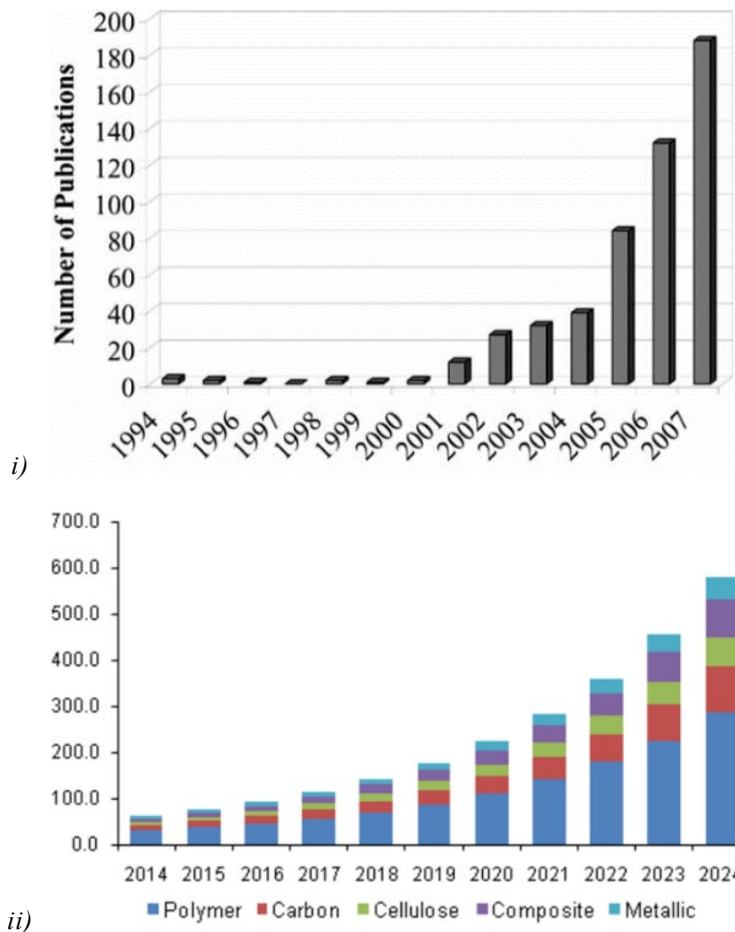


Figure 1.3 – i) Annual patents published in electrospinning until 2008 and ii) nanofiber production industry market capitalization as of 2015 with forecasts through 2024 [5], [6]

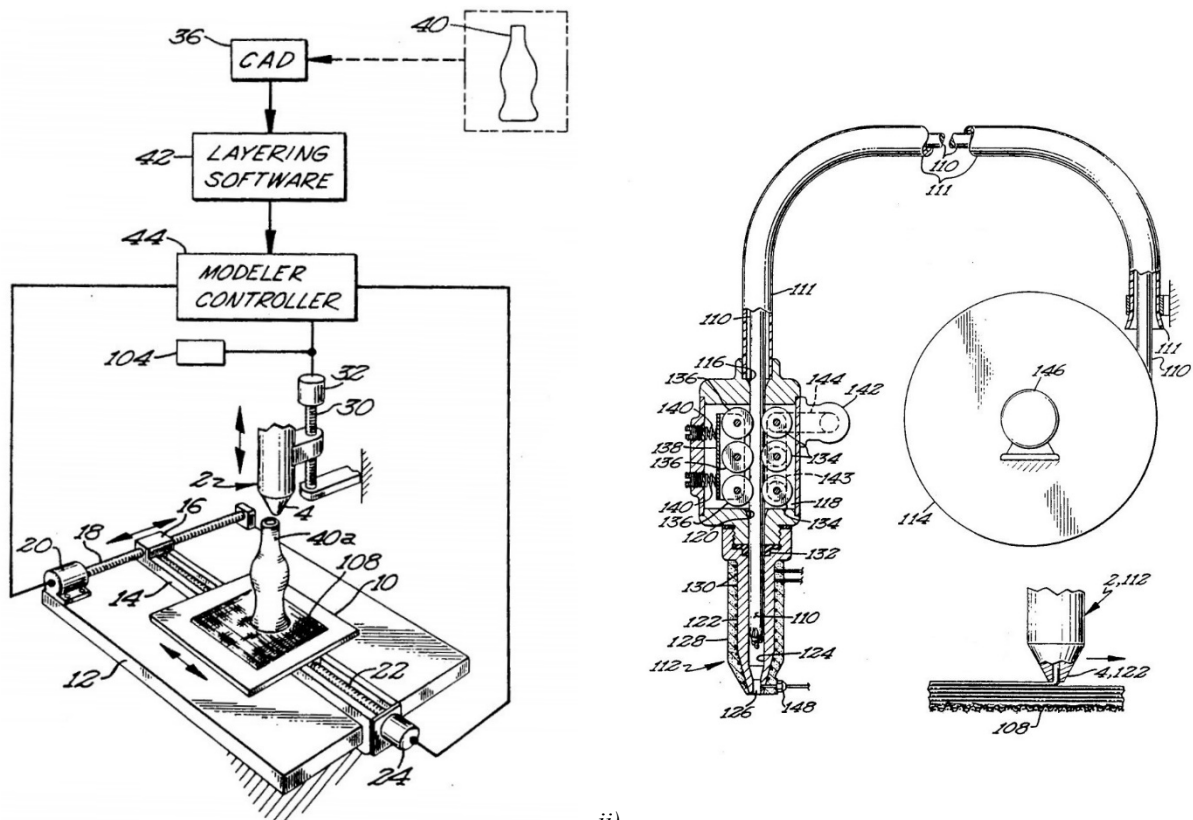
There is a recent drive towards developing engineered nanomaterials; as a consequence, electrospinning is emerging as a contender for the synthesis of these material systems. With the development and advancement of tools like scanning probe microscopy, transmission electron microscopy, and scanning electron microscopy, the design and analysis of these engineered nanomaterials is made easier and thus more feasible for commercial applications.

There are several other material formulation and process parameters that could affect the size and morphology of the resulting electrospun fibers. The material formulation parameters are typically type of solvent, type of polymer, polymer molecular weight and distribution, concentrations and additives. Process parameters include collector type, applied voltage, gap distance, syringe feed rate, needle tip diameter and environmental factors like humidity (or concentration of solvent) and temperature. Other parameters like control of the electric and magnetic fields in the whipping region are possible. Relevant parameters to this study will be discussed in more detail in the following chapters.

1.1.2 – 3D Printing (Fused Deposition Modeling)

Three-dimensional (3D) printing is an additive manufacturing (AM) process used to create 3D objects using computer-aided manufacturing (CAM) software. Many different AM processes exist for various materials with the common trait of the desired 3D object being built layer-by-layer. For polymers, various specific AM processes have been developed including: stereolithography (SLA) and digital light processing (DLP) for photopolymers; laminated object manufacturing (LOM) for polymer films; selective heat sintering (SHS) and selective laser sintering (SLS) for granular thermoplastic powders; and fused deposition modeling (FDM) for thermoplastic filaments and pellets. The focus of this exploration of new composite thermoplastics will be done primarily with the FDM process as the viable process herein.

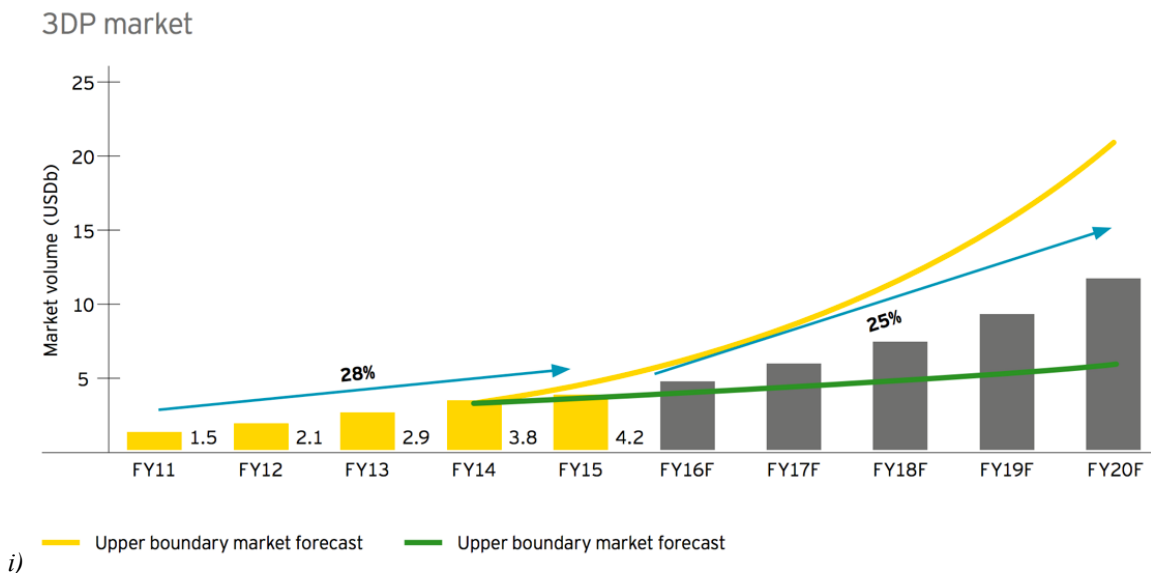
FDM works by passing a thermoplastic polymer filament through a nozzle heated above the melt temperature where the molten polymer is extruded through the nozzle. The polymer is deposited in the x and y directions (horizontal) creating a two-dimensional planar pattern on a build platform, the nozzle then raises slightly in the z axis (vertical) and continues with the next layer and so on, until the object is complete (see Figure 1.4 depicting the FDM fabrication of a soda pop bottle) [8].

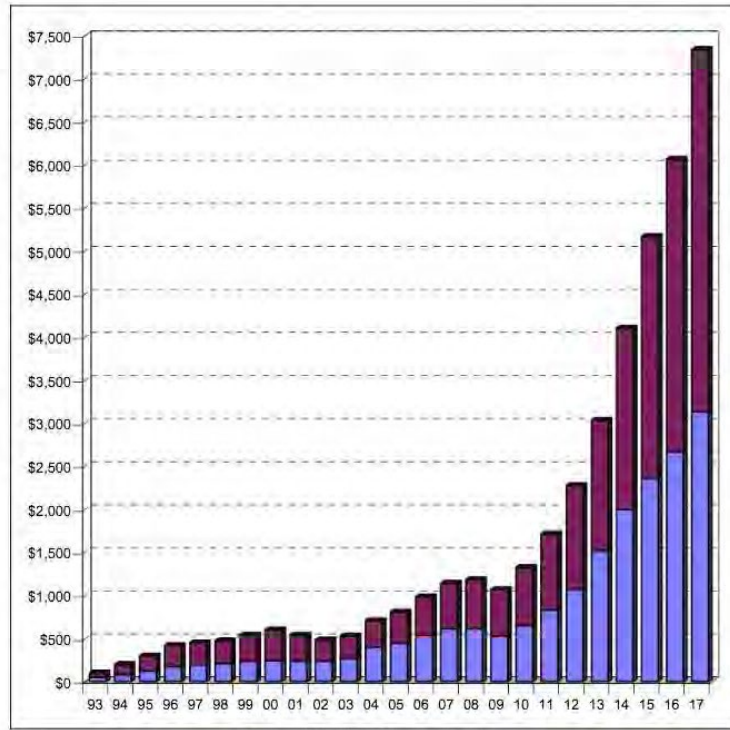


i) ii)
Figure 1.4 - Schematic diagrams of fused deposition modeling (FDM) of thermoplastics from the patent “Apparatus and method for creating three-dimensional objects” by S. Crump including an FDM i) 3D printer and ii) extrusion head [8]

Advantages of the fused deposition modeling (FDM) process over traditional process like compression and injection molding come from the customizability, rapid prototype iterations, and complex designs not previously capable with traditional manufacturing methods. Customizability is not feasible using traditional methods as they are intended for the mass production of the exact same object, with changes requiring new tooling; for example, in injection molding and compression forming. There are endless possibilities for mass customization and mass personalization in 3D printing, such as for personalized prosthetics and bone replacements that differ greatly from person to person. Hardware designers can now rapidly iterate their design process using FDM, being able to physically hold their device within minutes after each design change, as opposed to purchasing a one-off injection mold die and waiting weeks to months to hold their product. 3D printers are even being used to make molds and dies for injection molding for low production runs in the thousands to tens of thousands [9].

According to EY, in 2015 the 3D printing and services market was valued at about \$4.2B USD compared to about \$1.5B in 2011 [10]. The annual growth rate for these years was about 28%, but this growth rate decreased slightly in 2016 mainly attributable to declines by two of the major manufacturers. EY expects the annual growth rate to continue at about 25% until 2020 when the 3D industry will reach about \$12B in value as projected in Figure 1.5. The Wholers report on the 3D printing industry for 2016 suggests that the market is approximately \$6.06B USD in size [11]. Much of this growth is fueled by new technologies and materials such as metal 3D printing and adoption of the technologies by businesses. In April 2016, 24% of all 900 companies surveyed by EY perceive 3D printing as a strategic or important topic for their company, 24% of companies have some experience in the area and 12% of companies are considering adopting 3D printing [10].





Source: Wohlers Associates, Inc.

ii)

Figure 1.5 – i) EY 3D printing and services industry market capitalization as of 2016 with forecasts through 2020 and ii) Wohlers Associates’ annual industry report on additive manufacturing market capitalizations for equipment (purple) and materials (maroon) as of 2018, with projections [10], [11]

Companies like Stanley Black & Decker, Ford Motor Company, Boeing, Apple, Nike and others use FDM processes during their design phase [12]. In fact, around a third of the plastics, automotive and aerospace, and pharmaceutical companies that use 3D printing use it for end components or products [10]. Another very important advantage of the FDM process is the ability to create very complex designs, including an internal structure, that are impossible using any other process. For example, an intricate honeycomb design could be made inside an airplane wing to increase the strength to weight ratio, this can now be manufactured in a one-step process.

Although the FDM method appears very promising, there are some disadvantages compared to traditional polymer processing. This includes a much longer time required to manufacture a single item. Because it is only feasible for custom or high value-added parts, it will likely not disrupt traditional mass manufacturing techniques for common goods. Both the commercial and desktop 3D printers still require a large amount of knowledge and maintenance to operate; it has not yet met yet the ease of use of an ink-jet printer. At the moment, the materials, accuracy, and size of the 3D print also limit the overall AM process, but these boundaries are being pushed with new developments every day.

There is a potential to expand current 3D printing applications through increasing the material options to include thermoplastic composites, specifically nanocomposites. The inclusion of mechanical and functional nanoparticles into the plastic feedstock can modify the material properties of 3D printed parts. As this is a new area of research, material formulations and printing

processes need to be derived before the application benefits can be realized. This study will take a closer look at the creation of new 3D printer nanocomposite filaments containing cellulosic reinforcements, like Nanocrystalline Cellulose, to improve processing and resulting mechanical properties. The FDM processability of these new nanocomposites will also be explored to identify the parameters required for successful prints. 3D printing of different plastic matrices will also be explored and how the mechanical properties compare to traditional manufacturing methods like injection molding and compression molding.

1.1.3 – Nanocomposites

Thermoplastic composites are created through the introduction of a secondary material (or dispersed phase) into a polymer matrix; this process is a common practice in polymer technology to reduce the cost of formulation or to change the attributes or desirable property of the material. Typically, the composite will maintain the melt processability of the thermoplastic matrix, which is beneficial for manufacturing with it, while the additives impart some additional property benefit like an improvement of conductivity or mechanical properties. In general, when nanomaterials are added to a polymer matrix it is not done to decrease cost, but to achieve new properties or to change the attributes of the final systems which can lead to redesign and miniaturization of products.

For example, the incorporation of carbon nanotubes within the polymer matrix is carried out for improved mechanical, thermal, and electrical properties [13]. The increasing of mechanical properties can be attributed to the higher interface volume of the composite located near the interface of the reinforcement and polymer matrix. This interface layer, or interphase, has different properties than the bulk material depending heavily on the components and their compatibility and can extend 4 to 160 nm from the reinforcement surface. High aspect ratio reinforcements (fibers, whiskers, rods or plates) can also improve the mechanical properties through high flexural strength, high stiffness and easier percolation, and in the case of FDM or electrospinning, there is also the potential for nanoparticle alignment. Exploitation of these phenomena is desirable in the design of new high strength composites. [14]

There is a gap in literature with respect to the research and development in the area of nanocomposite thermoplastics for fused deposition modeling (FDM) and electrospinning. Most of the current literature is comprised of researchers trying to exploit the conductive properties of carbon-based nanomaterials, like carbon nanotubes. More experimentation and study should be carried out for improvements in mechanical properties. Using a nano-reinforcement like Nanocrystalline Cellulose also has the added benefit of being renewable, biocompatible, and biodegradable increasing the overall sustainability of the produced electrospun mat or 3D printed part.

1.1.4 – Nanocellulose Composites

A new natural nanoparticle derived from wood pulp, called Nanocrystalline Cellulose (NCC), is showing promising attributes for inclusion in polymer composites. The typical NCC whisker is on the order of 10 nm by 200 nm comprised of many cellulose β -glucan chains tightly bound together to form a very strong crystalline material. The theoretical strength of NCC is on the order

of stainless steel and carbon nanotubes but unlike these inorganic reinforcements, is made from renewable and biocompatible sources. The high strength makes this nanoparticle a great candidate for incorporation into composites and more specifically electrospun nanofibers. Nanocrystalline Cellulose sources are discussed in more detail in the following chapters. [15]

Polycarbonate (PC) is an engineering thermoplastic that has a broad range of physical material properties that are advantageous to nanofiber materials. These physical properties include great heat resistance, impact strength, rigidity, and toughness, which is why PC is used in a wide range of high-strength applications like armored vehicles, safety paneling, and architecture. The electrospinning of PC is also being extensively explored for high strength and biocompatible applications with various groups fabricating micro- and nano-porous materials. [16]

The incorporation of Nanocrystalline Cellulose into a polycarbonate matrix through thermal processing techniques has been previously explored in Leonardo Simon's lab – in fact it was the primary focus of my Master thesis, Cellulose-Polycarbonate Nanocomposites: A novel window alternative. The incorporation of NCC could provide improved mechanical properties like strength as well as increasing hardness while maintaining the toughness of the PC. This increased hardness is beneficial in increasing scratch resistance in bulk applications and pitting attributable to impact in filtration applications. Thermal degradation of the NCC occurred as a result of the high processing temperatures of melt compounding leading to less than desirable mechanical properties. [17], [18]

The incorporation of NCC within electrospun PC nanofibers is much more feasible technique for nanocomposite processing as it is a solvent based process that does not require the NCC to reach high temperatures. The hypothesis is that the inclusion NCC will further improve the already strong PC electrospun fibers expanding the potential applications in high strength nanotextile applications, like high throughput filtration for example.

NCC additives can also provide benefits to the area of 3D printing. Thermoplastic starch-resin copolymer (TPS) is a new polymer being developed that has beneficial properties over current commercial polymers. For example, TPS is developed from sustainable sources and is biocompatible and biodegradable with potential applications in packaging and consumer goods. Compounding the TPS with NCC can lead to an all-natural nanocomposite with enhanced mechanical properties as well as better ease and reliability of processing via fused deposition modeling 3D printing.

1.1.5 – Nomenclature

It is important to clarify the difference in nomenclature used within this document between nanofibers, nanofibril, nanowhiskers, and nanocrystals. A main differentiator between the terms is the aspect ratio of the nanomaterial, nanowhiskers and nanocrystals having an aspect ratio of about 20:1 (length to diameter ratio) and nanofibrils and nanofibers being much larger, typically greater than 100:1. Nanocrystals is a term that is used in place of nanowhisiker if the material is primarily crystalline, as is the case of Nanocrystalline Cellulose.

Whenever possible the term *nanocrystal* will be preferred over *nanowhisker* when referring to the crystalline cellulose materials. The use of the term *nanofibril* will be limited as the Nanocrystalline Cellulose (NCC) is typically derived from the nanofibrils and as there will be no NCC synthesis involved herein, thus the use of the term nanofibril will be minimal.

Cellulose nanowhiskers are a new material and are still referred to by various nomenclatures including cellulose nanocrystals (CNX or CNC) as well as Nanocrystalline Cellulose (NCC). The terms Nanocrystalline Cellulose and NCC have been trademarked by manufacturer CelluForce Inc., of which is the primary source of nanocellulose for this research. Herein, the term Nanocrystalline Cellulose or NCC will be used when referring to cellulose nanowhiskers or nanocrystals.

In the rest of this document the term *nanofiber* will be used specifically to address the electrospun polymer fibers and will be avoided as a descriptor of the NCC. Polymer nanofibers produced by electrospinning have diameter that can be as small as 20 nm with very long (hundreds of times the larger than its diameter) lengths making them nanoscale in one dimension. Some electrospun fibers produced may have diameters above 100 nm but may be referred as nanofibers; this will be a very small proportion of the spun fibers.

Another important naming distinction that should be noted is, that throughout the experimentation within this document, when the term 3D printing is used without further clarification, it is specifically referring to fused deposition modelling (FDM). This is commonplace in the additive manufacturing industry; if another additive manufacturing technique is discussed it will be mentioned by name.

Throughout the experimental section of this thesis, shorthand notation is often used for simplicity. For example, polylactic acid (PLA) that has been sourced from Mixshop Inc. has been coded mPLA. Each of the shorthand notations, or coding, have been outlined at the beginning of any relevant section.

1.2 – Thesis Objectives

The overarching objective for this thesis is to explore new processing methodologies, including advanced manufacturing techniques like electrospinning and fused deposition modeling (FDM), for their feasibility with the use of polymer thermoplastic nanocomposites.

The specific nanomaterial chosen for this study is Nanocrystalline Cellulose (NCC) from CelluForce, a project sponsor and the company where my co-supervisor, Dr. Richard Berry, acts as the Chief Technology Officer (CTO). The motivation with NCC is to explore the potential of this material for making improvements in the processing and resulting composite material properties and thus finding new commercial applications. For example, alignment and percolation of NCC within the electrospun nanofibers results in improved performance mats or improved melt viscosity and strength in the deposited microfibers of the FDM process.

The polymer matrices chosen for this study were based on literature review, industry preferences, Dr. Simon's laboratory focus, and my MASc research findings. One discovery of my MASc thesis

was temperature instability of the NCC while melt compounding with PC which can be alleviated if using low temperature solution-based mixing – like the case with electrospinning [18]. One desired property in FDM is flexible polymers, which, along with laboratory partnerships, led me to discover a new material termed thermoplastic starch-resin copolymer (TPS). Mixing of NCC with TPS for 3D printing should be more feasible than my MASc PC study because of the much lower melting temperature and processing of TPS.

1.2.1 – Electrospinning Objectives

The main objectives for the electrospinning research in this study primarily focus on the polycarbonate (PC) or polyamide-6,6 (PA 6,6) with Nanocrystalline Cellulose (NCC) systems and include developing a processing methodology for the electrospinning of high-quality polycarbonate and Nanocrystalline Cellulose reinforced composite nanofibers by minimizing defects and maximizing the uniformity of the nano-scale diameter. This will be completed through a series of designs of experiments (DOEs) where different processing parameters are explored and their effects on the resulting fiber’s morphological properties, or responses.

Also, a major objective is to select the ideal formulation parameters of the electrospun composite material to achieve improved morphological property performance like fiber diameters, number of defects (or beading density), and their size (bead diameter). The ideal formulation parameters are developed through the same DOEs as above in addition to basic experimentation and literature publications.

Studying the relationship of both the formulation and processing parameters allows us to build a linear regression model for each of the material systems studied and infer changes that can be made to tune the system and achieve desired material performance and characteristics.

Additional secondary electrospinning objectives that were explored include:

1. Exploring the use of modified NCC for improved composite mixing;
2. Using a rotating drum collector to collect axially aligned nanofibers; and
3. Exploring the application of electrospun nanofibers in a transparent coating by testing microhardness and transmission in the visible spectrum.

1.2.2 – 3D Printing Objectives

One of the main objectives for the fused deposition modeling research in this study focus on the comparison of TPS mechanical properties between FDM and other more traditional polymer processing methods like injection molding and compression molding. Although 3D printing allows for rapid manufacture and complete part customization, it is assumed there may be some reduction in material properties – like modulus – attributable to the small imperfections introduced by the individual microfiber tracks and layer by layer adhesion.

Another major objective, to improve upon the reduction of properties as a result of the FDM process, was to introduce a nano-reinforcement, specifically NCC, to the TPS polymer matrix.

Additional secondary fused deposition modeling objectives that were explored include:

1. Desktop production of composite filaments feedstock for FDM 3D printers; and
2. Scale-up evaluation of filament manufacture of the TPS and TPS/NCC systems.

1.3 – Thesis Layout

The overall layout of this thesis is presented here and brings together the relevant sections of this document, thus allowing the reader to quickly grasp the nature of this research work, its scope, materials and methodology. It also gives quick reference to the section numbers of the content. Chapter 3 through Chapter 6 present four different research studies that were completed for this thesis. Each of these chapters is presented as an independent paper prepared for publication.

Chapter 1 – Introduction

This initial chapter reveals background and motivations of this PhD research as well as the objectives that will be covered. Market factors, advantages, and disadvantages that effect the advanced manufacturing industry and the research and development that enable new fiber-based systems within the nanocomposite sector are explored. Specific focus will be on formulation and processing of polymer nanocomposites with NCC for applications in electrospinning and 3D printing processes.

Chapter 2 – Literature Review

This chapter covers relevant background information from literature that should be sufficient to understand the design of polymer nanocomposites, production through electrospinning and 3D printing, and the characterization techniques used. The different synthesis methods of the nanocomposites are discussed. Specifically, electrospinning and 3D printing techniques will be explored.

Chapter 3 – Preparation of Polycarbonate Nanofibers Containing Nanocrystalline Cellulose

At present there is not a large amount of research on electrospinning Nanocrystalline Cellulose (NCC) with polymers and virtually nothing using a polycarbonate matrix with NCC [19]. This work will explore the new developments in electrospinning of polycarbonate and polycarbonate reinforced with NCC. The objective is to achieve desirable fiber size and morphology. The five solvent systems investigated for PC were dimethyl sulfoxide (DMSO), tetrahydrofuran (THF), n,n-dimethylformamide (DMF), chloroform and a THF/DMF solvent mixture. The DMF and THF/DMF solvent mixture systems – with PC – were then electrospun with the incorporation of NCC.

Chapter 4 – Modeling Nanofibers of Polycarbonate Containing Nanocrystalline Cellulose Prepared by Electrospinning in Different Solvent Systems

This work will explore the production of polycarbonate (PC) polymer nanofibers containing Nanocrystalline Cellulose (NCC). The objective is to produce nanofibers using electrospinning, to characterize the nanofibers, and to correlate the type of nanofibers produced with the process parameters. Five different designs of experiment (DOEs) were analyzed as an investigative process to develop models for fiber diameter, bead diameter, and bead density of the material systems in study.

Linear regression models for fiber diameter, bead density, and bead diameter were developed for five material systems including a polycarbonate matrix. Solvent formulation performance including the turbidity and viscosity of the prepared solutions are also presented, including prediction models as a function of solvent formulation. Two solvent systems that were identified in Chapter 3, Preparation of Polycarbonate Nanofibers Containing Nanocrystalline Cellulose, were chosen for this study as there is not any current published literature for PC/NCC fibers with these solvent systems. The solvent systems explored include a 60:40 (w/w) mixture of tetrahydrofuran (THF) and n,n-dimethylformamide and chloroform.

Chapter 5 – Modeling of Nanofibers of Polyamide-6,6 Containing DDSA Modified Nanocrystalline Cellulose Prepared by Electrospinning for Coating Applications

At present, there is limited peer reviewed research on electrospinning of DDSA modified Nanocrystalline Cellulose and at the time of writing, there is no literature that includes the electrospinning of DDSA modified NCC (coded cNCC herein), including the use of a polyamide-6,6 (PA-6,6) thermoplastic matrix. This work will explore new developments in electrospinning of PA-6,6 reinforced with modified cNCC and the resulting effect on the fiber diameter of resulting fibers. A 2³ full factorial design of experiments has been developed to explore the fiber diameter effects of polyamide-6,6 concentration ([PA 6,6]), applied voltage, and gap distance of polyamide-6,6 composite nanofibers reinforced with 4-wt.% of cNCC. The objective is to create a regression model for fiber diameter of PA 6,6 and cNCC nanofibers that can be used to identify critical experimental formulation and performance parameters influencing the final fiber product.

The inclusion of cNCC in the polyamide 6,6 matrix will improve the mechanical properties of the final electrospun mat compared to PA 6,6 alone. This will be explored through the creation of transparent coatings with improved surface properties. The coatings will be comprised of embedded electrospun nanofibers in an epoxy matrix; prepared via rotating drum collection and compression forming methods. Transparency and surface mechanical properties will be tested for PA 6,6, and PA 6,6 reinforced with cNCC, as well as a comparison to the polycarbonate (PC) and PC reinforced with NCC (un-modified) electrospun fibers presented in earlier work. PA 6,6 and PC are choice engineering thermoplastics for applications that require strength, high modulus and toughness in high-temperature environments, such as light shrouding and engine covers in automotive applications. Improving the surface properties of these parts can increase the products lifetime as well as expand current usage applications, like windows and screens.

Chapter 6 – Mechanical Characterization of 3D Printed Thermoplastic Starch-Resin Copolymer Nanocomposites Reinforced with Nanocrystalline Cellulose

This study investigates the application of 3D printing for a new thermoplastic starch-resin copolymer (TPS) developed in Ontario, reinforced with Nanocrystalline Cellulose (NCC). This new TPS material has unique material properties (like ductility and flexibility as well as being biodegradable) that have strong potential as a consumer 3D printing material. The TPS matrix was also compounded with NCC to aid in processing both the filament feedstock for the 3D printers as well as the fused deposition modeling of a final product. The mechanical properties and trends are compared to literature values for injection molded TPS.

This study will look at the bench scale feasibility of producing TPS composite filaments for 3D printing; the effect of 3D printing parameters on mechanical properties; the advantages of addition of a biodegradable nano-reinforcement, specifically Nanocrystalline Cellulose (NCC), to create an all-green nanocomposite for 3D printing; and the production scale-up of TPS and NCC-TPS composite filaments. The final section takes the TPS and NCC-TPS systems from the bench scale and tests the scaling up of filament production. It is a preliminary investigation to explore increasing filament production from 1 foot per hour to over 500 feet per hour. This scale up trial tests the ability to take the material to market and what effects it may have on resulting mechanical properties.

Chapter 7 – Conclusions

This final chapter will summarize the main conclusions addressed by this study, how they can contribute to scientific literature, and address any work or direction that the study should take in the future.

Chapter 2. Literature Review

2.1 – Electrospinning

Electrostatic spinning, better known as electrospinning, is one of the most appropriate and scalable technologies for the production of quality nanofibers. There is currently commercial production of nanofibers produced through electrospinning for applications in filtration, medical devices and pharmaceuticals, and textiles. The typical diameters of polymeric nanofibers produced via electrospinning are 50 to 900 nm when properly controlled, and the mat can contain smaller fibers approaching 2 or 3 nm in diameter. Electrospun nanofibers are up to two orders of magnitude smaller with respect to common natural and textile fibers available commercially today, a short list of these materials with their typical diameters are included in Table 2.1. [2]

Table 2.1 - Diameters of electrospun, natural, and textile fibers [2]

Fiber	Diameter (μm)	Coefficient of Variation (%)
E-spun fiber	0.05-0.9	-
Spider silk	3.57	14.8
Bombyx mori silk	12.9	24.8
Merino wool	25.5	25.6
Human hair	89.3	17.0
Cotton	10-27	2.5
Polyester	12-25	4-5
Nylon	16-24	3-6

The following literature review will cover the history and current status of polymeric nanofibers, composite nanofibers, and their potential commercial applications.

2.1.1 – History of Electrospinning and Polymer Nanofibers

Lord Rayleigh first conceived the concept of electrostatic spinning in the late 19th century, over 100 years ago. The first documented accounts for the spinning a polymer solution into fibers using an electric field occurred in 1902, when Cooley and Morton filed the first patents on the technique. The patents identified the application of a polymer solution to the surface of a positively charged brass sphere that was then brought close to a sphere with opposite charge and a “cob-web like mass” was created. Little has changed in the fundamentals of the electrospinning technique over time. [2], [5]

A major improvement of the technique occurred through 1934 to 1944 when Formhals filed many patents on improvement of the process and apparatus. He designed a moving collector that was able to achieve some alignment of the fibers as well as a better understanding that the fibers should dry completely before striking the collector to achieve a smaller diameter. Formhals filed patents

on multi-component material systems that would include several types of nanofibers. It is interesting to note, as well, that the preferred polymer system for electrospinning by both Cooley and Formhals was cellulose acetate or cellulose nitrate in acetone, not too different in chemical makeup than the NCC used in this study. [2], [5]

Following the advancements by Formhals, Sir Geoffrey Taylor's work in the 1960s focused on the theoretical understanding of the electrospinning process. In 1969, Taylor published his work on the shape of a polymer droplet in the presence of an electric field [20]. He determined that the polymer droplet would form a conical shape when the surface tension and electrostatic forces were in balance. When the surface tension of the solution was overcome, it was always at the tip of this cone and resulted in a jet with diameters much less than that of the droplet. This conical shape was later referred to by him - and now most of the electrospinning industry - as the Taylor Cone. His interest later shifted into determining the effects that different processing parameters had on the resulting morphology. [2], [5]

In 1971, Peter Baumgarten began experimenting with viscosity (polymer concentration), applied voltage, and the use of a pump for longer spinning times [21]. Baumgarten claimed to achieve fiber diameters on the order of 500 to 1100 nm. In the 1980s, Larrondo and St. John Mandley reported the electrospinning of polyolefins via melt-electrospinning, which required higher processing voltages and temperatures (~200 °C) and resulted in larger fiber diameters. [2], [5]

The resurgence of electrospinning began in the 1990s when the imaging tools improved significantly and researchers such as the Reneker group demonstrated electrospinning of various polymer systems giving ultrathin fibers [22]. The resurgence was also driven by the appreciation of these fibers and the realization of potential applications as well as developments in fluid dynamics and electrostatics [23]–[25]. There were many difficulties facing the early experimentalists, including trying to understand the formation of “beads” within their samples and noticing how the bead shapes changed with the electric field [26], [27]. Up until now more than a hundred natural and synthetic materials have been successfully electrospun with the diameters ranging from a few nanometers up to several micrometers. [2], [5]

2.1.2 – Electrospinning of Polymer Nanofibers

Formulation Design

Numerous material systems have been explored via the electrospinning technique including polymers, inorganics, and composite systems. For example, poly(ethylene oxide) [26], poly(vinyl alcohol) [28], polypropylene [29], [30], polyethylene [31], polyamide [4] and polycarbonate [16], [32]–[34] solutions have been well documented in literature. This is not a comprehensive list, as stated earlier; over one hundred different natural and synthetic polymers have been examined. The focus of the formulation here will remain specific to polycarbonate (PC) materials.

Krishnappa et al. have completed an extensive study where the morphology of electrospun PC was analyzed as a function of the solvent and processing voltage. The bisphenol-A polycarbonate was spun at a concentration of 14% and 15% in both chloroform and a 1:1 mixture of THF and DMF.

The solution was placed in a pipette with an applied voltage between 6 and 30 kV over a gap distance ranging from 8 to 12 cm. [16]

Different morphological features of the PC fibers were analyzed including fiber diameter distribution, internal structure and bead density variation with respect to processing voltage. Each of these features was dependent on the solvent system used. The fiber diameter of chloroform-spun fibers ranged from sub-micron to several microns in diameter, with most of the fibers falling within 2 to 3 microns. The fiber diameters of the mixed THF and DMF solvent were smaller with fibers falling between 100 and 500 nm with the majority between 150 and 200 nm. Larger fibers (3-5 μm) spun with the chloroform solvent had a flattened or collapsed structure whereas the mixed solvent system did not exhibit any of the flat fibers. When the electric field is held constant the system with higher viscosity and volatility exhibited larger fiber diameters. [16]

The electrospun PC fibers also develop a raisin-like wrinkled surface that is observed in both solvent systems, this is depicted in Figure 2.1. This may be of benefit if a higher surface area is desired but will also likely lead to lower mechanical properties. These types of wrinkled fibers could have added value as they would likely have a higher scattering coefficient, which could help in high throughput filtration applications. They would also likely have less bonded area between fibers within the mat, which in some products might be valuable. Additionally, crazing of the surface of polycarbonate is observed in the presence of solvent in bulk as well as in the electrospun nanofibers. In both solvent systems, this puckering is observed in larger particles and beads, and can be attributed to the evaporation of the solvent within the fiber from surface inwards to the core. There is a dry surface before the jet is completely dry on the inside, as the solvent evaporates it creates a dry skin that collapses creating the morphology; a schematic for the dry-skin phenomena is seen in Figure 2.1(i). The same effect is attributed to fibers that warp or flatten. The mats were imaged using transmission electron microscopy (TEM). In chloroform, small bubbles are observed and seen in Figure 2.1(ii, iii). In the THF and DMF solvent mix there is a hollow core structure observed in Figure 2.1(iv, v). Crazing of the polycarbonate nanofiber surface is observed in chloroform in Figure 2.1(vi), with effects very similar to those observed in bulk PC, seen in Figure 2.1(vii). [16]

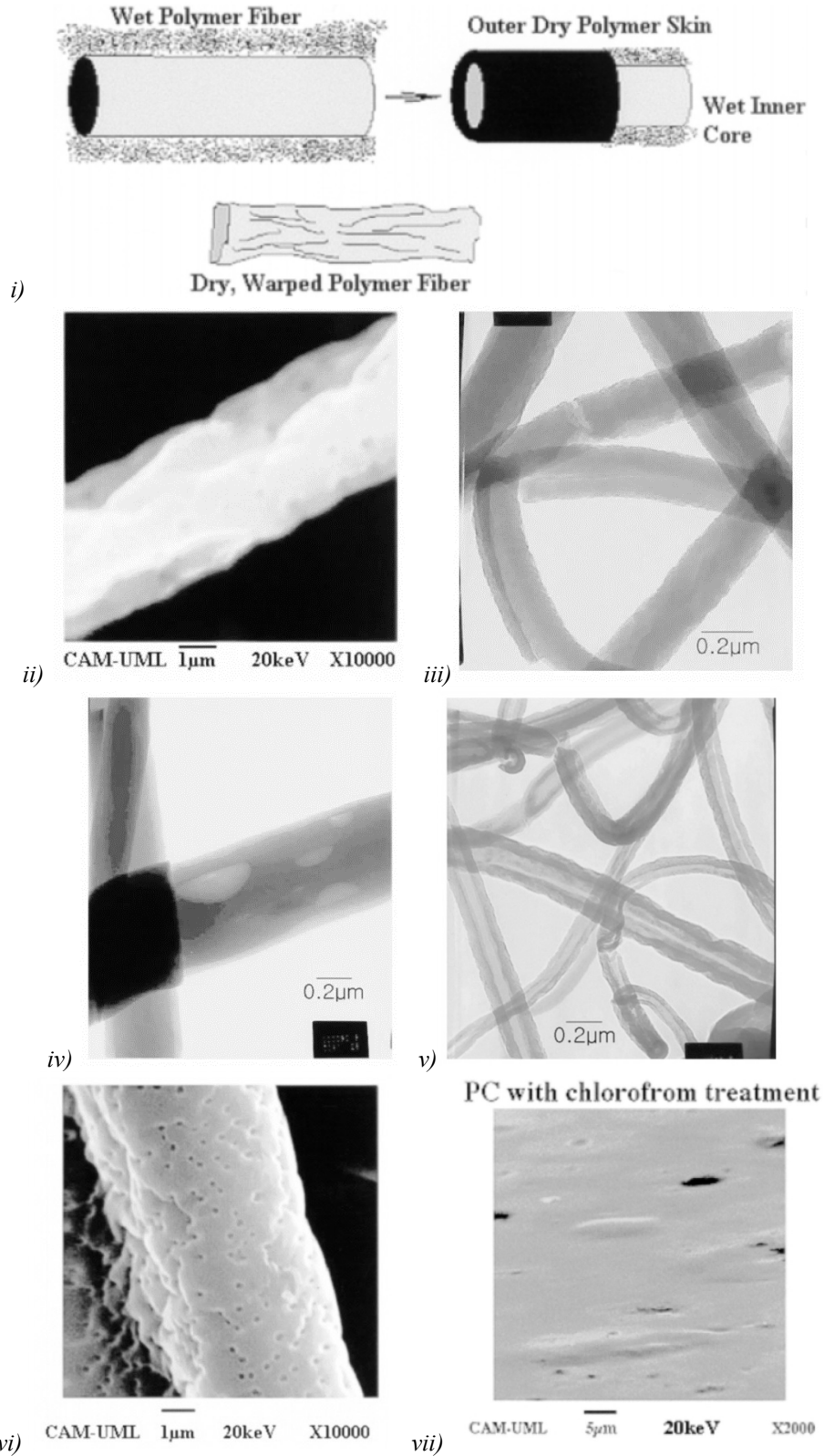


Figure 2.1 - i) a schematic for the dry-skin model for puckering observed in PC; puckering observed for ii) chloroform and iii) THF and DMF (1:1) solvent systems; the internal rarified core showing iv) small bubbles in chloroform and v) a hollow core in THF and DMF; and crazing observed in chloroform similar to vi) bulk PC [16]

A bead is defined as an irregularity in the electrospun fiber mat. In this study, the author proposes that the bead density begins to increase with higher processing voltage until a point where the higher voltage creates a bead occupying a larger area and are consumed into larger fibers decreasing the bead density, this effect is plotted by the author in Figure 2.2. The bead densities ranged from 10 to 70 beads per square mm with most samples falling between 20 to 40 beads per square mm. [16]

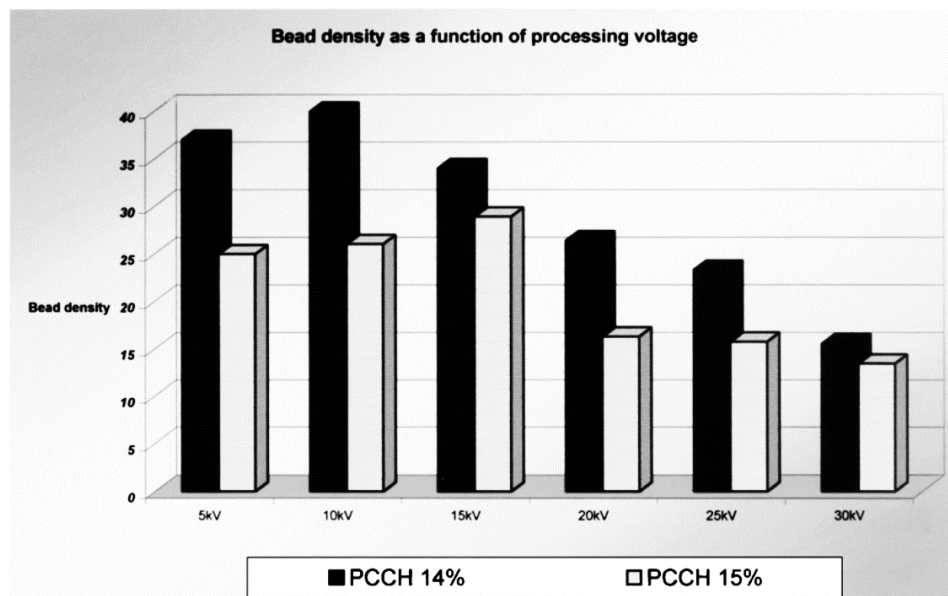


Figure 2.2 - Bar graph showing bead density as a function of process voltage for a PC-CH electrospun fiber-mat [16]

Another study by Shawon et al. analyzed the effect of mat morphology as a function of THF:DMF ratio, applied voltage, and viscosity of the polymer solution. The optimum conditions achieved were a 14% PC solution within a 60:40 THF to DMF ratio and an applied voltage of 25 to 30 kV. These conditions resulted in excellent fibers at the nanoscale with minimum bead density. The fibers were not completely uniform but the experimentation gave a set of process guidelines to produce the best PC fibers for this specific system. [34]

Similar to the works by Shawon, other authors Kattamuri and Sung achieved optimum fibers with 16% of PC in a (60:40) THF:DMF solution with an applied voltage of 30 kV over 25 cm. In this set up a syringe pump was used to keep the droplet at the edge of the tip, and a flow rate of 0.01 mL/minute was optimal. The process parameters were developed using a DOE looking at the effects of concentration (A), voltage (B), and flow rate (C) on the bead density. The order of effects and combined effects from highest to lowest are A, AB, B, ABC, BC, AC, and C, suggesting the most important factors are polymer concentration, concentration combined with voltage, and applied voltage. [33]

Meechaisue and Welle have explored polycarbonate for tissue scaffolding applications. Meechaisue used fast and slow degrading poly(desaminotyrosol-tyrosene ethyl ester carbonate) and co-polymer poly(desaminotyrosol-tyrosene ethyl ester -co- 20%desaminotyrosol-tyrosene

carbonate) and exploring the effects of solution and processing parameters such as polymer concentration, electric field, and solvent system on the surface morphology and fiber diameters. The fiber diameter was found to increase with increasing concentration and electric field. The solvent used was dichloromethane and resulted in fibers with a very smooth surface. Improvement of the electrospinnability was observed with the addition of methanol, a higher dielectric constant solvent. The fiber diameters ranged from 1.9 to 5.8 microns and the mats showed great ability for cell culture and growth over a period of 10 days. [35]

Similarly, Welle et al. synthesized poly(propyl carbonate) and poly(cyclohexyl carbonate) through living polymerization. These polymers were then electrospun resulting in bead-free mats with some porosity on the surface due to crazing. The surface of the fiber mat was then treated with UV irradiation, which affected the ability for plasma protein adsorption. This led to controlling the degradation of the aliphatic polycarbonate, as it is susceptible to enzymatic breakdown. The electrospun mats displayed good cell adhesion and viability, even for the delicate cells. [36]

Nanofiber Processing

The laboratory equipment used presently for electrospinning polymer nanofibers in research is very similar to the techniques discussed earlier in this Chapter. The hardware components required are similar, with improvements coming from the quality of the hardware. These improvements would include more stable power supply devices and pulse-free solution pumps, leading to more uniform processing and thus more uniform electrospun mats. Studies have been completed to see the effect of controlling the whipping instability region through modification of the electric field, this included incorporating a ring electrode at the needle tip to create a parallel plate electrode design [25], [37]. Inclusion of other electrodes just outside the gap area have been attempted to focus the collection of the fibers on the collector [38]. Systems with pulsed power supplies have also been developed to control the lengths of the nanofibers for applications like controlled release of therapeutics in drug delivery [39]. [2]

Another area of development of the electrospinning process is by experimenting with different geometries and dynamics of the collector. Typically, a flat plate is used as the collector, but other geometries such as a rotating drum, mandrel, or disc; rectangular, triangular, or wire cylinder frame; electrode pair arrangements (like parallel), single or multiple ring electrodes, mesh electrodes, and conical electrodes have been studied. Figure 2.3 below depicts some of these geometries [2].

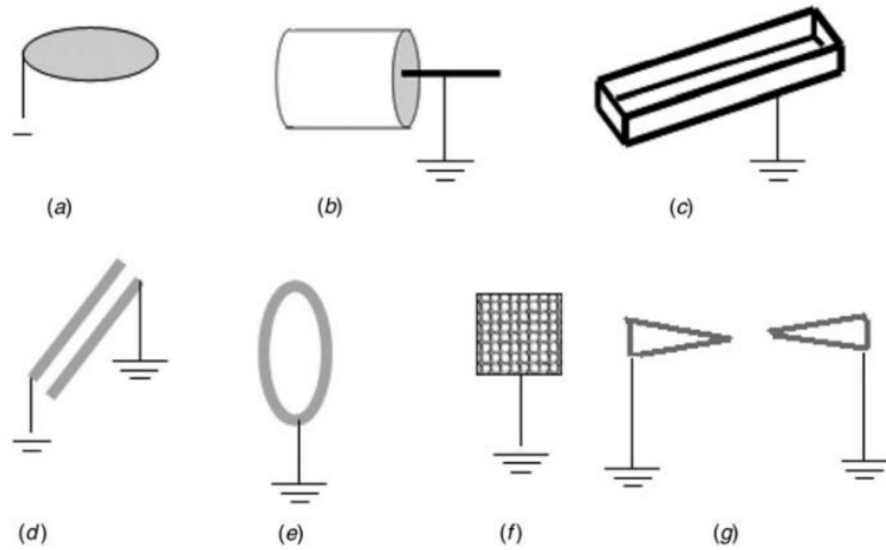


Figure 2.3 - Different types of collectors used in electrospinning [2]

Interest has also been placed on the scaling up of electrospinning systems. This is already evident by the large number of nanofiber products commercially available. Many of these techniques are proprietary although using a wide array of tips with densities of 100 to 400 tips per square foot have been conceptualized and fabricated [2]. Other apparatuses like the Elmarco NanoSpider Industrial Production Lines and FibeRio Cyclone Forcespinning System are commercially available for scaling up production of nanofibers (Figure 2.4) [40], [41]. Other companies design and produce large amounts of nanofibers using their own techniques, for example Donaldson make high quality filtration units and NanoSys fabricates materials for LCD screen and battery technologies.





ii)

Figure 2.4 - Scale-up nanofiber production equipment: i) Elmarco's NanoSpider and ii) FibeRio's Cyclone [40], [41]

2.1.3 – Electrospinning of Composite Nanofibers

A more recent trend in the area of electrospinning is the inclusion of nanoparticles into the polymer solution before spinning, thus allowing the creation of composite nanofibers. The addition of nanoparticles can result in materials with new attributes. Yingjie Li has explored the electrospinning of NCC water-in-oil emulsions with PLA [19], [42]. Another advantage of electrospinning composite nanofibers is the nanoparticle alignment that occurs as a result of the elongation of the polymer during the formation of the nanofiber. This effect can give rise to advantageous uniaxial properties in the fibers. For example, the inclusion of carbon nanotubes can be used to improve conductivity and tensile strength of the electrospun nanofiber mat [43]. At present there is not a large amount of research on electrospinning cellulose nanocrystals (CNC) with polymers and virtually nothing using a polycarbonate matrix with CNC. This review will explore the new developments in electrospinning of cellulose reinforced polymer systems, polycarbonate and polycarbonate composites in several solvent systems.

Hivechi et al. explored the ideal processing conditions for the production of CNC reinforced polycaprolactone, producing 233 nm composite nanofibers [44]. These fibers were analyzed to determine the ideal mechanical properties and biodegradability, which were observed with a 1 wt.-% loading of CNC. Huan et al. produced poly(vinyl alcohol) (PVA) nanofibers reinforced with up to 20 wt.-% of CNC and observed that larger CNC concentrations led to smaller fiber diameters [45]. It was also observed by Huan that a higher concentration of PVA, at constant CNC loading, tended to observe a larger crystallinity in the mat enhanced by improved fiber stacking and molecular interactions between the matrix and CNC nanoparticle.

There may be a need to assess the issues around compatibilization of NCC for polycarbonate. The inclusion of cellulose nanocrystals (CNX) from ramie fibers as a reinforcing agent in electrospun poly(ϵ -caprolactone) (PCL) nanofibers was analyzed by Zoppe et al. in 2009. This was done with and without surface modification through grafting of the CNX surface with low molecular weight PCL diols in attempt to improve interfacial bonding. The grafting was confirmed through spectroscopy (FTIR) and thermal analysis (TGA). The morphology and mechanical properties of the electrospun mats were analyzed through SEM and tensile techniques respectively. The levels of CNX loading in the PCL matrix were 2.5, 5, and 7.5 wt.-% and the solvent system used was DMF and this formulation was found to be colloiddally stable over extended periods of time. The polymer solution was prepared using reflux techniques and mixed with an ultrasonicated DMF solution of the CNXs and grafted-CNxs (g-CNxs). [46]

The electrospinning of those mats was carried out between 10 to 25 kV over 15 to 20 cm gap for a period of 30 minutes to an hour. As expected, some bead formation was observed in the samples and the fiber diameter distribution decreased with increasing electric field. The fiber diameters of the CNX-PCL and g-CNxs-PCL samples were lower than that of the pure PCL even though they displayed a higher viscosity; this is likely caused by the higher ionic strength introduced by the sulphate groups on the CNX surface from the acid hydrolysis. At low loadings (2.5%) of CNX and g-CNxs the fiber diameter was lower for the g-CNxs nanofibers, which can be attributed to the lower viscosity of the g-CNxs solution. As the CNX and g-CNxs loading was increased the fibers began to increase in diameter as the influence of viscosity overtook that of the sulphate groups. The percolation threshold of the CNX for this system was calculated to be about 3% so the concentrations larger than this might also have larger diameters as a result of fiber overlap. [46]

The morphology of such PCL fibers showed a neat continuous uniform distribution of the nanofiber mat, as did the samples with inclusion of the CNX reinforcements. There were differences observed for the mats electrospun with the g-CNxs. The g-CNxs-PCL fibers appeared to have fused together creating a more continuous film with a large number of nodes. This effect was explained by three phenomena: 1) suspension instabilities caused by aggregation of CNX; 2) the electrospinning conditions used were optimized for the pure PCL solution not the lower viscosity g-CNxs-PCL solution; and 3) slower crystallization rates for the lower molecular weight PCL grafted to the surface. The SEM images obtained for the different PCL, CNX-PCL, and g-CNxs-PCL fibers are included in Figure 2.5. [46]

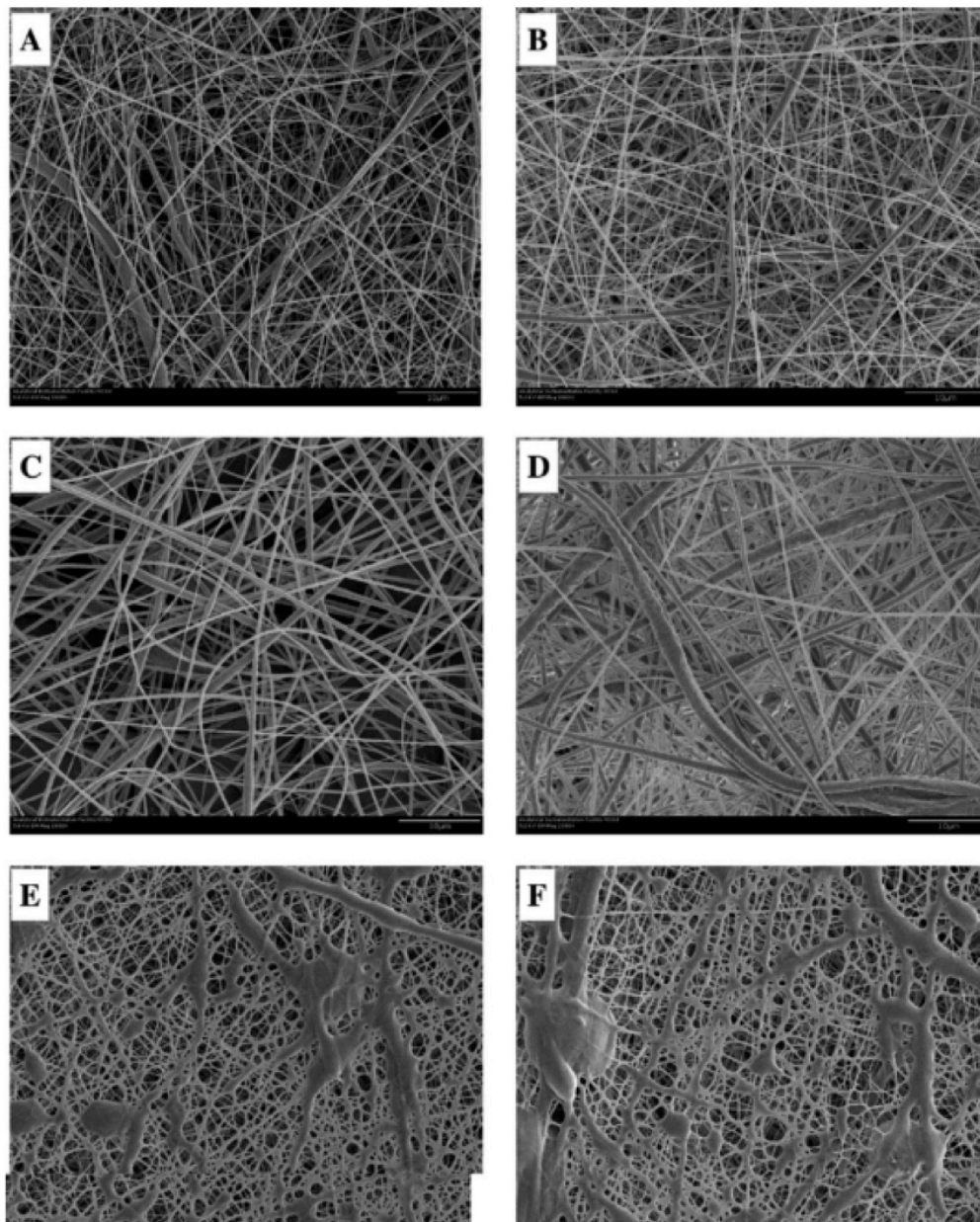
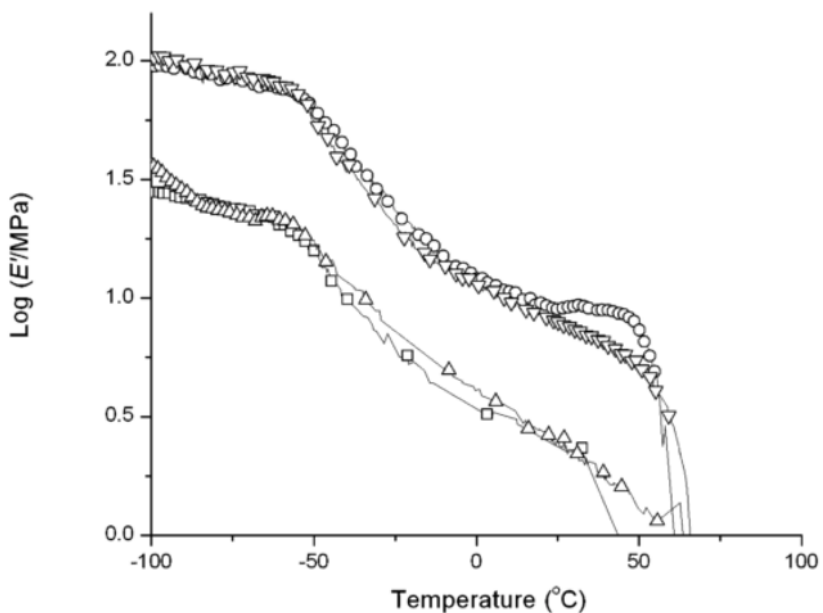


Figure 2.5 - SEM images of A) PCL nanofibers with loadings of B) 2.5% CNX, C) 5% CNX, D) 7.5% CNX, E) 2.5% g-CNX and, F) 5% g-CNX [46]

The thermomechanical and tensile properties for the PCL and CNX-PCL mats were carried out using dynamic mechanical analysis (DMA). Measurements were made at 1 Hz with a strain of 0.03% for temperatures of -100 to 100 °C with a heating rate of 3 °C/min. The gauge of the samples was 10 mm with a width of 6 mm and thicknesses on the order of 0.15 mm. The tensile tests on the mats were carried out in controlled force mode at 3 N/min. A higher storage modulus was observed for the 2.5 and 7.5% CNX samples than the pure PCL with the 5% CNX having a very similar storage modulus. The justification for this is that the 2.5% CNX-PCL fibers had the smallest fiber diameter and thus the most bonding between fibers in the mat leading to a stronger mat. At 5% the fiber diameter is on the order of the pure PCL and they exhibit nearly identical

storage modulus. At 7.5% the storage modulus increases again in this case because of the inherent strength added by the CNX. It is proposed that the CNX loading and fiber diameter are intimately related and an optimum loading would depend on that diameter. Another researcher, Wang, has also proposed that the mechanical properties of electrospun mats are very closely related to fiber orientation, bonding, and slippage more so than the mechanical properties of the individual fibers in the mat [47]. Similar properties were observed for the tensile tests of the PCL and CNX-PCL fibers. The mechanical properties for the g-CNX-PCL samples were not included in the results as they performed very poorly as a result of the defective morphology and deficiencies in stress transfer. The mechanical properties discussed are summarized in Figure 2.6. [46]



i)

sample	CNX content (%)	Young's modulus (MPa)	strength (MPa)	strain at break (%)
ES-PCL		3.89 ± 0.10	1.10 ± 0.08	43.5 ± 10.4
ES-PCL-CNX	2.5	6.54 ± 0.26	1.51 ± 0.06	64.8 ± 2.4
	5.0	3.94 ± 0.58	0.86 ± 0.08	82.6 ± 8.2
	7.5	6.26 ± 0.73	1.32 ± 0.21	85.8 ± 14.4

ii)

Figure 2.6 - i) DMTA results and ii) tensile test results for PCL(\square) and 2.5%(\square), 5%(\triangle), and 7.5%(∇) CNX-PCL [46]

There are few examples of composite fibers using polycarbonate in literature including fillers such as tetrapyrzinoindoloporphyrazine and carbon nanotubes (CNT).

Baek et al. have incorporated tetrapyrzinoindoloporphyrazine into electrospun PC nanofibers. Tetrapyrzinoindoloporphyrazine is a phthalocyanine that exhibits excellent chemical and thermal stability with optical and emission properties and can have applications in organic light emitting diode applications. Quality nanofibers were developed between 5 and 20 microns in chloroform

and fibers with a higher bead density were created in cyclohexane with fibers of 50 to 200 nm. Their future works included creating pH sensors using this material. [48]

Various studies have been completed with the incorporation of CNTs into polycarbonate matrices for different applications [49]–[51]. An interesting publication was presented by GM Kim et al. that looks into the deformation process of multi-wall CNTs (MWCNT) within an electrospun PC nanofiber through tensile tests within a TEM. The composite material was electrospun using chloroform as a solvent and individual rod-like MWCNT elements were observed highly aligned within the fiber. Slippage of the MWCNT within the fibers with applied tensile load leads to a much-enhanced strain at break. This mechanism might explain the improvement in toughness (strain at break observed by Zoppe) for NCC systems too. Pores on the nanofiber surface have highly concentrated stresses leading to nanonecking as a result of the plastic deformation. There was also simultaneous improvement of the tensile modulus. Figure 2.7 depicts the TEM micrographs of the tensile testing of the individual nanofibers as well as a schematic depicting the mechanical deformation process occurring in the fiber. [32]

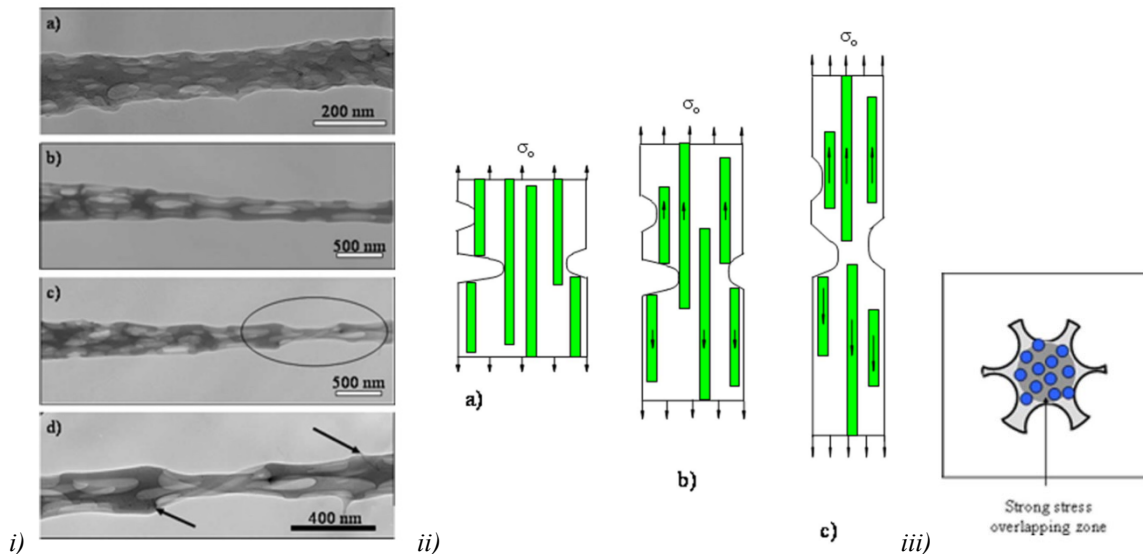


Figure 2.7 - i) TEM micrographs of the *in situ* tensile testing of the individual nanofibers as well as ii) a schematic depicting the mechanical deformation process occurring in the composite fiber and iii) the strong stress overlapping zone in the core of the fiber [32]

2.1.4 – Parameters Affecting Nanofiber Electrospinning

The process of electrospinning is simple to execute but extremely complex to control or to model effectively. There are numerous controllable input parameters that can affect the resulting desired nanofibers. Even more complexity is added, as these parameters will have combined effects that – after 100 years of electrospinning – are still not completely understood.

Two distinct categories can be made to classify the different factors: *formulation* and *processing*. In the case of either formulation or processing factors, a small change in any of the variables could alter another and cause significant changes in the output of the system – the fiber mat and the type of nanofibers. This is another reason to explore the possible combined effects in the DOEs.

- *Formulation* factors will include variables that pertain to the material system being electrospun, in this case would include the polymer, the solvent system, and any additives like NCC or compatibilizers and their percentages in a formulation.
- *Processing* factors include variables related to the electrospinning apparatus or its environment. For example, the most explored processing variables include electric field (voltage and gap distance), collector design, temperature and pressure. These factors are primarily varied between the DOEs.

The scope of this research will limit the formulation and processing factors that can be analyzed. Factors that are considered more important to explore are outlined below while also briefly discussing known factors that will be held constant through the electrospinning research.

2.1.4.1 – Formulation Parameters

Polymer System

Factors of the polymer system are quite important in electrospinning; they include molecular weight, chain architecture, branching, monomer arrangement in co-polymers and additives. Two parameters of the polycarbonate will be observed including the melt flow index (from two sources) and the overall concentration of polycarbonate in solution. Polyamide-6,6 was obtained from a single source and only solution concentration will be explored.

The melt flow index is proportional to the viscosity of the polymer; it will also give indirect molecular weight and branching of the polycarbonate. It is also important to consider any additives that may have been added into the polycarbonate during manufacturing, as typically a UV stabilizing agent is present. There are two polycarbonate sources being explored: StarPlastic Molding Grade PC (PC743) and SABIC Lexan PC Sheeting (XL10). The MFI for StarPlastic was measured to be 12.00 g/10min and reported as 11.00 g/10min in the material QC specification sheets. The MFI for Lexan PC was reported to be 18.00 g/10min. The specification sheets for these two grades of polycarbonate are included in Appendix A.

The concentration of polymer in solution is considered one of the dominating effects determining the resulting fiber diameter as well as the overall ability to electrospin. At low concentrations there is usually not enough chain entanglement to keep the chains together as they are accelerated towards the electrospinning collector forming the nanofiber. At low polymer concentrations small beads are formed instead of fibers, this is called electrospraying and is not a desirable result for this study. Typically, as the concentration increases the fiber diameter will increase. The solution viscosity is a metric that can help determine effect of concentration when different polymers or solvents are varied. [2]

As the polymer concentration in solution increases, the number defects or beading will begin to decline and lead to bead-free nanofiber mats. If the concentration is too high though, there can be processing errors such as solids in the solution, beads in the mat or blocking of the needle tip. The presence of solids in the solution can also slow down the stretching of the fibers in the whipping instability region leading to larger fibers and a smaller mat diameter on the collector plate due to the heavier fibers. [2]

From the preliminary studies and through literature review an understanding of the range of concentrations and viscosities required for electrospinning quality polycarbonate fibers has been gained. A concentration of about 5 wt.-% through 30 wt.-% of polycarbonate in various solvents has led to the formation of nanofibers [16], [33], [34]. This corresponds to a viscosity of approximately 50 cP up to about 700 cP measured with the Brookfield Viscometer at 100 RPM using spindle s63. A concentration of 10 wt.-% through 20 wt.-% was used in the fifth DOE using polyamide-6,6. This concentration parameter is easy to control in sample preparation and can be analyzed easily through the design of experiments.

Solvent System

The solvent system is very important to the electrospinning process as it determines various properties of the polymer solution effecting processing and morphology of the fibers. This includes the conformation of the polymer chains in solution, the ability to charge the polymer solution in the spinning jet, the cohesion of the polymer solution (surface tension), and the rate of drying of the polymer nanofiber through solvent evaporation. Specifically, the properties of the solvents that are the most critical in electrospinning are the conductivity, surface tension, dielectric properties, and volatility. [2]

The conductivity is important, as electrospinning requires the transfer of charge from the electrode to the tip of the needle for the formation of the Taylor cone. A very small conductivity is desirable to ensure the current is kept very low through the electric field; yet having no conductivity will result in no electrospinning at all. Surface tension is the main force that is opposing the Coulombic forces within the electric field and the balance of surface tension, electrostatic repulsion, and cohesive forces in the polymer determines the bending and whipping during the spinning. The dielectric constant will determine the amount of electrical charge that can be held by the solvent, and the more charge that can be held the evenly spread out on the surface those charges are leading to a higher quality surface of the fibers. Lastly, the volatility is quite important as the evaporation of the solvent leaves the solid polymer nanofibers. Ideally, the solvent should finish to evaporate just before striking the collector plate. This will ensure the best elongation of the fibers (smaller diameter) while avoiding the defects that may be caused if the fibers were wet while hitting the collector such as beading. [2]

Unfortunately, knowing these solvent parameters will only give an idea of the feasibility and quality of the electrospinning. Trial and error experimentation are usually necessary for each solvent system being analyzed and usually cannot be independently varied to optimize a solution. The solvents used in solution with polycarbonate are a 60/40 mix of THF and DMF by weight as well as chloroform. For the polyamide-6,6 system, formic acid was used.

Nanocrystalline Cellulose (NCC) Reinforcing Agent

The addition of any additive to the polymer solution will also cause many property changes affecting the overall electrospinnability of the material. The addition of a rigid nanoparticles (like the cellulose crystal) will change many of the properties of the system including the viscosity, conductivity, and surface tension. [2]

The concentration of the NCC in the polymer solution was explored. For the polycarbonate in THF/DMF DOEs the NCC concentration was explored at 2-wt.-% as well as 0 wt.-% to act as a baseline comparison. For the polycarbonate in chloroform DOEs the cNCC (surface modified) concentration was explored at 2-wt.-% as well as 0 wt.-% to act as a baseline comparison. For the polyamide-6,6 in formic acid DOE, the cNCC (surface modified) concentration was explored at 4-wt.-%.

2.1.4.2 – Processing Parameters

Applied Voltage

The applied voltage is what supplies the electrical charge to the surface of the droplet at the tip of the needle as well as the electrospinning jet. As a higher voltage is applied, more charge is supplied to the jet resulting in higher instability and stretching of the nanofiber, which will lead to smaller fiber diameters. This will lead to higher rates of solvent evaporation and more complete drying of the fibers with higher voltage. The effect of voltage on the nanofiber diameter is much smaller than the effect caused by the polymer concentration in solution. The applied voltage can also be considered in combination with the gap distance, giving the overall electric field. [2]

For the six DOEs in this study, the applied voltage was kept within the range 15 through 30 kV typically covering a 10 kV range, varied according to polymer and solvent system.

Gap Distance

The gap distance between the tip of the needle and the collector plays two important roles. It defines the strength of the electric field through the applied voltage as well as the time available for the solvent to evaporate before striking the collector. Typically increasing the gap distance while maintaining all other parameters constant will result in smaller nanofiber diameters. [2]

For the six DOEs in this study, the gap distance was kept within the range 10 through 25 cm typically covering a 10 cm range, varied according to polymer and solvent system.

Constants

Due to the scope of the project there are some processing parameters that must be kept constant at a level based on literature or through some optimization carried out during the preliminary research. This includes the collector shape and dynamics, the polarity of the applied voltage, the processing of the polymer solution prior to spinning, the tip diameter and length of the syringe needle, as well as the electrospinning temperature and humidity.

The collector to be used is a 6 by 6 inch stainless steel sheet covered in aluminum foil, allowing easy removal of the sample for analysis. It will also be a static collector with no rotation or movement during the spinning. The polarity will be held constant with the tip being negatively charged and the collector being electrically neutral; this decision is based on preliminary results showing better fibers in this configuration, also because of equipment limitations we can only negatively charge the polymer solution. The process for preparing the polymer and polymer composite solutions is constant between all samples and is addressed in detail in the preliminary results section. The needle diameter will be held constant by using blunt 18 G disposable needles.

Most literature on electrospinning includes data from electrospinning in air at standard ambient temperature (25 °C) and pressure with a relative humidity between 40% to 60% with slight variations from day to day changes in the environment. The present experimentation for this project has been carried out within these conditions. This is because these environmental effects directly affect the drying rate of the spun fibers within the instability region. Although the humidity will not significantly affect the evaporation rate of the polar solvents, it is important to consider, as polycarbonate and NCC are hydrophilic materials that can readily adsorb water.

Through the course of running these DOEs, the several experimental parameters held constant are summarized in Table 4.1 below.

Table 2.2 - Experimental process and formulation parameter constants for DOE#1

Process Constants	Fixed value
Collector	Stainless steel sheet (~6x6 inch), covered in aluminum foil; fixed
Syringe	5 mL with 18 G blunt tip
Relative Humidity	50+/-10%
Temperature	23 +/- 2 °C

Feed Rate

One last parameter that must be controlled is the feed rate of the syringe pump. It controls how quickly the droplet of solution is replenished as the electrospinning jet depletes it. The feed rate is measured in mL per hour and is controlled on a run-by-run basis. The goal is to achieve a droplet at the tip that will not drip or recede into the tip of the needle. Each of these cases will cause a drastic increase in the defects present in the electrospun mat. The feed rate is varied until the droplet reaches a steady state volume on the tip. The typical feed rate falls within 0.1 and 9 mL/hour for this apparatus and material system.

2.1.5 – Performance of Composite Nanofiber Electrospinning

The different performance responses explored will attempt to address the quality of the solutions and nanofibers including solution turbidity and viscosity, nanofiber diameter distributions, and bead diameter and densities.

Turbidity

Turbidity is a measure of the cloudiness of a solution typically as a result of the presence of particulates in suspension. This technique is quite popular for monitoring particulates in water treatment but can be used as a quantitative indicator of the concentration and solubility of the polymer and NCC reinforcements in their electrospinning solution. It is expected that the turbidity will increase with increasing concentration of polymer or NCC in solution and with solutions that may have poor solubility of polymer or NCC in the specific solvent used. Keeping turbidity low is beneficial to maintaining proper dissolution and dispersion of the polymer and NCC,

respectively, as well as to maintain the goal of maximizing transparency in the final electrospun fiber application.

Turbidity, quantified in nephelometric turbidity units (NTU), is measured by shining an incident light through a specimen solution and measuring the light that is scattered 90° to the incident. The measurement is compared to a set of calibration standards to determine the semi-quantitative NTU value; see Figure 4.1 for an example of the standards and their corresponding NTU values. The higher the concentration of particulates (i.e. the degree of polymer and NCC concentration or agglomeration) there is increases the scattering of light and therefore giving a higher turbidity value.



Figure 2.8 - Visible representation of turbidity in nephelometric turbidity units (NTUs) for <math><0.1</math>, 20, 200, 1000 and 4000 NTU [52]

Turbidity for all samples was measured using a 2100N Laboratory Turbidimeter designed by Hach. After cooling the refluxed solution (or dispersion in the case where NCC is added) the solution was transferred to a Hach turbidity flask and analyzed by the equipment. [53]

Viscosity

An additional solution property that is heavily influenced by the concentration, and has an effect of the final electrospun fibers, is the viscosity of the polymer solution. Viscosity is the measurement of the resistance to flow of a fluid, or on a micro level it is the internal friction of a fluid. As the internal friction of a material increases, a greater force is required to move, also known as shear, the material. A more viscous material would require more force to move than a less viscous material.

Typically, as the polymer concentration and chain entanglement increases, there is an exponential growth in resistance to flow of the solution due to the higher degree of intermolecular bonding.

Also, as a result of the increased forces within the system, the entanglement of polymer can hold a larger electric charge during electrospinning decreasing the likelihood of unwanted

electrospinning due to fibers breaking up into droplets. In electrospinning, typically as the viscosity increases it will result in larger fiber diameters; thus, there is an ideal range of viscosity for electrospinning experiments to minimize fiber diameter while avoiding electrospaying.

Viscosity was measured using a Digital Viscometer from Brookfield. The viscosity was measured immediately after measuring turbidity using the same dispersion using spindle s63 at a rate of 100 RPM, in most cases. [54]

Fiber Diameter

The fiber mats can be imaged at a reasonable magnification in order to be able to use image analysis software to measure the cross section of a fiber. Numerous measurements must be made for each sample, using the micrograph scale bar for calibration, in order to achieve a reliable estimate for average fiber diameter. In literature, at least 60 measurements are typically used and others have reported between 100 and 500 measurements [2]. A fiber diameter distribution can be used to display the distribution of sizes and the average should be reported with a standard deviation. Figure 4.2 shows an example of measuring 379.9 nm PC nanofiber diameter using Image J image analysis software and the strategy used to choose several measuring points. A grid of points was used, and measurements were made whenever a dot intersected with a fiber, with a goal of 100 measurements.

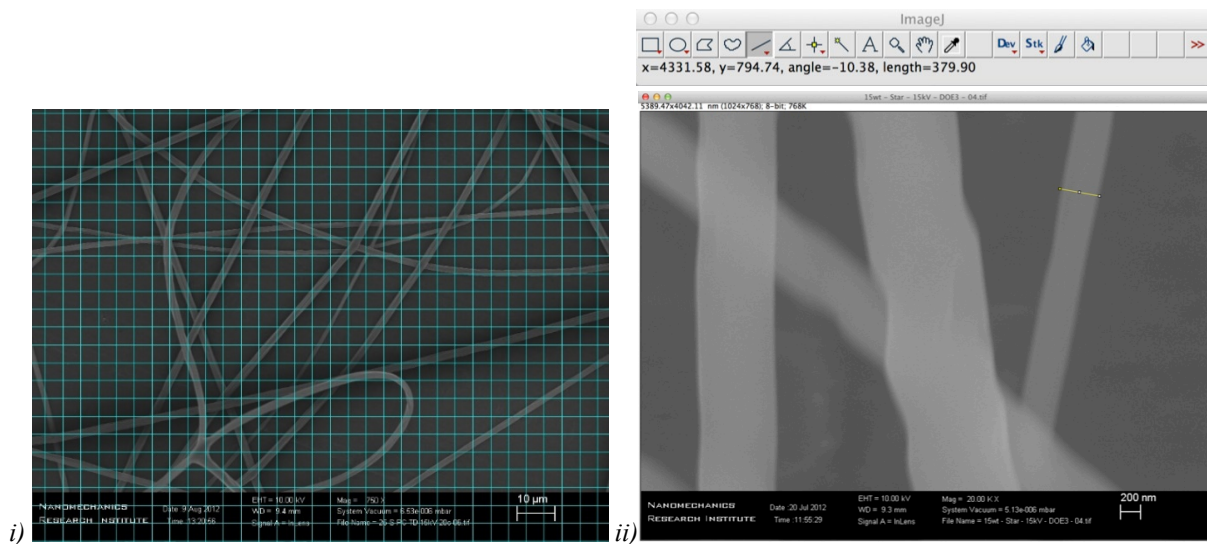


Figure 2.9 - i) Example of grid system used to choose measuring points as well as ii) measuring 379.9 nm PC nanofiber diameter using Image J image analysis software

Bead Diameter and Density

A bead is any large defect found in the electrospinning mat typically caused by instability in the jet during spinning when surface tension forces are greater than those acting to extend the fiber. The bead can take on various morphologies including spherical and spindle like shapes but also collapsed, flattened and prune like shapes. Similar to fiber diameter, bead diameter was measured using as many measurements as possible to determine a good distribution, a target of 60 measurements per sample was used in image analysis. Literature tends to report a density per unit area which is the method employed in this study. But it would be better to normalize this

measurement to determine a more relative metric, like beads per unit length of fiber, as the density of beads is not necessarily uniform across a sample mat on the collector and a single or even a few micrographs may not be typical of the entire system. Figure 4.3 depicts examples of low and high concentrations of bead density in electrospun mats.

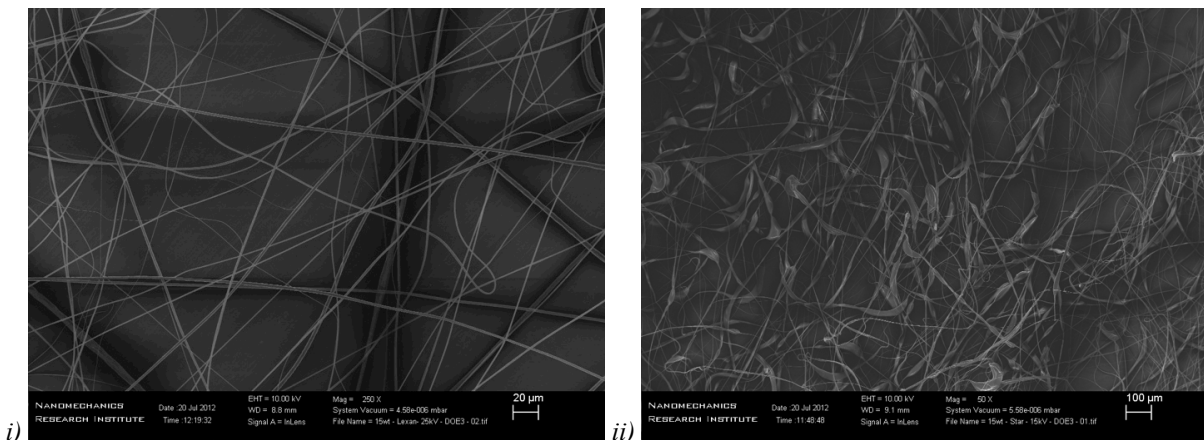


Figure 2.10 - Examples of low (left) and high (right) concentration of bead density electrospun mats

2.1.6 – Applications of Electrospun Nanofibers

Because such effort has been devoted to the characterization and control of the electrospinning process it has allowed the development of a wide range of possible materials. This range of materials has provided the potential for an even wider range of potential applications over many industries. These current applications can be categorized into three distinct classes: i) Biomedical, ii) Functional Materials and Devices and iii) Energy and Electronics. A brief overview of each of these categories will be given with specific examples of products that are or could be developed using nanofibers and electrospinning techniques. Several products have graduated from laboratory research and development stages and reached commercialization. This has spurred the attention and funding from academia, government, and industry all over the world. [55], [5]

Biomedical applications have great promise for nanofiber applications as many parts of the human body are comprised of complex hierarchical designs including nanostructured components. The application areas for biomedical applications include drug delivery, tissue engineering, wound dressing, and cosmetics. The advantage for drug delivery is the extremely large surface area of the electrospun fibers allows for an increased drug release rate. Fabrications of biodegradable poly(D,L-lactide-co- glycolide) (PLG) and poly(N-vinyl pyrrolidone) (PVP) blend (PLG/PVP: 20/80 w/w) fibers containing silver sulfadiazine (burn treatment) have been shown in vivo to take between 3 and 8 days to degrade [56]. Another example uses cellulose (degreasing cotton and wood pulp) with a degree of polymerization of 500–2500 as a carrier for nerve growth factor with electrospun fibers on the order of 500 nm [57]. The non-woven electrospun mat can be tailored to mimic the extracellular matrix required for tissue engineering giving a scaffold capable of engineering bone tissue [58], cartilage [59], 3D tissue [60], among many others often incorporating pharmacology materials, proteins, viruses, plasmid DNA, bacterial cells, or drug loaded nanoparticles. Wound dressings are another great application for electrospun mats, as the nanoscale pore sizes are small enough to block bacteria yet large enough to allow air and water to

facilitate healing [55]. There is also the potential for electrospun fiber use in cosmetic materials for treatment of skin and skin cleaning; an example is the inclusion of honey into the formulation to provide an antimicrobial scrub to be use as care wipes [61]. In many of these examples there is a possibility that the radical scavenging and antioxidant properties of NCC could be valuable. [5]

The use of nanofiber in also quite promising, and in some cases a reality, in functional materials and devices including smart textiles and protective clothing, composite materials, and filtration. Protective clothing can be developed from electrospun nanofibers as a way to block harmful airborne chemical agents (like mustard gas) through trapping and neutralization while maintaining air and water permeability [55], [62]. Smart textiles that mimic nature have also been electrospun such as a silver-ragwort-leaf-like super-hydrophobic nanoporous mat that has a contact angle near 160° exceeding that of the plant itself (147°) [63]. [5]

Filtration is an important area to consider electrospun nanofibers as it is expected to have a market of nearly \$700B US by 2020 [55]. Nanofibers have been used in filtration media for greater than 15 years because of their high surface area, high porosity, and great surface adhesion giving outstanding ability to filter particles in the sub-micron range. An example of nanofiber filtration media with superior properties was electrospun by Guo with titania incorporated giving the ability to filter micro- and nano-scale dust, viruses, micro-organisms, chlorinated hydrocarbons, Cl-containing compounds, and organic phosphorous toxic compounds not to mention the antimicrobial and other properties given by the TiO_2 [64]. There could be tremendous opportunities where the surface of the NCC could be modified or acts as a carrier of other active particles in a functional electrospun mat. Some other polymer systems to be used for filtration include polytetrafluoroethylene (PTFE), poly(ethylene terephthalate) (PET), and polycarbonate (PC) [65]. [5]

Sung Kim et al. have prepared electrospun polycarbonate nanofibrous membranes for use as antimicrobial filters. The formulation used was PC in chloroform solvent with the addition of a quaternary ammonium salt (benzyl triethylammonium chloride, BTEAC). The addition of the BTEAC lead to fibers with a decreased fiber diameter on average compared to only PC, from several microns to submicrons as a result of the small increase in conductivity of the sample. The samples incorporating the BTEAC showed improved antimicrobial properties. The PC nanofiber mat was shown to have a good filtration efficiency satisfying the criteria of a HEPA filter (or high efficiency particulate air) and displaying a pressure drop within the normal range. It is shown that PC electrospun fibers have great potential for ultrafiltration applications. Data of the filtration efficiency and pressure drop in comparison with a polypropylene HEPA are depicted in Figure 2.11. [66]

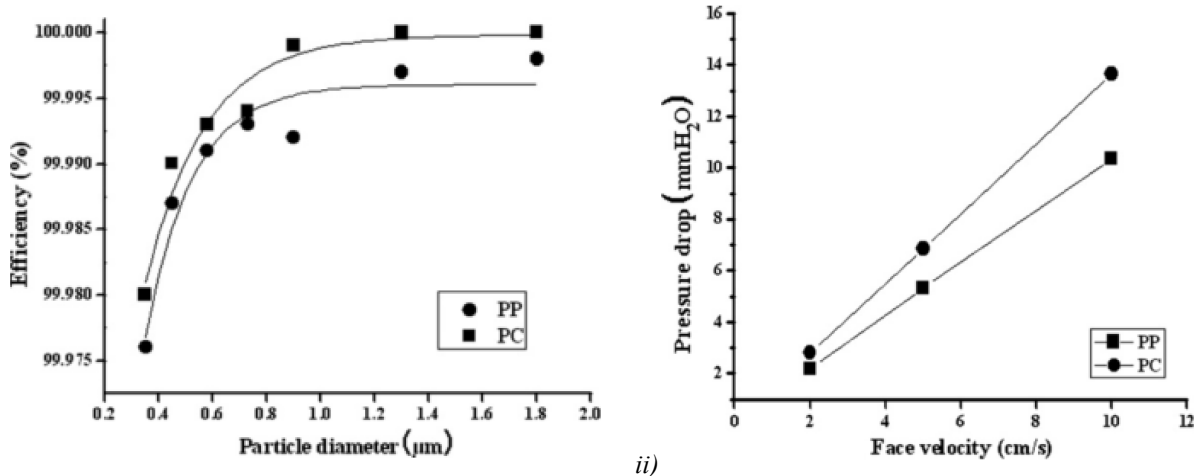


Figure 2.11 - i) Filtration efficiency and ii) pressure drop of PC nanofiber filter in comparison with a polypropylene HEPA filter (PP) [66]

There are many potential applications for electrospun nanofibers in the energy and electronics industries including batteries and capacitors for sustainable energy storage, sensors and catalysis; each of these applications relying on the extremely high surface area of the fiber mats. Electrochemical reactions within a battery cell is proportional to the exposed surface area of the electrode making nanofibers an option for electrode material like in a dye-sensitized solar cell electrode made of electrospun TiO₂ [63], [67]. Most sensors operate attributable to interactions like physical adsorption, chemical reaction, or light absorbance and by using high surface area materials the sensitivity will be higher; an example is an NH₃ sensor created with poly (acrylic acid) (PAA) and poly (vinyl acetate) (PVA) electrospun onto the surface of a quartz crystal microbalance [68]. Catalysis is also very dependent on the active surface area; Ding et al has developed a layer by layer (LbL) technique capable of coating cellulose acetate electrospun fibers with anatase titania capable of degradation of three toxic gases [69]. [5]

2.2 – 3D Printing

2.2.1 – History of Fused Deposition Modelling

The fused deposition modeling (FDM) process was invented around the late 1980s when Scott Crump attempted to make a toy frog for his daughter using a glue gun loaded with polyethylene and paraffin wax [70]. Crump then patented the FDM process and founded Stratasys Inc. in 1990, which is now the leading manufacturer of FDM equipment worldwide. A typical printer capable of high production quality is on the order of \$100 000 USD, with the price starting around \$15 000 USD for the most economical models [71]. In the past 10 years, desktop FDM machines have democratized the price to the point that many homes, schools and offices can afford a desktop scale printer. A major driver in this reduction and proliferation is the recent expiry of key FDM patents. Ultimaker, a leader in the desktop space, sell their flagship printer – the Ultimaker 3 – for around \$3000 USD and similar FDM ‘kits’ can be bought and assembled for under \$500. With this, the market and demand for the polymer filament feedstock or “ink” has risen significantly.

In 2005, driven by the patent expiries, Dr. Adrian Bowyer, of the University of Bath, initiated the open-sourced RepRap program with the clear goal of making a completely self-replicating manufacturer. Darwin -the first prototype - made the first 3D print successfully capable of replacing a commercially printed part in 2006 [72]. This prototype made its first ‘child’ replicator in Feb 2008 and by Sept 2008 there were over a hundred Darwin RepRap machines worldwide. A picture of Dr. Bowyer with the original Darwin and its first ‘child’ 3D printer is available in Figure 2.12 [73].

This RepRap movement, evolving by publishing the build design and fueled by continuous modifications by the community, has caused the barrier to entry for a hobbyist to drop significantly. The cost of an FDM printer capable of a 6” square build platform is on the order of \$1 000 USD, and if the builder is capable of sourcing all his own parts this could reduce to around \$500 USD. Some manufacturers are even selling printer kits around \$200 USD. Now in 2019, there have been thousands of offspring designs to the Darwin printer with thousands living in households, workshops and laboratories around the world capable of printing everything from polymers to chocolate [74]. Makerbot Industries Inc. received some seed funding from Dr. Adrian Bowyer as well as \$10 million USD from venture capitalists to commercialize the design; they have since released several new designs increasing in production capabilities [75]. They were acquired by Stratasys Inc. in 2013 for \$604 million.

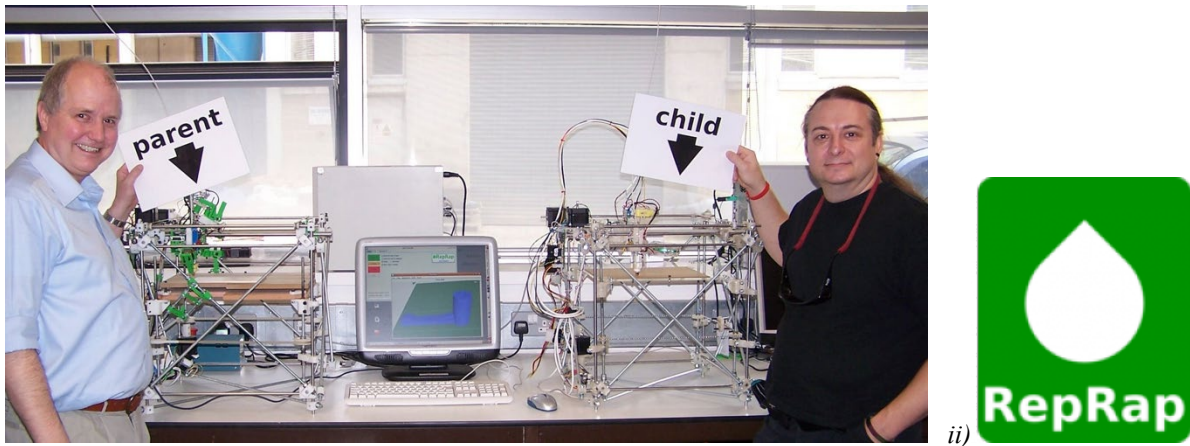


Figure 2.12 - i) Adrian Bowyer and Vik Olliver, of the ii) RepRap movement, with the first parent and child Darwin FDM printers [73]

Although still in its infancy, 3D printing is another way of molding plastics and composites. Advantages of the fused deposition modeling (FDM) process over traditional process like compression and injection molding come from the customizability, rapid prototype iterations, and complex designs not previously capable. Customizability is not feasible using traditional methods as they were intended for the mass production of the exact same object. There are endless possibilities for personalized prosthetics and bone replacements; there are even companies today where one can order a custom designed FDM prosthetic hand, like E-NABLE. Hardware designers can now rapidly iterate their design process using FDM, being able to physically hold their device within minutes.

2.2.2 – 3D Printing of Thermoplastics

Like electrospinning, 3D printing is a complex process with many factors that can contribute to the final performance of a 3D printed part. Goh et al. have recently published a review paper entitled, “Process–Structure–Properties in Polymer Additive Manufacturing via Material Extrusion: A Review,” which identifies several of these factors, which are summarized in Figure 2.13 [76]. This section will identify common raw materials (or thermoplastic 3D filaments) as well as FDM machines that can be used for bench-scale additive manufacturing research.

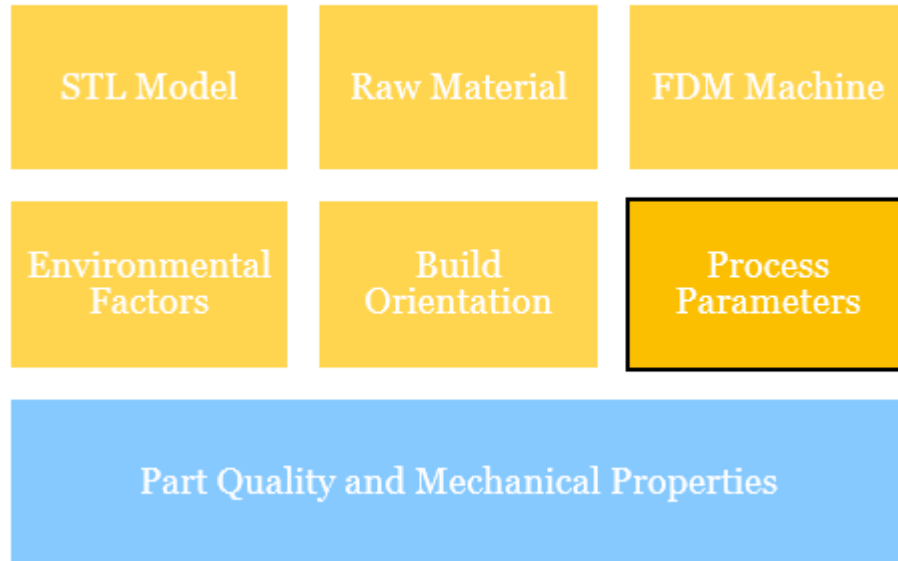


Figure 2.13 - Formulation and process factors in 3D printing that have an influence of the final part quality and performance [76]

Thermoplastic 3D Filaments

Currently, thermoplastics are the material of choice for fused deposition modeling (FDM) as the material can be heated passed its melting point and have viscous flow, then harden back to its glassy or crystalline state. It appears that the most common polymers used both commercially and by hobbyists are acrylonitrile-butadiene–styrene polymer (ABS) and polycarbonate (PC), including PC-ABS blends, due to their balance of properties and low melt processing temperatures [77]. Another common consumer material is polylactic acid (PLA) as it is bio-based and releases fewer toxic fumes during processing; this is important when the typical consumer 3D printer is in a household and is printing toys and gadgets for children or pets. Other thermoplastics used include polyamides (Taulman’s 618 nylon and ULTEM 9085), polypropylene (PP), polyethylene (PE), polyvinyl alcohol (PVA) for water solubility, thermoplastic elastomers (TPE) like NinjaFlex for flexibility, and polyvinyl chloride (PVC).

Thermoplastics for FDM style 3D printing come in the form of a cylindrical wire, referred to as a filament. There are two primary filament diameter standards – 1.75 mm and 3.00 mm – although this is a ceiling value and the actual diameter can be as low as 1.65 mm or 2.85 mm, respectively. The actual diameter can be input into the computer control software – called a slicer – to achieve

the correct volume throughput of filament from batch to batch. In general, the thicker 3.00 mm filament is used for faster throughput whereas the thinner 1.75 mm filament is desired for higher precision and print quality, but with the development and engineering progress of the 3D printer extruders over the past few years this is less of the case. For example, the Ultimaker 3 printer has quick-change 3.00 mm extruders with different capabilities (like soft and flexible filament) that can print layers of 0.06 mm (60 microns) at speeds of 90 mm/s.

The filament often comes in a 1 kg spool that can easily be mounted and loaded into a standard 3D printer. Larger weight and more specialized spools are becoming commonplace like with print parameters preloaded on an RFID chip to accelerate the printing process. The typical pricing for one kilogram of this material in filament form begins around \$35 USD for a consumer printer and increases upwards of \$300 USD for Stratasys branded filament [78]. Images of 3D printer filament used in Dr. Simon's lab are included in Figure 2.14.



Figure 2.14 - 3.00 mm Thermoplastic filament spools typical of FDM processes.

Much of the filament variety is available online or at local 3D printing shops but is limited to specified thermoplastic materials and colors. If a user or researcher wants to use a custom formulation, they are required to pay a hefty sum to a toll manufacturer (for very large quantities) or use a bench-top filament extruder such as the Filastruder, Filabot, or Redetec Protocycler. For example, the Filastruder (Figure 2.15) allows the extrusion of polymer resin beads or powder into 3D printer filament. The Kickstarter version 1.0 of the Filastruder that was procured for the lab would take the polymer from the hopper and pass it through a PID heated steel shaft. The molten polymer was moved using a single screw rotation producing about 12 to 18 inches of filament per minute, or about 1 to 2 kg per day using either a 1.75 mm or 3.00 mm extrusion die. The Filastruder v1.0 is capable of reaching temperatures over 210 °C making it suitable for producing many thermoplastic and composite filament for research applications.

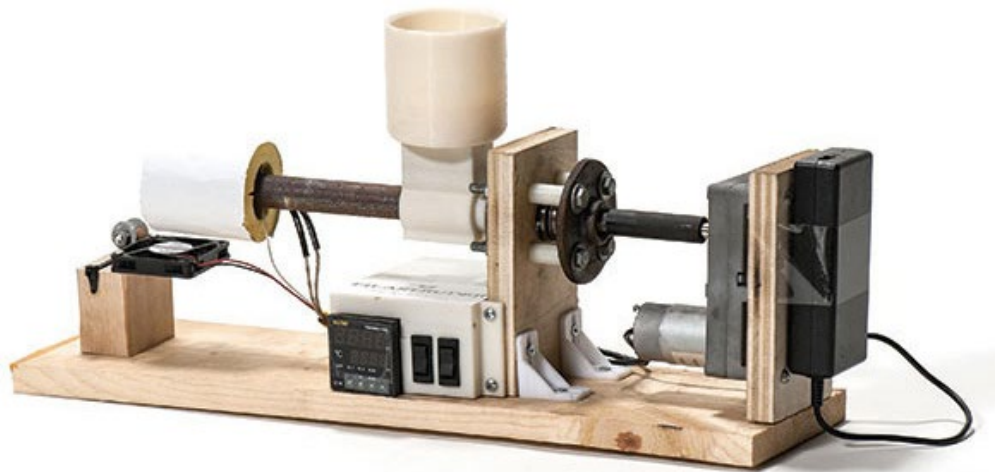


Figure 2.15 - Filastruder 1.0 bench-top 3D printer filament extruder [79]

FDM 3D Printer

A fused deposition modelling (FDM) 3D printer has a few primary components that are common across different models. The main function of the FDM printer is to arrange a thermoplastic material into a desired 3D shape by melting the polymer and depositing it layer-by-layer from the bottom up into a final part. There are many processes running in parallel to achieve the final product: a computer processor that can interpret the sliced gcode (more on this later); a set of axes that can move in 3 dimensions to control the precise location of the print head; a print head containing one or more extruders that can melt and deposit the plastic; and a platen or print bed that acts as the platform the print is being built upon. As the 3D printer follows the machine instructions from the gcode it heats, moves the print head, and extrudes a 2 dimensional ‘layer’ on the print bed before moving up slightly to deposit a second layer on top of the first. This layer-by-layer process continues until the part is completed.

The computer processor that runs the operations of a 3D printer takes an input in the form of gcode loaded through an SD card, a USB stick, or through a network - like Wi-Fi - and turns it into specific motor movements or heating changes within the 3D printer system. A typical subset of gcode instructions may look like this:

```
G1 Z0.500 F3600.000
G1 X18.310 Y21.260
G1 F1800.000 E1.00000
G1 X18.960 Y20.770 F540.000 E1.05501
G1 X19.420 Y20.490 E1.09140
G1 X19.900 Y20.250 E1.12766
...
```

This is the initial portion of a gcode generated for printing an ASTM D790 flexural testing specimen bar. G1 is a standard gcode command stating set Extruder #1 to specific parameters or position. In the first line, Z0.500 is moving the extruder to 0.5 mm off of the print bed surface in the Z (vertical) direction and F3600 sets the feed rate of Extruder #1 to 3600 mm/min. The second line of code then moves Extruder #1 to an X/Y position of 18.31/21.26 mm from origin (usually

the corner of the bed). The third line of code then reduces the feed rate in half before extruding 1 mm of extrudate, or in other words, move the filament forward through the extrusion nozzle by 1 mm. The code then continues this pattern of moving XY position while extruding plastic material essentially creating a single ‘slice’ of the final 3D printed part. When this slice, or layer, is completed the gcode will instruct to move up slightly in the Z axis to begin the next layer in a similar fashion.

The gcode instructs the printer head to move by a specific distance in the X, Y, or Z axis as well as the filament in the E axis. Each of these axes are controlled by a stepper motor connected to a threaded lead screw or timing belt. The 3D printer is calibrated to know how many steps (discrete and quantifiable movements of the motor) are required to move 1 mm. This calibration value for each X, Y, Z, and E axis are stored in the printer’s memory as an EEPROM value and can be tuned to improve precision of the printer. A small subset of FDM 3D printers use a Delta format where the motors are not controlled in an XYZ Cartesian format like above, but rather a transformed axis with 3 arms connected to linear actuators in a parallelogram fashion. This Delta format reduces inertia of the print head resulting in faster printing speeds. Representations of both the Cartesian and Delta style 3D printers are depicted in Figure 2.16.

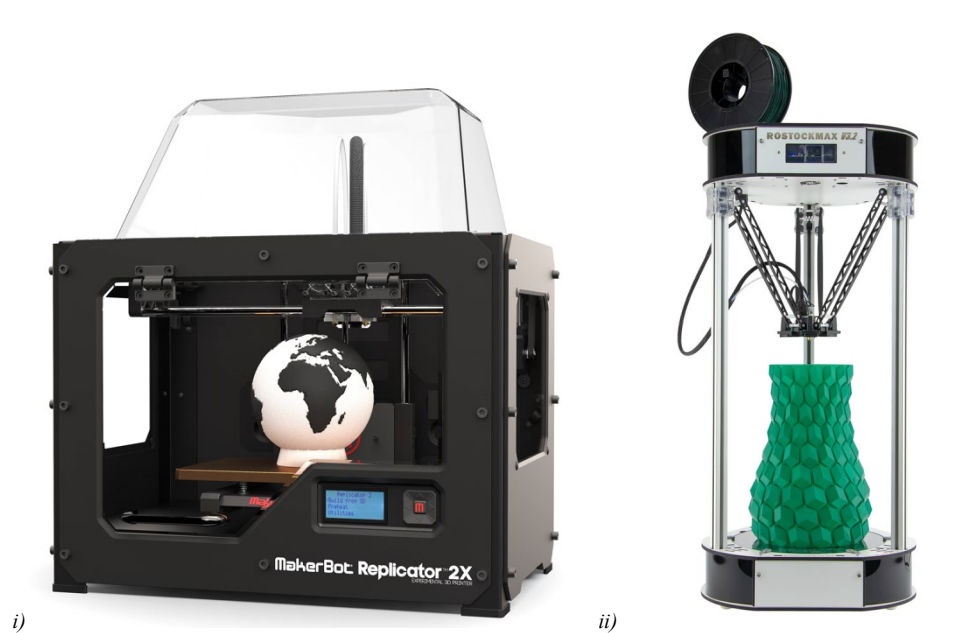


Figure 2.16 - i) Cartesian style Makerbot Replicator 2X and ii) Delta style SeeMeCNC Rostock Max v3.2 3D printers [80], [81]

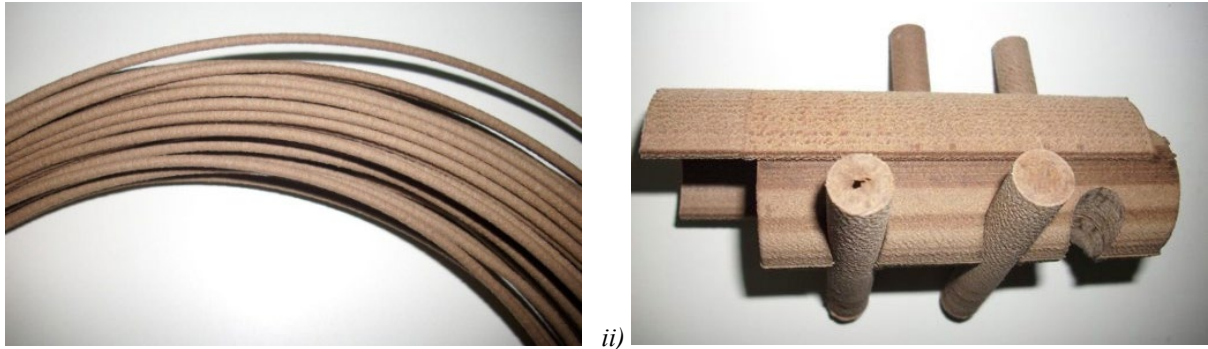
The print head on a 3D printer is essentially one or more extruders used to process the molten plastic and deposit it according to the gcode. An extruder consists of a stepper motor, sometimes geared down appropriately, to push filament through a hot end. The hot end is a heated channel the width of the filament with a die at the end with a specific diameter, usually on the order of 0.1 to 1 mm. Most 3D printer extruders follow this basic design, as laid out by Crump in his original patent, but developments have improved control and precision, throughput, changing between materials and colors, amongst others.

As the molten plastic leaves the hot end nozzle, it is deposited in a smearing manner onto the print bed as the first layer, or onto a subsequent layer of the same print. The print bed acts as a substrate for the 3D print product to be assembled. The adhesion of the first layer to the print bed is critical in the success of the final product, so the surface preparation as well as temperature is controlled to optimize this. Depending on the plastic being used, a substrate material is added to the surface of the bed. Common substrates are blue 3M painters tape for ABS, glue stick applied to glass for PLA, and kapton tape for materials like PC or nylon. These substrate materials ensure that the plastic sticks well enough to the base forming the first layer thus avoiding lateral or vertical shift resulting from shrinkage during crystallization or hardening. Yet these substrate base can be easily removed after completion. To aid in reducing stresses attributable to shrinkage during the solidification, heating is often used to slow the crystallization process. The bed temperature is typically set 10 to 20 °C below the glass transition temperature or melting temperature of the polymer.

The majority of FDM 3D printer systems follow the basic process as outline above. Additional features are added to many printers to alleviate some issues that may occur while printing, but they may vary from printer to printer due to patent infringement. A useful addition to many 3D printers is a full temperature-controlled enclosure, this removes any outside air flow that can cause large temperature gradients and stresses within the printed parts, leading to defects. Other common enhancements include multiple extruders for multicolor and multi-material prints, auto bed leveling and nozzle cleaning to reduce failure points, and even remote monitoring through a camera and a mobile phone application.

2.2.3 – 3D Printing of Nanocomposites

Most of the development of the fused deposition modeling (FDM) approach has been on the design of the device and its mechanical control, like increasing layer resolution (typically between 20-300 μm), controlling the environment (to avoid shrinkage/warping), and increasing the number of print heads (to print multiple materials). Because of these increased capabilities of the printers, a wider range of thermoplastic materials can be considered to exploit their applications on FDM processes. This has already begun to some degree, with manufacturers adding some additives like phosphorescent (glow-in-the-dark), metallic flecks, or fillers (like talc, zinc oxide, and calcium carbonate). There is a leading reinforced fiber polymer (RFP) filament currently on the market for FDM processes. It is called LAYWOO-D3, a 40% wood fiber reinforced thermoplastic composite [82] depicted in Figure 2.17.



i) *ii)*
 Figure 2.17 - a) LAYWOO-D3 40% wood-based composite for FDM and b) the tree ring effect observed [82]

A major advantage of using composite materials is the added mechanical strength that can be added to the printed object. An added benefit is the potential alignment or directionality of the particles that can be controlled to some degree by the movement of the print head. One possible downside to both FDM 3D printing and the addition of particles is the creation of voids during the process [76], this is depicted in Figure 2.18. In FDM, the computer design and control could be augmented to improve orientation of the fibers when the polymer is dispensed, and consequently tune the mechanical properties of the printed object. Skorski et al. showed that the incorporating only a few percent by weight of inorganic nanoparticle TiO_2 into an ABS filament can result in mechanical property improvements. The average stress, Young's modulus, and flexural strength of 3D printed TiO_2 -ABS composites decreased for 1% loading but then showed improvement in all areas over the base ABS polymer with 5 and 10% incorporation [83]. Niaza et al. also showed that incorporating hydroxyapatite (HA) nanorods into a PLA matrix and producing a filament resulted in 3D printed specimens with increased compression strength and modulus over similar loadings of microscale HA [84]. Other composite systems explored for FDM in literature include iron and copper particles suspended in an ABS matrix for improved storage modulus [85], [86], as well as aluminum and aluminum oxide particles in Nylon-6 for a reduced frictional coefficient [87].

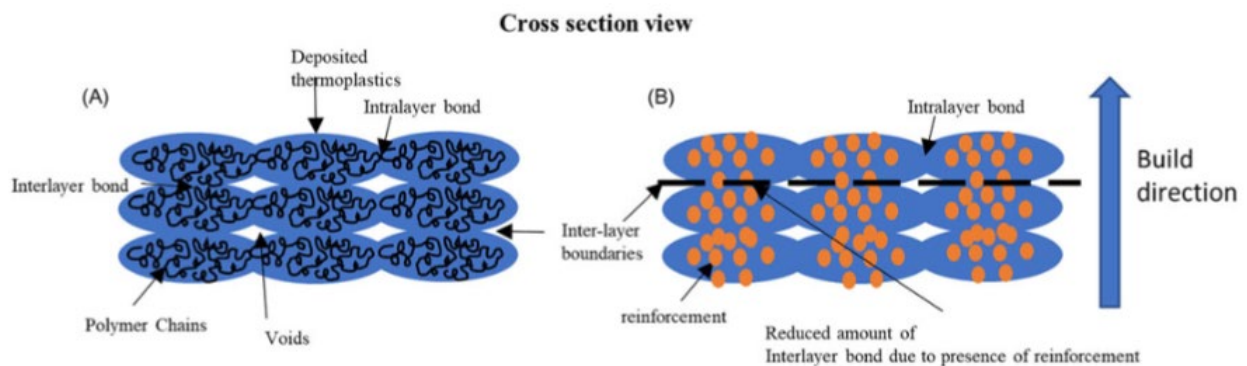


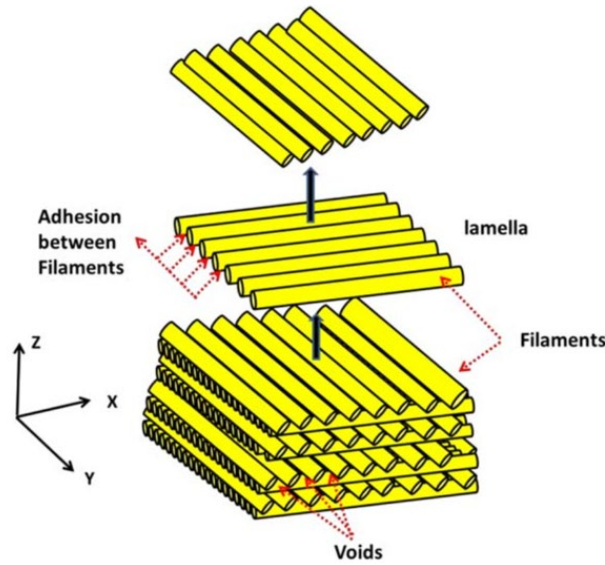
Figure 2.18 -Cross sectional view of a 3D printed specimen identifying A) thermoplastic polymer chain entanglement and B) reinforcement dispersion therein, identifying how voids may be created [76]

The statements made above for the mechanical properties of reinforced composites could also be seen by using metal fillers and their conducting (semi-conducting), thermal, and dielectric properties. Some researchers have been exploring this area including Dr. Bowyer - RepRap

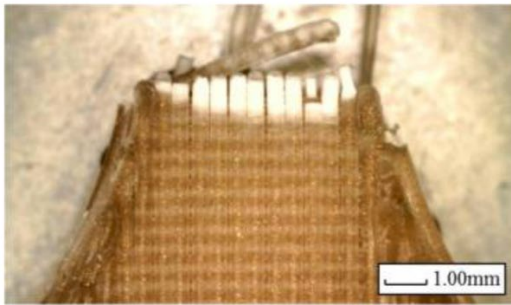
founder and mechanical engineer – by incorporating silver particles into a polymer matrix for improved force sensor conductivity [88]. The incorporation of iron and copper in ABS by Nikzad and Hwang, mentioned previously, also recorded a reduction in the coefficient of thermal expansion of their 3D printed composites [85], [86]. Isakov et al. also demonstrated that the incorporation of BaTiO₃ and CaTiO₃ particles in ABS and polypropylene filaments respectively, resulted in an improved dielectric permittivity and tunable resonance frequency [87]. Similar properties – improved dielectric, x-ray attenuation, and impact resistance – were seen with tungsten particles incorporated into polycarbonate for FDM applications [89].

Unfortunately, there are potential problems with the use of composite materials, especially as the layer resolution quality increases over time (smaller feature sizes) and 3D print speeds go up. One of the most critical problems comes from the clogging and blockage of the tip of the nozzle. The common nozzle die size is 0.35 to 0.5 mm, so particles must be smaller than this to be dispensed. In fact, hourglass specialists dealing with a similar problem state that the diameter should be about 1/5th in ratio of the nozzle size [90]. This suggests a particle size on the order of 70 μm or smaller to be safe. Also, if these particles have some aspect ratio, the longer axis should be below 70 μm. Another issue is that most nozzles are currently made of brass or aluminum, which are relatively soft metals prompt to abrasion and erosion over time as demonstrated by Gnanasekaran while 3D printing carbon nanotube and graphene loaded polymer composites [91].

One possible solution would be to incorporate nanomaterials, as opposed to micro-scale materials, into the thermoplastic matrices to obtain the desired properties. There is a gap in literature with respect to the research and development in the area of nanocomposite thermoplastics for fused deposition modeling. It is important to consider that at the micro-scale the properties of each 3D printed layer are decided primarily by the quality of filaments used, the adhesion between the filaments, and the void density. Figure 2.19 is a diagram of a typical hierarchical structure observed in an FDM printed part including the inter-layer and intra-layer adhesion issues and the voids that are created, as well as a micrograph of this effect occurring in a fractured PLA tensile specimen [92], [93].



i)



ii)

Figure 2.19 - i) diagram representing the typical hierarchical structure of an FDM assembled part and ii) microscope images of a fractured PLA FDM tensile specimen [92], [93]

Although there are definite advantages to FDM, the mechanical properties do not match with traditional technologies like injection molding. Addition of nano-reinforcements into thermoplastics is known to improve mechanical strength, rigidity, toughness, dimensional stability, thermal stability, and aging resistance while having little to no effect on melt viscosity and surface quality of final products. Therefore, it is practical to explore the addition of nanoparticles for improvements in FDM processability and overall performance. [92]

Most of the current literature is comprised of researchers trying to exploit the conductive properties of carbon-based nanomaterials. For example, Simon Leigh et al. of the University of Warwick produced a conductive filament for 3D printing using approximately 15 wt.-% of carbon black (CB) in polycaprolactone (PCL) [94]. The CB particle size was not published but appears distributed around the several hundreds of nanometer range, deducing from the SEM image. Using this material, they were successfully able to fabricate 3D printed flex sensors and gloves, pressure sensors, and a smart ‘vessel’ that could indicate the amount of liquid remaining by measuring the change in resistivity as shown in Figure 2.20.

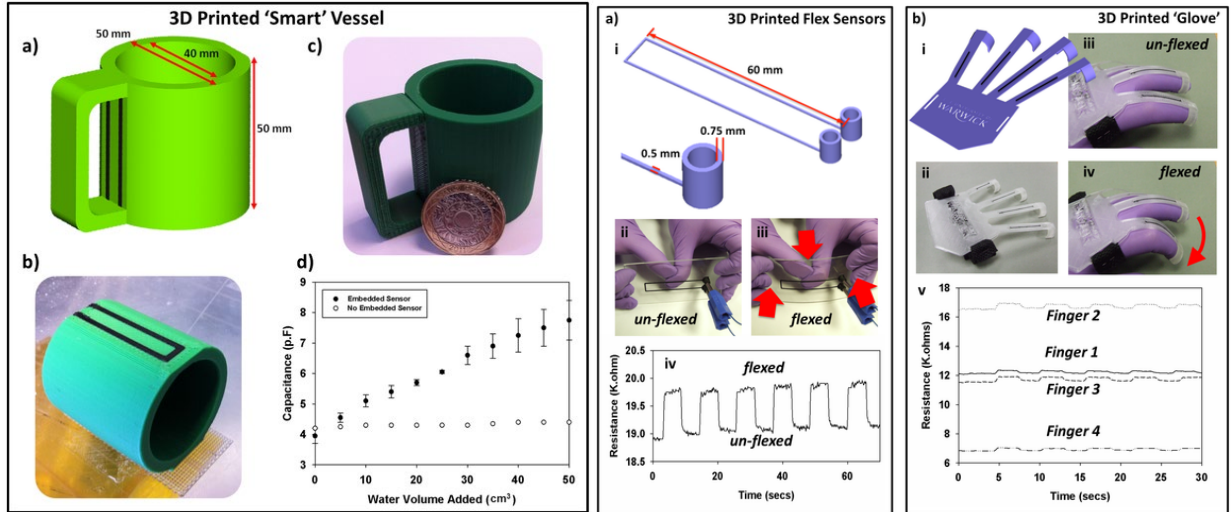


Figure 2.20 - 3D Printed smart 'vessel' and flex sensors fabricated using conductive nanoscale carbon black reinforced polycaprolactone (PCL) as conductive sensors [94]

M. L. Shofner et al. from Rice University used vapor grown carbon fibers (VGCF) as a practical model for carbon nanotubes in ABS [95]. They observed some alignment of the nanofibers in the filament before processing and in the FDM material after processing suggesting orientation attributable to shear in the processing. Tensile strength and modulus increased 39% and 60%, respectively, with 10 wt.-% VGCF loading in ABS. Gnanasekaran et al. also demonstrated that many of these nanocomposite filaments can be easily printed on a commercially available desktop 3D printer, such as the Ultimaker 2 [91]. He 3D printed carbon nanotube and graphene loaded polybutylene terephthalate (PBT) nanocomposites and demonstrated an increase in conductive and mechanical properties.

There are a few publications in literature where the addition of nanoparticles was demonstrated to produce desirable mechanical improvements to the 3D printed materials. TiO₂ added to ABS has been shown to improve the tensile modulus, tensile strength, and reduced elongation at break [96]. Carbon nanofibers or montmorillonite added to ABS has shown improvements in tensile strength and modulus as well as flexural strength and modulus [95], [97].

There is the possibility for future investigation of numerous nanocomposite systems that could take advantage of the fused deposition modeling process to create endless applications from electronic sensors to high-strength/low-weight materials for aerospace and automotive applications. Many current nanomaterials could be exploited to take advantage of their unique properties developed through extremely high surface area; these properties include mechanical strength, conductivity, magnetism, labeling/tagging, anti-microbial, UV-stabilizing.

In a recent review publication in the Journal of Forestry (J-FOR), researchers from FP Innovations in Canada took a look at the potential opportunities for wood-based materials in 3D printing [98]. The potential application benefits for forestry products as feedstock includes giving a new appearance and texture to 3D printed parts, improving sustainability of materials, and increasing desired properties. Cellulose nanocrystals (like CNC) and other cellulosic additives were not identified as a mechanical reinforcement for 3D printer filament in the review, but this could be a

very valuable area of research as many other groups are beginning to see the benefits and explore [99].

Murphy of the University of Limerick has shown successful 3D printing of a microcrystalline cellulose (MCC) and polylactic acid (PLA) composite that also demonstrated morphological, mechanical, and thermal benefits over just PLA [100]. Murphy used a twin-screw extruder to make a fully degradable MCC-PLA biocomposite filaments. The addition of MCC showed an increase in crystallinity over PLA for all composites and DMTA analysis results show that the storage modulus for all composites increased over pure PLA. The developed materials were also successfully 3D printed on a desktop FDM printer.

A brief publication by Wang and Gardner also showed the potential for creating cellulose nanofibril (CNF) and polypropylene (PP) filaments for FDM [47]. Their results showed that loading of up to 30% by weight of spray-dried CNF did not affect the shear thinning behavior suggesting that the FDM process should not be altered much from printing neat PP. Also, flexural strength and modulus of injection molded CNF-PP composites showed an increase for all composites tested.

Park et al. of Simon Fraser University have also presented their work of FDM conductive cellulose composites for 3D printed electronics [101]. Instead of extruding a molten thermoplastic, a slurry of silver nanowires (AgNW) in a carboxymethyl cellulose (CMC) matrix was extruded through a Structur3d Printing FDM paste extrusion system. Successful 3D printing of battery electrode pastes is demonstrated with cellulose's strong thixotropic rheology improving the printability of the paste in a three-layer lithium battery. In a similar fashion, FDM paste printing, Siqueira created 3D objects of anisotropic cellulose nanocrystals (CNC) using direct ink writing [102]. The CNC crystals were dispersed in both water and a photopolymer matrix and 3D printed; the resulting structures demonstrated CNC alignment analogous to the micro-reinforcing effect of cellulose in a plant's cell wall. This research produced textured CNC composites with increased stiffness in the direction of printing and is an early step in realizing the benefits of printing cellular architectures with tunable mechanical properties. This inspires the question: Could one 3D print a tree, or more practically, create a process for AM of wood for construction?

2.2.4 – Slicing and Print Processing Parameters

The gcode that is used by most 3D printers follows the NIST standard that is often used in CNC milling machines and similar devices, although some manufacturers use proprietary versions of standard gcode. Even still, the proprietary code follows the basic concept of standard gcode and is modified or obfuscated for other reasons. Gcode can be entered by hand, but for large complex 3D models this would be too difficult and time consuming so a slicer, or slicing algorithm is employed. [103]

A slicing program takes a 3D CAD (computer-aided design) model, breaks it down into several 2D layers (analogous to slicing a loaf of bread), and determines the gcode required to print each layer. Using a slicing program on a computer is the easiest way to generate gcode; there are many slicing programs that can be used. For example, Slic3r, Cura, and Skeinforge are three free and

open-sourced slicing programs that can be used. Whereas, a slicing program like Simplify3D is a pay software that has its own proprietary library of algorithm parameters improving on many open-sourced options. In fact, now most 3D printers will come bundled with either a proprietary or open-sourced slicer program. [74]

In addition to the 3D CAD model of the final print, the slicing programs use a set of printing parameters to determine the final gcode. These are some of the parameters that were used in the Slic3r 0.9.9 software to create the gcode for 3D printing an ASTM flexural specimen:

```
; generated by Slic3r 0.9.9 on 2013-04-04 at 14:54:57
; layer_height = 0.4
; perimeters = 3
; top_solid_layers = 3
; bottom_solid_layers = 3
; fill_density = 0.4
; perimeter_speed = 30
; infill_speed = 60
; travel_speed = 90
; nozzle_diameter = 0.5
; filament_diameter = 2.90
; extrusion_multiplier = 1
; perimeters extrusion width = 0.53mm
; infill extrusion width = 0.53mm
; solid infill extrusion width = 0.53mm
; top infill extrusion width = 0.53mm
; first layer extrusion width = 1.00mm
```

These are user generated parameters (with some guidance) that will affect the final outcome of the 3D print, like the quality, the time to print, as well as internal geometry and integrity.

The most important, and first chosen parameter for 3D printing is the layer height. This is essentially the thickness of the slices that are to be generated and how tall each layer of the final print will be. The layer height is directly related to the surface quality of the final print, with a lower layer height giving a higher resolution print. The major tradeoff with a lower layer height is that more layers will be required often taking a longer time to fabricate on the printer. The layer height is typically dictated by the nozzle diameter of the printer and should not exceed the nozzle diameter. An ideal layer height is about 50% to 75% of the nozzle diameter. In the example above, the nozzle diameter was 0.5 mm so a layer height of 0.4 mm is acceptable, but slightly larger than ideal.

The number of perimeters for a 3D print is also important, it dictates the thickness of the shell of the 3D print. Each layer is assembled by defining and extruding around the perimeter of the slice and then filling it in, similar to how a child may color in a coloring book to stay within the lines. The top and bottom solid layers are also in a way similar to the perimeter parameter, they define how much shell will be on the top and bottom of the print. In the example above, each the perimeter, top, and bottom solid layers are set to 3, meaning that there are 3 solid layers around the entirety of the outside of the final print.

The fill density parameter dictates how dense the final print will be within the shell that was detailed above and is sometimes referred to as the infill density or simply infill percentage. It is the ratio of the volume of polymer to the volume of air within a print shell. An infill percentage of 100% would result in a completely filled solid 3D print. A 3D print, depending on application,

may not be required to be a complete solid and a reduced infill percentage can be used. For example, if the final print is to be used for a non-functional prototype – like getting a feel for the size in your hand – an infill as low as 10% can be used. Also, many mechanical properties of the final print are near to a complete solid as low as 25% infill.

If the infill is less than 100%, the hollow (or air filled) sections of the internal geometry will be defined by the infill pattern. The infill pattern is the manner the polymer filled areas will be deposited within a perimeter for a specific layer. For example, in Slic3r there are 7 different infill pattern offerings: linear, rectilinear, concentric, honeycomb, Hilbert curve, Archimedean chord, and octagram spiral. A schematic of linear, rectilinear, and honeycomb infill patterns are displayed in Figure 2.21 as well as how a rectilinear pattern may change for different infill percentages. [104]

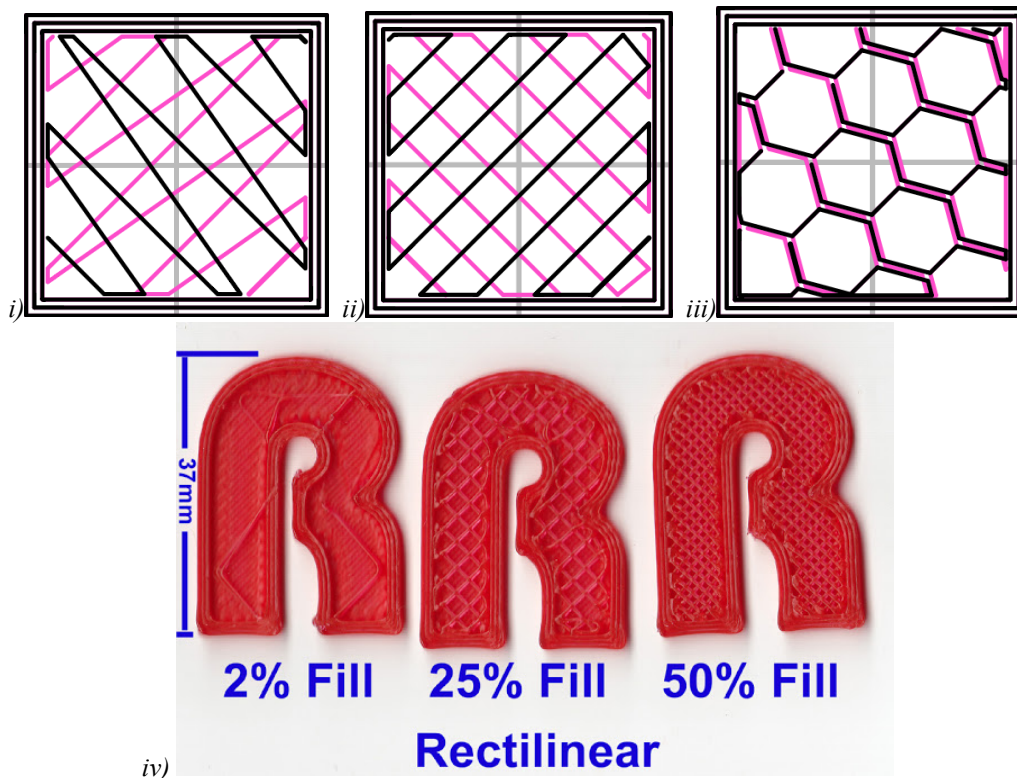


Figure 2.21 - 3D printed sample showing rectilinear fills with three different fill percentages [104]

The perimeter speed, infill speed, and travel speed define how fast the print head moves in mm/s while the printer is completing one of those sections. For the example above, the perimeter speed is 30 mm/s, the infill speed is 60 mm/s, and the travel speed is 90 mm/s. The perimeter is set to the lowest speed as this is where the observable shape of the final print is defined and directly correlates to the aesthetics of the print. A slower perimeter reduces any defects that may be caused by the relaxation (or crystallization) of the polymers as they are deposited onto the previous layer. As well, the residence time is slightly higher for any particular spot resulting in more heat transfer from the nozzle to previous layer improving interlayer adhesion. The infill speed is where the bulk of the print is typically operated and is set as high as possible with no extrusion difficulties. This really depends on the quality and performance of the printer itself. For a high-quality 3D printer this typically reaches a maximum around 100 mm/s. Finally, the travel speed is the operating

speed while not extruding any material. It occurs when the print head needs to move to a new section to resume printing and can be set relatively high as there is little chance of defect. When the speed is calculated it not only scales the X, Y, and Z axis speed but also the E (extruder) axis throughput, all at the same time to ensure consistent geometry.

The filament diameter parameter was mentioned earlier and is the exact diameter of the filament being used. Depending on the manufacturer or supplier the filament may not actually be exactly 1.75 mm or 3.00 mm. This diameter should be measured with a caliper prior to printing and the appropriate slicer parameter adjusted. In this example, the filament used was actually 2.90 mm and proper volume throughput adjustments are made in the algorithm to ensure proper geometry in the print. If the filament diameter cannot be measured, or changes over the length of the filament the extrusion multiplier can be used. This parameter essentially scales the E axis factor that was given earlier independent of the print head speed (x, y, and Z) resulting in more extrudate per unit of time.

The last parameters listed are extrusion widths for perimeter, infill, solid infill, top layer, and first layer. The extrusion width is the horizontal width of the individual polymer tracks being put down and is usually equal to or larger than the layer height. In this example with a 0.4 mm layer height, the extrusion widths for the perimeter, infill, solid infill, and top layer are all set to 0.53 mm. This is slightly larger (6%) than the extruder nozzle diameter and the extra width comes from the smearing down of the polymer to the previous layer. This extrusion width also dictates how much distance the print head will move between different tracks in the X and Y directions. The first layer is set higher to 1.0 mm in this example to ensure good adhesion to the print bed surface. This is typically done if there are any issues with bed leveling or quality to ensure any gaps are filled and create a good layer for the rest of the print to be built.

After combining all of these print parameters with the 3D CAD file, the slicing algorithm will then generate the gcode that can be interpreted by the printer. Other, more complex, parameters can be included in the gcode that are outside of the scope of this research but should be mentioned. Instead of adjusting the first layer extrusion height and width, a brim or raft can be printed that acts as an anchor to the bed platform and easily removed from the final print. This is often done for prints that may have a small contact with the bed in order to increase surface area or for polymers with a high propensity to curl or warp.

2.3 – Polymer Composites

A composite is a multiphase material with significant proportions of each phase. The different phases can consist of metals, ceramics and/or polymers. A typical reinforced or filled polymer composite would consist of two component phases: a continuous polymer phase called the matrix; and a dispersed particulate or networked phase called the filler or reinforcement, this concept is depicted in Figure 2.22 [18]. The motivation for designing a polymer composite is to obtain properties that are not possible from each of the phases alone, such as chemical properties, physical properties or cost. A common commercial example of a polymer composite is a glass-reinforced plastic, which uses short glass fibers in a plastic matrix. Glass-fiber reinforced composites (FGRC)

combine the best properties of each of its components: strength from the glass fibers and toughness and processability from the polymer. By combining the different phases, properties behave differently; the result is a material superior to either of the phases on their own. Additional additives that are typically present in a composite material are antioxidants, plasticizers, stabilizers, flame-retardants, colorants or pigments - these also help provide specific characteristics to the composite.

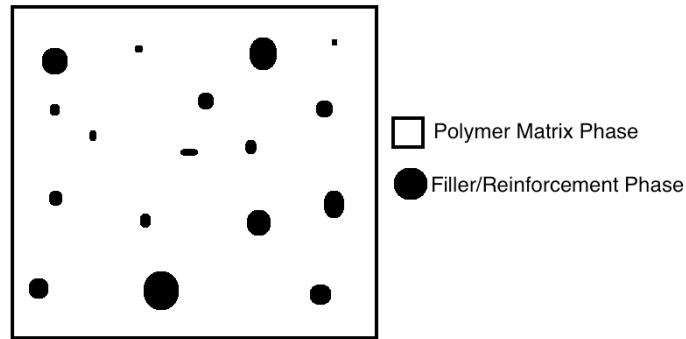


Figure 2.22 - Simple diagram of a two-phase polymer composite material [18]

Thermoplastics are polymers that soften when the temperature is increased, thus allowing for easy processing. The polymer softens because the polymer melts (like in polyethylene) or because the temperature is raised above the glass transition (like in polystyrene). In thermoplastic composites the processing occurs by increasing the temperature and melting the matrix, without melting or softening of the dispersed phase. Thermoplastics have relatively low melting temperature as compared to metals or glasses; thus, the manufacturing costs can be lower. The role of the polymer matrix in a composite is to comprise a majority of the material's volume yet transfer a good portion of the stresses to other stronger reinforcement phases of the material. The polymer matrix holds the reinforcements in place and also acts as a barrier to protect the reinforcing phases from environmental effects and damage. A composite's matrix can be comprised of other materials such as ceramics or metals, but the primary focus in this thesis is on thermoplastic-based composites.

The dispersed filler enhances the inherent properties of the matrix. In a polymer composite, this is often seen as an increase in elastic modulus, uniaxial stress, tensile strength, flexural strength, creep resistance, and density, to name a few attributes. The filler strengthens the polymer by restricting chain mobility, but is typically used as a volume replacement, providing stability and reducing costs. Reinforcements, as a specific type of filler, are used to improve strength and stiffness of the polymer by absorbing a good portion of the applied stresses because of a high aspect ratio. Good interfacial bonding between the polymer and reinforcement within the composite and complete dispersion of the fiber reinforcements is essential in achieving the optimal enhanced properties, maximizing transfer of stress. [105]

If the matrix is intimately bonded to the reinforcing fibers the strain of both the matrix and the fibers should be the same, this is called isostrain. This condition is held true even if the elastic moduli of each composite component are quite different, in fact, this condition holds true for most material properties giving an equation to predict composite properties based on those the individual

components. This equation, known as the rule of mixtures, assumes linearly oriented fibers within the matrix. This relationship for composite material properties, X_c , is expressed in Equation 2.1.

$$X_c = v_m X_m + v_f X_f \quad (\text{Equation 2.1})$$

Where X can represent different properties depending on the modeling approach, X can be: elastic modulus, E_e ; diffusivity, D , thermal conductivity, k ; or electrical conductivity, σ ; and v represents the volume fraction of the matrix (m) and reinforcing fibers (f). A multiplying factor for the $v_f X_f$ term of 3/8 can be used for a uniform statistical planar distribution of the reinforcing fibers or 1/6 for a uniform statistical three-dimensional distribution for the specific case of mechanical properties. The derivation of Equation 2.1 can be found in the text, “Principles of Polymer Composites” by Alexander Berlin [106].

There are a number of complications when dealing with polymer composites that should be outlined and considered herein. Attention should be given to these five possible factors that will result in a less than ideal polymer composite:

1. Agglomeration of the filler particles can also lead to reduced strength as the surface area between the polymer and filler is reduced, this is especially a problem when considering nano-scale fibers.
2. Shear and heat during processing must be controlled to minimize fiber degradation.
3. Porosity can also be formed easily through the production process, as poor wettability of the fiber by the polymer matrix, or degassing of the fiber, will create voids around the surface of the fiber; voids are initiation points for cracks and thus the strength is compromised.
4. Coefficient of thermal expansion between polymer and filler often differ by 10 times, which leads to residual stresses within the composite.
5. A major effect of incorporation of filler within the polymer matrix is a change in the recrystallization mechanism, resulting in a much different crystallization of the composite compared to an unfilled polymer. [106], [107]

2.3.1 – Nanocomposites

Nanotechnology is the field of observing features in the nanoscale, and also controlling these features in functional engineering design. The nanoscale refers to the size-range between 1 and 100 nanometers, but this range is flexible depending on field of study and application. As a polymer materials engineer, designing nano-scale functional devices is of lesser importance than understanding the relationship between chemical structure and bulk properties of a material: the cornerstone of materials science and engineering. For example, maintaining small grain sizes on the nanoscale can significantly improve mechanical properties of the bulk material, like the yield strength [108].

Dispersing nanoparticles, like NCC, into a polymer matrix to add and improve electrical, thermal, and mechanical properties creates a polymer nanocomposite [109]. Nanoparticles have been used in the past to create more desirable attributes in materials such as unusual combinations of stiffness

and toughness, among other properties. For example, carbon nanotubes can be used in a polymer nanocomposite to improve strength, conductivity, and thermal conductivity to name a few attributes [108].

Because this is such a new industry, this nanocomposite research has been more empirical (learning through experimentation), especially with a new material like NCC and Equation 2.1 presented earlier for material property predictions is no longer valid. A prime example of this empirical nanotechnology is automotive tires; carbon black nanoparticles have been used to reinforce the elastomeric rubber in tires long before it was understood ‘why’ the carbon black improved strength, toughness, and permeability to air. Now, as more resources are being focused on advanced materials, polymer nanocomposites can be better understood, and new materials can be better engineered. This thesis will contribute to the bank of knowledge being generated for NCC composites.

Materials at the nanoscale have unique surface characteristics; going from a bulk material to the nanoscale causes the surface area to volume ratio to increase exponentially as the particles approach small dimensions. This allows for stronger interactions between the polymer matrix and the exposed surface of the nanoparticles. Moreover, the distance between the nanoparticles is decreased. When filler particles have nanoscale dimensions, the fraction of atoms on the surface of the particles becomes very significant as does the amount of interfacial material and thus surface properties will dominate. This effect is depicted in Figure 2.23; a decrease in the reinforcing particles diameter by one order of magnitude – from 10 to 1 μm – will increase the number of particles 1000 times and increase the available surface area by an order of magnitude. Decreasing from micro- to nano-scale – 1 μm to 10 nm particles – increases the number of particles by 1 million times and the surface area shoots up by two orders of magnitude. [110]

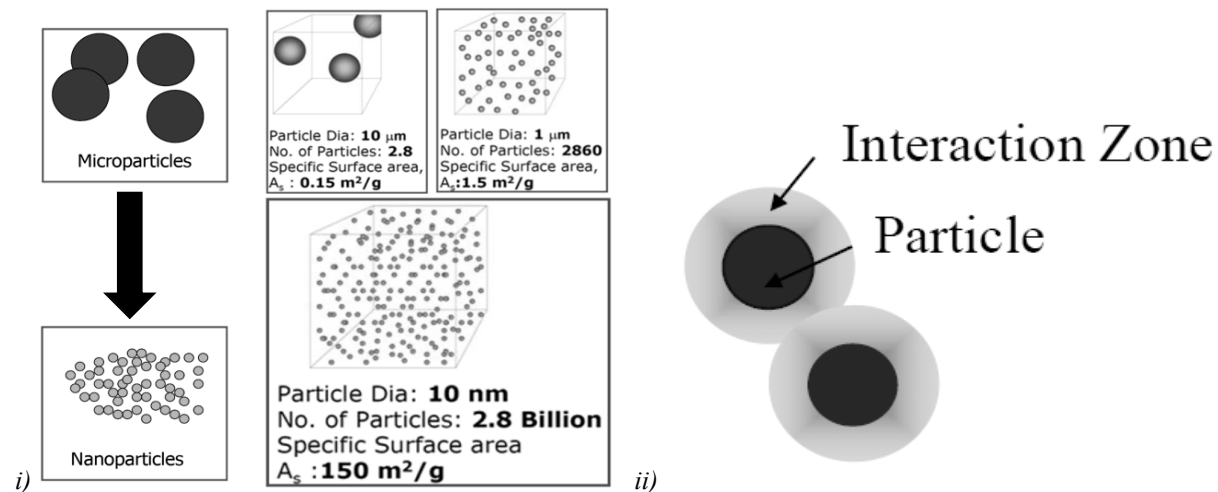


Figure 2.23 - i) Effect of the nano-scale on number of particles and surface area and ii) the interaction zone between the filler particle and matrix [110]

When considering nano-scale reinforcements, incorporation of only a few percentages by mass into the matrix is required to achieve mechanical properties that were achieved previously with greater than 30% microparticle incorporation. This effect of decreasing particle size versus the resulting elastic modulus is shown in Figure 2.24, it is seen that a much smaller concentration of

nanotubes is required to achieve the same modulus as reinforcing the polypropylene with talc, about 2% and 35% respectively for an increase in modulus from 1.37 GPa to 3.5 GPa. This increase in properties is once again because a good portion of the matrix located at the nanofiber interface, and conversion of bulk polymer into interfacial polymer is the key to improved property profiles.

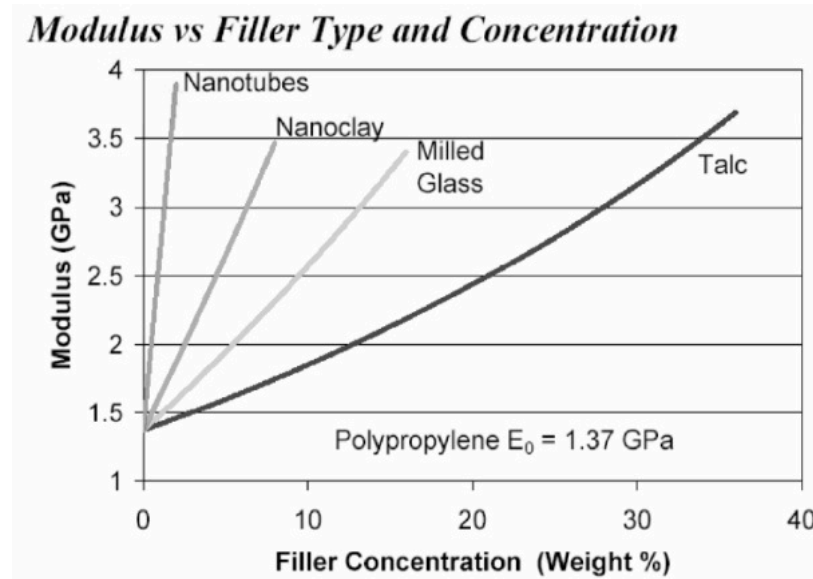


Figure 2.24 - Effect of particle size and filler concentration on mechanical properties in polypropylene [110]

2.3.2 – Thermoplastic Matrices

Polymers are a category of materials formed by long molecular chains obtained by polymerization. Typical classifications of polymers based on properties are thermoplastics, thermosets and elastomers. Thermoplastics are typically ductile or deformable material that are available for many applications in fibers, thin-films, sheets, foams, molding, and in bulk. Intermolecular forces hold the chains together and depending on the chain length (the molecular weight) and crosslinking networks, the polymers can have different levels of rigidity or different working temperatures.

Thermoplastics are a subcategory of polymers that can lose rigidity or be melted with increased temperature and then become rigid or crystallize again after cooling. Thermoplastics are long-chain polymers, with a high molecular weight, that have weak intermolecular bonding. As temperature is elevated, intermolecular bonds like Van der Waals forces, hydrogen bonding, or dipole-dipole interactions are broken by thermal energy allowing the polymer to flow, when heat is removed these bonds strengthen. Some common commercial thermoplastics include polyethylene, polypropylene, polystyrene, polyvinylchloride, and polycarbonate. Thermoplastics are processed using mainly injection molding, extrusion molding, blow molding, and some compression molding.

2.3.3 – Cellulose Nanocrystal Reinforcements

A trend in composite manufacturing is the use of natural fibers as the filler or reinforcing material in polymer composites. Among the driving forces are high specific properties, utilization of

renewable feedstock, lower energy for processing and aspects related to the crashworthiness of the materials. In the context of this thesis, the term natural fiber is limited to plant fiber and does not include natural inorganic fibers (like asbestos for example). The idea of using natural fibers as polymer reinforcement has been around since the 1920s, when Henry Ford recognized the utility of hemp fibers in his vehicles. Consumer demands are now requiring composites engineers to look to natural fibers for renewability and cost reduction by replacing material volume in a vehicle with natural fibers or bio-based materials. These natural fibers can come from a variety of natural sources, for example: sawmill waste (trees); rice husk; banana leaves and stalk; coconut husk; groundnut shell; jute fiber; rice and wheat straw; sisal fibers; seaweed; and cotton stalk [111].

In the past, plant fibers have been one of the most popular choices for use as a filler material in polymers. Wood and wood flour had been the filler of choice until about the year 2000, when industry research shifted to focus on cellulosic and lignocellulosic plant fibers; the components of the plant that have the most appropriate properties for polymer composites. These properties include low-density, non-abrasive nature, high filler loading, biodegradability, renewability and mechanical strength. Less valuable components of the plant fibers, like hemicellulose, were removed using chemical and mechanical processes.

As it looks, the next generation of composites will begin to use more refined natural fibers, like Nanocrystalline Cellulose, as the reinforcing agents in composite materials [112]. A recent realization is that a stronger nanocomposite material would require a reduced volume or mass compared to the original component material. This stronger nanocomposite material would allow for component redesign and miniaturization [113]. For example, Mathew of Norwegian University of Technology and Science has worked with the extrusion of NCC-Poly(lactic acid) for improved mechanical properties; an increase in the composite's elastic modulus from 2.0 to 2.4 GPa was observed, an increase of nearly 20% with only 5% incorporation of NCC [114]. Similarly, Petersson observed an increase in tensile strength by 12% with a solution casted Microcrystalline Cellulose-PLA composite [115]. In 2005, researcher Yano reported the first example of an optically transparent composite with bacterial cellulose loading as high as 70%, observing mechanical properties five times that of some engineered plastics [116].

2.3.2.1 – Nanocrystalline Cellulose

This section on Nanocrystalline Cellulose (NCC) will serve as an overview and brief history of the material, including its chemical structure as well as techniques for isolating the nanofibers, which will help in understanding the degradation mechanisms.

Nanocrystalline Cellulose is a new and innovative use for wood pulp, developed by Canadian researchers in association with the forestry industry of Canada. It is an unconventional nanomaterial with certain properties matching and exceeding that of current standard nanomaterials such as carbon nanotubes. Nanocrystalline Cellulose has very unique optical, electrical, magnetic and strength properties. Some other inherent properties of the NCC nanocrystals - which will prove beneficial - are that they are sustainable, biodegradable, non-toxic, and fully recyclable.

A typical Nanocrystalline Cellulose particle is about 200 nm long and 10 nm wide and consists of a small bundle of the crystalline cellulose strands tightly bound together. Table 2.2 shows a comparison in sizes and the resulting surface area increase of 6000 times of NCC over traditional pulp fillers, which are also primarily cellulose based [15].

Table 2.3 - Comparison of the cellulosic dimensions of NCC and pulp [15]

Dimension	Nanocrystalline Cellulose (NCC)	Pulp
Fiber Length	200 nm	1.5 m
Fiber Diameter	10 nm	30 μm
Relative Surface Area	6000	1

Cellulose is naturally strong as its main function in nature is to provide strength and protection to the cell wall of a living plant. These inherent strengths, through hydrogen bonding, also makes the isolation of individual nanocrystals quite difficult. It is reported that the tensile strength of typical Cellulose Nano Whiskers (CNWs) is about 10000 MPa with an elastic modulus of 150-250 GPa [114]. A whisker is classified as having an aspect ratio of approximately 20-60, whereas NCC often has an aspect ratio greater than 100. Table 2.3 includes some potential, future applications for Nanocrystalline Cellulose [15].

Table 2.4 - Potential applications for Nanocrystalline Cellulose [15]

<i>Nanocrystalline Cellulose (NCC) Applications</i>
Reinforced polymers
High strength spun fibers and textiles
Advanced composite materials
Films for better barrier and other properties
Additive for coatings, paints, lacquers, and adhesives
Switchable optical devices
Pharmaceuticals and drug delivery
Bone replacement and teeth repair
Improved paper, packaging, and building products
Additive for foods and cosmetics
Aerospace and transportation

Most of the research into NCC composites has been very recent, with most development happening after the year 2000. Dispersing microfibril cellulose into organic polymer composites for improved properties has been practiced for a few decades [117], [118]. As processing techniques

for NCC were improved their applicability as a reinforcing agent with superior mechanical properties was quickly discovered [119]–[121]. Various matrices have been studied with a Nanocrystalline Cellulose source including poly(lactic acid) [122]–[125], polyurethane [126], polyolefins [126], and even an all-cellulose composite [127], [128].

Chapter 3. Preparation of Polycarbonate Nanofibers Containing Nanocrystalline Cellulose

Chapter 3 has been published in full in the peer reviewed journal J-FOR: The Journal of Science and Technology for Forest Products and Processes:

A. C. Finkle and L. C. Simon, "Preparation of polycarbonate nanofibers containing nanocrystalline cellulose," *J-FOR*, vol. 2, no. 6, 2012. [129]

Abstract: Nanofibers offer great potential for new products like composites, catalysts, filters, textiles and batteries. Developing reinforced polymer nanofibers using an electrospinning technique is being explored here. The objective of this work is to prepare polycarbonate (PC) nanofibers with nanocrystalline cellulose (NCC) well dispersed within these nanofibers. The final product is non-woven composite nanofibers with individual diameters in the range of 10-1000 nm. This investigation looks at different electrospinning parameters (specifically solvent, concentration and electric field) for five PC systems and two NCC-PC composite systems. Five solvent systems were investigated: dimethyl sulfoxide (DMSO), tetrahydrofuran (THF), n,n-dimethylformamide (DMF), chloroform and a THF/DMF solvent mixture. Nanofibers of PC and PC-NCC were successfully produced with diameters as low as 40 nm using the mixture of THF:DMF solvents. The results indicate that the different electrospinning parameters explored define the nanofiber diameter and morphology.

Keywords: electrospinning, composites, nanofibers, nanocrystalline cellulose (NCC), polycarbonate (PC)

3.1 - Introduction

Electrospinning is a technique to make micro and nanoscale fibers using a strong electric field to draw a polymer solution out of a fine tip. The expected benefits of the composite nanofibers include extremely high surface area to volume ratio, control of fiber diameter, alignment of nanoparticles within the nanofibers, and high strength to weight ratio. These fibers typically have a nano-scale diameter (on the order of 100 nm) and have countless possible applications. Because of the benefits of the extremely high surface area to volume ratio at the nanoscale, electrospinning is opening a new processing field, which hopes to find new applications for well-known polymer systems. Electrospinning is a simple and low-cost method to achieve fibers with desired properties like high surface area and high porosity in the non-woven mat, with applications in industries such as catalysis and ultra-fine filtration.

There are several material formulation and process parameters that control the size and morphology of the electrospun fibers. The material parameters observed are typically: type of solvent, type of polymer, polymer molecular weight and distribution, concentrations and additives.

Process parameters include: collector type, applied voltage, gap distance, syringe feed rate, needle tip diameter and environmental factors like humidity and temperature.

Numerous material systems have been explored via the electrospinning technique including polymers, inorganics, and composite systems. For example, poly(ethylene oxide) [26], poly(vinyl alcohol) [28], polypropylene [30], polyethylene [31], polyamide [4] and polycarbonate [16], [33]–[36], [48] solutions have been well documented in literature. Most reports in the literature are based on polymer systems using water as a solvent. Polycarbonate (PC) in particular has been explored for tissue scaffolding [35], [36] and other authors have reported on the fabrication of pH sensors using polycarbonate/tetrapyrzinoindoloporphyrazine composite electrospun nanofibers [48]. Different solvent systems are known to affect the resulting size and morphology of the PC nanofiber mat. Shawon et al. have determined an optimal ratio of THF and DMF for electrospinning polycarbonate to achieve the lowest amount of bead formation [34].

A more recent trend in the area of electrospinning is the inclusion of nanoparticles into the polymer solution before spinning, thus allowing the creation of composite nanofibers. The addition of nanoparticles can result in materials with new attributes. Yingjie Li has explored the electrospinning of nanocrystalline cellulose (NCC) water-in-oil emulsions with poly(lactic acid) (PLA) [42]. Another advantage of electrospinning composite nanofibers is the nanoparticle alignment that occurs as a result of the elongation of the polymer during the formation of the nanofiber. This effect can give rise to advantageous uniaxial properties in the fibers. For example, the inclusion of carbon nanotubes was reported to improve conductivity and tensile strength of the electrospun nanofiber mat [32], [130].

Objective

At present there is not a large amount of research on electrospinning nanocrystalline cellulose (NCC) with polymers and virtually nothing using a polycarbonate matrix with NCC [19]. This work will explore the new developments in electrospinning of polycarbonate and polycarbonate reinforced with NCC. The objective is to achieve desirable fiber size and morphology. The five solvent systems investigated for PC were dimethyl sulfoxide (DMSO), tetrahydrofuran (THF), n,n-dimethylformamide (DMF), chloroform and a THF/DMF solvent mixture. The DMF and THF/DMF solvent mixture systems – with PC – were then electrospun with the incorporation of NCC.

3.2 – Materials

The cellulose nanocrystals (CNC) were manufactured and supplied by FP Innovations Inc. of Quebec, Canada. Their product has since been commercialized and trademarked as Nanocrystalline Cellulose (NCC) by CelluForce Inc. and will be referred to as Nanocrystalline Cellulose or NCC herein. As received, the NCC was slightly off-white in color and in the form of freeze-dried translucent flakes. The typical NCC particle size is approximately 200 nm in length and 10 nm in diameter. The tensile strength of NCC-FP is estimated to be about 10000 MPa with an elastic modulus of about 150 GPa [15].

The polycarbonate (PC) sample was received from PolyOne distributors; it was produced by StarPlastic Inc. of Millwood, WV. The trade name of the resin is StarPlastic PC743R-CLS112 Molding Grade PC. It is safe for ultraviolet light, water exposure, immersion, and acceptability for outdoor use in accordance with UL 746C. The PC has a tensile strength of 62.1 MPa and an elastic modulus of 2.41 GPa [131].

The solvents used herein are reagent grade chloroform, dimethyl sulfoxide (DMSO), tetrahydrofuran (THF), and n,n-dimethylformamide (DMF) obtained from Sigma Aldrich and Caledon Labs and used as received.

3.3 – Methods

Electrospinning uses an applied voltage – typically in the range of 5 kV to 30 kV – to draw out very fine fibers from a liquid droplet. The droplet of polymer solution is formed at a charged syringe tip that is fed with a polymer solution typically via a syringe pump. A Taylor cone is formed at the tip of the droplet due to the accumulation of charges on the droplet surface. Small amounts of solution are pulled away from the droplet, as the surface tension is broken due to a force imbalance caused by the electric field. This forms a long fiber as it whips through the gap distance towards the grounded base; this region is also referred to as the instability region. The nanofibers are gradually deposited on a grounded collector several centimeters below the needle in a non-woven pattern. A typical electrospinning apparatus is depicted in Figure 3.1; it is considered a vertical alignment as the needle is above the collector.

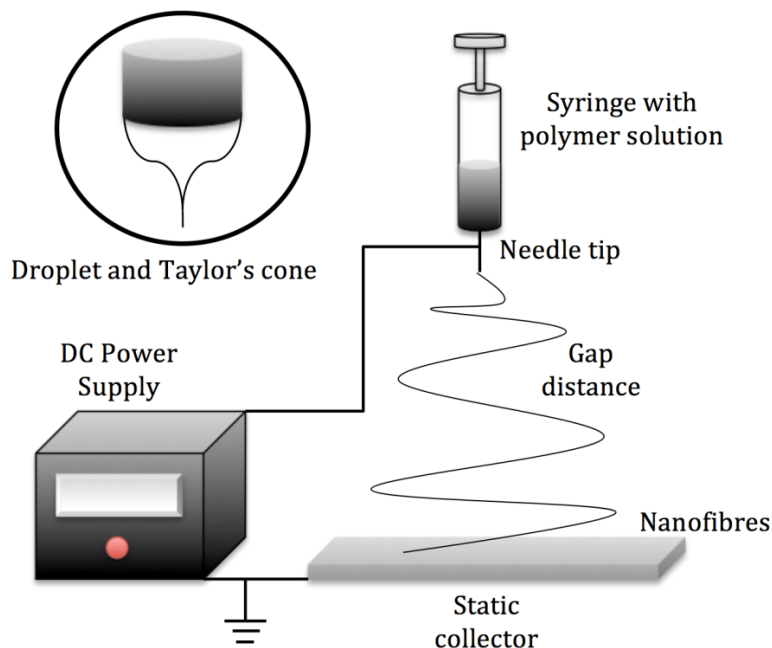


Figure 3.1 – Schematic diagram of a typical vertical electrospinning apparatus.

The polymer solution preparation technique was constant regardless of the solvent system being used. The correct volume of solvent was brought to a boil in a reflux apparatus followed by the

addition of the polycarbonate pellets. The solution was stirred and refluxed for two hours at a temperature slightly above the solvent boiling point until a homogenous and viscous solution was achieved. The solution was allowed to cool back to room temperature before electrospinning. For the NCC-PC composite system, the cellulose was ultrasonicated in the solvent for twelve hours prior to the reflux with PC. This procedure was developed to ensure a good dispersion of the NCC. The polymer solution was then loaded into a 5 mL syringe with 1.5” 18 G blunt needle and placed in a syringe pump for electrospinning. The collector used was aluminum foil on a static stainless-steel plate. The foil was later transferred to a scanning electron microscopy (SEM) stub for imaging. The electrospinning apparatus used was aligned vertically with the needle above the static collector and a positive charge was applied at the needle tip.

The morphology and diameter of the nanofibers and the non-woven mat produced by electrospinning were investigated with scanning electron microscopy. The microscope used for imaging was a Carl Zeiss Leo 1530 Gemini Field Emission SEM operating in secondary electron mode with an applied voltage of 5 to 10 kV. The electrospun samples were sputtered with gold to ensure the sample was conductive prior to imaging.

The six polycarbonate-solvent systems are listed in Table 1 for chloroform, dimethyl sulfoxide (DMSO), tetrahydrofuran (THF), and n,n-dimethylformamide (DMF), (60:40) THF/DMF mixture. The composite nanofiber parameters are also listed for the (60:40) THF/DMF mixture with nanocrystalline cellulose (NCC). The DMF system was also tested with NCC but electrospinning was unsuccessful.

Table 3.1 – PC and NCC/PC electrospinning solutions process and formulation parameters.

Experiment Solvent	Chloroform	DMSO	THF	DMF	THF/DMF (60:40)	THF/DMF (60:40) + NCC
Polycarbonate (wt-%)	15	15	15	14.7 (98% in solid)	15	19.8 (95% in solid)
NCC-FP (wt-%)	0	0	0	0.3 (2% in solid)	0	1.04 (5% in solid)
Solvent (wt-%)	85	85	85	85	85	79.2
Applied Voltage (kV)	10,15,20	5,10,15	10,15,20	10,15,20	15,20,25	15, 20, 25
Distance (cm)	15	15	15	15	15	15
Time (s)	180	180	180	30	30	30
Flow Rate (ml/min)	1.00	0.65	1.00	2.50	1.00	9.00
Temperature (°C)	23	70+	23	23	23	23

3.4 – Results and Discussion

Preliminary experiments with polycarbonate were completed with chloroform, DMSO, THF, DMF and a mixture of THF and DMF as a formulation parameter. These experiments were carried out to achieve a comparative evaluation of the solvent systems in producing nanoscale fibers. Parameters such as polymer concentration, applied voltage, time elapsed, and syringe feed rate were varied and adjusted throughout the experimentation and eventually tended towards an appropriate range. For example, polymer concentrations of approximately 15 to 20% by weight were preferred because with a concentration lower than 15% there was an increased chance of electrospinning and above 20% it was difficult to pump the solution because the increased viscosity. The applied voltage was started around 10 kV over a short distance of about 10 cm (1 kV/cm electric field). It was found that as the applied voltage was increased (to a maximum of 25 kV) the fiber diameter was reduced; as well increasing the gap distance aided in solvent evaporation and decreased fibers welding together after overlapping on the collector. A gap distance of 15 cm was quickly found to be more appropriate and held constant for all of the experiments. The length of time of the electrospinning was reduced to 30 seconds as there was enough fiber collected for analysis with the scanning electron microscope. Syringe feed rate was typically dependent on the viscosity of the solution; a feed rate was found to avoid the droplet at the tip of the needle from falling to the collector but also from receding up into the tip during spinning. The typical feed rate for each system is listed in Table 1; typical feed rates were about 1-10 mL/hr.

Chloroform

The first solvent system tested was chloroform, as it is known to be a good solvent for polycarbonate. The boiling point for chloroform is 62.1 °C with a dielectric constant of 4.81 and density of 1.498 g/mL. Chloroform is considered a non-polar solvent. Figure 3.2 shows the fibers electrospun using chloroform. For the most part, the chloroform-PC system can be electrospun resulting in a fairly narrow distribution of fiber diameter. There was some beading of the PC material, this can be seen in Figure 3.2(i) and is considered an undesired defect. The beads have a raisin-like morphology resulting from the solvent evaporating from a polymer solution sphere and subsequent collapse. Figure 3.2(ii) and (iii) show surface porosity that appears along the length of the PC fibers from the solvent evaporating during spinning; the fiber also appears wrinkled or puckered due to the shrinkage from the same dry-skin effect [33]. The tiny pores are caused by a crazing phenomenon; this increases the surface area but may decrease the mechanical properties of a smooth surface [33]. The dispersion of NCC in chloroform was attempted, but because the solvent is non-polar, the polar NCC separates into a second phase and settles easily to the bottom of the container. Our observations concluded that chloroform as a solvent was suitable for the electrospinning of polycarbonate but with the incorporation of nanocrystalline cellulose there are dispersion issues.

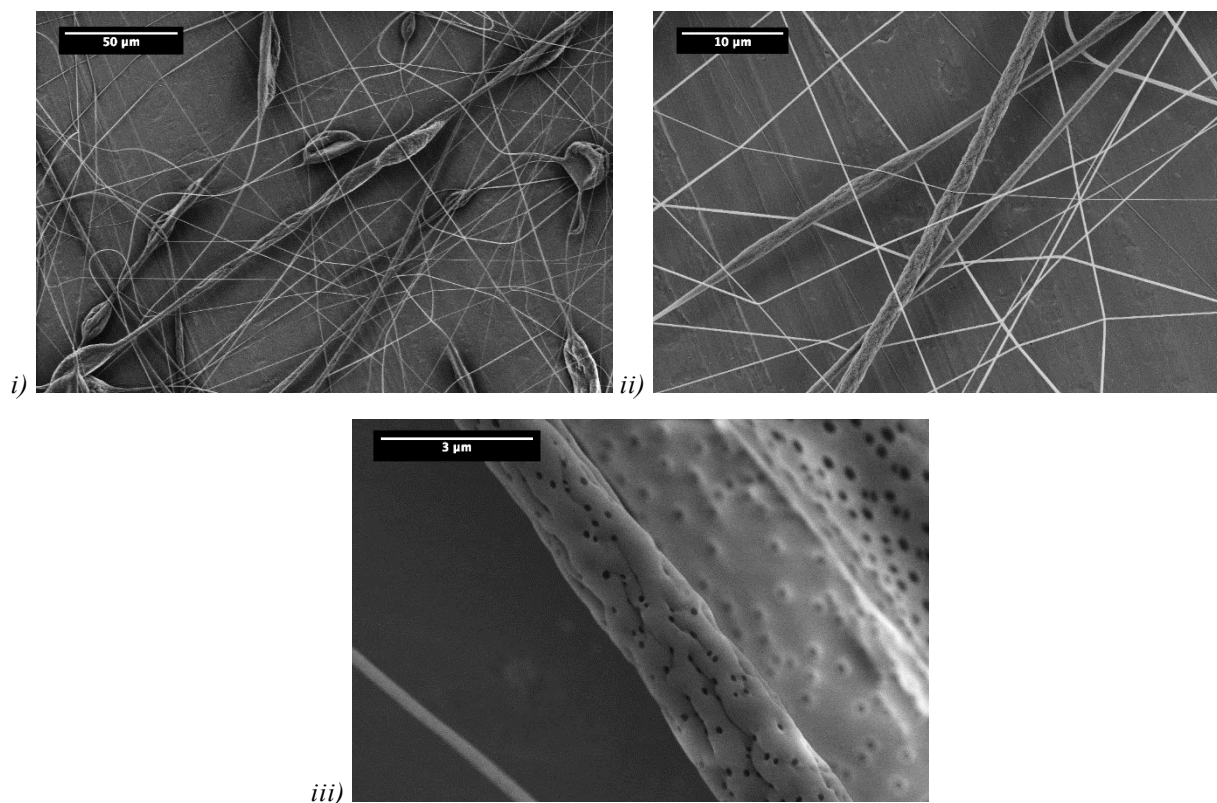


Figure 3.2 – SEM micrographs of 15 wt-% PC nanofibers electrospun using chloroform. Fibers i) and ii) were electrospun using $V_{app} = 20 \text{ kV}$ and iii) using $V_{app} = 15 \text{ kV}$ over a gap distance of 15 cm.

Dimethyl sulfoxide (DMSO)

The second solvent system tested was dimethyl sulfoxide (DMSO), which has a boiling point of 189 °C, a dielectric constant of 46.7, and a density of 1.092 g/mL. DMSO is a polar aprotic solvent. Figure 3.3 shows the fibers electrospun using DMSO. The fiber diameter had a somewhat narrow distribution. DMSO had the highest boiling point and polarity of the chosen solvents. The DMSO-PC system was not stable at room temperature and began to solidify as it cooled to room temperature. To attempt to avoid the hardening of the polymer, the syringe was preheated above 70 °C before the electrospinning was completed. After about 20 s of the electrospinning, partial solidification of the droplet at the needle tip was observed thus causing the formation of multiple Taylor cones branching out from each other. The lengths of the experiments were reduced to 30 seconds from 180 because of this solidification. Figure 3.3(i) shows the non-woven mesh that was created by the multiple Taylor cones spinning simultaneously. Many of the fibers welded together creating a thicker structure, with fibers supporting themselves several microns above the surface of the collector, much thicker than the other experiments where most the fibers were deposited directly on the collector surface. Figure 3.3(ii) shows some fibers that coiled or collapsed into each other. Figure 3.3(iii) shows the rough surface of the PC fibers that were formed. This morphology is attributed to the solidification of the solution and the high boiling point solvent (DMSO). Dispersion of NCC within DMSO was unsuccessful.

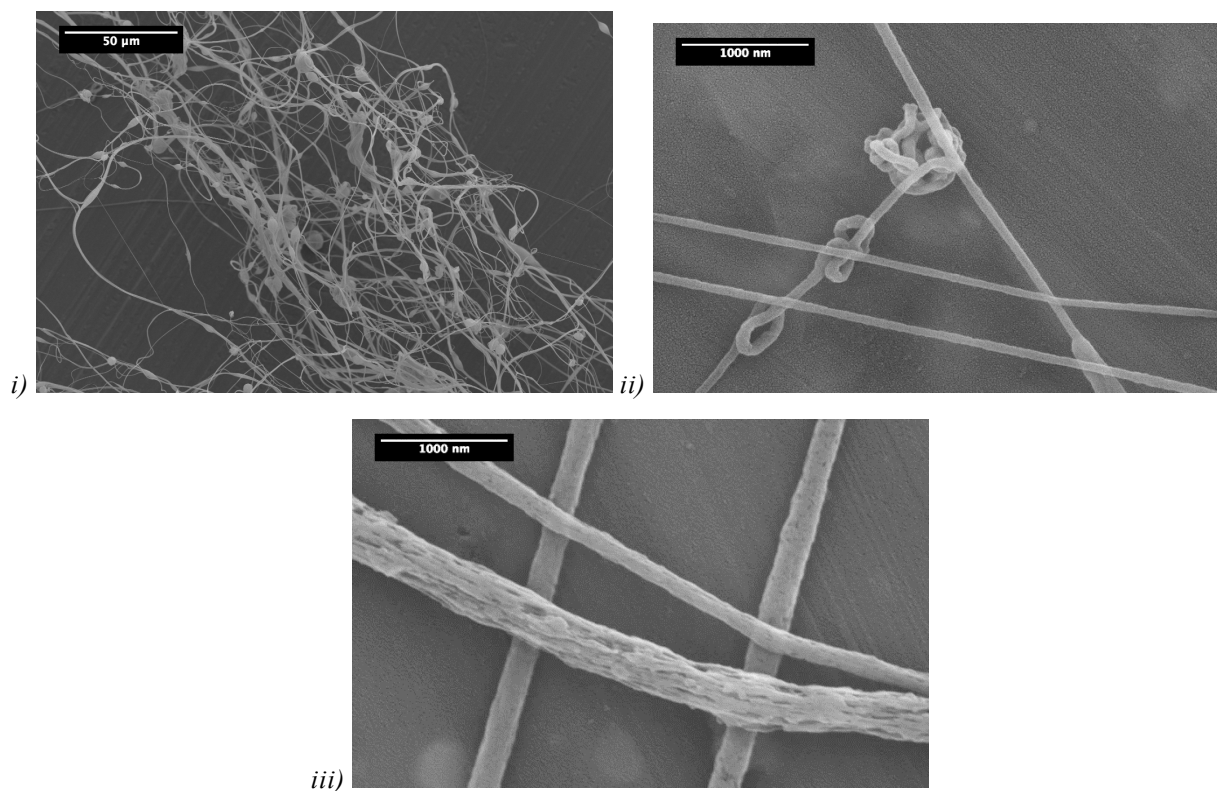


Figure 3.3 – SEM micrographs of 15 wt-% PC nanofibers electrospun using DMSO. Fibers i) were electrospun using $V_{app} = 5$ kV, ii) using $V_{app} = 15$ kV and iii) using $V_{app} = 20$ kV over a gap distance of 15 cm.

Tetrahydrofuran (THF)

The third system that was electrospun with polycarbonate was tetrahydrofuran (THF). THF is a polar aprotic solvent with a boiling point of 66 °C, density of 0.886 g/mL, and a dielectric of 7.5. Figure 3.4 shows the resulting nanofibers. In Figure 3.4(i), it is seen that there is a large amount of beading in this system. This behavior is attributed to that fact that THF is not a good solvent for PC. A white opaque solution is formed rather than a mostly transparent solution formed with each of the other solvents. This effect has been reported in literature, and the addition of DMF has been used to make a more compatible solvent [34]; this approach will be explored later in this section. Compared to the chloroform solvent, the beading density is greater and the ratio of bead diameter to fiber diameter appears much larger. The morphology of the beads is visible in Figure 3.4(ii) and (iii); again, the raisin shape is observed and is elongated. Surface porosity is observed on the beads and to a lower degree on the surface of the fiber segments. Good dispersion of NCC into THF was unsuccessful.

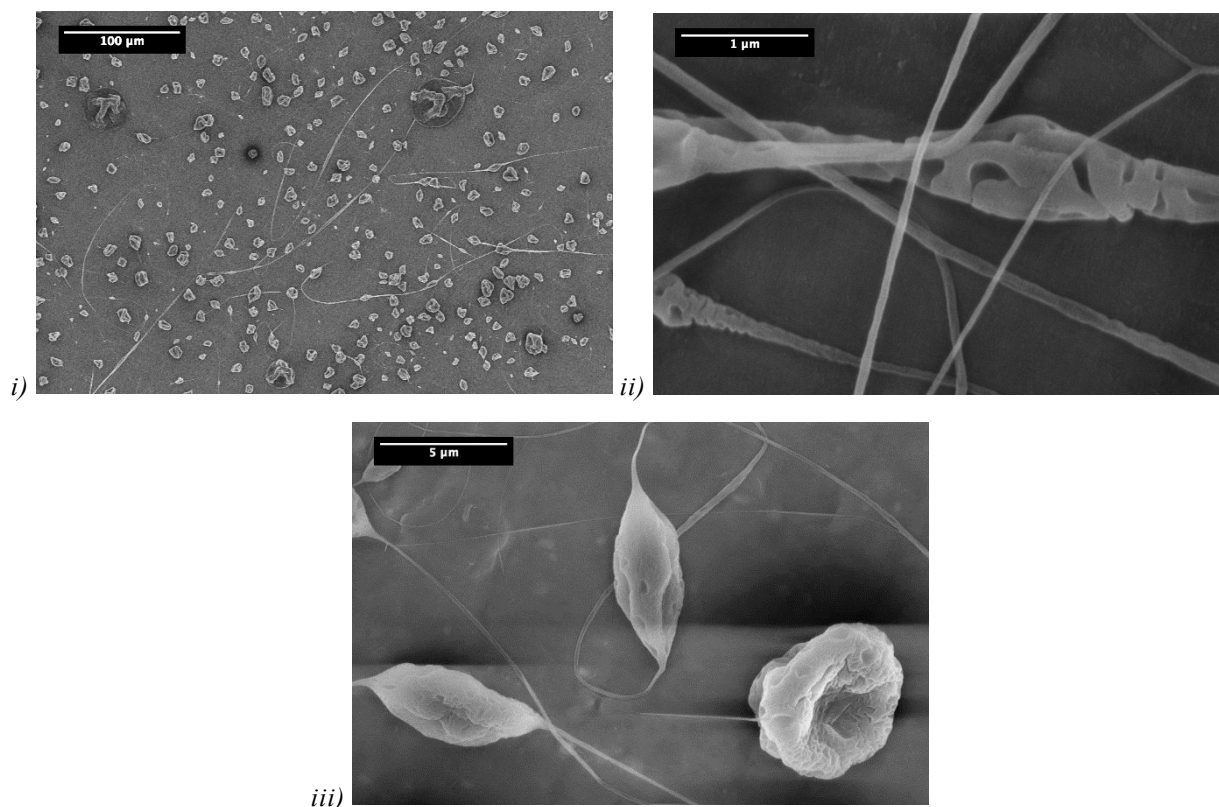


Figure 3.4 – SEM micrographs of 15 wt-% PC nanofibers electrospun using THF. Fibers i) were electrospun using $V_{app} = 20$ kV, ii) using $V_{app} = 25$ kV and iii) using $V_{app} = 25$ kV over a gap distance of 15 cm.

n,n-Dimethylformamide (DMF)

The fourth solvent used for electrospinning was n,n-dimethylformamide (DMF), which is polar aprotic, with a boiling point of 153 °C, density of 0.944 g/mL, and dielectric constant of 38. Figure 3.5 shows the beads electrospayed using DMF. DMF is a good solvent for polycarbonate and makes a nice solution at 15% by weight. However, it did not electrospin successfully as seen in Figure 3.5(i). Instead, electrospaying was observed. This behavior is probably due to the low viscosity of the solution. It is likely that the polymer chains were not entangled enough to stay together when the solution is pulled by the electric field. Since NCC can be dispersed within the DMF solvent to some degree, the system was also tested using the composite system at 2 wt-%.

The polymer or composite solution broke up as it left the needle tip; spheres were formed instead and deposited at the collector. It is possible the NCC in the composite solution acted as a plasticizer and lead to the electrospaying effect being observed. The distribution of spheres is quite large, spanning from a few hundred nanometers up to several microns, as seen in Figure 3.5(ii) and (iii). Additionally, some of the spheres were flocculated on the collector. None of the spheres had the raisin-like morphology as previously seen.

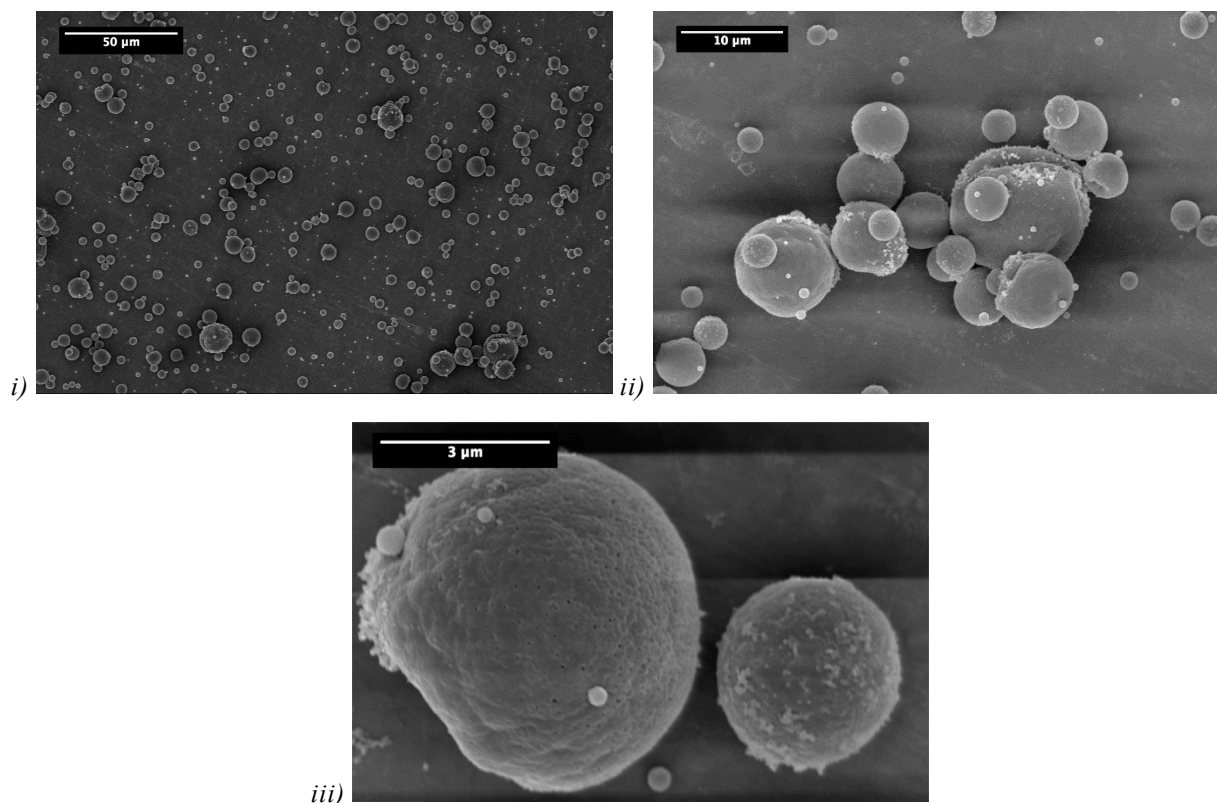


Figure 3.5 – SEM micrographs of 15 wt-% (98:2) PC/NCC spheres electrosprayed using DMF. Spheres i), ii), and iii) were sprayed using $V_{app} = 20$ kV over a gap distance of 15 cm.

60:40 wt-% Tetrahydrofuran:n,n-Dimethylformamide (THF:DMF) mixture

The final solvent evaluated was a mixture 60:40 ratio by weight of THF to DMF; this translates into a volume ratio of approximately 61.5:38.5. The volume-weighted boiling point is about 99.5 °C with a density of 0.908 g/mL and dielectric constant of 19.24. Figure 3.6 shows the nanofibers electrospun using the THF/DMF mixture. The synergistic effect of these two solvents allows the polycarbonate to form nanofibers very nicely via electrospinning, seen in Figure 3.6(i). It is likely that this effect can be attributed to the decrease in boiling point and increase in dielectric as compared with THF alone. The distribution of the nanofiber diameters is relatively narrow with most fibers < 2 μm. The number of beads and branching of fibers is low as seen in Figure 3.6(i), although there is some branching or splitting of the fibers observed. The resulting morphology is consistent with Shawon et al. [34]. Figure 3.6(ii) shows a very smooth surface morphology of the fibers, as the solvent was able to diffuse out through the surface of the nanofiber.

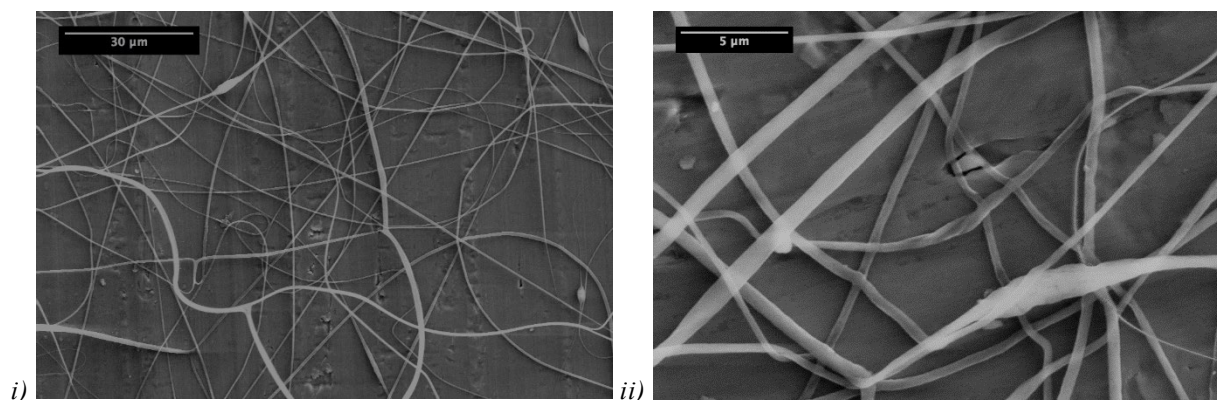


Figure 3.6 – SEM micrographs of PC nanofibers electrospun using (60:40 wt-%) THF/DMF. Fibers i) were electrospun at 10 wt-% PC using $V_{app} = 10$ kV and ii) at 5 wt-% PC using $V_{app} = 15$ kV over a gap distance of 15 cm.

Nanocrystalline cellulose (NCC) + (60:40) THF:DMF

The solvent system used with the NCC and polycarbonate composite was the 60:40 wt-% THF-DMF mixture from the previous experiment (61.5:38.5 vol-%). To reiterate, the combined boiling point is about 99.5 °C with a density of 0.908 g/mL and dielectric constant of 19.24. Figure 3.7 shows the NCC composite nanofibers electrospun using the THF/DMF mixture. Here the PC concentration was increased to 19.8% by overall weight of the solution and 1% by overall solution mass is NCC. After solvent evaporation, the resulting solid should be 95% PC reinforced with 5% NCC, by weight. In Figure 3.7(i), the diameter of the nanofibers is more homogeneous and beads are observed. This may be a result of the solution sitting for an extended period of time before electrospinning; an identical solution was prepared and spun the same day as made and is seen in Figure 3.7(ii). The bead formation significantly decreased. It is suspected that the NCC-THF:DMF system is not stable for long periods of time and agglomeration or flocculation of the materials may occur over time. A higher viscosity solution or a lower voltage may also reduce the bead formation, as the viscosity will dominate the surface tension of the Taylor cone longer and jetting will not occur prematurely. Figure 3.7(iii) depicts that there is a distribution of the fiber diameters ranging from <100 nm to >1 μm. Figure 3.7(iv) confirms that composite nanofibers can be formed with a diameter on the order of 40-50 nm.

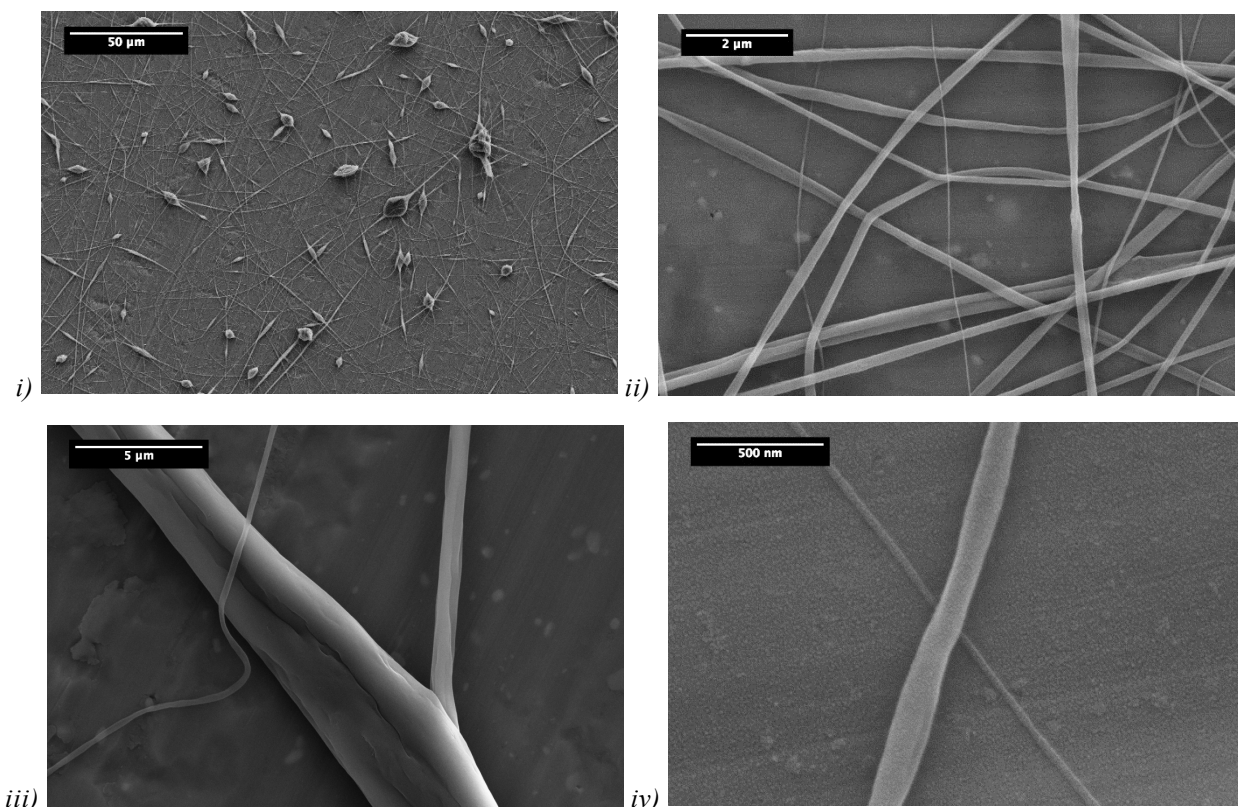


Figure 3.7 – SEM micrographs of (5:95 wt-%) NCC-FP/PC nanofibers electrospun using (60:40 wt-%) THF/DMF. Fibers i) were electrospun using $V_{app} = 20$ kV, ii) using $V_{app} = 25$ kV, iii) using $V_{app} = 20$ kV, and iv) using $V_{app} = 20$ kV over a gap distance of 15 cm.

3.5 – Conclusions

In the present work various electrospinning process parameters were explored for the formation of polycarbonate nanofibers and then utilized for the preparation of polycarbonate nanofibers containing nanocrystalline cellulose. The primary focus was placed on the selection of solvent system to be used, since a homogeneous solution is necessary to achieving nanofibers with controlled diameter and surface morphology. Other parameters that were explored included the electric field (adjustment of the applied voltage) and solution viscosity (polymer concentration). These parameters affected the fiber diameter, beading and surface morphology. Using a 60:40 wt-% ratio of THF to DMF mixture of solvents, nanofibers of polycarbonate with nanocrystalline cellulose were created with diameters in the sub-100 nm range. Although not uniformly distributed, it does show the process works for composite nanofibers and can be improved through future works.

Chapter 4. Modeling Nanofibers of Polycarbonate Containing Nanocrystalline Cellulose Prepared by Electrospinning in Different Solvent Systems

4.1 – Introduction

Polycarbonate fibers have been successfully electrospun in various solvents like chloroform [16], tetrahydrofuran [132], mixtures of tetrahydrofuran (THF) and n,n-dimethylformamide (DMF) [34], THF and n,n-dimethylacetamide (DMAc) [133], and DMF and dichloromethane (DCM) [134].

It is also expected that the incorporation of Nanocrystalline Cellulose (NCC) in PC nanofibers could significantly improve the properties of the electrospun fibers and mats. The inclusion of NCC has been explored in polyvinyl alcohol (PVA) [135]–[137], poly(lactic acid) [138], poly(methyl methacrylate) [139], polystyrene [137], [140], poly(ethylene oxide) [141], [142], lignin with PVA [143], poly(vinyl pyrrolidone) and silver nanoparticles [144], and all-cellulose electrospun fibers [145].

The author, Andrew Finkle, has published preliminary work where he explored the electrospinning of polycarbonate in several solvent systems and produced NCC/PC fibers in a 60:40 (w/w) THF and DMF solvent system under a single set of conditions [129]. At present there are no publications exploring the formulation and processing conditions of polycarbonate electrospun nanofibers reinforced with NCC.

Objective

This work will explore the production of polycarbonate (PC) polymer nanofibers containing Nanocrystalline Cellulose (NCC). The objective is to produce nanofibers using electrospinning, to characterize the nanofibers, and to correlate the type of nanofibers produced with the process parameters. Five different designs of experiment (DOEs) were analyzed as an investigative process to develop models for fiber diameter, bead diameter, and bead density of the material systems in study.

Linear regression models for fiber diameter, bead density, and bead diameter were developed for five material systems including a polycarbonate matrix. Solvent formulation performance including the turbidity and viscosity of the prepared solutions are also presented, including prediction models as a function of solvent formulation. Two solvent systems that were identified in Chapter 3, Preparation of Polycarbonate Nanofibers Containing Nanocrystalline Cellulose, were chosen for this study as there is not any current published literature for PC/NCC fibers with these

solvent systems. The solvent systems explored include a 60:40 (w/w) mixture of tetrahydrofuran (THF) and n,n-dimethylformamide.

The main objective of the six design of experiments (DOE) is to establish an optimal model for electrospinning Nanocrystalline Cellulose (NCC) reinforced thermoplastic composite nanofibers. The collected experimental data can then be analyzed using statistical software to develop models to predict responses based on specific input parameters. This model could then be used to facilitate creation of electrospin nanofibers with desirable diameters and variability for specific applications such as transparent mats and coatings.

The formulation parameters chosen to explore within the DOEs are the polymer concentration in the solution, the concentration of additives (NCC). The processing parameters chosen to explore within each DOE included the applied voltage, Voltage, and gap distance, Gap Distance. Between the DOEs two other formulation parameters were explored. This included the solvent the polycarbonate solution was made in either a 60/40 (w/w) THF/DMF mixture or chloroform, both good solvents for PC. The second variable introduced between DOEs with the same solvent was 2-wt.-% of NCC (or DDSA-modified NCC, cNCC) in the solid mass (not including solvent). The DOEs explored and ranges of the parameters tested are summarized in Table 4.1 below.

Table 4.1 - Summary of factors, levels, and formulation parameters for each DOE#0 through DOE#5

DOE	[Polymer] (wt.-%)	Polymer Source	Solvent	[NCC] (wt.-%)	Voltage (kV)	Gap Distance (cm)
(DOE#1)	15-25	StarPlastic PC	60/40 THF/DMF	0	15-25	10-20
(DOE#2)	15-25	StarPlastic PC	60/40 THF/DMF	2	15-25	10-20
(DOE#0)	15-25	StarPlastic PC	60/40 THF/DMF	0-2	15-25	10-20
(DOE#3)	5-15	StarPlastic & Lexan PC	Chloroform	0	15-25	15
(DOE#4)	12.5-17.5	StarPlastic PC	Chloroform	2 (cNCC)	20-30	20-30

4.2 – Materials

StarPlastic PC743R Polycarbonate

Polycarbonate is a special type of polyester based on carbonic acid. Polycarbonate's chemical structure has functional groups connected through a series of carbonate groups (-O-(C=O)-O-). In polycarbonate formed from Bisphenol A (BPA) and phosgene monomers, the polymer backbone consists of two large aromatic groups that lead to the polymers high strength, through steric

hindrance limiting bending of the molecule. The repeating unit for BPA-phosgene polycarbonate can be seen in Figure 4.1.

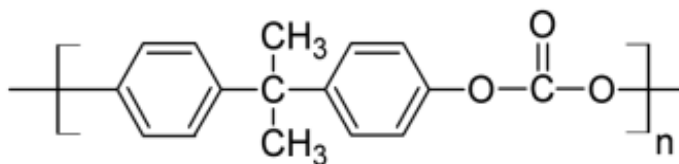


Figure 4.1 - Repeating unit of BPA-phosgene polycarbonate

The polycarbonate sample was received from PolyOne distributors; it was produced by StarPlastic Inc. of Millwood, WV. The trade name of the resin is StarPlastic PC743R-CLS112 Molding Grade PC. According to the specification documentation (available in Appendix A.3.1 and A.3.2), it is safe for ultraviolet light, water exposure, immersion, and acceptability for outdoor use in accordance with UL 746C. The PC has a documented tensile strength of 62.1 MPa and an elastic modulus of 2.41 GPa. The melt flow index of the StarPlastic PC is 12.00 g/10min at 300 °C. Injection and compression molding applications of this material were studied in my MASc thesis, results and discussion can be found in “Cellulose-Polycarbonate Nanocomposites: A novel automotive window alternative,” for PC systems with and without cellulose additives [18]. Mechanical and other material properties for StarPlastic are documented in the specification sheet and certificate of analysis in Appendix A, Figure A.1 and Figure A.2, respectively.

SABIC Lexan XL10 Polycarbonate

A new grade and source of PC is presently being investigated for this study. Lexan XL10 transparent sheeting is produced by SABIC and was purchased from Home Depot Waterloo. The Lexan sheet has high impact strength for vertical and overhead glazing applications. The XL10 sheet is coated on one side with a UV-resistant material. The material is backed against yellowing, loss of transmission, and breakage and is intended for long life-cycle applications [146]. The melt flow index of the Lexan PC is 18.00 g/10min at 300 °C. Mechanical and other XL10 material properties are documented in the specification sheet in Appendix A, Figure A.3.

FP Innovations Ultra Nanocrystalline Cellulose

Some characterization has been completed previously on the FP-Innovations source of NCC, herein referred to as NCC-FP, to quantify the materials physical and chemical properties. The preliminary characterization was completed during my MASc thesis, and can be found in more detail in, “Cellulose-Polycarbonate Nanocomposites: A novel automotive window alternative,” [18]. At that time in 2010, CelluForce had not yet incorporated and the technology behind the company was being developed at FP Innovations Inc. The NCC-FP was received as a low-density freeze-dried cake and had a slightly off-white color. The cellulose is dispersible in water near a neutral pH leaving a transparent dispersion at a few percentages, suggesting a material on the nanoscale on one or more dimensions. The sample supplied by FP Innovations is based out of Quebec and the cellulose is a product of Canadian wood sources. The typical crystallite is 200 nm long and 10 nm in diameter. The preliminary analysis was completed on this FP sample before the technology was scaled to pre-commercial sized operations.

CelluForce Ultra Nanocrystalline Cellulose

The second source, Ultra Nanocrystalline Cellulose (NCC) used in the electrospinning and 3D printing studies, was donated by Dr. Richard Berry, my co-supervisor, of CelluForce Inc. CelluForce is one of the primary manufacturers of cellulose nanocrystals (CNC) and has trademarked the name Nanocrystalline Cellulose (NCC). As received, the NCC was a very fine white powder sealed in 500 g plastic bag labeled Ultra #85 and dated January 30th, 2013. The typical NCC whisker is about 200 nm long and 10 nm in diameter; this particle size has been confirmed with dynamic light scattering techniques and scanning electron microscopy. The tensile strength of NCC is about 10000 MPa with an elastic modulus of about 150 GPa; these are theoretically modeled properties. [15]

A brief overview of the characterization results and discussion is given in Chapter 5. For more material property details, please refer to the MASc thesis document, Chapter 5.3 [18].

CelluForce DDSA Modified Nanocrystalline Cellulose

Surface modified Ultra Nanocrystalline Cellulose for dispersion in a chloroform solvent (coded cNCC) was also donated to the electrospinning research by CelluForce Inc. This modified NCC was received in a 10% by weight solution in chloroform and had a milky white appearance. The NCC surface was modified by grafting (2-dodecen-1-yl) succinic anhydride (DDSA) to the surface hydroxyl groups. This resulted in a dispersibility of the C-NCC in organic solvents with a wide range of polarities [147]. The chemical structure of the DDSA molecule is included in Figure 4.2.

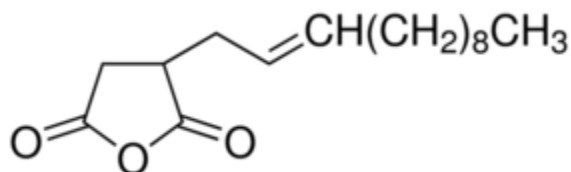


Figure 4.2 - Chemical structure of modifying agent (2-dodecen-1-yl) succinic anhydride (DDSA)

Tetrahydrofuran

Tetrahydrofuran (THF) was used in the electrospinning study and was sourced from Caledon Labs with product code 8900-1 and purity of 99.0% (measured by assay; corrected for water). The specifications noted on the 4 L bottle include a density of 0.89 kg/L, molecular weight of 72.11 g/mol, APHA color of maximum 20 (clear liquid), and a water concentration of 0.05%. The production lot of the DMF is 80148. No further modification or purification was made to the solvent; it was used as received.

N,N-Dimethylformamide (DMF)

Reagent grade N,N-dimethylformamide (DMF) was used in the electrospinning study and was sourced from Caledon Labs with product code 3800-1 and purity of 99.8% (measured by GC assay; corrected for water). The specifications noted on the 4 L bottle include a density of 0.94 kg/L, molecular weight of 73.09 g/mol, APHA color of maximum 15 (clear liquid), and a water concentration of 0.15%. The production lot of the DMF is 80453. No further modification or purification was made to the solvent; it was used as received.

Chloroform

American Chemical Society grade chloroform (coded CH) was used in the electrospinning study and was sourced from University of Waterloo's ChemStores with a purity of 99.8% (measured by assay). The specifications provided by ChemStores include a density of 1.49 kg/L, molecular weight of 119.38 g/mol, APHA color of maximum 10 (clear liquid), and a water concentration of less than 0.03%. The chloroform was stabilized with 0.75% ethanol. No further modification or purification was made to the solvent; it was used as received. [148]

4.3 – Methods

4.1 – Design of Experiment Methodology

This section will describe the methodology for developing five different 2 level, 3 factor (2^3) full factorial design of experiments (DOEs) and one 2 level, 4 factor (2^4) DOE. These six DOES will vary experimental factors over two levels, high (coded as +1) and low (-1). The main factors to be tested are i) the concentration of polycarbonate in solution ([PC]); ii) the voltage applied across the tip to collector (Voltage); iii) the gap distance (Gap Distance); and iv) the source of polymer used. Midpoint (0) experiments were also run to allow model verification and determine variance in experimentation. This accounts for 8 experiments with 3 center point replicates for a total of 11 experiments run per DOE. DOE#0 explores a fourth factor, the concentration of NCC, [NCC] and will include 16 runs with no center points.

The high and low constraints on the different factors were chosen based on literature review and preliminary experimentation of the electrospinning system, see Chapter 3. The concentration of polymer in solution is in the ideal range for a viscous solution allowing polymer chain entanglement, for most DOEs this varied from 15 to 25 wt.-%. The applied voltage is in the range encountered in literature and verified through preliminary experimentation, typically 15 to 25 kV. The gap distance was chosen to achieve an electric field from the tip to collector in the ranges observed in literature and verified through preliminary experimentation (about 1 kV/cm), so the levels used are 10 to 20 cm. The concentration of NCC for DOE#0 was varied between 0 and 2 wt.-%. The different factors can also be coded (a through d) for ease of analysis as seen in the table below.

NOTE, the *source of polymer* factor used was only used in the DOE#3 to determine effects in the grade of polycarbonate used. In each of the other DOEs the main factors were concentration, applied voltage, and gap distance.

The entire 2^3 full factorial DOE including the three different factors tested (coded a, b, and c) with their low (-1), high (+1), and center point (0) values could be easily summarized as shown in Table 4.2. Note, these values have been chosen for demonstration only, but correspond to levels for DOE#1.

Table 4.2 - 2³ full factorial DOE#1, including the three different factors tested (coded a, b, c, and d*) with their low (-1), high (+1), and center point (0) values

Factors	Low (-1)	High (+1)	Centre Point (0)
a = [PC] (wt.-%)	15	25	20
b = Voltage (kV)	15	25	20
c = Gap Distance (cm)	10	20	15
*d = [NCC] (wt.-%SOLID)	0	2	N/A

*DOE#0 only.

Continuing with this coding scheme, each of the 11 experiments, termed the standard order, for each DOE could be summarized as shown in Table 4.3. The table shows what factor levels, high or low, are to be used for each experiment.

Table 4.3 - Standard order of experiments for a 2³ full factorial DOE including the treatment shorthand notation and coded factor levels; high (1), center (0), and low (-1)

Standard Order	Treatment	a=[PC]	b=V	c=d
1	(1)	-1	-1	-1
2	a	1	-1	-1
3	b	-1	1	-1
4	ab	1	1	-1
5	c	-1	-1	1
6	ac	1	-1	1
7	bc	-1	1	1
8	abc	1	1	1
Replicates				
9	Centre	0	0	0
10	Point	0	0	0
11	Replicates	0	0	0

The treatment column is a shorthand way to summarize the specific experiment, each letter representing a factor being tested at its highest level (+1).

The DOE outcomes that will be analyzed, the responses, include viscosity, turbidity, fiber diameter, bead diameter and bead density. A linear regression model for each response will be established with the significant factors and validated by means of residual analysis and lack of fit tests. The DOE modeling was analyzed using Minitab 17 statistical analysis software's DOE

toolset. Finer detail of the DOE analysis performed in Minitab available in the results and discussion section. The final regression model for each model will have the form of Equation 4.1, with $\hat{\beta}_n$ representing the uncoded effect for each factor or cofactor of A, B, or C

$$y = \hat{\beta}_0 + \hat{\beta}_1xA + \hat{\beta}_2xB + \hat{\beta}_3xC + \hat{\beta}_4xAB + \hat{\beta}_5xAC + \hat{\beta}_6xBC + \hat{\beta}_7xABC + \epsilon \quad (\text{Equation 4.1})$$

Some important considerations have been considered to design the experiment properly to maximize analysis and minimize error. To prevent the effect from other potential factors not considered in the study, they were held constant to the best of the experimenter's ability. To eliminate biases in the response time caused by trends in errors or other independent variables, experiments were done in random order. Center points were replicated three times, in order to estimate error and test the model. The experimental runs and regression equation for a 2^4 DOE are included later in the section.

DOE#1 - 60:40 wt.-% Tetrahydrofuran:n,n-Dimethylformamide (THF:DMF) mixture

The first DOE was run to model an ideal baseline electrospinning system. Polycarbonate in a THF/DMF solvent mixture has shown excellent results in literature and through preliminary experimentation. This DOE will determine the effect of different process and formulation factors on the resulting polycarbonate (PC) fibers synthesized through electrospinning. The factors being analyzed include (a) concentration of PC in solvent solution [PC], (b) voltage applied during electrospinning process (Voltage), as well as (c) the gap distance between needle tip and collector (Gap Distance).

The different factors tested for the first DOE along with their low, high, and center point levels can be summarized as shown in Table 4.4 as well as visually presented in 3-dimensional space as a cube plot in Appendix B, Figure B.1.

Table 4.4 - 2^3 full factorial DOE#1, including the three different factors tested (coded a, b, and c) with their low (-1), high (+1), and center point (0) values

Factors	Low (-1)	High (+1)	Centre Point (0)
a = [PC] (wt.-%)	15	25	20
b = Voltage (kV)	15	25	20
c = Gap Distance (cm)	10	20	15

Using the coding scheme, each of the 11 experiments for the first DOE could be represented as shown in Table 4.3.

Through the course of running this DOE, several experimental parameters were held constant and are summarized in Table 4.5 below.

Table 4.5 - Experimental process and formulation parameter constants for DOE#1

Process Constants	Fixed value
Feed Rate	1.0 mL/hour
Run time	30 seconds
Formulation Constants	Fixed value
Solvent System	60:40 ratio by weight of THF:DMF
Polymer	12.00 g/10min StarPlastic PC
Additives	none

The different responses to be analyzed through this first DOE include turbidity, viscosity, fiber diameter, bead diameter and bead density. The turbidity and viscosity are only a function of the (a) factor of [PC] concentration, whereas each of the other responses are a function of all three factors: a, b, and c.

To run each experiment for the desired time, and to account for any losses through the process, a 50 g solution was prepared for each experimental run. The mass of polycarbonate and 60:40 THF/DMF solutions for each experiment were calculated as shown in Appendix B, Table B.2.

Regression will be used to calculate the model parameters and to determine effects of parameters and whether they are statistically significant.

DOE#2 - Nanocrystalline Cellulose (NCC) + (60:40) THF:DMF

The second DOE was run as a comparison to the first DOE, using PC and 60:40 THF/DMF, only now including NCC at a 2 wt.-% loading in the solid mass. This DOE will determine the effect of different process and formulation factors on the resulting PC-NCC fibers synthesized through electrospinning. The factors being analyzed include (a) concentration of PC in solvent solution [PC], (b) voltage applied during electrospinning process (Voltage), as well as (c) the gap distance between needle tip and collector (Gap Distance).

The different factors tested for the second DOE along with their low, high, and center point levels can be summarized as shown in Table 4.6 as well as visually presented in 3-dimensional space as a cube plot in Figure B.4.

Table 4.6 - 2³ full factorial DOE#2, including the three different factors tested (coded a, b, and c) with their low (-1), high (+1), and center point (0) values

Factors	Low (-1)	High (+1)	Centre Point (0)
a = [PC] (wt.-%)	15	25	20
b = Voltage (kV)	15	25	20
c = Gap Distance (cm)	10	20	15

Using the coding scheme, each of the 11 experiments for the first DOE could be represented as shown in Table 4.3.

Through the course of running this DOE, several experimental parameters were held constant and are summarized in Table 4.7 below.

Table 4.7 - Experimental process and formulation parameter constants for DOE#2

Process Constants	Fixed value
Feed Rate	1.0 mL/hour (TBD)
Run time	30 seconds
Formulation Constants	Fixed value
Solvent System	60:40 ratio by weight of THF:DMF
Polymer	12.00 g/10min StarPlastic PC
Additives	none

The different responses to be analyzed through this second DOE include turbidity, viscosity, fiber diameter, bead diameter and bead density. The turbidity and viscosity are only a function of the (a) factor of [PC] concentration, whereas each of the other responses are a function of all three factors: a, b, and c.

To run each experiment for the desired time, and to account for any losses through the process, a slightly larger than 50 g solution was prepared for each experimental run. The mass of polycarbonate, NCC, and 60:40 THF/DMF solutions for each experiment were calculated as shown in Appendix B, Table B.4.

Regression will be used to calculate the model parameters and to determine effects of parameters and whether they are statistically significant.

DOE#0 - Nanocrystalline Cellulose (NCC) + (60:40) THF:DMF (combining DOE#1 and DOE#2)

The zeroth DOE was analyzed as a combination of the data from the first and second DOEs. Originally, DOEs 1 and 2 were performed separately, but combining their data to create a 4-factor, 2-level regression gives further insight into the inclusion of NCC (the differing factor between DOEs 1 and 2).

This DOE will determine the effect of different process and formulation factors on the resulting polycarbonate (PC) fibers synthesized through electrospinning. The factors being analyzed include (a) concentration of PC in solvent solution [PC], (b) voltage applied during electrospinning process (Voltage), (c) the gap distance between needle tip and collector (Gap Distance), and (d) the concentration of NCC in the solid spun fibers [NCC].

The different factors tested for the first DOE along with their low and high levels can be summarized as shown in Table 4.8 as well as visually presented in 3-dimensional space as a cube plot in Figure B.11. No center point replicates were performed for this DOE.

Table 4.8 - 2⁴ full factorial DOE#0, including the four different factors tested (coded a, b, c, and d) with their low (-1) and high (+1) values

Factors	Low (-1)	High (+1)
a = [PC] (wt.-%)	15	25
b = Voltage (kV)	15	25
c = Gap Distance (cm)	10	20
d = [NCC] (wt.-%SOLID)	0	2

Using the coding scheme, each of the 16 experiments for the first DOE could be represented as shown in Appendix B, Table B.5.

Through the course of running this DOE, several experimental parameters were held constant and are summarized in Table 4.9 below.

Table 4.9 - Experimental process and formulation parameter constants for DOE#0

Process Constants	Fixed value
Feed Rate	1.0 mL/hour
Run time	30 seconds
Formulation Constants	Fixed value
Solvent System	60:40 ratio by weight of THF:DMF
Polymer	12.00 g/10min StarPlastic PC
Additives	none

The different responses to be analyzed through this first DOE include turbidity, viscosity, fiber diameter, bead diameter and bead density.

To run each experiment for the desired time, and to account for any losses through the process, a 50 g solution was prepared for each experimental run. The mass of polycarbonate and 60:40 THF/DMF solutions for each experiment were calculated as shown in Appendix B, Table B.6.

Regression will be used to calculate the model parameters and to determine effects of parameters and whether they are statistically significant. The final regression model for each model will have the form of Equation 4.2, with δ_n representing the uncoded effect for each factor or cofactor of A, B, C, or D

$$y = \delta_0 + \delta_{1x}A + \delta_{2x}B + \delta_{3x}C + \delta_{4x}D + \delta_{5x}AB + \delta_{6x}AC + \delta_{7x}BC + \delta_{8x}AD + \delta_{9x}BD + \delta_{10x}CD + \delta_{11x}ABC + \delta_{12x}ABD + \delta_{13x}ACD + \delta_{14x}BCD + \delta_{15x}ABCD + \epsilon$$

(Equation 4.2)

DOE#3 - Chloroform

The third DOE was run to model an ideal baseline electrospinning system. Polycarbonate in a

chloroform solvent has shown excellent results in literature and through preliminary experimentation [16]. This DOE will determine the effect of different process and formulation factors on the resulting polycarbonate (PC) fibers synthesized through electrospinning. The factors being analyzed include (a) concentration of PC in solvent solution [PC], (b) voltage applied during electrospinning process (Voltage), as well as (c) the source of the polycarbonate, represented as PC (grade).

The different factors tested for the third DOE along with their low, high, and center point levels can be summarized as shown in Table 4.10 as well as visually presented in 3-dimensional space as a cube plot in Figure B.17.

Table 4.10 - 2³ full factorial DOE#3, including the three different factors tested (coded a, b, and c) with their low (-1), high (+1), and center point (0) values

Factors	Low (-1)	High (+1)	Centre Point (0)
a = [PC] (wt.-%)	5	15	10
b = Voltage (kV)	15	25	20
c = PC (grade)	StarPlastic	Lexan	-

Using the coding scheme, each of the 14 experiments for the first DOE could be represented as shown in Appendix B, Table B.7. There are 3 additional center point replicates that are required to be run for this DOE as they must be run for each PC (grade) as there is no possible midpoint value for this factor.

Through the course of running this DOE, several experimental parameters were held constant and are summarized in Table 4.11 below.

Table 4.11 - Experimental process and formulation parameter constants for DOE#3

Process Constants	Fixed value
Gap Distance	15 cm
Feed Rate	1.5 mL/hour
Run time	30 seconds
Formulation Constants	Fixed value
Solvent System	Chloroform
Polymer	12.00 g/10min StarPlastic PC 18 g/10min Lexan from SABIC
Additives	none

The different responses to be analyzed through this third DOE include turbidity, viscosity, fiber diameter, bead diameter and bead density. The turbidity and viscosity are only a function of the

(a) factor of [PC] concentration, whereas each of the other responses are a function of all three factors: a, b, and c.

To run each experiment for the desired time, and to account for any losses through the process, a 50 g solution was prepared for each experimental run. The mass of polycarbonate and chloroform for each experiment were calculated as shown in Appendix B, Table B.9.

Regression will be used to calculate the model parameters and to determine effects of parameters and whether they are statistically significant.

DOE#4 - DDSA-modified Nanocrystalline Cellulose (cNCC) + Chloroform

The fourth DOE was run as an evolution to the third DOE, using PC and chloroform, only now including cNCC at a 2 wt.-% loading in the solid mass. StarPlastic is used as the only source of polycarbonate in this DOE. This DOE will determine the effect of different process and formulation factors on the resulting PC-NCC fibers synthesized through electrospinning. The factors being analyzed include (a) concentration of PC in solvent solution [PC], (b) voltage applied during electrospinning process (Voltage), as well as (c) the gap distance between needle tip and collector (Gap Distance).

The different factors tested for the fourth DOE along with their low, high, and center point levels can be summarized as shown in Table 4.12 as well as visually presented in 3-dimensional space as a cube plot in Figure B.24.

Table 4.12 - 2³ full factorial DOE#4, including the three different factors tested (coded a, b, and c) with their low (-1), high (+1), and center point (0) values

Factors	Low (-1)	High (+1)	Centre Point (0)
a = [PC] (wt.-%)	12.5	17.5	15
b = Voltage (kV)	20	30	25
c = Gap Distance (cm)	20	30	25

Using the coding scheme, each of the 11 experiments for the first DOE could be represented as shown in Table 4.3.

Through the course of running this DOE, several experimental parameters were held constant and are summarized in Table 4.13 below.

Table 4.13 - Experimental process and formulation parameter constants for DOE#4

Process Constants	Fixed value
Collector	VWR Aluminum Pan
Feed Rate	1.5 mL/hour
Run time	30 seconds (after cooling in fridge)
Formulation Constants	Fixed value
Solvent System	Chloroform
Polymer	12.00 g/10min StarPlastic PC
cNCC Concentration	2 wt.-% of solid mass (no solvent)

The different responses to be analyzed through this fourth DOE include turbidity, viscosity, fiber diameter, bead diameter and bead density. The turbidity and viscosity are only a function of the (a) factor of [PC] concentration, whereas each of the other responses are a function of all three factors: a, b, and c.

To run each experiment for the desired time, and to account for any losses through the process, a 75 g solution was prepared for each experimental run. The mass of polycarbonate, cNCC, and chloroform for each experiment were calculated as shown in Appendix B, Table B.11.

Regression will be used to calculate the model parameters and to determine effects of parameters and whether they are statistically significant.

4.2 – Experimental Setup

Electrospinning Equipment

A fourth-year design project team from the Nanotechnology Engineering class of 2010 designed the vertical electrospinner used for this experimentation. It was designed as a low-cost apparatus with functionality like a commercial system, depicted in Figure 4.3.

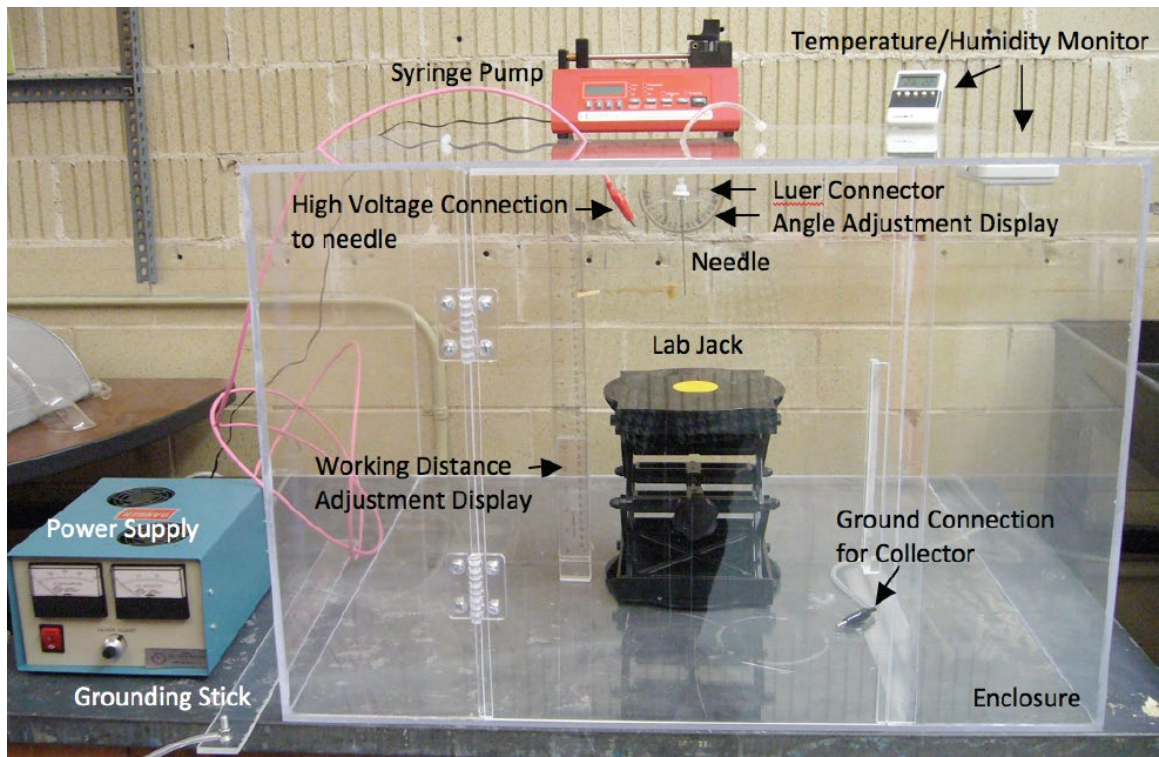


Figure 4.3 - The electrospinning apparatus used for the production of fibers in this study

The electrospinning system consisted of a high voltage supply, a syringe pump, and a collector plate all contained in a 1 m cubed plexiglass shroud. The voltage supply used was a Gamma ES30, which allowed control between 0 and 30 kV of applied voltage. The programmable syringe pump used was an NE-1000 model that allowed control over the dispersion flow rate to the system and a 5 mL polymer syringe was used for electrospinning. The syringe had an 18-gauge blunt stainless-steel tip where the voltage was applied.

Solution Preparation

To prepare the polymer and polymer composite solutions used in the six DOEs the following method was followed consistently. The solutions were each prepared the same day that the electrospinning experiments were to be run to eliminate any possibility of unnecessary evaporation, agglomeration, or contamination. This also resulted in only one sample being prepared at a time, which also reduced any possible error from the experimenter.

All glassware and equipment was thoroughly cleaned, rinsed with alcohol, and dried in an oven to ensure no contamination or moisture.

- 1) First, A stirring magnet was added to a 250 mL round bottom flask.
- 2) The proper amount of appropriate solvent was weighed and added to the flask.
- 3) If a composite is being electrospun, the additive, such as NCC, is added to the solvent and ultrasonicated with a probe at 20 kHz for 20 minutes total, switching between 1 minute on and 1 minute off. This was to ensure full dispersion of nanoparticles in solvent prior to addition of polymer to ensure the best distribution in solution.

- 4) The round bottom flask is set inside an oil bath atop a heated stir-plate and an appropriate stir speed is found to create a vortex.
- 5) The polymer beads were then added slowly to avoid disruption of the vortex or clumping together.
- 6) A reflux condenser is now attached to the round bottom flask and mounted firmly in place with cool water flowing through.
- 7) The heat of the plate was then increased slowly to the desired set point, typically about 20 °C above the boiling point of the solvent.
- 8) The solution was then allowed to stir until all of the polymer has dissolved to a homogeneous solution as well as for an additional 10 minutes to ensure complete dissolution.
- 9) The heat of the stir-plate is then turned off and when the temperature of the oil is safe to the touch, the oil bath is removed.
- 10) The polymer solution continues to stir in the round bottom flask until it reaches room temperature as measured with a laser thermometer.
- 11) From here the solution is directly transferred to a couple sterilized syringes ready for electrospinning.

The solution preparation was usually carried out in the morning the same day of electrospinning in the afternoon to reduce the time between preparation and spinning.

Electrospinning procedures

Some minor modifications had been made to the machine, but for the DOE experiments it was used as designed with the following procedure. Proper safety was followed and warning signs were posted during any experiment run.

- 1) The collector is an approximately 20 by 20 cm steel plate that has been carefully covered in aluminum foil to avoid wrinkles or creasing. The aluminum foil allows easy removal, storage, and preparation of characterization samples.
- 2) The collector is then placed onto the grounding lead, which has been centered on a plastic bench-top laboratory jack stand. A piece of paper towel is placed on top of the collector for time being to avoid any spills or drips before the experimentation begins.
- 3) A blunt 18 G tip is added to the 5 mL syringe and connected to a syringe pump that sits on top of a large plexiglass box. There is a small hole that the tip passes through into the box where the collector is located.
- 4) The distance between the end of the tip and the collector plate is adjusted to the correct gap distance, this can be seen in the image in Figure 4.4 below.

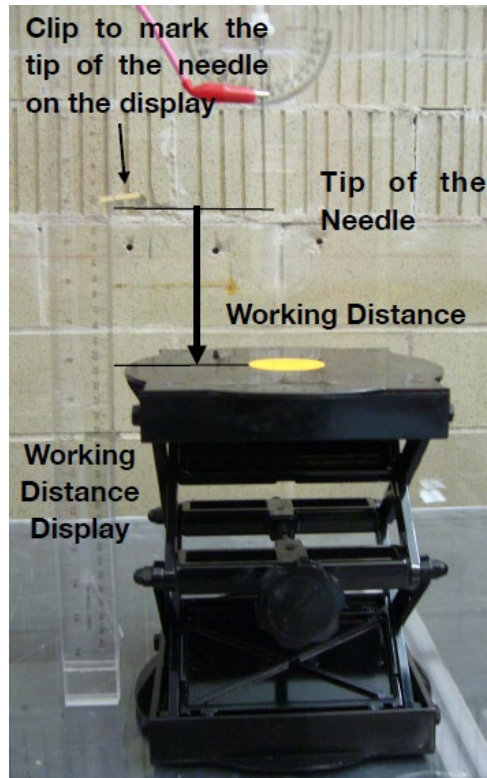


Figure 4.4 - Working area of electrospinning equipment showing working (gap) distance, adjustable collector, and needle positioning

- 5) The positive lead from the voltage supply is connected to the stainless-steel needle via an alligator clip. The paper towel is then removed to expose the collector.
- 6) The plexiglass box is then sealed and the relay safety is reset. This relay disconnects the power immediately if the door is opened during any experiment.
- 7) The syringe pump is then started along with the desired applied voltage for the experiment.
- 8) After the desired time has elapsed, the pump and voltage are stopped and the plexiglass box is purged for several minutes with nitrogen gas to remove any evaporated solvent.
- 9) The sample is then relocated to the fume hood for further drying (if necessary) and finally transferred to a sample container for later characterization.
- 10) Additional experimental runs are then completed for the same polymer solution following the same procedure.

The six DOEs explored are summarized in detail in the following section.

4.4 – Results and Discussion

DOE#1 - 60:40 wt.-% Tetrahydrofuran:n,n-Dimethylformamide (THF:DMF) mixture

The different factors tested for the first DOE along with their low, high, and center point levels are summarized in Table 4.1. The 3 factors examined (with low, center, and high levels) include: StarPlastic PC concentration, [PC], (15, 20, 25 wt.-%); applied voltage, V, (15, 20, 25 kV); and gap distance, d, (10, 15, 20 cm). For the 2³-factorial design of experiment, there are 3 factors being

adjusted between 2 different levels, high and low. As well as 3 center-point replicates, resulting in 11 total runs for a full-factorial design of experiment. The absolute error between the target and actual mass values for all measurements falls below |1%|.

For the dry weighing of the PC in pellet form, the actual mass is slightly above the target mass in 10 of the 11 runs. For the weighing of solvents, the actual mass of THF tended lower than the target whereas for DMF the actual mass tended to be higher. The two solvents were measured using a graduated cylinder and their reference density and then added to a round-bottom flask already containing the PC pellets. The mass discrepancies can be attributed to experimenter error and the volatility of the solvents. These errors can be attributed to a systemic user error and can be eliminated through better laboratory practices but are within an acceptable range for this analysis.

Table 4.14 summarizes the target and actual concentrations calculated for each run based on the recorded masses. The actual THF concentration, [THF], is approximately 1.5% below target and DMF, [DMF], about 1.5% above target; polycarbonate, [PC], appears to be normally distributed around its target concentrations. It is important to note that the PC concentrations listed are with respect to the sum total of all components of the solution (polymer and solvent) whereas the solvent concentrations are calculated with respect to the total amount of solvent (polymer not included). Thus, a 60:40 (w/w) THF and DMF solution refers to the total 100% of solvent only and does not consider the polymer in the solution.

Table 4.14 - DOE#1 target and actual concentration calculations for StarPlastic PC in 60:40 (w/w) THF/DMF for each 11 runs

Std. Order	[PC]Target (%TOTAL)	[PC]Actual (%TOTAL)	[THF]Target (%SOLVENT)	[THF]Actual (%SOLVENT)	[DMF]Target (%SOLVENT)	[DMF]Actual (%SOLVENT)
1 (1)	15	15.0	60	58.5	40	41.5
2 (a)	25	25.0	60	58.2	40	41.8
3 (b)	15	15.0	60	58.4	40	41.6
4 (ab)	25	25.0	60	58.2	40	41.8
5 (c)	15	15.0	60	58.4	40	41.6
6 (ac)	25	25.0	60	58.7	40	41.4
7 (bc)	15	15.0	60	58.4	40	41.6
8 (abc)	25	25.0	60	58.6	40	41.5
9 (0)	20	20.0	60	58.3	40	41.7
10 (0)	20	20.0	60	58.4	40	41.6
11 (0)	20	20.1	60	58.3	40	41.7

(Note: All percentages listed are with respect to weight (w/w) of noted system; total, solvent, etc.)

Solvent Formulation Performance

The concentration of polymer within the solution is typically an important factor in most electrospinning experiments. The concentration of polycarbonate will determine the amount of chain entanglement that is present within the solution as well as the degree of miscibility in the selected solvent, which is 60:40 (w/w) THF/DMF in this design of experiment. How concentration effects the solution performance in electrospinning can be analyzed through turbidity and viscosity measurements.

Turbidity

The measured turbidity for each run of the DOE#1 is summarized in Table 4.15 in Nephelometric Turbidity Units (NTU).

Table 4.15 - Turbidity measurements for StarPlastic PC in 60:40 (w/w) THF/DMF solvent for each run of DOE#1

Run	[PC] Act. (%_{TOTAL})	Turbidity (NTU)
1 (1)	15.0	4.5
2 (a)	25.0	3.6
3 (b)	15.0	6.1
4 (ab)	25.0	5.2
5 (c)	15.0	4.8
6 (ac)	25.0	10.8
7 (bc)	15.0	1.9
8 (abc)	25.0	11.5
9 (0)	20.0	4.0
10 (0)	20.0	11.8
11 (0)	20.1	16.0
Pure THF/DMF	-	0.2

It is expected that with an increase of polycarbonate within the solution that the turbidity should increase. NTU is a measurement of light that has been diffracted 90° from incident, so more PC chains present in solution should result in more diffracted light. Figure 4.5 plots the 11 turbidity measurements of StarPlastic Polycarbonate in 60:40 (w/w) THF/DMF solvent, taken from each run of DOE#1.

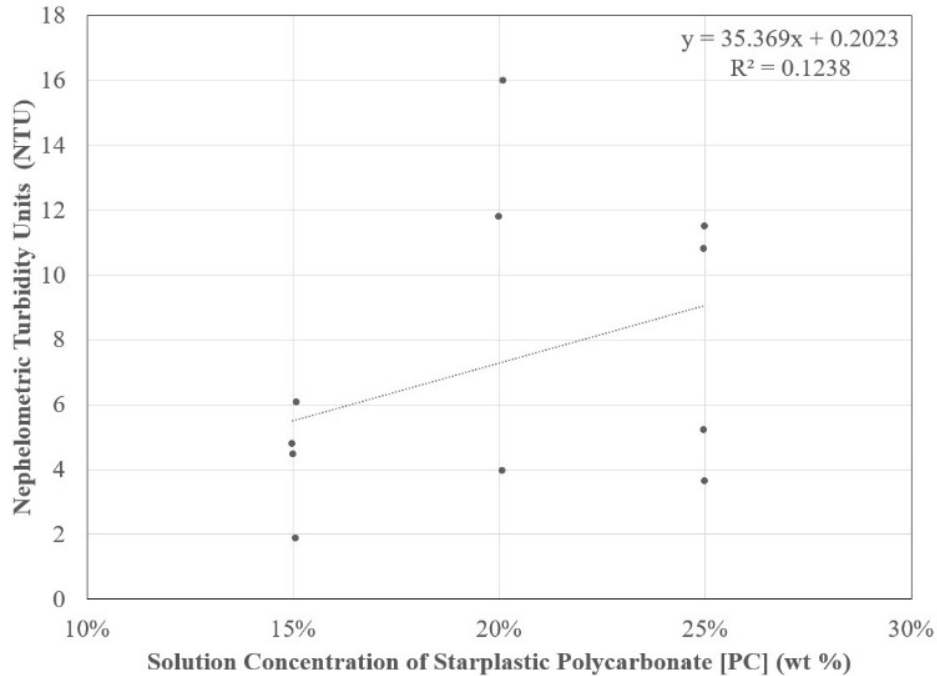


Figure 4.5 - Turbidity versus StarPlastic PC concentration in 60:40 (w/w) THF/DMF solvent for each run of DOE#1

The turbidity does appear to increase with the concentration of PC, following the linear relationship:

$$\text{Turbidity (NTU)} = 35.369 [\text{PC}] + 0.2023 \quad (\text{Equation 4.3})$$

The linear model in Equation 4.3, has an R^2 value of only 12.4% suggesting that the model only weakly explains the variability present in the system. It is anticipated that most of the variability is introduced through the equipment used to measure turbidity, as noise and drift of the measurement values would routinely appear during experimentation. Developing a routine testing procedure was practiced removing as much user introduced error as possible, including taking the measurement at the same elapsed time for each run. It also appears that the center-point replicates at 20% polycarbonate concentration have the highest variability in turbidity measurements.

The turbidity of PC appears to increase about 35.4 NTU for each percent addition of PC in the overall solution. The intercept at 0% PC has a turbidity of about 0.20 which is very close to the measured turbidity of a pure THF/DMF solvent mix.

Viscosity

An additional solution property that is heavily influenced by the concentration, and has an effect of the final electrospun fibers, is the viscosity of the polymer solution. Typically, as the concentration and chain entanglement increases, there is more resistance to flow of the solution due to the higher degree of intermolecular bonding. Also, as a result of the increased forces within the system, the entanglement of polymer can hold a larger electric charge during electrospinning decreasing the likelihood of unwanted electrospinning attributable to fibers breaking up into droplets. In electrospinning, typically as the viscosity increases it will result in larger fiber

diameters; thus, there is an ideal range of viscosity for electrospinning experiments to minimize fiber diameter while avoiding electrospaying. The measured viscosity and standard deviation for each run of the DOE#1 is summarized in Table 4.16 in centipoise (cP).

Table 4.16 - Viscosity measurements for StarPlastic PC in 60:40 (w/w) THF/DMF solvent for each run of DOE#1

Run	[PC] Act. (%TOTAL)	Viscosity (cP)	St. Dev. (cP)
1 (1)	15.0	53	3
2 (a)	25.0	367	14
3 (b)	15.0	50	7
4 (ab)	25.0	623	28
5 (c)	15.0	70	5
6 (ac)	25.0	617	26
7 (bc)	15.0	62	10
8 (abc)	25.0	456	63
9 (0)	20.0	145	8
10 (0)	20.0	120	14
11 (0)	20.1	167	12
Pure THF/DMF	-	0.7	-

(Note: Viscosity measurements were made at 100 RPM using spindle s63)

The resulting scatter plot for the viscosity as a function of polycarbonate concentration is presented in Figure 4.6 with the data fit to an exponential model Equation 4.4 with the y-intercept set to the viscosity of the THF/DMF solvent mixture alone.

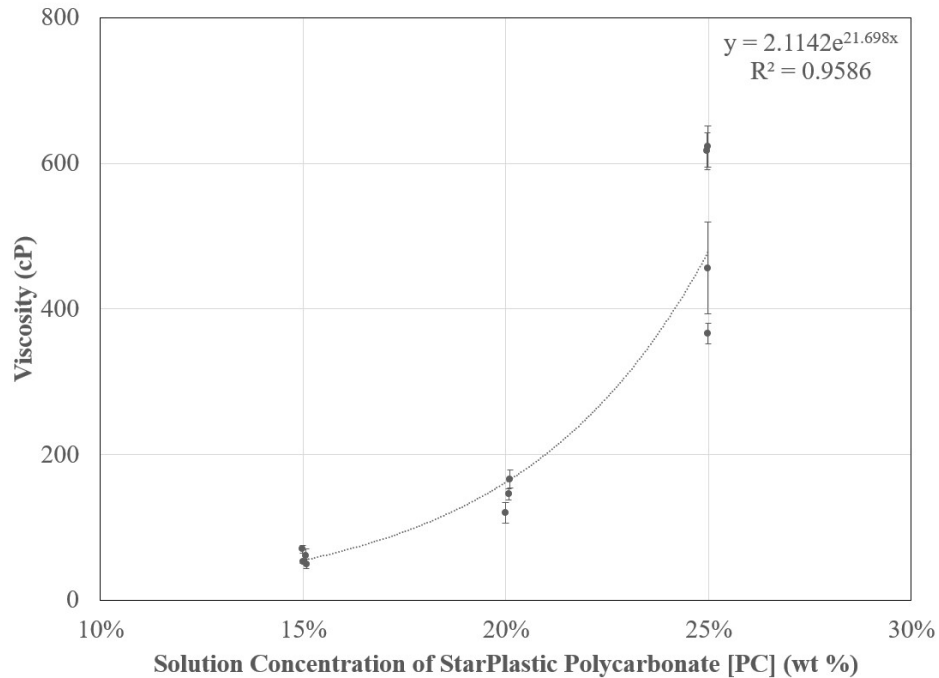


Figure 4.6 - Viscosity versus StarPlastic PC concentration in 60:40 (w/w) THF/DMF solvent for each run of DOE#1

The resulting exponential relationship is:

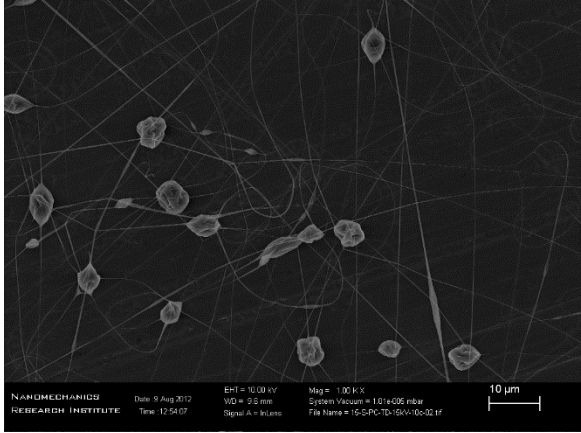
$$\text{Viscosity (cP)} = 2.1142 \exp[21.698 [\text{PC}](\text{wt.}\%)] \quad (\text{Equation 4.4})$$

The exponential model in Equation 4.4, has a high goodness-of-fit as indicated by the R^2 value of 95.86% suggesting that the variability of the data is well fit by the model.

Figure 4.6 also shows that StarPlastic polycarbonate begins to saturate the solvent system above a concentration of about 20 wt.-%, this is indicated through the sharp rise in viscosity after a relatively linear trend when concentration is less than 20 wt.-%. Above 20 wt.-%, the polymer chains experience an exponential growth of intermolecular forces through the chain entanglement which is ideal for electrospinning desirable nanofibers. Overall, the viscosity measurements indicate that the two levels chosen for the [PC] factor in DOE#1 – 15 and 25 wt.-% - are ideal for analyzing this system. Much lower than 15 wt.-% will result in more electrospaying due to lack of entanglement and much higher than 25 wt.-% will result in insufficient dissolution in the solvent and leave beads of undissolved polymer as undesired artifacts in the spun fibers. The pure THF/DMF viscosity of 0.656 falls close to the predicted 2.1 cP.

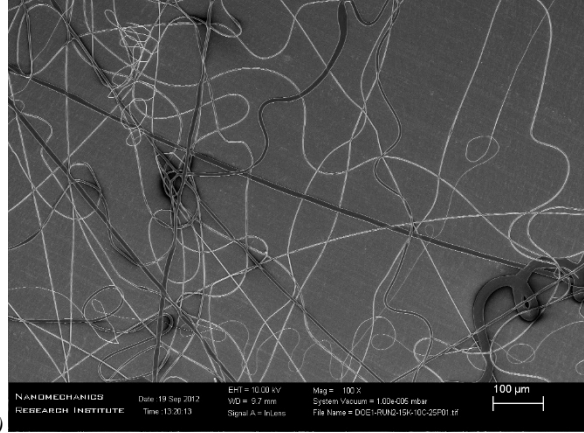
Linear Regression of PC Fiber Diameter

Following the 11 electrospinning runs for the 2^3 full-factorial DOE#1 the collected fiber mats of StarPlastic PC fibers were collected for SEM imaging. The images chosen for ImageJ analysis of fiber diameter, bead density, and bead diameter are included in Figure 4.7 for each run. The location and magnification of each image were chosen to depict a representative area of the electrospun mat, where fibers were neither too dense nor too scarce for measurement. Special care was taken to choose a similar location on each sample to minimize experimental error.



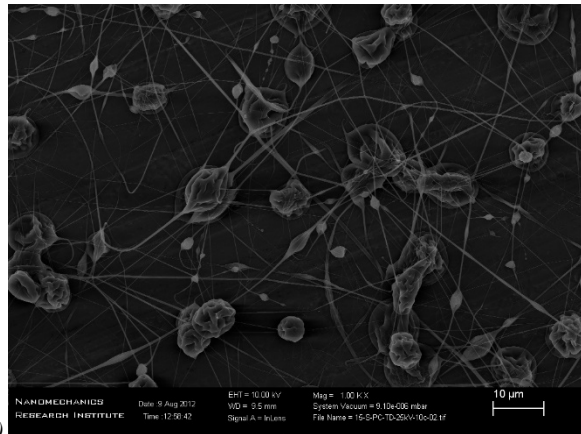
i)

15% | 15 kV | 10 cm



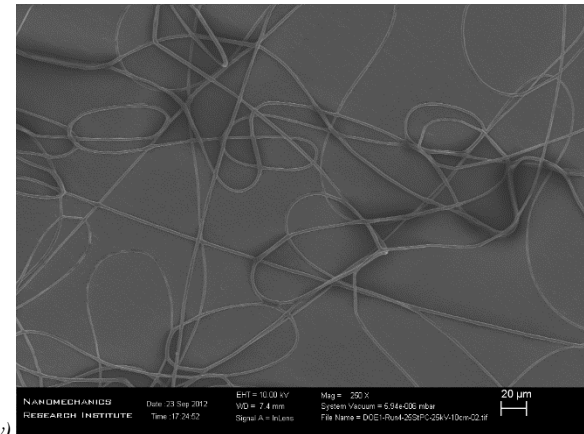
ii)

25% | 15 kV | 10 cm



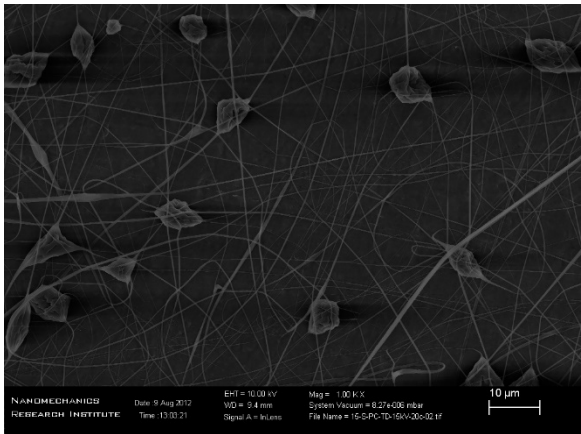
iii)

15% | 25 kV | 10 cm



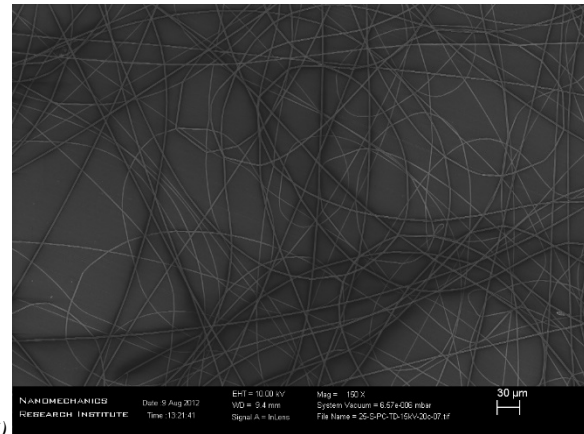
iv)

25% | 25 kV | 10 cm



v)

15% | 15 kV | 20 cm



vi)

25% | 15 kV | 20 cm

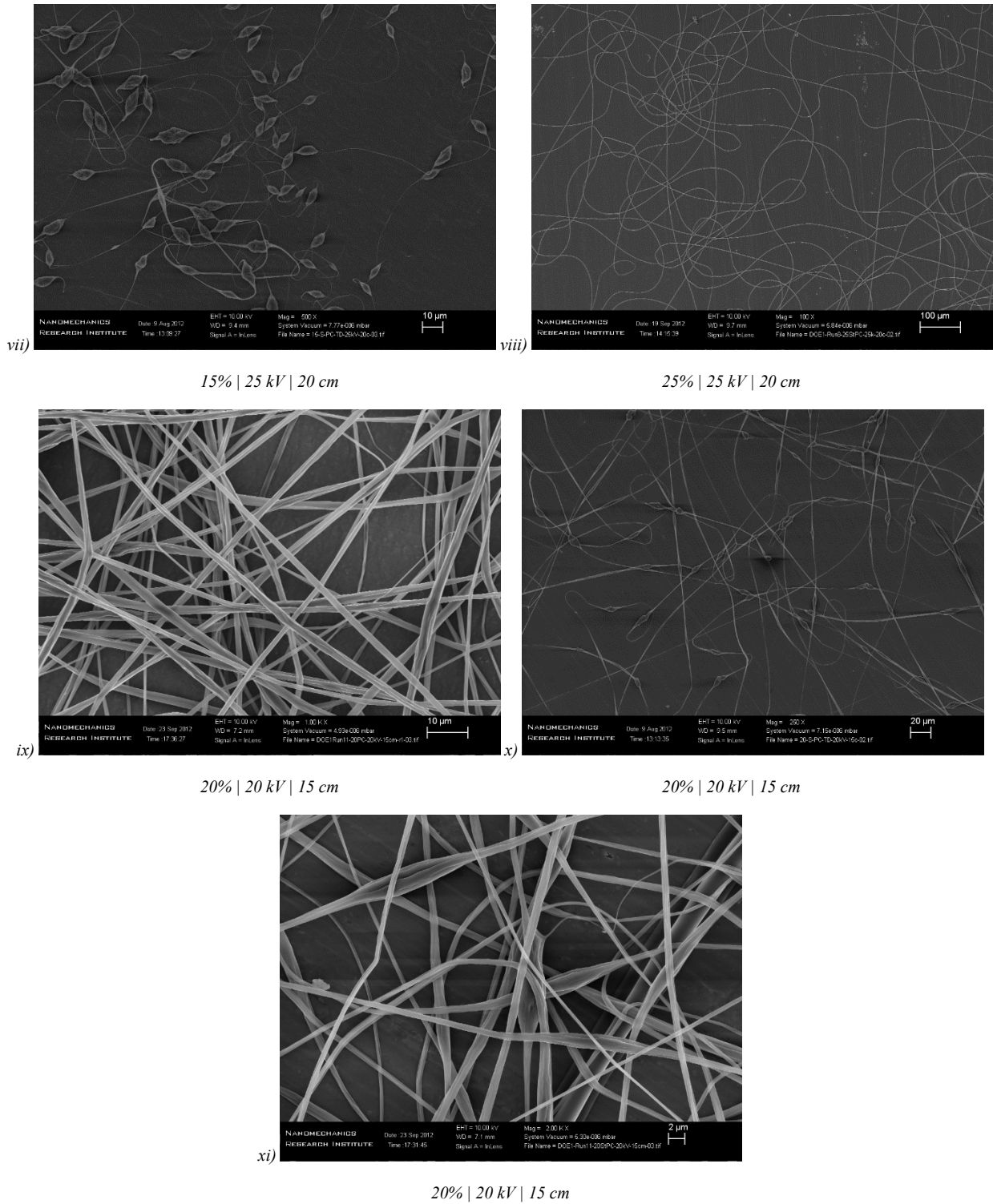


Figure 4.7 - Scanning electron micrographs of StarPlastic PC electrospun fibers for each run (i-xi) of DOE#1

Table 4.17 lists the measured fiber diameters for each run including the number of measurements (counts) and the standard deviation. The method for fiber diameter measurement is included in Chapter 4.

Table 4.17 - Fiber diameter, standard deviation, and measurement counts for StarPlastic PC electrospun fibers made for each run of DOE#1

Run	Fiber Diameter (μm)	St. Dev. (μm)	Counts
1 (1)	0.25	0.13	49
2 (a)	7.68	6.31	101
3 (b)	0.37	0.33	66
4 (ab)	2.90	1.20	59
5 (c)	0.30	0.17	85
6 (ac)	1.50	0.34	71
7 (bc)	0.53	0.22	28
8 (abc)	2.00	0.68	60
9 (0)	1.18	0.84	146
10 (0)	1.13	0.46	41
11 (0)	1.79	0.60	190

Linear regression of the design of experiments data can be used to create a model to describe the response of fiber diameter as a function of the three factors tested: concentration of PC, applied voltage, and the gap distance. Minitab 17 software's DOE analysis tool was used to fit the experimental data to the three chosen factors. First, an *analysis of variance* (ANOVA) table is generated in order to test the significance of each effect as well as the 2-way and 3-way interaction effects. Next, the *model summary* output describes how well the linear regression model fits the collected data using S and R² values. The *coded coefficients* are then calculated to determine the relationship or change the effect has on the mean response. And finally, the coded coefficients are scaled to the actual magnitude of the effect and combined to create the *regression equation in uncoded units*, this is our model equation for the measured response of fiber diameter in micrometers.

The results from Minitab's DOE analysis for DOE#1 are included below. The analysis was completed following a backwards elimination of terms that had less than 90% confidence, or where the P-value is greater than $\alpha = 0.1$. This means that if any of the factors have less than 90% confidence in predicting the response that term is removed from the model and the data is refit with the new set of factors or interactions. This process is iterated until no additional factors are removed.

Backward Elimination of Terms (α to remove = 0.1)

Analysis of Variance

Source	DF	Adj SS	Adj MS	F-Value	P-Value
Model	7	44.0582	6.2940	18.92	0.017
Linear	3	27.7622	9.2541	27.82	0.011
[PC] (wt-%)	1	19.9238	19.9238	59.90	0.004
Voltage (kV)	1	1.9336	1.9336	5.81	0.095
Gap Dist (cm)	1	5.9048	5.9048	17.75	0.024
2-Way Interactions	3	12.9510	4.3170	12.98	0.032
[PC] (wt-%)*Voltage (kV)	1	2.6924	2.6924	8.09	0.065
[PC] (wt-%)*Gap Dist (cm)	1	6.6339	6.6339	19.94	0.021
Voltage (kV)*Gap Dist (cm)	1	3.6248	3.6248	10.90	0.046
3-Way Interactions	1	3.3450	3.3450	10.06	0.050
[PC] (wt-%)*Voltage (kV)*Gap Dist (cm)	1	3.3450	3.3450	10.06	0.050
Error	3	0.9978	0.3326		
Curvature	1	0.7229	0.7229	5.26	0.149
Pure Error	2	0.2749	0.1374		
Total	10	45.0560			

Model Summary

S	R-sq	R-sq(adj)	R-sq(pred)
0.576724	97.79%	92.62%	0.00%

Coded Coefficients

Term	Effect	Coef	SE Coef	T-Value	P-Value	VIF
Constant		1.784	0.174	10.26	0.002	
[PC] (wt-%)	3.156	1.578	0.204	7.74	0.004	1.00
Voltage (kV)	-0.983	-0.492	0.204	-2.41	0.095	1.00
Gap Dist (cm)	-1.718	-0.859	0.204	-4.21	0.024	1.00
[PC] (wt-%)*Voltage (kV)	-1.160	-0.580	0.204	-2.85	0.065	1.00
[PC] (wt-%)*Gap Dist (cm)	-1.821	-0.911	0.204	-4.47	0.021	1.00
Voltage (kV)*Gap Dist (cm)	1.346	0.673	0.204	3.30	0.046	1.00
[PC] (wt-%)*Voltage (kV)*Gap Dist (cm)	1.293	0.647	0.204	3.17	0.050	1.00

Regression Equation in Uncoded Units

$$\begin{aligned} \text{Fiber Diam (um)} = & -43.2 + 2.878 [\text{PC}] (\text{wt}\%) + 1.514 \text{ Voltage (kV)} + 2.087 \text{ Gap Dist (cm)} \\ & - 0.1008 [\text{PC}] (\text{wt}\%)*\text{Voltage (kV)} - 0.1399 [\text{PC}] (\text{wt}\%)*\text{Gap Dist (cm)} \\ & - 0.0765 \text{ Voltage (kV)*Gap Dist (cm)} \\ & + 0.00517 [\text{PC}] (\text{wt}\%)*\text{Voltage (kV)*Gap Dist (cm)} \end{aligned}$$

Looking first at the P-values in the ANOVA table, we can see that all linear factors, 2-way, and 3-way interactions are less than $\alpha = 0.1$. This means that all seven factors correctly predict the fiber diameter response with at least a 90% confidence. The largest P-values, and thus weakest predictors of response, occur for the Voltage term – at 0.095 – as well as the 2-way interaction between Voltage and concentration of PC in solution – at 0.065.

The best predictors of the fiber diameter are the concentration of PC with a P-value of 0.004 and the 3-way combined interaction of PC concentration, Voltage, and Gap Distance. Due to all P-values being lower than our chosen α , no terms are removed from the first iteration of the regression and the model is fit with all terms.

Using the center-points, the P-value for curvature was calculated as 0.149, which is greater than $\alpha = 0.1$, giving confidence that there is no curvature in the system.

The model summary is then given to show how well the model fits our data. S represents a standard error or deviation of the collected data versus the fitted model data in units of the measured response, this would be about 0.58 μm for fiber diameter predictions. Ideally, a lower S represents a better model fit but should not be used alone for indicating the model meets model assumptions. For the fiber diameters measured for DOE#1, a deviation of 0.58 μm is not ideal, but it is ok as it

falls in line with the standard deviations between the measurements within a single experiment run. The R^2 value for the goodness of fit is given to be 97.79%, which suggests that the variance in the fiber diameter response is well explained by the regression model. The R^2 value is typically higher with more predictors in the model; this can be adjusted to compare with models containing different numbers of predictors. The adjusted R^2 value for the goodness of fit of our fiber diameter model is 92.62% which is also very good. The final value given is the predicted R^2 , which predicts how well the model will predict the fiber diameter for new observations. In the case of DOE#1, the predicted R^2 is 0% which is significantly lower than the adjusted R^2 . This likely means that our model is over-fit and there may be terms that appear significant to the individual sample data collected but is not representative of the overall population of data being analyzed. Using a lower α of 0.05 – or a 95% confidence – may produce a model that better predicts new observations. [149], [150]

The next table output from Minitab, *Coded Coefficients*, gives the estimates for the effects of each term, the corresponding regression model coefficients still coded to +/- 1 for each factor, the standard error (SE) for the coefficient, the T-value for the t-test that the model term is 0 (null hypothesis) and corresponding P-value, as well as the VIF (variance inflation factor).

The effect column gives the magnitude and direction of the relationship between the term and the response, or in this DOE#1, how a specific term results in larger or smaller fiber diameters. We can see the largest positive effect on the fiber diameter is for the PC concentration ($A = 3.156$) and the largest negative effect is the interaction of PC concentration with gap distance ($A*C = -1.821$), further discussion of the effects is included below with Pareto and normal plots of the effects. The coefficient (coef) column also gives the coded relationship between term and response and is equal to half of the effect. This is the coefficient that would be used in the uncoded regression model.

The standard error of the coefficient (SE coef) is the next column, it represents the variability possible in the potential estimated coefficients if samples are taken several times over and over again from the same population. Dividing the coefficient estimates by their standard error results in the T-value. The T-value is then effectively the ratio between a coefficient and its error, so a higher T-value would suggest more significance in the term. Since coefficients could have different degrees of freedom, it's often better to use the P-value which is a function of the T-value and degrees of freedom. The P-value probability can be directly compared to α to determine that the coefficient is significantly different than 0.

The variance inflation factor (VIF) shows how much the variance in the coefficients is grown because of correlations between factors tested. A VIF value of 1 is common in most DOEs and means there is no correlations between factors or no multicollinearity. In this design of experiment all VIF values are 1 indicating no multicollinearity in our model terms. [151]

Now that the coded coefficients have been calculated they can be transformed back into the uncoded units and combined to form the *regression equation in uncoded units*. The results generated by Minitab are listed in the output but are neatly formatted below in Equation 4.5.

This equation is the regression model fit for the fiber diameter of PC electrospun nanofibers in THF/DMF solvent as a function of PC concentration ($[PC]$), voltage ($Voltage$), and gap distance ($Gap\ Dist.$) within our chosen factor ranges.

$$\begin{aligned}
 \text{Fiber Diameter (um)} = & - 43.2 && \text{(Equation 4.5)} \\
 & + 2.878 [PC] \text{ (wt.\%)} \\
 & + 1.514 \text{ Voltage (kV)} \\
 & + 2.087 \text{ Gap Distance (cm)} \\
 & - 0.1008 [PC] \text{ (wt.\%)} * \text{Voltage (kV)} \\
 & - 0.1399 [PC] \text{ (wt.\%)} * \text{Gap Distance (cm)} \\
 & - 0.0765 \text{ Voltage (kV)} * \text{Gap Distance (cm)} \\
 & + 0.00517 [PC] \text{ (wt.\%)} * \text{Voltage (kV)} * \text{Gap Distance (cm)}
 \end{aligned}$$

Now, if we were to plug into this equation the target high and low values for each of the eight the corner-points we can calculate the fitted means and see how well they correspond to our measured means. The calculated fitted means are summarized in Figure 4.8, they are presented in a cube plot which shows the 3-dimensional space that the DOE covers. We can see from the fitted means that they correlate nicely with our observed means with only slight deviation. More detail on this deviation, termed the residual, are included later in this section.

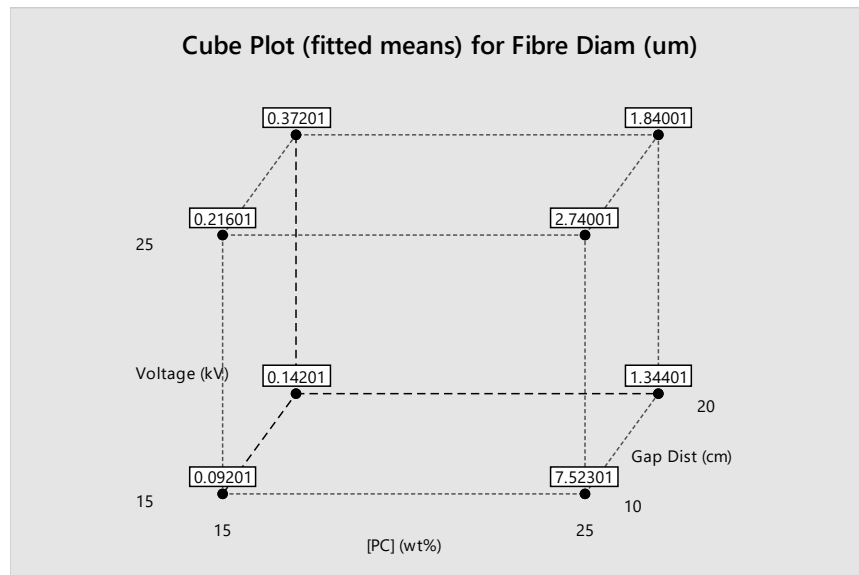


Figure 4.8 - Cube plot of fitted means for the fiber diameter regression model for StarPlastic PC electrospun fibers in DOE#1

The Pareto chart lists the values for the standardized effects for all of the terms that were attempted to be fit to the model from largest to smallest effect. There is also a line fit where the effects become statistically significant relative to the α that was chosen, any term falling below this line are not considered significant. Since the Pareto chart uses the absolute values for the chart, it is impossible to determine if that effect increases or decreases the response, or fiber diameter in this case. In order to visualize the direction of the effect, a Normal plot of the standardized effects is employed. In a Normal plot the standardized effects are plotted relative to a distribution fit line

where all of the effects would be 0. The positive standardized effects (T-values) that increase the response going from the low to high value are plotted to the right of the line whereas the negative effects will be plotted to the left. The terms are plotted with the distance to the line (in the x-axis only) being the value of the effect. Therefore, larger and more significant effects will fall farther from the line and the not significant terms will fall closer to the line. The value of α will again determine the distance from the null hypothesis line required to be considered significant.

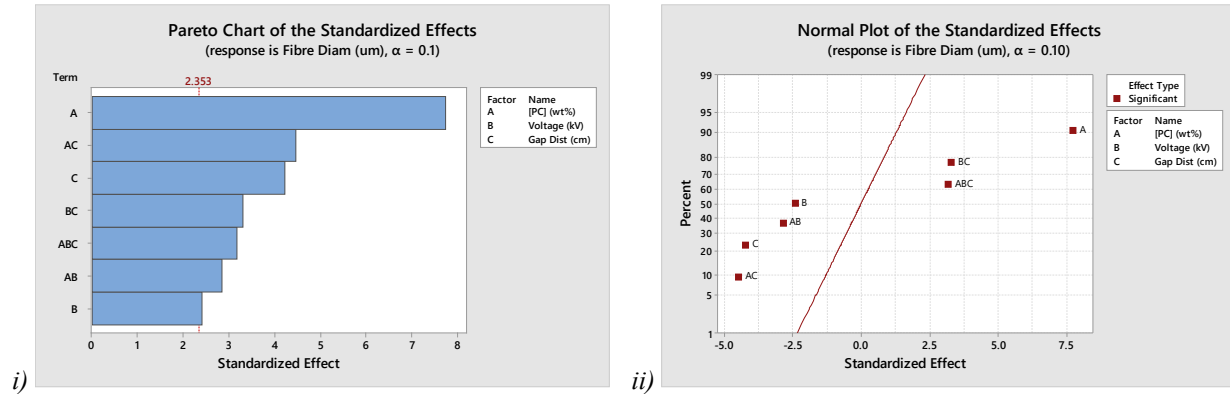


Figure 4.9 - Pareto chart (i) and normal plot (ii) of the standardized effects for the StarPlastic PC electrospun nanofiber diameter response of DOE#1

Figure 4.9 shows the Pareto chart for the fiber diameter response in DOE#1 with the standardized effect values drawn from the T-value column (t-test of the null hypothesis) of the coded coefficients table generated in Minitab. Different than the P-value which showed the confidence in having an effect, the Pareto chart displays which of these effects has the largest impact on the desired response of fiber diameter. As was already seen, all terms fall above the statistically significant effect line of 2.353 which corresponds to the chosen α of 0.1. The terms that show the largest effect on the fiber diameter are PC concentration (A), PC concentration interacting with gap distance (A*C), followed by gap distance (C). Terms that have the lowest effect on the fiber diameter response are voltage (B) followed by the voltage-PC concentration interaction (A*B).

Figure 4.9 displays the normal plot for standardized effects on the fiber diameter for DOE#1. Now we can see that an increased concentration of PC will have a largely positive effect on the response, meaning that a higher concentration will tend to lead to larger fibers. As well, a larger gap distance will have a large negative effect on the response, meaning smaller fiber diameters. Again, due to the chosen α of 0.1, all of the terms are far enough away from the line to be considered significant.

To better visualize these effects and how the different tested factors affect the measured response main and interaction plots can be used. For main effects plots, the fitted means (listed in Figure 4.8) are plotted at the high and low levels of each factor and connected with a line. The slope of this line allows for a quick comparison of effects to determine if they will increase (positive slope) or decrease (negative slope) the response and by how much (the magnitude of the slope). Similarly, the interaction plots show the two-way interactions by plotting four points at each of the high and low values for each of the two variables (low/low, low/high, high/low, and high/high); let's call them A and B. Two lines are connected between the four points to show the change in A from low to high with B held high (line 1) and the change in A from low to high with B held

low (line 2). Similar to the main effects plots, the magnitude and direction of the slope indicate the effect on the response. The difference is now we can determine how that effect changes with the interaction of another factor effect by comparing the two lines within a plot. The main and interaction plots for the PC fiber diameter in THF/DMF are included in Figure 4.10.

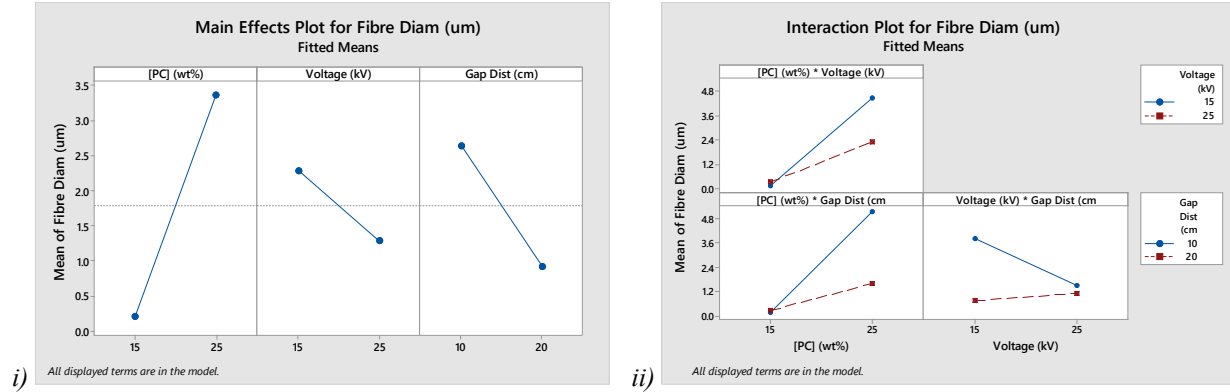


Figure 4.10 - Main (i) and interaction (ii) effects plots for the StarPlastic PC electrospun nanofiber diameter response in DOE#1

Looking at the main effects plot for PC fiber diameter we can see the three plots for each factor and their effect: PC concentration, voltage, and gap distance. The first observation we can see is that PC concentration has the largest effect, followed by gap distance (kV), and finally voltage. Next, we can see that increasing the PC concentration has a positive effect on the fiber diameter (larger fibers) but increasing the voltage or gap distance has a negative effect on the fiber diameter (smaller fibers). This matches with the observations we saw in the Pareto and normal plots of the effects (Figure 4.9) as well as the hypothesis that more PC in solution will lead to more entanglement, less whipping in the instability region, and therefore less stretching and thinning of the fibers.

It can also be seen from the main effects plot for voltage that the average fiber diameter decreases with a larger voltage, this is also in line with the fact that a higher voltage (at a constant or average gap distance) there is more charge supplied to the surface of the spun fiber and Taylor cone as well as a higher electric field between tip and collector; this will apply more force during the instability region. Finally, the main effects of gap distance show a similar effect to the voltage factor but slightly more pronounced. In this case, as the gap distance increases it lowers the electric field but the fibers are still smaller. This is due to the larger instability region, the distance the fibers are allowed to whip back and forth (and elongate and thin) is more significant than the magnitude of the electric field, again reiterating the observations from the Pareto and normal effects plots.

Now turning to the interaction effects plots, we have 3 two-way interactions to look at: PC concentration and voltage, PC concentration and gap distance, and voltage and gap distance.

For the PC concentration and voltage two-way interaction there are two lines with positive slope. The solid blue line shows the PC concentration effect on the response when the voltage is held at its low value (15 kV) and the dashed red line is the PC concentration effect when the voltage is high (25 kV). The solid blue line has a larger slope than the dashed red line indicating that a change in PC concentration is more effective at increasing the fiber diameter at a lower voltage

than at a higher voltage by roughly 2 times. Physically, this makes sense because less force and stretching of fibers happens at a lower voltage leading to larger fibers.

For the PC concentration and gap distance two-way interaction the solid blue line shows the effect of PC concentration when gap distance is low (10 cm) and the dashed red line is when the gap distance is high (20 cm). The solid blue line has roughly 3 to 4 times the slope of the dashed red line meaning that the effect PC concentration has on increasing the fiber diameter is about 3 to 4 times greater at a gap distance of 10 cm compared to a gap distance of 20 cm. Similar to the voltage, less distance leads to less stretching and whipping of fibers resulting in larger fibers.

Another interesting observation is the overlap of the effects points for low PC concentration in both the voltage and gap distance plots. This also corroborates that the low concentration of PC may be too low. Essentially, this overlapping of points means that the increase of both voltage and gap distance had little to no effect on the fiber diameter at the 15% (w/w) of PC.

The final two-way interaction effect plot is for voltage and gap distance and has a different trend than what was observed for PC concentration. In this plot, the solid blue line shows the effect of voltage when the gap distance is low (10 cm) and the dashed red line shows the effect of voltage when the gap distance is high (20 cm). The solid blue line has a negative slope meaning that when the gap distance is held at 10 cm the increase in voltage will reduce fiber diameter. Again, this makes physical sense as the electric field is increased and more force applied to fibers. The dashed red line tells a different story, it has a very slightly positive slope only a small amount above horizontal (no change) meaning that increasing the voltage will increase the fiber diameter at a large gap distance (20 cm). There are two possible justifications for this: the first being that the larger gap distance facilitates more whipping in the instability region which even at low voltage (15 kV) allows the fibers to reach a saturated level of stretching because the larger distance gives more time and distance to allow solvent to escape; and the second being the noted issue that the data is skewed slightly because of poor spinning at low PC concentrations.

Another set of graphs that can be analyzed for goodness of fit include the residual plots which help determine if assumptions in the least squares regression is being met. The residuals are calculated as the difference between the observed measurement and the fitted model estimate. Four common residual plots are included:

1. The *normal probability plot* graphs residuals against a line representing the normal distribution around 0 and gives a good visual indication of how normally distributed the residuals are;
2. The *histogram* also displays the residual distribution in a bar chart fashion which allows visual identification of skewed or outlying residuals;
3. Residuals *versus fits* is plotted to determine if there is a consistent variance between residuals and outliers can be identified; and
4. Residuals versus observation plots can be used to identify any trends or outliers as a result of experimentation. The observation order is the randomized chronological order the experiments were run.

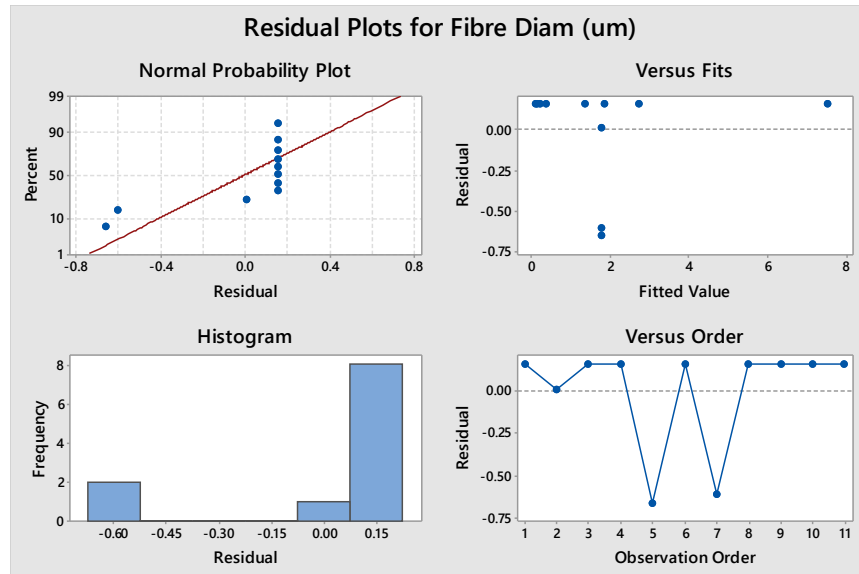


Figure 4.11 - Residual plots for the StarPlastic PC electrospun nanofiber diameter response in DOE#1

The residual plots for modelling the fiber diameter response for electrospun PC in THF/DMF (DOE#1) are included in Figure 4.11. Observing the normal probability plot we can observe that most residuals follow a straight line except there may be two (and possibly a third) significant outliers in the measured fiber diameters. This is also observed in the histogram where most residuals are distributed close to zero, but there are two residuals that have a large negative value. This is also reinforced by the residuals versus fit and order plots. In the versus fits plot, most residuals have a constant value but two are significantly lower and a third slightly lower. In the versus order plot we can identify the specific runs that are falling below the mean residual; observation runs 5 and 7 are significant outliers and run 2 could be another less significant outlier.

If we compare observation order versus to DOE standard alias order, we see that these outliers correspond to the 3 center-point replicates: standard order runs 9 (observation 7), 10 (observation 5), and 11 (observation 2). Going back to look at the measured fiber diameters and SEM images for these three observations and comparing to the other eight observations gives some interesting insight. The three center point replicates, despite having a larger average fiber diameter, actually have some of the most pristine electrospun fibers of all DOE#1 runs. Perhaps the best tradeoff of miscibility and chain entanglement of the polycarbonate into THF/DMF occurs in a tighter range around 20 % (w/w) of PC.

The corner values (high and low selection) used in the design of experiment may be outside of the ideal linear region due to lack of chain entanglement on the low selection and incomplete miscibility on the high selection. This indicates that the eight corner runs may be considered outliers. I believe that the factor of polymer concentration would have the largest impact on improving the model in this design of experiment for the physical reasons listed above. As well, the fact that observing the SEM images did show electrospun spun fibers in all cases yet the most defects were observed with the corner experiments. For example, large bead defects were observed only in the experiments using the low 15 % (w/w) PC and not at the high 25% (w/w) and larger branching density was seen at only the high PC concentrations. Future exploration in this

polycarbonate in THF/DMF solution should use concentrations closer to 20 % (w/w) such as 17.5 and 22.5 % (w/w) to improve the regression model and better predict the outcome of experiments within that range. One possible solution would be to screen the PC variable by running a series of experiments with electric field held constant and vary the PC concentration one point at a time between 15 and 25 % (w/w) to determine a tighter ideal range. [152]

Two final plots that can be used to visualize the mean response values of fiber diameter over the continuous range for two model factors are the contour and surface plots. The contour plot has a different model factor on each the X and Y axes and contour lines of the discrete response values are plotted to show regions of different response ranges; the third factor is held constant at its midpoint for each plot. The contour plot can be used to identify factor values that correspond to ideal responses as well as notice how the trend between factors may change throughout the two-dimensional XY space. The surface plots are quite similar to the contour plots except plotted in three dimensions with the Z axis corresponding to the model response value. The surface plots will have better resolution of the response value at a specific coordinate as the surface is not discrete as in the case with the contour plot. The contour plot is more ideal for analysis when printing on two-dimensional paper (such as this thesis); whereas the surface plot can be more beneficial when rotated in 3D space such as on a computer screen or with virtual reality goggles.

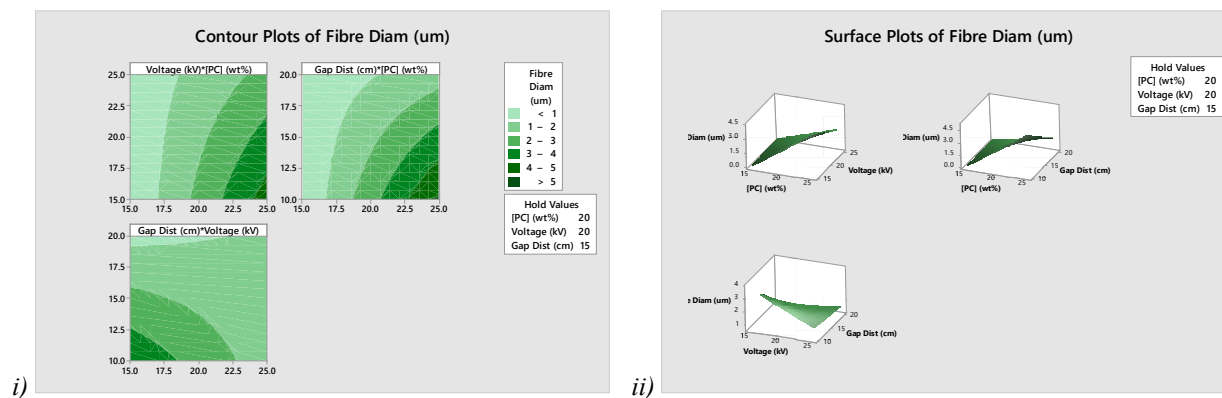


Figure 4.12 - Contour (i) and surface (ii) plots for the StarPlastic PC electrospun nanofiber diameter response in DOE#1

The contour plots for fiber diameter of electrospun fibers of PC in THF/DMF (DOE#1) are included in Figure 4.12. Starting from the top left is the voltage versus PC concentration contour plot, with the voltage from 15 through 25 kV plotted on the Y axis and PC concentration from 15 to 25% (w/w) on the X axis. From the contours, it can be seen that the sub-micron (<1) fibers are observed below about 17% (w/w) PC for all applied voltage values. As the PC concentration increases, the voltage has an increasing effect on the resulting fiber diameter. For example, at 25% (w/w) PC at the lowest voltage (15 kV) fibers larger than 5 microns are expected whereas it could decrease down to roughly 3 microns at 25 kV applied. The surface plot for voltage versus PC concentration can be seen in the top left of the surface plots chart. Due to the angle the image was captured in 3D space, the surface's shape can be interpreted in a different way. This image matches with the conclusions from the contour plot, that the slope of fiber diameter versus voltage has a lower magnitude at the lower PC concentration than the higher concentration.

A similar trend was observed for the contour and surface plots of the gap distance and PC concentration, seen in the top right of the contour chart. Summarizing, the gap distance has more effect on the fiber diameter at higher concentrations than low concentrations. The major difference observed is the closer the contour lines get as they approach the low gap distance and high concentration area, meaning the slope will be rising faster in the case of gap distance versus voltage when comparing to PC concentration. This phenomenon is observed in the surface plot (top-right) where the corner with the highest response rises to a sharper peak for gap distance compared to voltage.

The final contour and surface plots are for the gap distance versus voltage, observed in the bottom left for each chart. This contour profile is a bit different, at low voltage the gap distance plays a very large effect giving a range of fiber diameters between 0 and 4 microns. At the high voltage setting the range is much smaller between 1 and 2 microns. This suggests that the adjustment of the electric field (voltage divided by gap distance) by increasing the gap distance only has a larger effect at low voltage than high voltage. This suggests that the charge supplied at the higher voltage was enough to whip the fibers even at a low gap distance, but with the lower charge supplied to the surface of the fibers (low kV) the increased gap distance (and time in whipping instability region) is much more critical to get smaller fibers.

Through running the 2^3 -full factorial DOE for the response of fiber diameter of electrospun PC fibers in a 60:40 (w/w) THF/DMF solvent solution a regression model was developed (Equation 4.6) with the factors PC concentration, applied voltage, and gap distance as well as their 2 and 3-way interaction terms. A backwards elimination of the analysis of variance (ANOVA) was run with a cutoff of $\alpha=0.1$ for removal of terms; which in this DOE did not remove any terms. Of the seven terms used in the model, the PC concentration (A) had the largest positive effect on the fiber diameter whereas the PC concentration interacting with gap distance had the largest negative effect on the fiber diameter. The weakest effects were observed for applied voltage (C) and the 3-way interaction effect (ABC) although still significant enough to include in the model with an α between 0.05 and 0.1. The different effects can be better visualized through the Pareto, normal, main and interaction effects plots. The resulting model had an R^2 value of 97.79% indicating a high goodness of fit.

Through analyzing the effects charts, conclusions can be drawn on why certain variables act the way they do on the system. PC concentration has the largest effect on fiber diameter because the increased chain entanglement at larger concentrations resists the applied force from the electric field. The gap distance also plays a large role but in decreasing the fiber diameter, even at high PC concentrations as it increases the whipping instability region and time of travel of the fibers allowing more time under stress to elongate the fibers. The voltage seems to have the least effect on the fiber diameter, even to the point where an increase in electric field at a high gap distance does little to (or even slightly increases) the fiber diameter. To refine this study to generate a better predictability model would be to narrow the range of PC concentration to 17.5 to 22.5 % (w/w) and perhaps extend the range for applied voltage down to around 5 to 10 kV on the low end.

Linear Regression of PC Bead Density

Table 4.18 lists the measured bead density in beads per cubic millimeter (beads/mm²) for each run of DOE#1 including the bead count and measurement area used.

Table 4.18 - Bead density and measurement counts for StarPlastic PC electrospun fibers made for each run of DOE#1

Run	Bead Count	Measurement Area (mm ²)	Bead Density (beads/mm ²)
1 (1)	28	8.584e-3	3262
2 (a)	0	8.584e-3	0
3 (b)	81	8.584e-3	9437
4 (ab)	0	8.584e-3	0
5 (c)	62	3.439e-2	1803
6 (ac)	0	8.584e-3	0
7 (bc)	68	3.439e-2	1978
8 (abc)	0	8.584e-3	0
9 (0)	0	8.584e-3	0
10 (0)	52	1.373e-1	379
11 (0)	1	1.375e-3	727

The regression equation in uncoded units for bead density while electrospinning PC nanofibers, with THF/DMF solvent, as a function of PC concentration ($[PC]$) is presented in Equation 4.6.

$$\text{Bead Density (beads/mm}^2\text{)} = + 9838 - 412 [PC] \text{ (wt.\%)} \quad (\text{Equation 4.6})$$

Backwards elimination of factors was used during regression analysis with $\alpha = 0.1$. This elimination removed most factors and co-factors from the response model. This correlates with observations that a low concentration of PC leads to poor entanglement and spraying or beading occurs. If the equation is solved for no (0) beading density, the resulting concentration is about 23.9%, or just below the high value chosen for this experiment. The model has a goodness-of-fit (R^2) value of 42.75%, which suggests a poor fit.

The P-values for curvature and lack of fit (LoF) were calculated as 0.292 and 0.020, respectively. This suggests that there is no curvature in the system and the model does not adequately describe the relationship presented; including more terms in the model could improve the fit.

The calculated fitted means for bead density are summarized in Figure 4.13, they are presented in a cube plot which shows the 3-dimensional space that the regression model for DOE#1 covers.

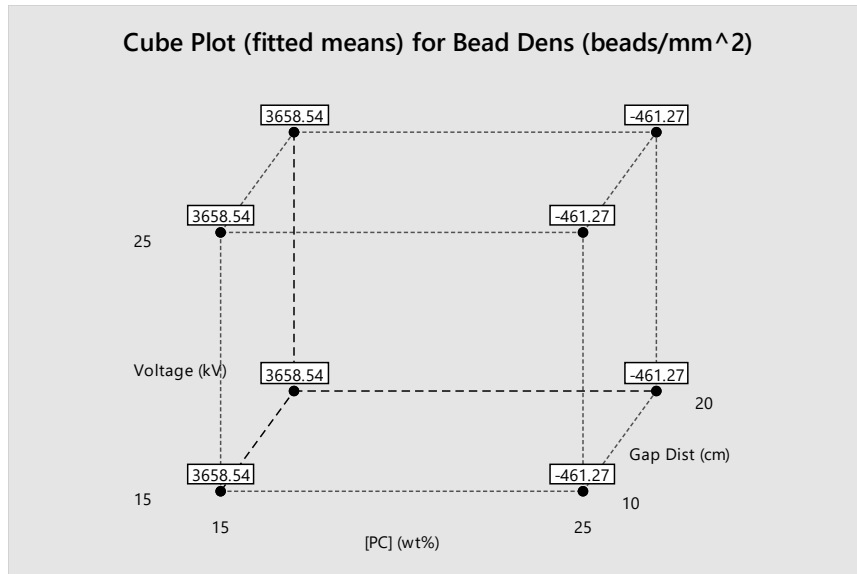


Figure 4.13 - Cube plot of fitted means for the bead density regression model for StarPlastic PC electrospun fibers in DOE#1

The cube plot represents the linear relationship of bead density, one observation that can be made is that the bead density should be greater than zero physically, or the model is true below the beading threshold of 23.9% noted earlier.

The contour plots for bead density of electrospun fibers of PC in THF/DMF (DOE#1) are included in Figure 4.14.

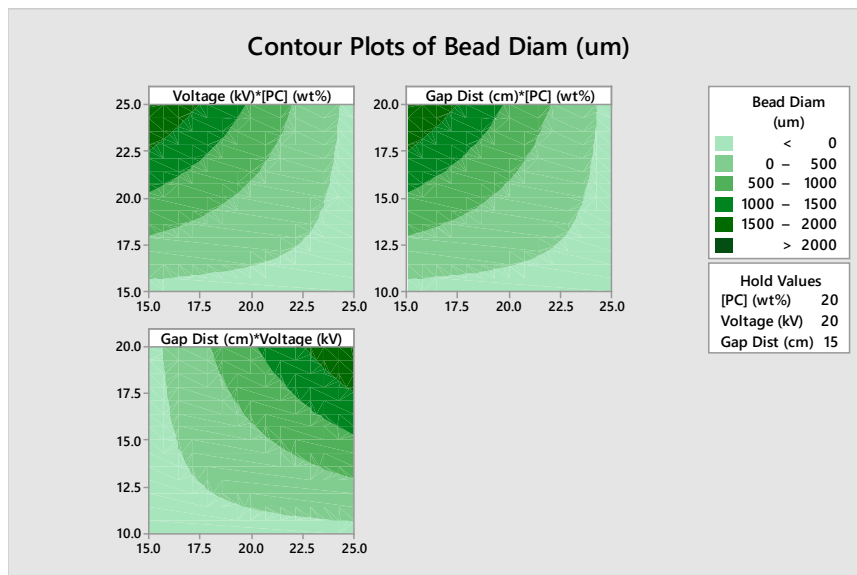


Figure 4.14 - Contour plots for the StarPlastic PC electrospun bead density response in DOE#1

From the top left, Voltage vs. PC concentration, it is observed that beading tends to occur when there is a low concentration of PC and quickly reduces beyond about 23.9% at all voltages. A lower voltage for lower concentrated solutions can reduce beading in the system. The top right plot, gap distance vs. PC concentration, shows a similar trend for gap distance, meaning a smaller

gap distance may reduce the breaking up of fibers in lower concentrated solutions. Finally, for the last contour plot, gap distance vs. voltage, at a PC concentration below our threshold (held to 20 wt.-%), it is seen that no beading occurs when the voltage is below about 16 kV at all gap distances. Also, no beading occurs below about 11 cm gap distance at all voltages. Overall, the main takeaway from the contour plots is that beading can be reduced in low concentration solutions by minimizing the whipping instability by either reducing the gap distance or applied voltage, but preferably both. This is why commercial research electrosp spinners use much lower gap distances and voltages, while maintaining a consistent electric field (voltage/gap distance). The scale used for these experiments is more consistent with larger production devices like the Elmarco device introduced in the literature review. Complete results and outputs from the regression analysis in Minitab are included in Appendix B.

Linear Regression of PC Bead Diameter

Table 4.19 lists the measured bead diameter in micrometers (μm) for each run of DOE#1 including the number of measurements (counts) and the standard deviation.

Table 4.19 - Bead diameter, standard deviation, and measurement counts for StarPlastic PC electrospun fibers made for each run of DOE#1

Run	Bead Diameter (μm)	St. Dev. (μm)	Counts
1 (1)	3.18	1.49	8
2 (a)	0	0	0
3 (b)	7.92	2.79	72
4 (ab)	0	0	0
5 (c)	4.66	1.31	23
6 (ac)	0	0	0
7 (bc)	4.36	1.21	30
8 (abc)	0	0	0
9 (0)	0	0	0
10 (0)	3.38	1.24	24
11 (0)	0	0	0

The regression equation in uncoded units for bead diameter while electrospinning PC nanofibers, with THF/DMF solvent, as a function of PC concentration ($[PC]$), applied voltage ($Voltage$), and gap distance ($Gap\ Distance$) is presented in Equation 4.7.

$$\text{Bead Diameter (um)} = + 16152$$

(Equation 4.7)

$$- 652 [\text{PC}] (\text{wt.-%})$$

$$- 1086 \text{ Voltage (kV)}$$

$$- 1631 \text{ Gap Distance (cm)}$$

$$+ 43.5 [\text{PC}] (\text{wt.-%}) * \text{Voltage (kV)}$$

$$+ 65.2 [\text{PC}] (\text{wt.-%}) * \text{Gap Distance (cm)}$$

$$+ 108.8 \text{ Voltage (kV)} * \text{Gap Distance (cm)}$$

$$- 4.35 [\text{PC}] (\text{wt.-%}) * \text{Voltage (kV)} * \text{Gap Distance (cm)}$$

Backwards elimination of factors was used during regression analysis with $\alpha = 0.1$; no factors were removed. The model has a goodness-of-fit (R^2) value of 96.24%, which suggests a very good fit, but this tends to be higher with more terms. The adjusted R^2 , which removes the dependence on number of factors, is 87.5%, which is also a good fit.

The calculated fitted means for bead diameter are summarized in Figure 4.15, they are presented in a cube plot which shows the 3-dimensional space that the regression model for DOE#1 covers.

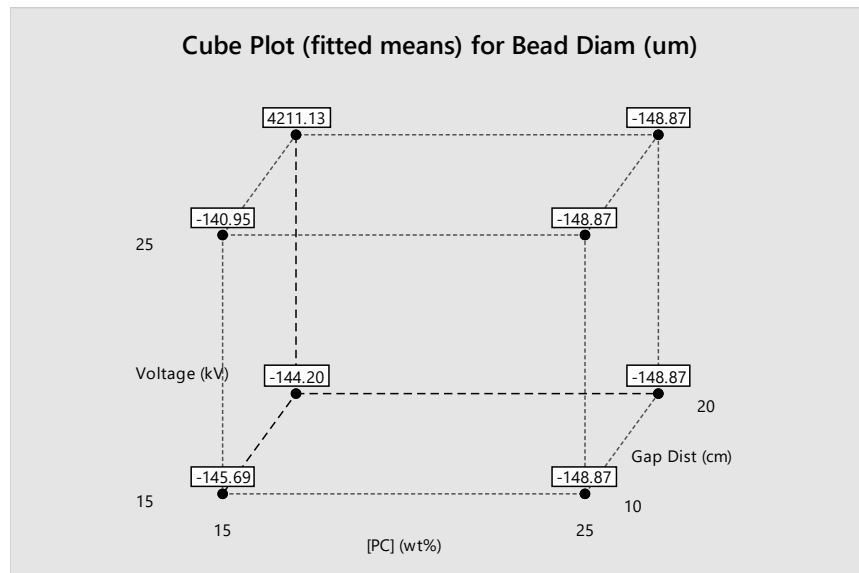


Figure 4.15 - Cube plot of fitted means for the bead diameter regression model for StarPlastic PC electrospun fibers in DOE#1

In the cube plot it is seen that the model only predicts positive bead diameters when the PC concentration is low and gap distance and voltage are high (run 7bc). This suggests the model may not do well at predicting the actual bead diameter, but does indicate where beading is the most present, when PC concentration is low.

The contour plots for bead diameter of electrospun fibers of PC in THF/DMF (DOE#1) are included in Figure 4.16.

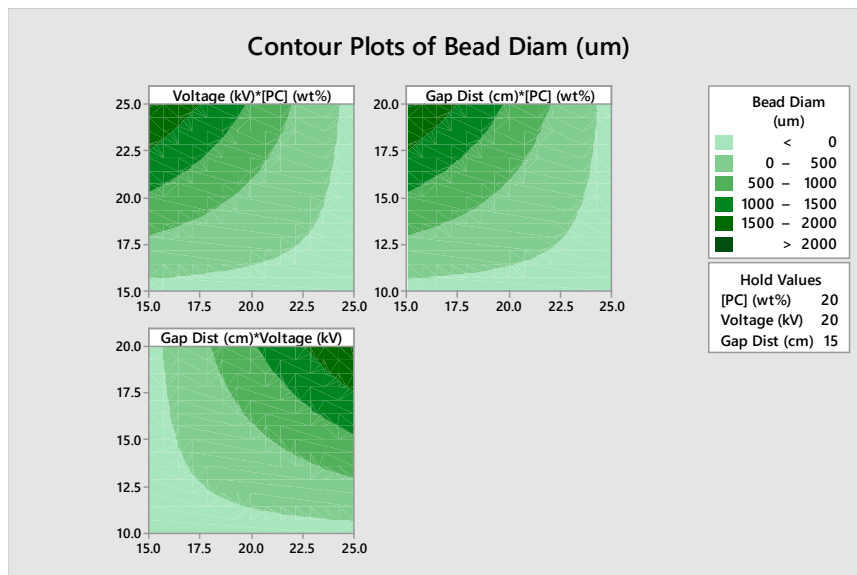


Figure 4.16 - Contour plots for the StarPlastic PC electrospun bead diameter response in DOE#1

The contour plots for beading diameter have nearly identical results as the beading density in section 5.1.3. So similarly, beading can be reduced in low concentration PC solutions by minimizing the whipping instability by either reducing the gap distance or applied voltage, but preferably both. Another solution, if the gap distance or voltage cannot be modified would be to increase the concentration above 24% to avoid beading. Complete results and outputs from the regression analysis in Minitab are included in Appendix B.

DOE#2 - Nanocrystalline Cellulose (NCC) + (60:40) THF:DMF

The different factors tested for the second DOE along with their low, high, and center point levels are summarized in Table 4.1. The 3 factors examined (with low, center, and high levels) include: StarPlastic PC concentration, [PC], (15, 20, 25 wt.-%); applied voltage, V, (15, 20, 25 kV); and gap distance, d, (10, 15, 20 cm). For the 2³-factorial design of experiment, there are 3 factors being adjusted between 2 different levels, high and low. As well as 3 center-point replicates, resulting in 11 total runs for a full-factorial design of experiment.

Each sample included 2 wt.-% of NCC incorporated with the StarPlastic PC to observe any different effects with its inclusion. The next section, DOE#0, combines DOE#1 and DOE#2 by adding a fourth factor of NCC concentration.

Table 4.20 summarizes the target and actual concentrations calculated for PC in solution and NCC in solid for each run based on the recorded masses.

Table 4.20 - DOE#2 target and actual concentration calculations for StarPlastic PC and NCC in 60:40 (w/w) THF/DMF for each 11 runs

Std. Order	[PC] Tar. (%TOTAL)	[PC] Act. (%TOTAL)	[NCC] Tar. (%SOLID)	[NCC] Act. (%SOLID)
1 (1)	15	15.0	2	2.0
2 (a)	25	24.9	2	2.0
3 (b)	15	15.1	2	2.1
4 (ab)	25	25.0	2	2.0
5 (c)	15	15.0	2	2.1
6 (ac)	25	24.9	2	2.0
7 (bc)	15	15.0	2	2.1
8 (abc)	25	24.9	2	2.0
9 (0)	20	20.0	2	2.0
10 (0)	20	19.9	2	2.1
11 (0)	20	19.9	2	2.0

(Note: All percentages listed are with respect to weight (w/w) of noted system; total, solid, etc.)

2 wt.-% NCC/PC in 60:40 (w/w) THF/DMF Solvent Formulation Performance

The measured turbidity, in Nephelometric Turbidity Units (NTU), and viscosity, in centipoise (cP) with standard deviation, for each run of the DOE#2 are summarized in Table 4.21 as well as the actual concentration of PC and NCC.

Table 4.21 - Turbidity and viscosity measurements for StarPlastic PC and NCC in 60:40 (w/w) THF/DMF solvent for each run of DOE#2

Run	[PC] Act. (%TOTAL)	[NCC] Act. (%SOLID)	Turbidity (NTU)	Viscosity (cP) [100 RPM]	St. Dev. (cP)
1 (1)	15.0	2.0	221	95	10
2 (a)	24.9	2.0	325	583	18
3 (b)	15.1	2.1	247	79	9
4 (ab)	25.0	2.0	226	631	20
5 (c)	15.0	2.1	182	58	6
6 (ac)	24.9	2.0	277	964	47
7 (bc)	15.0	2.1	193	61	7
8 (abc)	24.9	2.0	162	926	11
9 (0)	20.0	2.0	226	211	12
10 (0)	19.9	2.1	170	215	27
11 (0)	19.9	2.0	224	246	16
Pure THF/DMF	-	-	0.2	0.7	-

Figure 4.17 plots the 11 turbidity measurements of StarPlastic PC and 2-wt.-% NCC in 60:40 (w/w) THF/DMF solvent, taken from each run of DOE#2. The trend from DOE#1 is included for comparison, as the only difference in parameters is the inclusion of NCC.

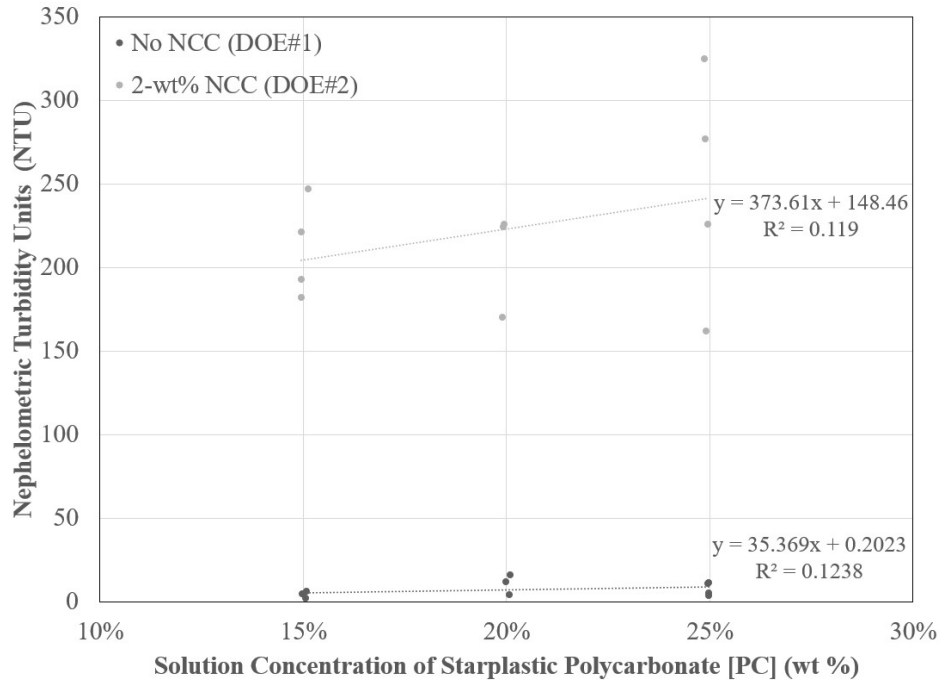


Figure 4.17 - Turbidity versus StarPlastic PC concentration in 60:40 (w/w) THF/DMF solvent with (DOE#2, grey) and without (DOE#1, black) 2-wt.-% NCC incorporation for all runs

The turbidity does appear to increase with the concentration of PC, following the linear relationship:

$$\text{Turbidity (NTU)} = 373.61 [\text{PC}] (\text{wt.-%}) + 148.46 \quad (\text{Equation 4.8})$$

The linear model for turbidity of 2% NCC/PC in 60:40 THF/DMF in Equation 4.8, has an R^2 value of only 11.9% suggesting that the model only weakly explains the variability present in the system.

The turbidity of 2% NCC/PC in THF/DMF appears to increase about 373.61 NTU for each percent addition of PC in the overall solution. As this is a faster rise of turbidity with the addition of PC than without the NCC, it is expected there is some combined effect of the two. Perhaps the NCC flocculations in the THF/DMF solvent may increase in the presence of PC. The intercept at 0% PC has a turbidity of about 148.46 NTU which is near to the turbidity of 291 NTU a 1 wt.-% NCC in THF/DMF solution measured in the lab.

Figure 4.18 plots the 11 viscosity measurements of StarPlastic PC and 2 wt.-% NCC in 60:40 (w/w) THF/DMF solvent, taken from each run of DOE#2. The error bars represent the standard deviation of measurements. The trend from DOE#1 is included for comparison, as the only difference in parameters is the inclusion of NCC.

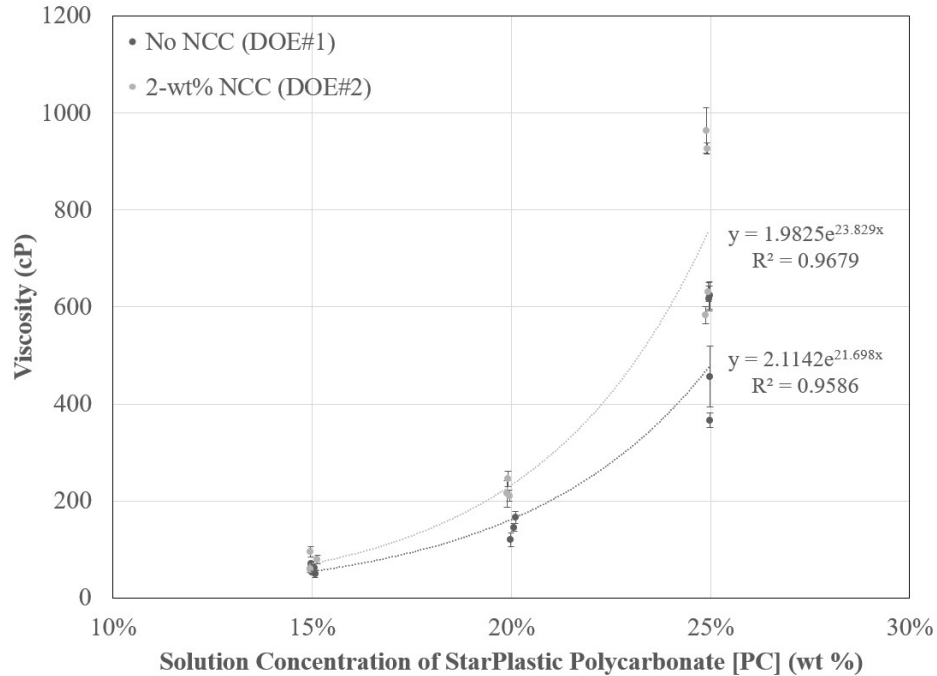


Figure 4.18 - Viscosity versus StarPlastic PC concentration in 60:40 (w/w) THF/DMF solvent with (DOE#2, grey) and without (DOE#1, black) 2-wt.-% NCC incorporation for all runs

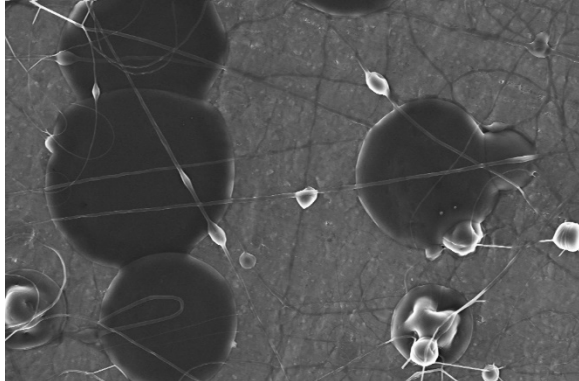
The viscosity does appear to increase with the concentration of PC, following the exponential relationship:

$$\text{Viscosity (cP)} = 1.9825 \exp[23.829 [\text{PC}](\text{wt.-%})] \quad (\text{Equation 4.9})$$

The exponential model for viscosity of 2% NCC/PC in 60:40 THF/DMF in Equation 4.9, has an R^2 value of only 96.79% suggesting that the model is good at explaining the variability present in the system. It is also observed that the presence of NCC increases the viscosity more at higher PC concentrations, further confirming interaction effects of PC and NCC.

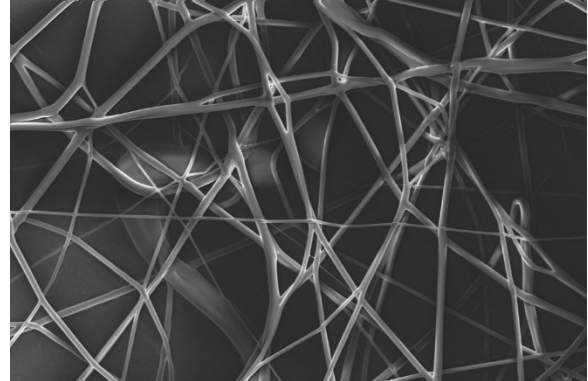
Linear Regression of 2 wt.-% NCC/PC Fiber Diameter

Following the 11 electrospinning runs for the 2^3 full-factorial DOE#2 the collected fiber mats of 2 wt.-% NCC/PC fibers were collected for SEM imaging. The images chosen for ImageJ analysis of fiber diameter, bead density, and bead diameter are included in Figure 4.19 for each run.



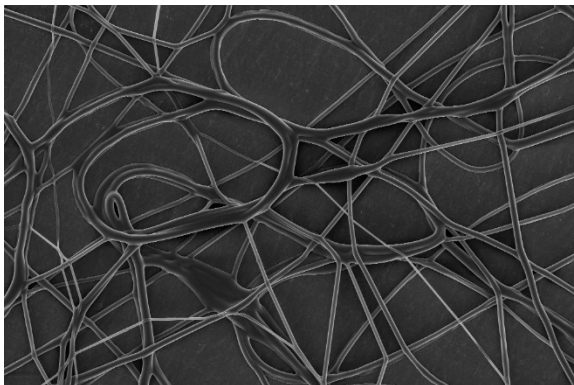
i)

15% | 15 kV | 10 cm



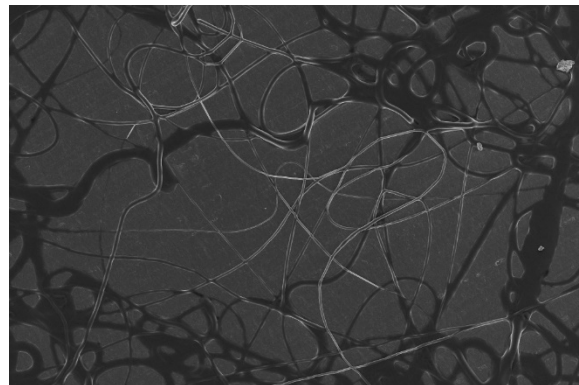
ii)

25% | 15 kV | 10 cm



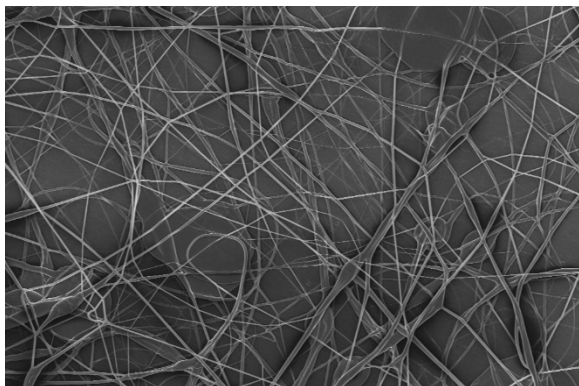
iii)

15% | 25 kV | 10 cm



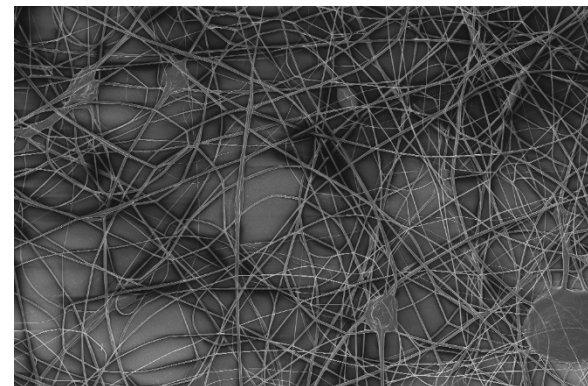
iv)

25% | 25 kV | 10 cm



v)

15% | 15 kV | 20 cm



vi)

25% | 15 kV | 20 cm

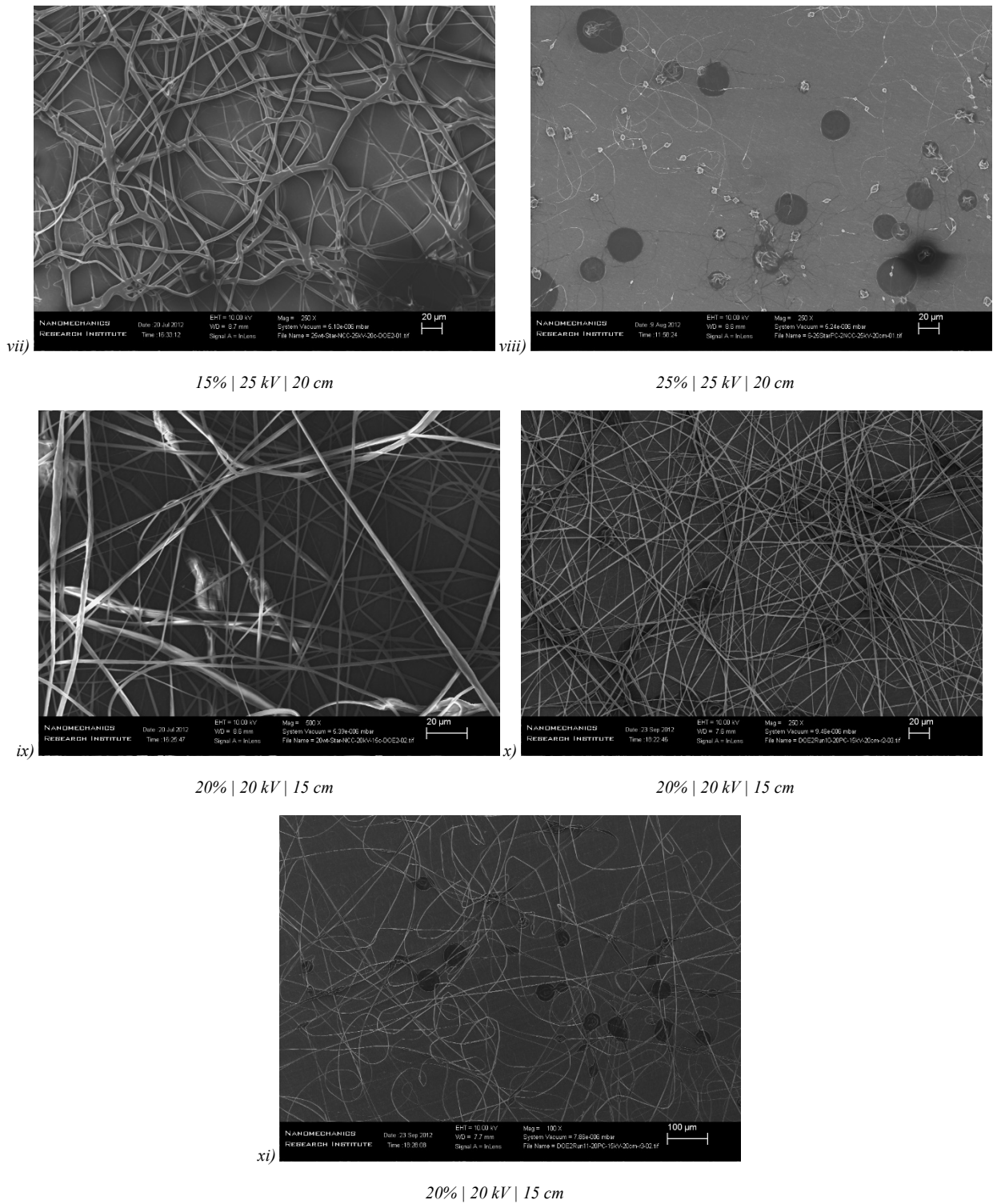


Figure 4.19 - Scanning electron micrographs of StarPlastic PC and 2 wt.-% NCC electrospun fibers for each run (i-xi) of DOE#2

Table 4.22 lists the measured StarPlastic PC and 2 wt.-% NCC fiber diameter in micrometers (μm) for each run of DOE#2 including the number of measurements (counts) and the standard deviation.

Table 4.22 - Fiber diameter, standard deviation, and measurement counts for StarPlastic PC and 2% NCC electrospun fibers made for each run of DOE#2

Run	Fiber Diameter (μm)	St. Dev. (μm)	Counts
1 (1)	0.74	1.74	91
2 (a)	3.60	3.02	171
3 (b)	9.53	6.27	160
4 (ab)	5.49	2.69	112
5 (c)	3.64	2.07	103
6 (ac)	3.37	1.50	104
7 (bc)	4.30	2.39	186
8 (abc)	0.61	0.73	30
9 (0)	1.97	1.78	200
10 (0)	1.21	0.74	147
11 (0)	2.19	1.28	85

The regression equation in uncoded units for fiber diameter of 2% NCC/PC nanofibers, with THF/DMF solvent, as a function of PC concentration ($[PC]$), applied voltage ($Voltage$), and gap distance ($Gap\ Distance$) is presented in Equation 4.10.

$$\begin{aligned}
 \text{Fiber Diameter (um)} = & - 35.4 && \text{(Equation 4.10)} \\
 & + 0.903 [PC] \text{ (wt.-%)} \\
 & + 2.205 Voltage \text{ (kV)} \\
 & + 1.091 Gap Distance \text{ (cm)} \\
 & - 0.0516 [PC] \text{ (wt.-%)} * Voltage \text{ (kV)} \\
 & - 0.0639 Voltage \text{ (kV)} * Gap Distance \text{ (cm)}
 \end{aligned}$$

Backwards elimination of factors was used during regression analysis with $\alpha = 0.1$. This elimination removed some factors and co-factors from the response model. The model has a goodness-of-fit (R^2) value of 80.59%, which suggests a good fit.

The P-values for curvature and lack of fit (LoF) were calculated as 0.023 and 0.174, respectively. As curvature could not be ruled out of the system, center-point data can be included in the model to account for this. The LoF P-value suggests the model does adequately describe the functional relationship between fiber diameter and the factors included.

If the center-point data is included in the model, the regression equation in uncoded units for fiber diameter of 2% NCC/PC nanofibers, with THF/DMF solvent, as a function of PC concentration (*[PC]*), applied voltage (*Voltage*), and gap distance (*Gap Distance*), is then presented in Equation 4.11.

$$\begin{aligned}
 \text{Fiber Diameter (um)} = & - 34.82 && \text{(Equation 4.11)} \\
 & + 0.903 [PC] \text{ (wt.-%)} \\
 & + 2.205 \text{ Voltage (kV)} \\
 & + 1.091 \text{ Gap Distance (cm)} \\
 & - 0.0516 [PC] \text{ (wt.-%)} * \text{Voltage (kV)} \\
 & - 0.0639 \text{ Voltage (kV)} * \text{Gap Distance (cm)} \\
 & - 2.118 \text{ CtPt}
 \end{aligned}$$

Backwards elimination of factors was used during regression analysis with $\alpha = 0.1$. This elimination removed some factors and co-factors from the response model. The model has a goodness-of-fit (R^2) value of 90.13%, which suggests a very good fit.

The model includes all first order factors as well as co-factors [PC]/Voltage and Voltage/Gap Distance and is nearly identical to Equation 4.10 except for the constant term and center-point term (CtPt). This suggests the original model overestimates the fiber diameter in the center of the factor space explored.

The P-value for lack of fit (LoF) was calculated as 0.174, suggesting the model adequately describes the relationship between the factors and fiber diameter.

The calculated fitted means for PC/NCC fiber diameter for both models are summarized in Appendix B, Figure B.5, they are presented in a cube plot which shows the 3-dimensional space that the regression model for DOE#2 covers.

From the fitted means, we can see they correlate well with the measured data; thus, they have a good residual distribution. The response model that includes the center-point better fits the high factor level run (8abc) at 0.5225 μm compared to the measured 0.608 μm . The model that did not include the center-point data had the predicted value for 8abc as negative.

The contour plots for fiber diameter of electrospun fibers of PC/NCC in THF/DMF (DOE#2) are included in Figure 4.20.

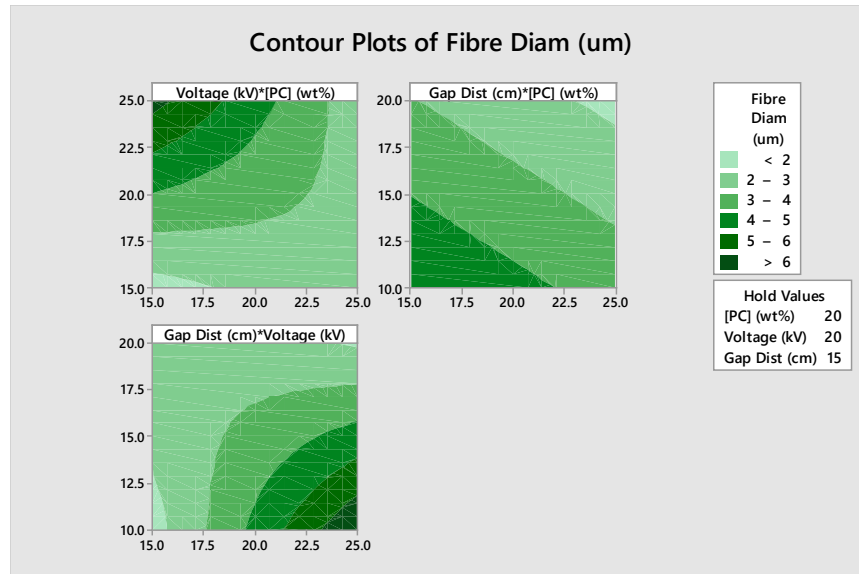


Figure 4.20 - Contour plots for the StarPlastic PC and NCC electrospun fiber diameter response in DOE#2

From the contour plots, it can be observed that to minimize fiber diameter, and maximize fiber performance, one could:

1. Use a low voltage with low concentration of PC,
2. Use a high gap distance with high concentration of PC, and/or
3. Use a low gap distance and low voltage.

Combining these findings, we see a similar result to DOE#1, now with the inclusion of 2 wt.-% NCC. That is, that in addition to minimizing beading, reducing all three factor levels simultaneously will also produce smaller fiber diameters. Complete results and outputs from the regression analysis in Minitab are included in Appendix B.

Linear Regression of 2 wt.-% NCC/PC Bead Density

Table 4.23 lists the measured bead density in beads per cubic millimeter (beads/mm²) for each run of DOE#2 including the bead count and measurement area used.

Table 4.23 - Bead density and measurement counts for StarPlastic PC and NCC electrospun fibers made for each run of DOE#2

Run	Bead Count	Measurement Area (mm²)	Bead Density (beads/mm²)
1 (1)	18	8.584e-3	2097
2 (a)	1	3.439e-2	29
3 (b)	1	3.439e-2	29
4 (ab)	0	3.439e-2	0
5 (c)	18	1.373e-1	131
6 (ac)	7	8.584e-1	8
7 (bc)	0	1.373e-1	0
8 (abc)	86	1.373e-1	626
9 (0)	7	3.439e-2	203
10 (0)	16	1.373e-1	116
11 (0)	32	8.584e-1	37

The regression equation in uncoded units for bead density while electrospinning 2% NCC/PC nanofibers, with THF/DMF solvent, as a function of PC concentration (*[PC]*), applied voltage (*Voltage*), and gap distance (*Gap Distance*) is presented in Equation 4.12.

$$\begin{aligned}
 \text{Bead Density (beads/mm}^2\text{)} = & + 15773 && \text{(Equation 4.12)} \\
 & - 514 [PC] \text{ (wt.\-%)} \\
 & - 513 \text{ Voltage (kV)} \\
 & - 553 \text{ Gap Distance (cm)} \\
 & + 13.94 [PC] \text{ (wt.\-%)} * \text{Voltage (kV)} \\
 & + 13.00 [PC] \text{ (wt.\-%)} * \text{Gap Distance (cm)} \\
 & + 12.92 \text{ Voltage (kV)} * \text{Gap Distance (cm)}
 \end{aligned}$$

Backwards elimination of factors was used during regression analysis with $\alpha = 0.1$. This elimination removed some factors and co-factors from the response model. The model has a goodness-of-fit (R^2) value of 90.90%, which suggests a very good fit.

The P-values for curvature and lack of fit (LoF) were calculated as 0.274 and 0.032, respectively. This suggests that there is no curvature in the system and but model does not adequately describe the relationship presented.

The calculated fitted means for bead density are summarized in Appendix B, Figure B.6, they are presented in a cube plot which shows the 3-dimensional space that that the regression model for DOE#2 covers.

The cube plot shows that the fitted means do not well correlate with the measured data for bead density below zero, but the residuals are not too high for the positive density levels. This could explain the LoF P-value partially.

The contour plots for bead density of electrospun fibers of PC/NCC in THF/DMF (DOE#2) are included in Figure 4.21.

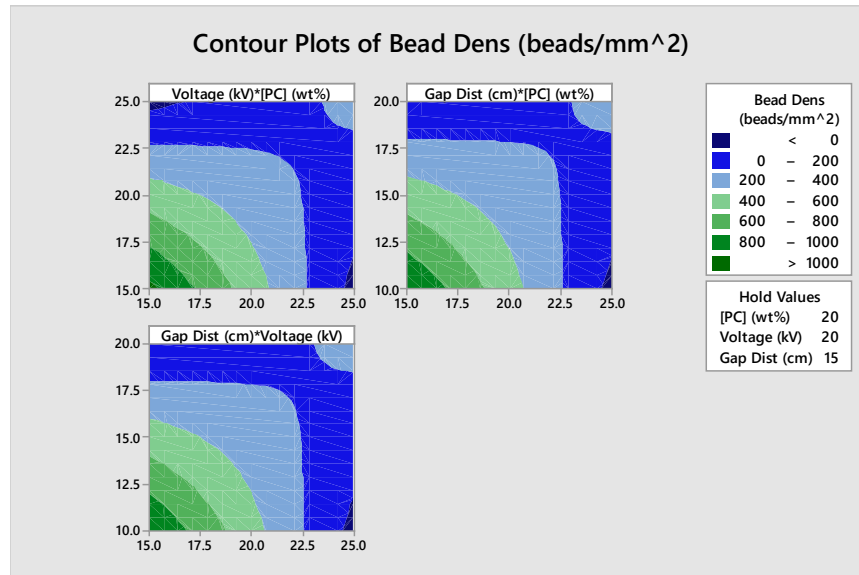


Figure 4.21 - Contour plots for the StarPlastic PC and NCC electrospun bead density response in DOE#2

From the contour plots, it can be observed that to minimize bead density, and maximize fiber performance, one could:

1. Use high voltage with high PC concentration,
2. Use a high gap distance with high PC concentration, and/or
3. Use a high gap distance with high voltage.

Combining these findings, we see a very different result to DOE#1, although higher PC concentration is preferred, a larger whipping region (both gap distance and voltage) is also required to reduce beading density. The reasoning for this may be the change in charge distribution on the fiber and Taylor cone due to the inclusion of NCC as well as the increased entanglement. A final reason may be the simplicity of the previous model and the poor model prediction capabilities below 0 beading.

Looking at the SEM images for this DOE, we do see overall reduction of beading with the inclusion of NCC but the amount of branching (fusion and splitting of fibers) seems to increase. Perhaps, the above suggestion to use a larger whipping region may also an ideal solution to reduce branching and allow fibers to fully form (remove all solvent) before being deposited to the collector. Complete results and outputs from the regression analysis in Minitab are included in Appendix B.

Linear Regression of 2 wt.-% NCC/PC Bead Diameter

Table 4.24 lists the measured bead diameter in micrometers (μm) for each run of DOE#2 including the number of measurements (counts) and the standard deviation.

Table 4.24 - Bead diameter, standard deviation, and measurement counts for StarPlastic PC and NCC electrospun fibers made for each run of DOE#2

Run	Bead Diameter (μm)	St. Dev. (μm)	Counts
1 (1)	13.94	5.11	73
2 (a)	0	0	0
3 (b)	0	0	0
4 (ab)	0	0	0
5 (c)	28.23	11.47	33
6 (ac)	44.19	15.04	45
7 (bc)	0	0	0
8 (abc)	6.39	1.18	15
9 (0)	0	0	0
10 (0)	0	0	0
11 (0)	51.98	15.72	41

Backwards elimination of factors was used during regression analysis with $\alpha = 0.1$. This removed all terms from the model. The data collected was not sufficient enough to produce a working model. Complete results and outputs from the regression analysis in Minitab are included in Appendix B.

DOE#0 - Nanocrystalline Cellulose (NCC) + (60:40) THF:DMF (combining DOE#1 and DOE#2)

The different factors tested for the zeroth DOE along with their low and high levels are summarized in Table 4.1. The 4 factors examined (with low, and high levels) include: StarPlastic PC concentration, [PC], (15, 20, 25 wt.-%); applied voltage, V, (15, 20, 25 kV); gap distance, d, (10, 15, 20 cm), and NCC concentration, [NCC], (0,2 wt.-%). For the 2^4 -factorial design of experiment, there are 4 factors being adjusted between 2 different levels, high and low, resulting in 16 total runs for a full-factorial design of experiment.

The 16 runs of this DOE are a combination of the primary 8 runs from each DOE#1 and DOE#2.

Table 4.25 summarizes the target and actual concentrations calculated for PC in solution and NCC in solid for each run based on the recorded masses.

Table 4.25 - DOE#0 target and actual concentration calculations for StarPlastic PC and NCC in 60:40 (w/w) THF/DMF for each 16 runs

Std. Order	[PC] Tar. (%TOTAL)	[PC] Act. (%TOTAL)	[NCC] Tar. (%SOLID)	[NCC] Act. (%SOLID)
1 (1)	15.0	15.01	0.00	0.00
2 (a)	25.0	24.99	0.00	0.00
3 (b)	15.0	15.08	0.00	0.00
4 (ab)	25.0	24.98	0.00	0.00
5 (c)	15.0	14.99	0.00	0.00
6 (ac)	25.0	24.97	0.00	0.00
7 (bc)	15.0	15.06	0.00	0.00
8 (abc)	25.0	24.99	0.00	0.00
9 (d)	15.0	14.97	2.00	1.96
10 (ad)	25.0	24.88	2.00	2.04
11 (bd)	15.0	15.14	2.00	2.08
12 (abd)	25.0	24.95	2.00	2.03
13 (cd)	15.0	14.95	2.00	2.09
14 (acd)	25.0	24.90	2.00	2.03
15 (bcd)	15.0	14.96	2.00	2.09
16 (abcd)	25.0	24.92	2.00	2.03

Linear Regression of PC and 2 wt.-% NCC/PC Fiber Diameter

The regression equation in uncoded units for fiber diameter while electrospinning PC and NCC/PC nanofibers, with THF/DMF solvent, as a function of PC concentration ($[PC]$), NCC concentration ($[NCC]$), applied voltage ($Voltage$), and gap distance ($Gap\ Distance$) is presented in Equation 4.13.

$$\begin{aligned}
\text{Fiber Diameter (um)} = & - 6.7 && \text{(Equation 4.13)} \\
& + 1.064 [\text{PC}] \text{ (wt.\-%)} \\
& + 0.246 \text{ Voltage (kV)} \\
& - 0.710 \text{ Gap Distance (cm)} \\
& - 11.22 [\text{NCC}] \text{ (wt.\-%)} \\
& - 0.0374 [\text{PC}] \text{ (wt.\-%)} * \text{Voltage (kV)} \\
& - 0.2220 [\text{PC}] \text{ (wt.\-%)} * [\text{NCC}] \text{ (wt.\-%)} \\
& + 0.0269 \text{ Voltage (kV)} * \text{Gap Distance (cm)} \\
& + 0.837 \text{ Voltage (kV)} * [\text{NCC}] \text{ (wt.\-%)} \\
& + 0.901 \text{ Gap Distance (cm)} * [\text{NCC}] \text{ (wt.\-%)} \\
& - 0.0454 \text{ Voltage (kV)} * \text{Gap Distance (cm)} * [\text{NCC}] \text{ (wt.\-%)}
\end{aligned}$$

Backwards elimination of factors was used during regression analysis with $\alpha = 0.1$. The initial model was saturated so the elimination removed all 3rd and 4th level co-factors to arrive at the regression model. The model has a goodness-of-fit (R^2) value of 87.43%, which suggests a good fit.

The calculated fitted means for 2 wt.-% NCC/PC fiber diameter are summarized in Appendix B, Figure B.12; they are presented in 2 cube plots which shows the 4-dimensional space that the regression model for DOE#0 covers.

From the fitted means in the cube plot, we can see they correlate well with the measured data; thus, they have a relatively good residual distribution.

The contour plots for fiber diameter of electrospun fibers of PC and PC/NCC in THF/DMF (DOE#0) are included in Figure 4.22.

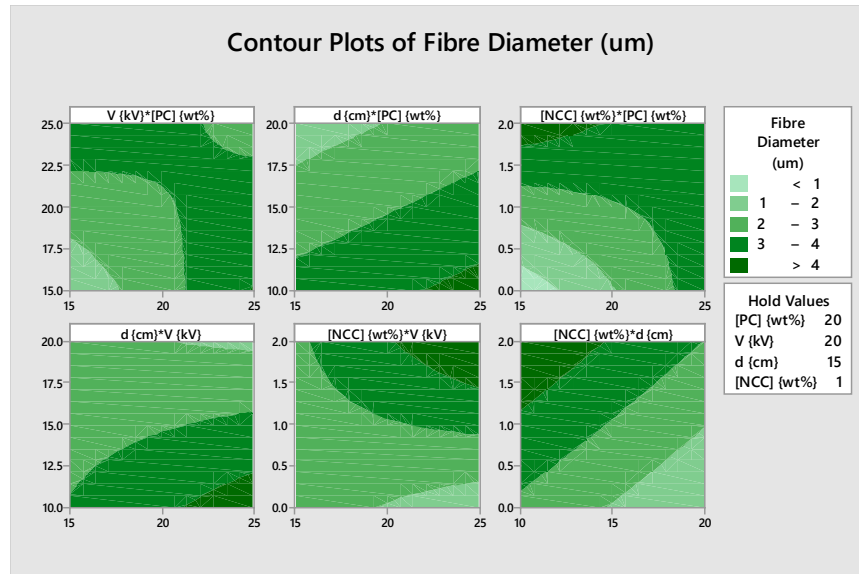


Figure 4.22 - Contour plots for the StarPlastic PC and PC/NCC electrospun fiber diameter response in DOE#0

From the contour plots, we can draw some specific information on the inclusion of NCC in the system:

1. From the [NCC]*[PC] contour plot, NCC has a larger effect increasing fiber diameter at lower PC concentrations,
2. From the [NCC]*Voltage plot, NCC has a larger effect increasing fiber diameter at higher voltages,
3. From the [NCC]*Gap Distance plot, with constant NCC, increasing gap distance linearly reduces fiber diameter.
4. Overall, the inclusion of NCC increases fiber diameter.

Complete results and outputs from the regression analysis in Minitab are included in Appendix B.

Linear Regression of PC and 2 wt.-% NCC/PC Bead Density

The regression equation in uncoded units for bead density while electrospinning PC and NCC/PC nanofibers, with THF/DMF solvent, as a function of PC concentration ($[PC]$) and NCC concentration ($[NCC]$) is presented in Equation 4.14.

$$\begin{aligned}
 \text{Bead Density (um)} = & + 10300 && \text{(Equation 4.14)} \\
 & - 412 [PC] \text{ (wt.-%)} \\
 & - 4569 [NCC] \text{ (wt.-%)} \\
 & + 186.1 [PC] \text{ (wt.-%)} * [NCC] \text{ (wt.-%)}
 \end{aligned}$$

Backwards elimination of factors was used during regression analysis with $\alpha = 0.1$. This elimination removed some factors and co-factors from the response model. The model has a goodness-of-fit (R^2) value of 51.91%, which suggests a poor fit. Increasing either PC or NCC concentrations leads to a reduction in bead density.

The calculated fitted means for bead density are summarized in Appendix B, Figure B.13, they are presented in a cube plot which shows the 2-dimensional space that regression model for DOE#0 covers.

The contour plot for bead density of electrospun fibers of PC and PC/NCC in THF/DMF (DOE#0) are included in Figure 4.23.

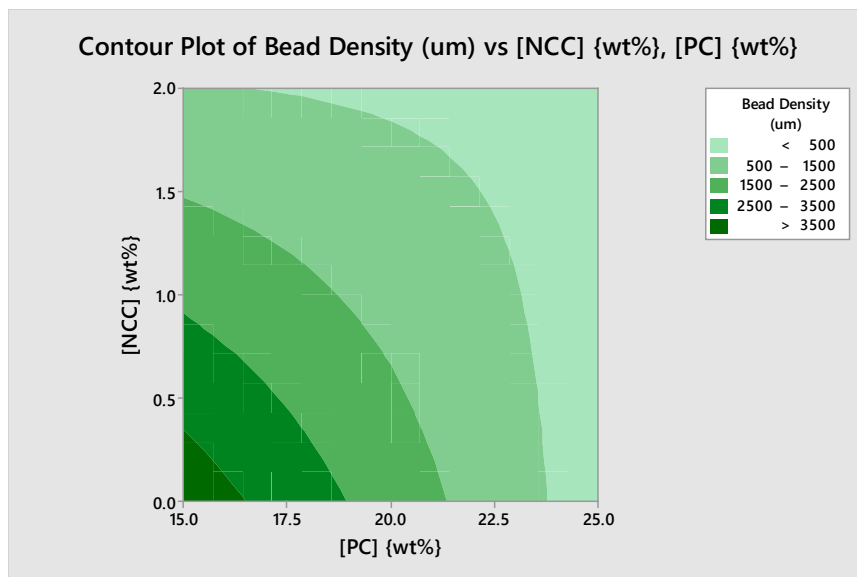


Figure 4.23 - Contour plot for the StarPlastic PC and PC/NCC electrospun bead density response in DOE#0

Both the cube and contour plots show that increasing PC and/or NCC concentrations leads to a reduced bead density. Complete results and outputs from the regression analysis in Minitab are included in Appendix B.

Linear Regression of PC and 2 wt.-% NCC/PC Bead Diameter

Backwards elimination of factors was used during regression analysis with $\alpha = 0.1$. This removed all terms from the model. The data collected was not sufficient enough to produce a working model. Complete results and outputs from the regression analysis in Minitab are included in Appendix B.

DOE#3 - Chloroform

The different factors tested for the second DOE along with their low, high, and center point levels are summarized in Table 4.1. The 3 factors examined (with low, center, and high levels) include: StarPlastic PC concentration, [PC], (5, 10, 15 wt.-%); applied voltage, V, (15, 20, 25 kV); and PC Source (StarPlastic, Lexan PC). For the 2³-factorial design of experiment, there are 3 factors being adjusted between 2 different levels, high and low. As well as 6 center-point replicates, resulting in 11 total runs for a full-factorial design of experiment. As PC source is a discrete factor, 3 center point replicates were run for each variant.

Table 4.26 includes the target and actual masses and concentrations of PC and Chloroform for each run to formulate a 50 mL solution for electrospinning.

Table 4.26 - DOE#3 target and actual concentration measurements for StarPlastic and Lexan PC in chloroform for each 14 runs

Std.	[PC] Tar.	[PC] Act.
Order	(%TOTAL)	(%TOTAL)
1 (1)	5	5.0
2 (a)	15	15.0
3 (b)	5	5.0
4 (ab)	15	15.0
5 (c)	5	5.1
6 (ac)	15	14.7
7 (bc)	5	5.0
8 (abc)	15	15.0
9 (0)	10	9.9
10 (0)	10	10.1
11 (0)	10	9.6
12 (0)	10	10.1
13 (0)	10	10.0
14 (0)	10	10.1

PC in Chloroform Solvent Formulation Performance

The measured turbidity, in Nephelometric Turbidity Units (NTU), and viscosity, in centipoise (cP) with standard deviation, for each run of the DOE#3 are summarized in Table 4.27 as well as the actual concentration of PC and PC Grade.

Table 4.27 - Turbidity and viscosity measurements for StarPlastic and Lexan PC in chloroform for each run of DOE#3

Run	[PC] Act. (% _{TOTAL})	PC Grade	Turbidity (NTU)	Viscosity (cP) [100 RPM]	St. Dev. (cP)
1 (1)	5.0	StarPlastic	0.9	20	3
2 (a)	15.0	StarPlastic	6.0	383	5
3 (b)	5.0	StarPlastic	0.9	19	2
4 (ab)	15.0	StarPlastic	5.0	394	6
5 (c)	5.1	Lexan	4.6	22	4
6 (ac)	14.7	Lexan	16.0	532	9
7 (bc)	5.0	Lexan	4.1	24	5
8 (abc)	15.0	Lexan	16.7	642	8
9 (0)	9.9	Lexan	7.8	109	8
10 (0)	10.1	Lexan	7.7	100	7
11 (0)	9.6	Lexan	7.2	84	6
12 (0)	10.1	StarPlastic	1.3	81	4
13 (0)	10.0	StarPlastic	1.9	86	20
14 (0)	10.1	StarPlastic	1.3	81	10
Pure Chloroform	-	-	0.1	0.5	-

Figure 4.24 plots the 14 turbidity measurements of StarPlastic and Lexan PC, separately, in 60:40 (w/w) THF/DMF solvent, taken from each run of DOE#3.

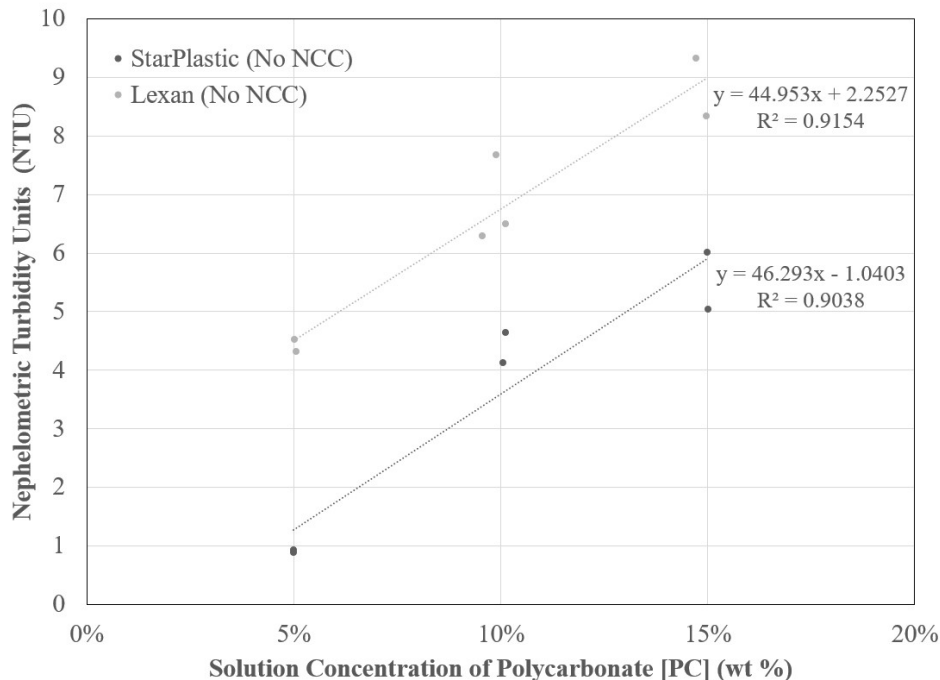


Figure 4.24 - Turbidity versus PC concentration in chloroform solvent for StarPlastic (black) and Lexan (grey) PC for each run of DOE#3

The turbidity does appear to increase with the concentration of PC, following the linear relationships for StarPlastic and Lexan PC, respectively:

$$\text{Turbidity (NTU)} = 46.293 [\text{StarPlastic PC}] - 1.0403 \quad (\text{Equation 4.15})$$

$$\text{Turbidity (NTU)} = 44.953 [\text{Lexan PC}] + 2.2527 \quad (\text{Equation 4.16})$$

The linear model for turbidity of StarPlastic PC in 60:40 THF/DMF in Equation 4.15, has an R^2 value of 90.38% suggesting that the model is good at explaining the variability present in the system. Similarly, the turbidity model in Equation 4.16 for Lexan PC, has an R^2 value of 91.54% suggesting that the model also has an acceptable goodness of fit.

The turbidity of StarPlastic PC appears to increase about 46.3 NTU for each percent addition of PC in the overall solution. The intercept at 0% PC has a negative turbidity which is close to the measured turbidity of pure chloroform.

The turbidity of Lexan PC appears to increase about 45.0 NTU for each percent addition of PC in the overall solution. The intercept at 0% PC has a turbidity of about 2.3 NTU which is close to the measured turbidity of pure chloroform.

Figure 4.25 plots the 14 viscosity measurements of StarPlastic and Lexan PC, separately, in 60:40 (w/w) THF/DMF solvent, taken from each run of DOE#3.

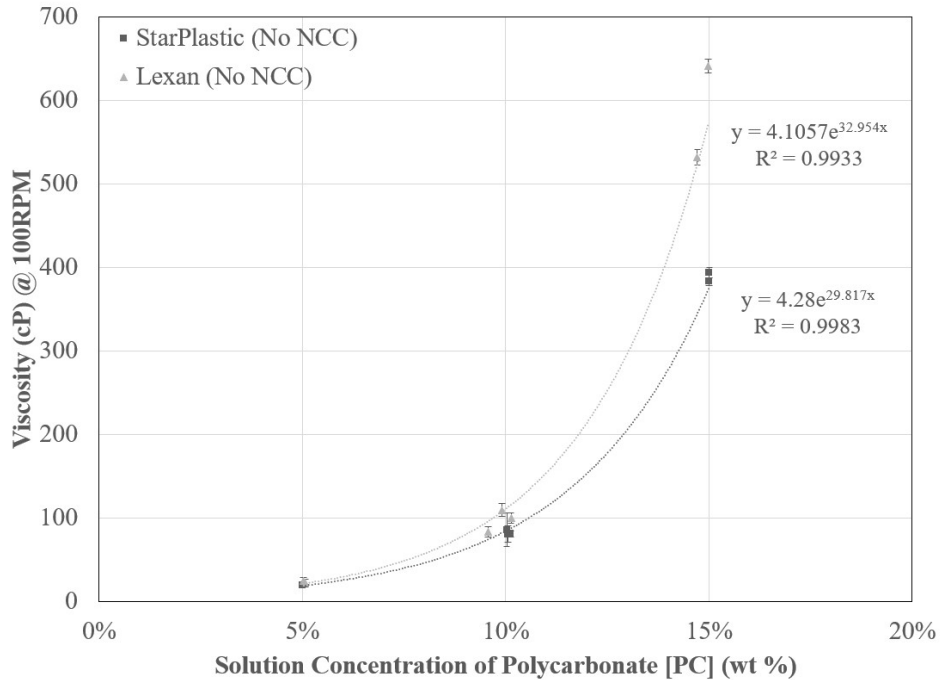


Figure 4.25 - Viscosity versus PC concentration in chloroform solvent for StarPlastic (black) and Lexan (grey) PC for each run of DOE#3

The viscosity does appear to increase with the concentration of PC, following the exponential relationships for StarPlastic and Lexan PC, respectively:

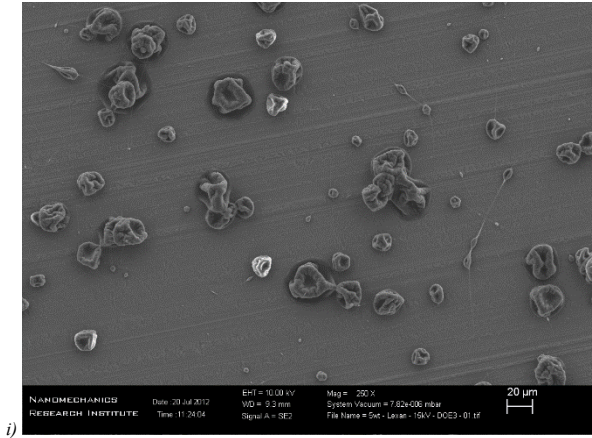
$$\text{Viscosity (cP)} = 4.28 \exp[29.817 [\text{StarPlastic PC}](\text{wt.-%})] \quad (\text{Equation 4.17})$$

$$\text{Viscosity (cP)} = 4.1057 \exp[32.954 [\text{Lexan PC}](\text{wt.-%})] \quad (\text{Equation 4.18})$$

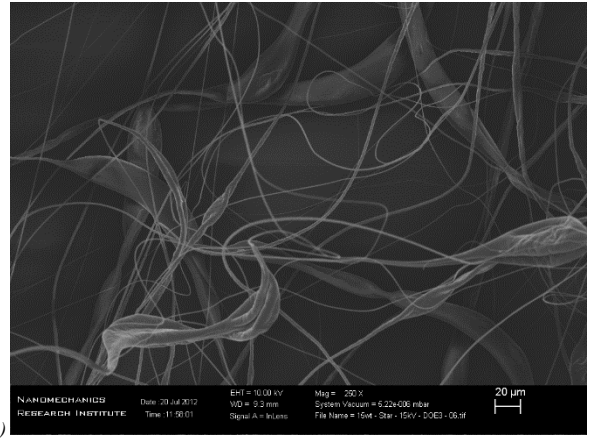
The exponential model for viscosity of StarPlastic PC in chloroform in Equation 4.17, has an R^2 value of only 99.83% suggesting that the model is good at explaining the variability present in the system. Similarly, the viscosity model in Equation 4.18 for Lexan PC, has an R^2 value of 99.33% suggesting that the model also has an acceptable goodness of fit. Both variants of PC have a similar viscosity at lower concentrations, but Lexan PC increases viscosity much faster than StarPlastic with increase of PC concentration, suggesting more polymer chain entanglement present with Lexan PC.

Linear Regression of PC Fiber Diameter

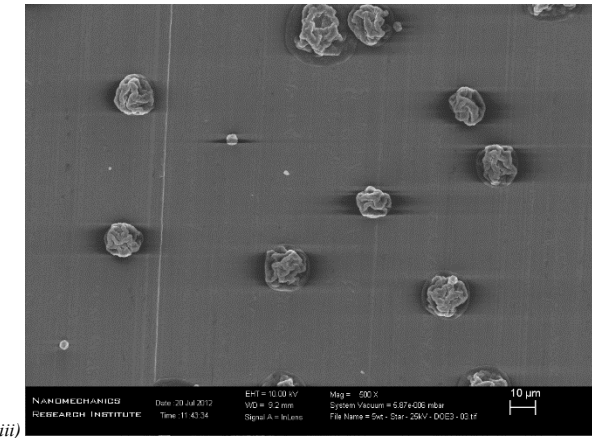
Following the 14 electrospinning runs for the 2^3 full-factorial DOE#3 the collected fiber mats of StarPlastic and Lexan PC fibers were collected for SEM imaging. The images chosen for ImageJ analysis of fiber diameter, bead density, and bead diameter are included in Figure 4.26 for each run.



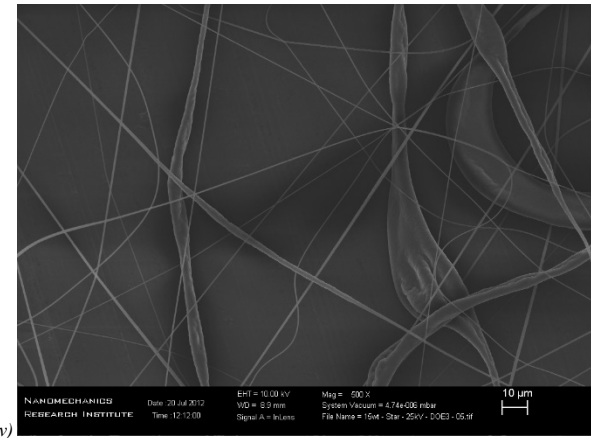
5% | 15 kV | StarPlastic PC



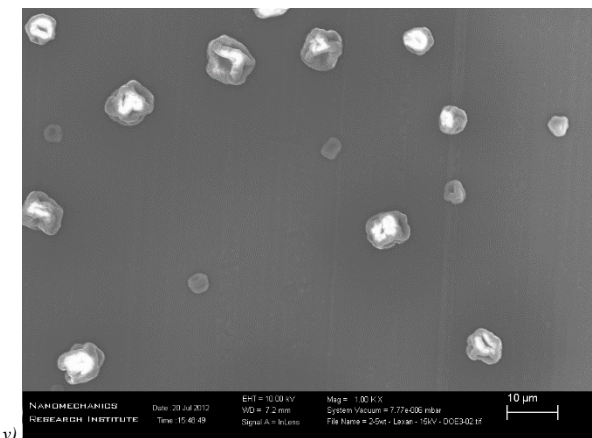
15% | 15 kV | StarPlastic PC



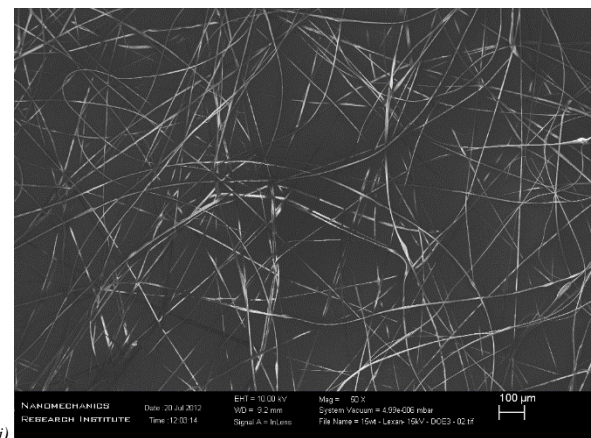
5% | 25 kV | StarPlastic PC



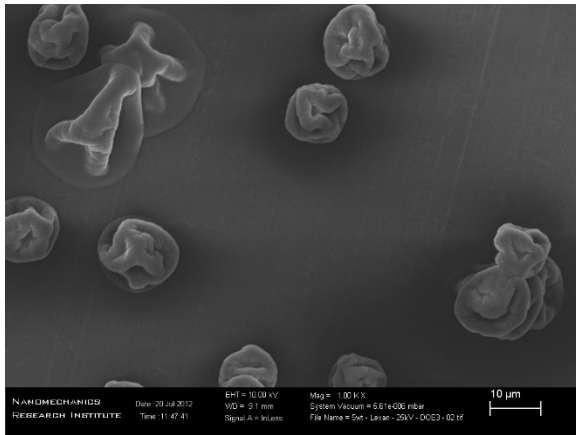
15% | 25 kV | StarPlastic PC



5% | 15 kV | Lexan PC

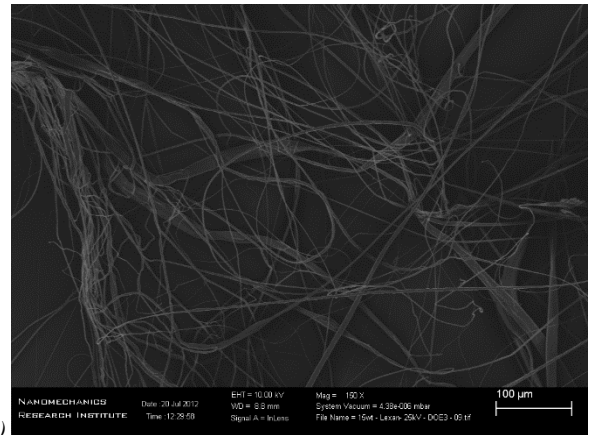


15% | 15 kV | Lexan PC



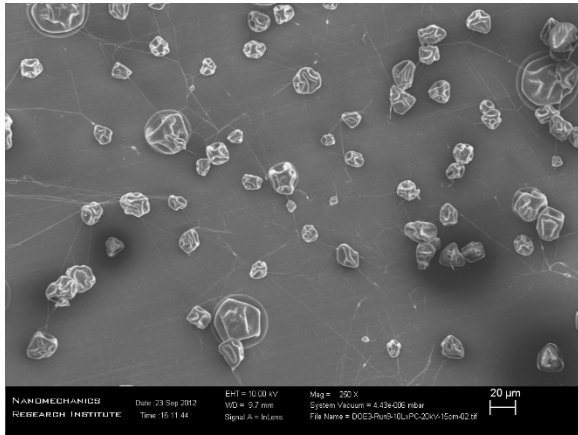
vii)

5% | 25 kV | Lexan PC



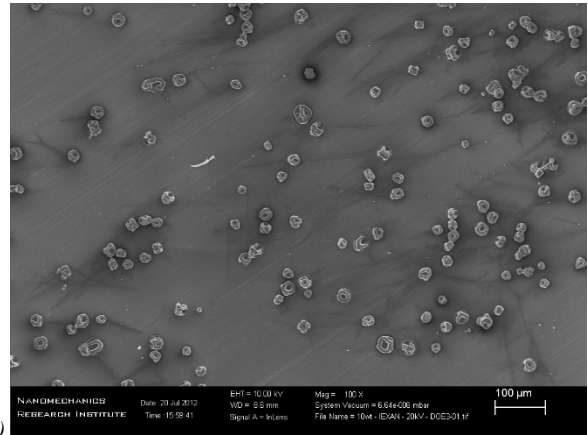
viii)

15% | 25 kV | Lexan PC



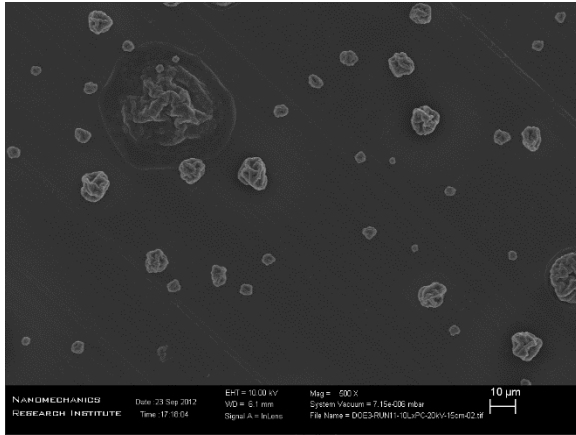
ix)

10% | 20 kV | Lexan PC



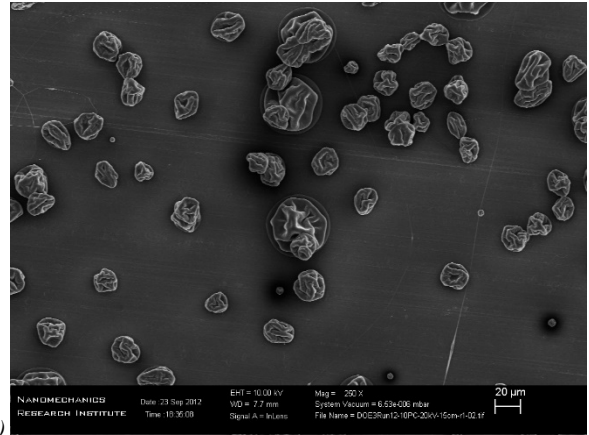
x)

10% | 20 kV | Lexan PC



xi)

10% | 20 kV | Lexan PC



xii)

10% | 20 kV | StarPlastic PC

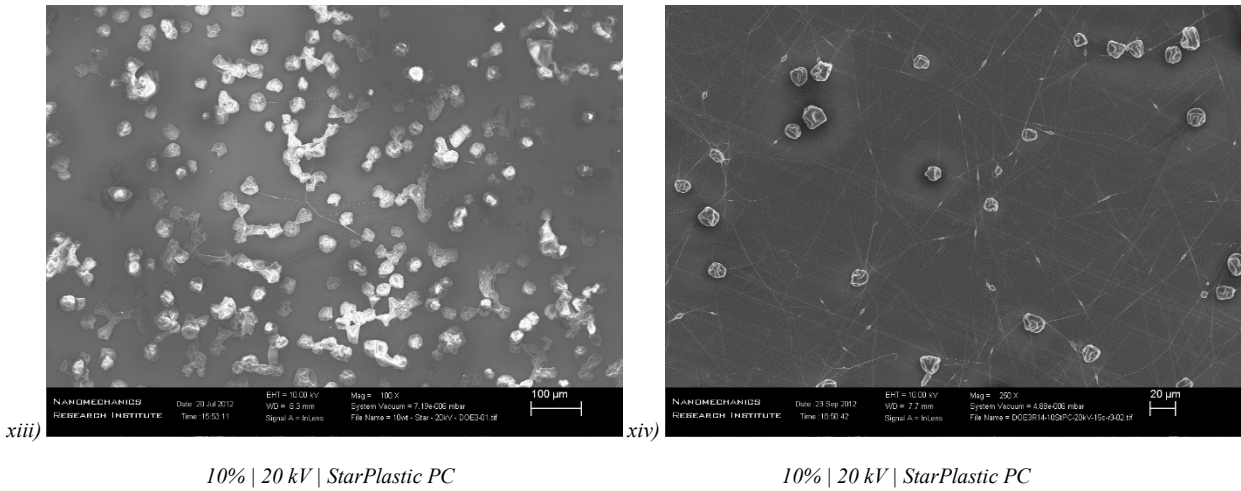


Figure 4.26 - Scanning electron micrographs of StarPlastic and Lexan PC electrospun fibers for each run (i-xiv) of DOE#3

Table 4.28 lists the measured StarPlastic and Lexan PC fiber diameter in micrometers (μm) for each run of DOE#3 including the number of measurements (counts) and the standard deviation.

Table 4.28 - Fiber diameter, standard deviation, and measurement counts for StarPlastic and Lexan PC electrospun fibers made for each run of DOE#3

Run	Fiber Diameter (μm)	St. Dev. (μm)	Counts
1 (1)	0.25	0.13	11
2 (a)	1.06	0.48	9
3 (b)	0	0	0
4 (ab)	0.84	0.45	17
5 (c)	0	0	0
6 (ac)	7.65	0.20	172
7 (bc)	0	0	0
8 (abc)	1.37	0.63	20
9 (0)	0.53	0.20	30
10 (0)	0	0	0
11 (0)	0	0	0
12 (0)	0	0	0
13 (0)	0.58	0.27	8
14 (0)	0.97	0.25	94

The regression equation in uncoded units for fiber diameter of PC nanofibers, with chloroform solvent, as a function of PC concentration (*[PC]*), applied voltage (*Voltage*), and PC Source (*PC Source*) is presented in Equation 4.19. PC Source has a value of 0 for the StarPlastic PC source and 1 for the Lexan PC Source.

$$\begin{aligned}
 \text{Fiber Diameter (um)} = & - 4.60 && \text{(Equation 4.19)} \\
 & + 0.892 [PC] \text{ (wt.\-%)} \\
 & + 0.144 \text{ Voltage (kV)} \\
 & - 4.68 \text{ PC Source} \\
 & - 0.0313 [PC] \text{ (wt.\-%)} * \text{Voltage (kV)} \\
 & + 0.816 [PC] \text{ (wt.\-%)} * \text{PC Source} \\
 & + 0.170 \text{ Voltage (kV)} * \text{PC Source} \\
 & - 0.0316 [PC] \text{ (wt.\-%)} * \text{Voltage (kV)} * \text{PC Source}
 \end{aligned}$$

Backwards elimination of factors was used during regression analysis with $\alpha = 0.1$, no factors were removed. The model has a goodness-of-fit (R^2) value of 88.19%, which suggests a good fit.

The P-values for curvature and lack of fit (LoF) were calculated as 0.035 and 0.035, respectively. This suggests that there may be curvature in the model, but also that the current model does not well represent the relationship between fiber diameter and the factors used.

If the center-point data is included in the model, the regression equation in uncoded units for fiber diameter of PC nanofibers, with chloroform solvent, as a function of PC concentration (*[PC]*), applied voltage (*Voltage*), and PC Source (*PC Source*) is presented in Equation 4.20. PC Source has a value of 0 for the StarPlastic PC source and 1 for the Lexan PC Source.

$$\begin{aligned}
 \text{Fiber Diameter (um)} = & - 4.15 && \text{(Equation 4.20)} \\
 & + 0.892 [PC] \text{ (wt.\-%)} \\
 & + 0.144 \text{ Voltage (kV)} \\
 & - 4.68 \text{ PC Source} \\
 & - 0.03125 [PC] \text{ (wt.\-%)} * \text{Voltage (kV)} \\
 & + 0.816 [PC] \text{ (wt.\-%)} * \text{PC Source} \\
 & + 0.170 \text{ Voltage (kV)} * \text{PC Source} \\
 & - 0.03158 [PC] \text{ (wt.\-%)} * \text{Voltage (kV)} * \text{PC Source} \\
 & - 1.048 \text{ Ct Pt}
 \end{aligned}$$

Backwards elimination of factors was used during regression analysis with $\alpha = 0.1$, no factors were removed. The model has a goodness-of-fit (R^2) value of 95.53%, which suggests a very good fit.

The P-value for lack of fit (LoF) was calculated as 0.540, which now better represents the relationship of the model.

The calculated fitted means for PC/NCC fiber diameter are summarized in Appendix B, Figure B.18 for both models, they are presented in a cube plot which shows the 3-dimensional factor space that the regression model for DOE#3 covers.

Observing the cube plots, including the center-points reduces the residuals and improves the model, except for where no fibers were present (negative values).

Taking a step back, looking directly at the SEM images, it can be seen that fibers are only present in acceptable quantities at high PC concentration level runs (2, 4, 6, and 8) and are of desirable fiber diameter with StarPlastic PC only (runs 2 and 4). Moving forward, higher concentrations of StarPlastic PC should be used in chloroform, and Lexan PC to be avoided.

The contour plot for fiber diameter of electrospun fibers of StarPlastic PC in Chloroform (DOE#3) are included in Figure 4.27. It does not present too much information as the factor levels tested largely produced beading and the areas with fibers were limited. Further exploration with a higher PC concentration range should be explored to produce more pristine fibers, as presented in the next section. Complete results and outputs from the regression analysis in Minitab are included in Appendix B.

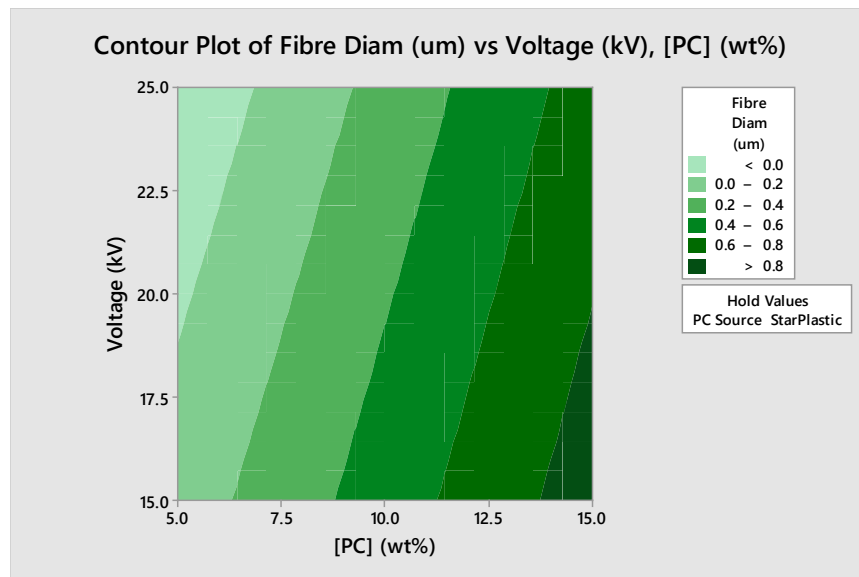


Figure 4.27 - Contour plots for the StarPlastic and Lexan PC electrospun fiber diameter response in DOE#3

Linear Regression of PC Bead Density

Table 4.29 lists the measured bead density in beads per cubic millimeter (beads/mm³) for each run of DOE#3 including the bead count and measurement area used.

Table 4.29 - Bead density and measurement counts for StarPlastic and Lexan PC electrospun fibers made for each run of DOE#3

Run	Bead Count	Measurement Area (mm ²)	Bead Density (beads/mm ²)
1 (1)	58	1.373e-1	422
2 (a)	10	1.373e-1	73
3 (b)	14	3.439e-2	407
4 (ab)	4	3.439e-2	116
5 (c)	15	8.584e-3	1748
6 (ac)	11	3.436	3
7 (bc)	9	8.584e-3	1049
8 (abc)	11	3.881e-1	28
9 (0)	68	1.373e-1	495
10 (0)	135	8.584e-1	157
11 (0)	39	3.439e-2	1134

The regression equation in uncoded units for bead density during the spinning of PC nanofibers, with chloroform solvent, as a function of PC concentration ($[PC]$) and PC Source ($PC\ Source$) is presented in Equation 4.21 (StarPlastic=0, Lexan=1).

$$\begin{aligned}
 \text{Bead Density (beads/mm)} = & + 1342 && (\text{Equation 4.21}) \\
 & - 85.1 [PC] \text{ (wt.\-%)} \\
 & + 621 PC\ Source \\
 & - 53.1 [PC] \text{ (wt.\-%)} * PC\ Source
 \end{aligned}$$

Backwards elimination of factors was used during regression analysis with $\alpha = 0.1$. This elimination removed some factors and co-factors from the response model. The model has a goodness-of-fit (R^2) value of 66.03%, which suggests a poor to ok fit.

The P-values for curvature and lack of fit (LoF) were calculated as 0.900 and 0.540, respectively, suggesting the data does not have curvature and the relationship presented may be adequate.

From the model it can be seen that to reduce beading density, using StarPlastic PC (value of 0) and a higher concentration will reduce beading. This is consistent with the observations from the SEM images.

The calculated fitted means for bead density are summarized in Appendix B, Figure B.19, they are presented in a cube plot which shows the 2-dimensional space that regression model for DOE#3

covers. The fitted means correlate weakly with the measured data, meaning high residual values. Complete results and outputs from the regression analysis in Minitab are included in Appendix B.

Linear Regression of PC Bead Diameter

Table 4.30 lists the measured bead diameter in micrometers (μm) for each run of DOE#3 including the number of measurements (counts) and the standard deviation.

Table 4.30 - Bead diameter, standard deviation, and measurement counts for StarPlastic and Lexan PC electrospun fibers made for each run of DOE#3

Run	Bead Diameter (μm)	St. Dev. (μm)	Counts
1 (1)	27.36	13.57	23
2 (a)	12.84	9.58	47
3 (b)	22.00	11.11	64
4 (ab)	12.88	6.91	22
5 (c)	7.58	1.53	50
6 (ac)	0	0	0
7 (bc)	18.70	8.10	49
8 (abc)	15.77	6.53	63
9 (0)	15.95	10.10	120
10 (0)	28.64	8.36	130
11 (0)	10.79	4.57	203

Backwards elimination of factors was used during regression analysis with $\alpha = 0.1$. This removed all terms from the model. The data collected was not sufficient enough to produce a working model. Complete results and outputs from the regression analysis in Minitab are included in Appendix B.

DOE#4 - DDSA-modified Nanocrystalline Cellulose (cNCC) + Chloroform

The different factors tested for the second DOE along with their low, high, and center point levels are summarized in Table 4.1. The 3 factors examined (with low, center, and high levels) include: StarPlastic PC concentration, [PC], (12.5, 15, 17.5 wt.-%); applied voltage, V, (20, 25, 30 kV); and gap distance, d, (20, 25, 30 cm). For the 2^3 -factorial design of experiment, there are 3 factors being adjusted between 2 different levels, high and low. As well as 3 center-point replicates, resulting in 11 total runs for a full-factorial design of experiment.

Each sample included 2 wt.-% of cNCC incorporated with the StarPlastic PC to observe any different effects with its inclusion.

Table 4.31 summarizes the target and actual concentrations calculated for PC in solution and cNCC in solid for each run based on the recorded masses.

Table 4.31 - DOE#4 target and actual concentration calculations for StarPlastic PC and cNCC in chloroform for each 11 runs

Std.	[PC] Tar.	[PC] Act.	[cNCC] Tar.	[cNCC] Act.
Order	(%TOTAL)	(%TOTAL)	(%SOLID)	(%SOLID)
1 (1)	12.5	12.5	2	2.0
2 (a)	17.5	17.4	2	2.0
3 (b)	12.5	12.5	2	2.0
4 (ab)	17.5	17.4	2	2.0
5 (c)	12.5	12.4	2	2.1
6 (ac)	17.5	17.4	2	2.0
7 (bc)	12.5	12.5	2	2.0
8 (abc)	17.5	17.4	2	2.0
9 (0)	15	14.9	2	2.0
10 (0)	15	14.9	2	2.0
11 (0)	15	15.0	2	2.0

(Note: All percentages listed are with respect to weight (w/w) of noted system; total, solid, etc.)

2 wt.-% cNCC/PC in Chloroform Solvent Formulation Performance

The measured turbidity, in Nephelometric Turbidity Units (NTU), and viscosity, in centipoise (cP) with standard deviation, for each run of the DOE#4 are summarized in Table 4.32 as well as the actual concentration of PC and cNCC.

Table 4.32 - Turbidity and viscosity measurements for StarPlastic PC and cNCC in chloroform for each run of DOE#4

Run	[PC] Act. (%TOTAL)	[cNCC] Act. (%SOLID)	Turbidity (NTU)	Viscosity (cP) [100 RPM]	St. Dev. (cP)
1 (1)	12.5	2.0	19.6	179	15
2 (a)	17.4	2.0	27.4	1134	132
3 (b)	12.5	2.0	25.9	208	15
4 (ab)	17.4	2.0	30.9	987	132
5 (c)	12.4	2.1	21.1	198	15
6 (ac)	17.4	2.0	35.4	833	132
7 (bc)	12.5	2.0	24	212	15
8 (abc)	17.4	2.0	57.7	1080	132
9 (0)	14.9	2.0	22.4	480	16
10 (0)	14.9	2.0	26.8	492	16
11 (0)	15.0	2.0	26.1	460	16
Pure Chloroform	-	-	0.1	0.5	-

Figure 4.28 plots 10 turbidity measurements of StarPlastic PC and 2-wt.-% cNCC in chloroform, taken from each run of DOE#4. The trend from StarPlastic PC in DOE#3 is included for comparison, as the main difference in parameters is the inclusion of cNCC as well as covering a lower range of PC concentration.

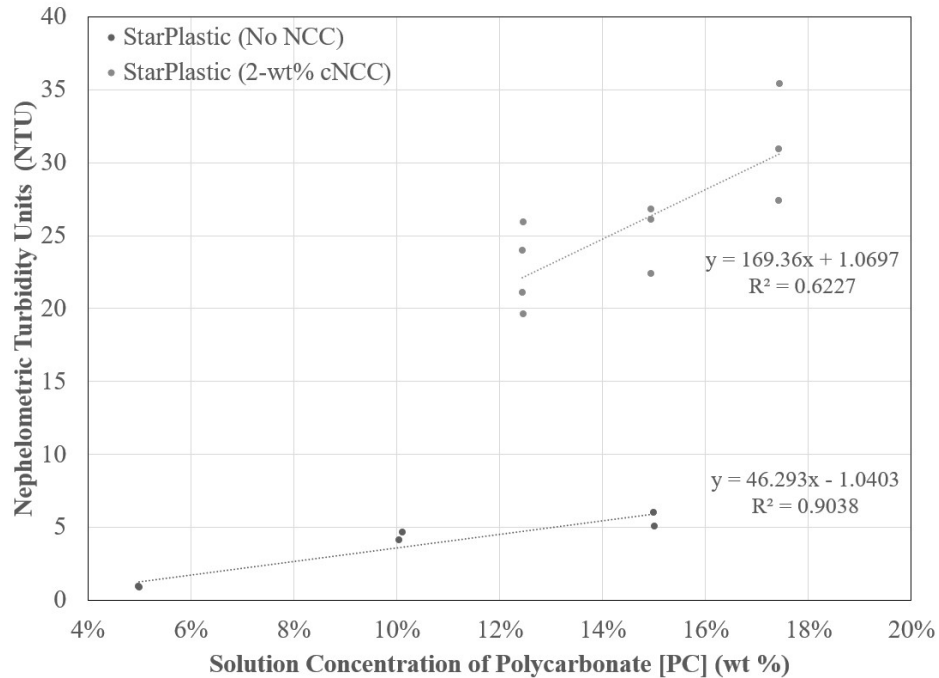


Figure 4.28 - Turbidity versus StarPlastic PC concentration in chloroform solvent with (DOE#4, grey) and without (DOE#3, black) 2-wt.-% cNCC incorporation for all runs

The turbidity does appear to increase with the concentration of PC, following the linear relationship:

$$\text{Turbidity (NTU)} = 169.36 [\text{StarPlastic PC}] + 1.0697 \quad (\text{Equation 4.22})$$

The linear model for turbidity of PC in chloroform in Equation 4.22, has an R^2 value of 62.27% suggesting that the model is ok at explaining the variability present in the system.

The turbidity of PC appears to increase about 169.4 NTU for each percent addition of PC in the overall solution. The intercept at 0% PC has a turbidity of about 1.1 NTU which is close to the measured turbidity of pure chloroform. The larger increase in turbidity with the addition of NCC is observed similar to the THF/DMF system studied in DOE#1 and DOE#2.

Figure 4.29 plots 10 viscosity measurements of StarPlastic PC and 2-wt.-% cNCC in chloroform, taken from each run of DOE#4. The trend from StarPlastic PC in DOE#3 is included for comparison, as the main difference in parameters is the inclusion of cNCC as well as covering a lower range of PC concentration.

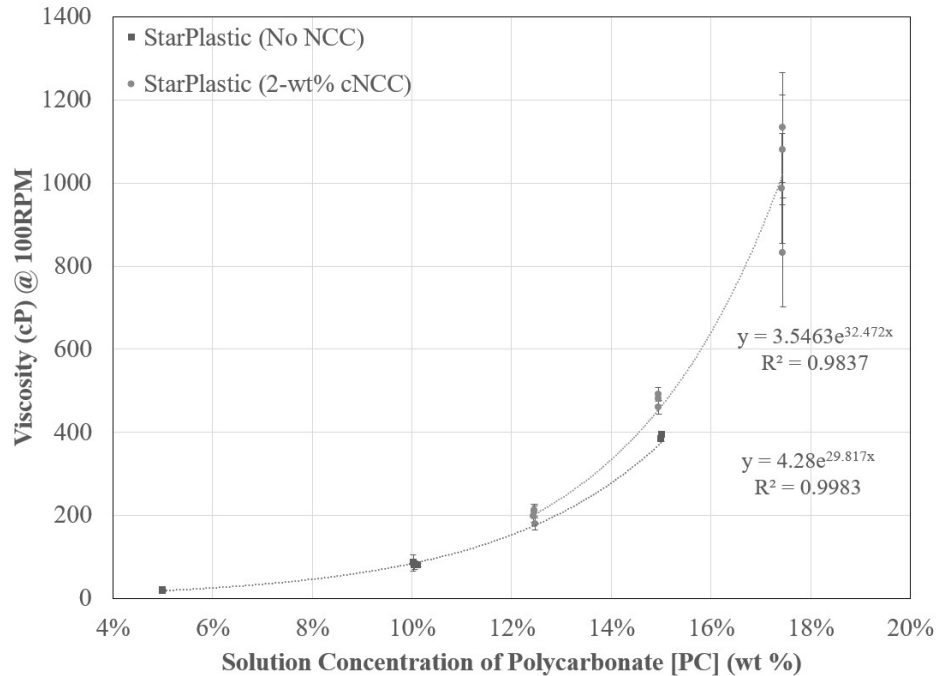


Figure 4.29 - Viscosity versus StarPlastic PC concentration in chloroform solvent with (DOE#4, grey) and without (DOE#3, black) 2-wt.-% cNCC incorporation for all runs

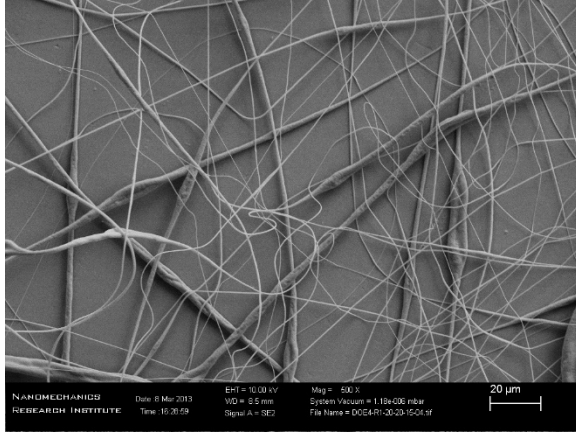
The viscosity does appear to increase with the concentration of PC, following the exponential relationship:

$$\text{Viscosity (cP)} = 3.5463 \exp[32.472 [\text{PC}](\text{wt.-%})] \quad (\text{Equation 4.23})$$

The exponential model for viscosity of StarPlastic PC in chloroform in Equation 4.23, has an R^2 value of only 98.37% suggesting that the model is good at explaining the variability present in the system. The comparison of the viscosity of PC in chloroform (without NCC) is also included in Figure 4.29. It can be seen that the addition of cNCC slightly increases the viscosity of the solution.

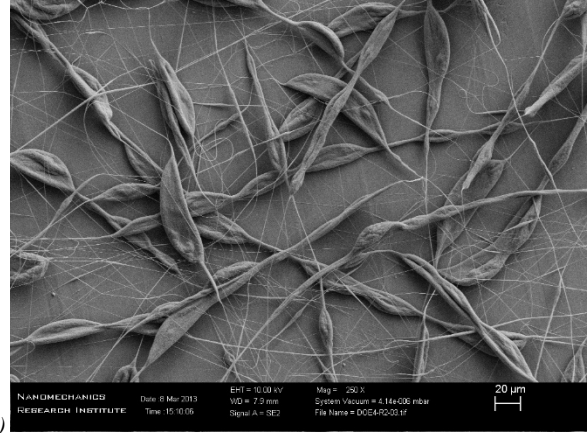
Linear Regression of 2 wt.-% cNCC/PC Fiber Diameter

Following the 11 electrospinning runs for the 2^3 full-factorial DOE#4 the collected fiber mats of 2 wt.-% NCC/PC fibers were collected for SEM imaging. The images chosen for ImageJ analysis of fiber diameter, bead density, and bead diameter are included in Figure 4.30 for each run.



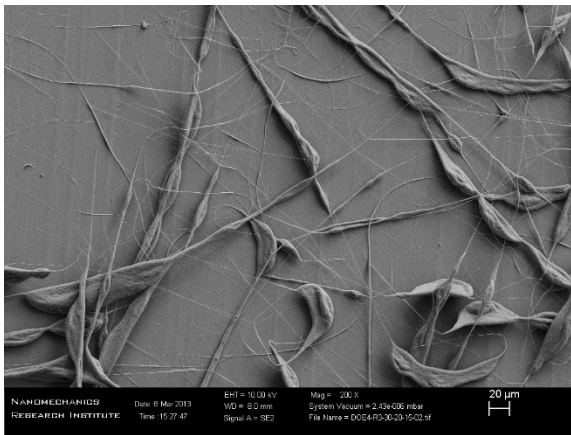
i)

12.5% | 20 kV | 20 cm



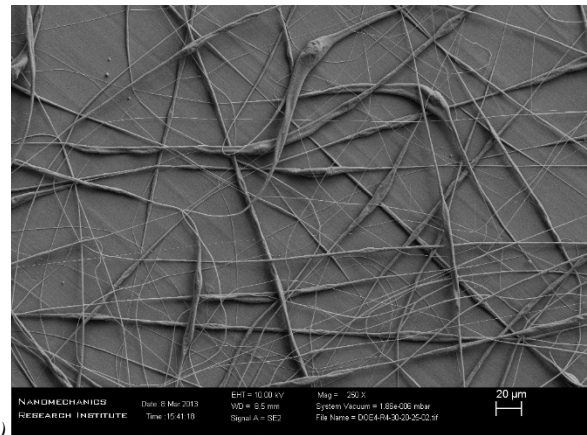
ii)

17.5% | 20 kV | 20 cm



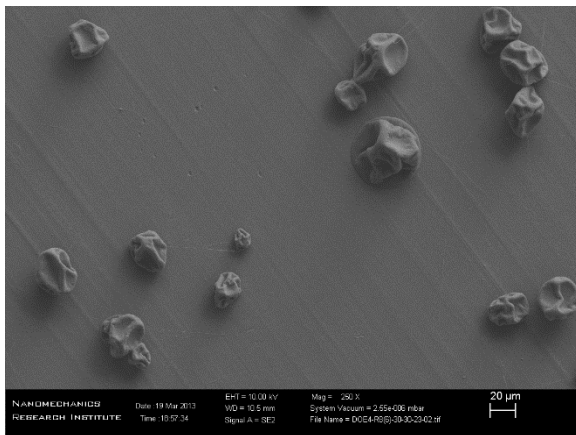
iii)

12.5% | 30 kV | 20 cm



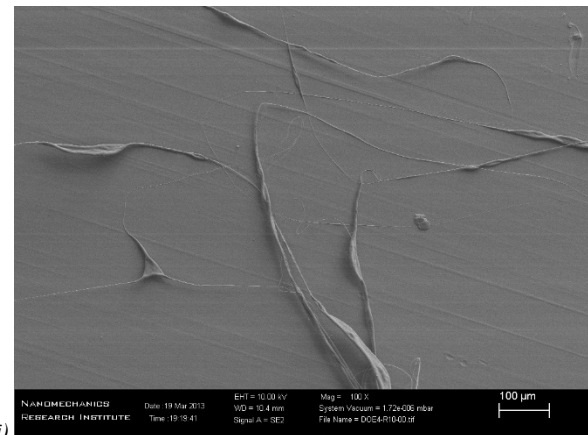
iv)

17.5% | 30 kV | 20 cm



v)

12.5% | 20 kV | 30 cm



vi)

17.5% | 20 kV | 30 cm

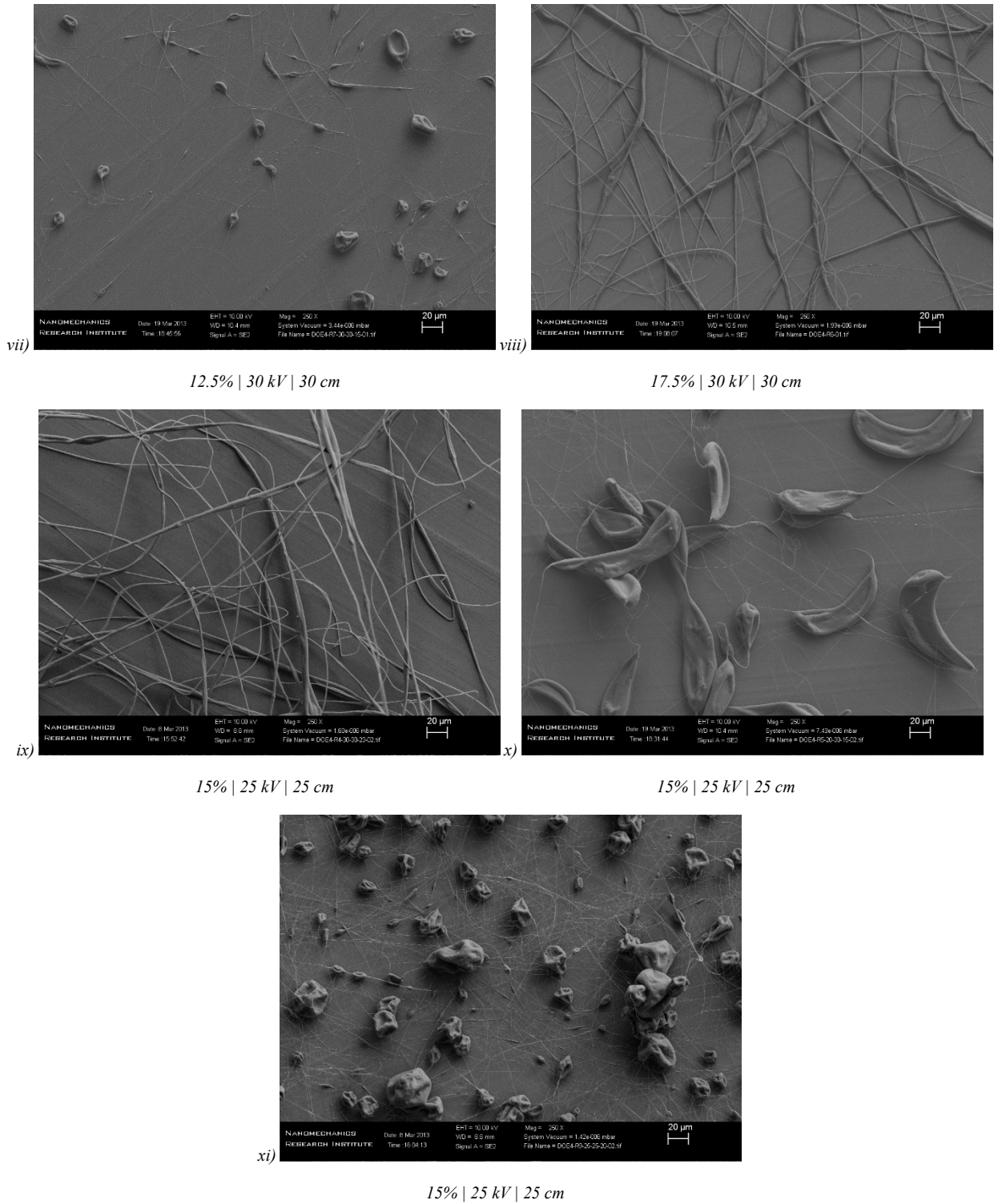


Figure 4.30 - Scanning electron micrographs of StarPlastic and Lexan PC and cNCC electrospun fibers for each run (i-xi) of DOE#4

Table 4.33 lists the measured StarPlastic PC and 2 wt.-% cNCC fiber diameter in micrometers (μm) for each run of DOE#4 including the number of measurements (counts) and the standard deviation.

Table 4.33 - Fiber diameter, standard deviation, and measurement counts for StarPlastic PC and cNCC electrospun fibers made for each run of DOE#4

Run	Fiber Diameter (μm)	St. Dev. (μm)	Counts
1 (1)	1.94	1.85	188
2 (a)	1.03	0.80	55
3 (b)	0.54	0.23	59
4 (ab)	3.44	2.58	169
5 (c)	0.33	0.09	4
6 (ac)	8.26	5.18	28
7 (bc)	0.44	0.34	34
8 (abc)	3.69	3.10	82
9 (0)	3.54	2.42	168
10 (0)	0.48	0.16	27
11 (0)	0.38	0.17	179

The regression equation in uncoded units for fiber diameter of 2% cNCC/PC nanofibers, with chloroform solvent, as a function of PC concentration ($[PC]$) is presented in Equation 4.24.

$$\mathbf{Fiber\ Diameter\ (\mu m) = - 7.69} \quad (\text{Equation 4.24})$$

$$\mathbf{+ 0.658 [PC] (wt.-%)}$$

Backwards elimination of factors was used during regression analysis with $\alpha = 0.1$. This elimination removed all factors and co-factors from the response model except PC concentration. The model has a goodness-of-fit (R^2) value of 36.50%, which suggests a poor fit.

The P-values for curvature and lack of fit (LoF) were calculated as 0.507 and 0.452, respectively, suggesting the data does not have curvature and the relationship presented may be adequate. Again, this reiterates that a PC concentration is an important factor influencing the diameter, more so than gap distance and voltage (and all co-factors) in this case.

The calculated fitted means for PC/cNCC fiber diameter are summarized in Appendix B, Figure B.25, they are presented in a cube plot which shows the 3-dimensional space that the regression model for DOE#4 covers. As the model has $[PC]$ as the only factor the fitted means do

not well match the measured data and the residuals are high. Complete results and outputs from the regression analysis in Minitab are included in Appendix B.

Linear Regression of 2 wt.-% cNCC/PC Bead Density

Table 4.34 lists the measured bead density in beads per cubic millimeter (beads/mm²) for each run of DOE#4 including the bead count and measurement area used.

Table 4.34 - Bead density and measurement counts for StarPlastic PC and cNCC electrospun fibers made for each run of DOE#4

Run	Bead Count	Measurement Area (mm²)	Bead Density (beads/mm²)
1 (1)	13	3.439e-2	378
2 (a)	42	1.373e-1	306
3 (b)	49	1.373e-1	357
4 (ab)	24	1.373e-1	175
5 (c)	15	1.373e-1	109
6 (ac)	12	8.584e-1	14
7 (bc)	44	1.373e-1	320
8 (abc)	24	1.373e-1	175
9 (0)	16	1.373e-1	117
10 (0)	21	1.373e-1	153
11 (0)	116	1.373e-1	845

Backwards elimination of factors was used during regression analysis with $\alpha = 0.1$. This removed all terms from the model. The data collected was not sufficient enough to produce a working model. Complete results and outputs from the regression analysis in Minitab are included in Appendix B.

Linear Regression of 2 wt.-% cNCC/PC Bead Diameter

Table 4.35 lists the measured bead diameter in micrometers (μm) for each run of DOE#4 including the number of measurements (counts) and the standard deviation.

Table 4.35 - Bead diameter, standard deviation, and measurement counts for StarPlastic PC and cNCC electrospun fibers made for each run of DOE#4

Run	Bead Diameter (μm)	St. Dev. (μm)	Counts
1 (1)	0	0	0
2 (a)	13.14	6.08	247
3 (b)	10.21	5.38	74
4 (ab)	0	0	0
5 (c)	39.52	12.56	63
6 (ac)	0	0	0
7 (bc)	8.69	4.89	36
8 (abc)	0	0	0
9 (0)	0	0	0
10 (0)	20.41	7.24	115
11 (0)	18.18	8.85	179

Backwards elimination of factors was used during regression analysis with $\alpha = 0.1$. This removed all terms from the model. The data collected was not sufficient enough to produce a working model. Complete results and outputs from the regression analysis in Minitab are included in Appendix B.

4.5 – Conclusions

Novel Contributions

In the present work, regression models were developed for the successful production of polycarbonate (PC) and Nanocrystalline Cellulose (NCC) electrospun nanofibers in two solvent systems, chloroform and 60:40 (w/w) mixture of tetrahydrofuran (THF) and n,n-dimethylformamide (DMF). For each system, the electrospun mat morphology was modeled through responses for fiber diameter, bead diameter, and bead density. Full-factorial design of experiments were explored for each response to model the fiber diameter as a function of the PC concentration, NCC concentration, applied voltage, and gap distance. Center-point measurements were conducted to test the curvature of the model as well as to account for this curvature in the model. Solution properties were also documented, including the turbidity and viscosity and liner relationships were developed for them.

The results of the effects and responses presented here can be used as a basis for any researcher to explore the electrospinning of polycarbonate fibers with Nanocrystalline Cellulose. As the

electrospinning process is complex and can be influenced by many factors, including combined factors, the knowledge from this study provides an excellent groundwork for this material system.

Challenges

The primary challenge in this work involved managing the variance introduced through the electrospinning process. As there are many variables influential on the final electrospun fiber morphology, it is important to control the noise of the system as best as possible to achieve significant results. For the majority of the experimentation, this involved: following a particular schedule, often electrospinning as soon as possible following sample preparation; minimizing any error in formulation and mixing of solutions; repeatable collection of nanofiber mats, as well as sample collection, preparation, and imaging of experimental specimens. Although controlled as best as possible, some anomalies have still appeared. In particular, the center point replicates of DOE#4 - DDSA-modified Nanocrystalline Cellulose (cNCC) + Chloroform observed in Figure 4.30 show significant variance even though the experimental conditions were identical. This demonstrates that not only that electrospinning in volatile solvents like chloroform at room temperature is difficult to control, but that all possible variables for electrospinning must be considered carefully to achieve desired results.

Adding the results for the work with polycarbonate and Nanocrystalline Cellulose to the body of work for electrospinning will allow fellow researchers to observe the particular factors I chose to explore and how I chose to explore them. This will give confidence to their overall experimental setup and ideally help them predict to a better certainty what to expect as an output, as at the moment there are no universal models for electrospinning of fibers.

Chapter 5. Modeling of Nanofibers of Polyamide-6,6 Containing DDSA Modified Nanocrystalline Cellulose Prepared by Electrospinning for Coating Applications

5.1 – Introduction

Numerous researchers have published on the electrospinning of polyamide nanofibers. For example, the effects of formulation and processing conditions [4], [153], [154], polyamide chain composition [154], internal structure and crystallinity [155], and solvent system and electrode polarity [156], [157]. Composite nanofibers of polyamide have also been produced including reinforcements of montmorillonite nanoclays [158] as well as natural materials like chitosan [159], [160]. Many of the applications explored for electrospun PA nanofibers include biomedical and wound dressings [159], and filtration [154]. Joshi et al. have successfully electrospun nylon-6 nanofibers reinforced with cellulose acetate and analyzed morphology and biomimetic effects for potential biomedical applications [161]. Sobolciak et al. have also explored the electrospinning of co-polyamide 6,12 modified with cellulose nanocrystals and they observed enhanced mechanical properties as well as increased hydrophobicity for oil and water separation [162].

Objective

At present, there is limited peer reviewed research on electrospinning of DDSA modified Nanocrystalline Cellulose and at the time of writing, there is no literature that includes the electrospinning of DDSA modified NCC (coded cNCC herein), including the use of a polyamide-6,6 (PA-6,6) thermoplastic matrix. This work will explore new developments in electrospinning of PA-6,6 reinforced with modified cNCC and the resulting effect on the fiber diameter of resulting fibers. A 2³ full factorial design of experiments has been developed to explore the fiber diameter effects of polyamide-6,6 concentration ([PA 6,6]), applied voltage, and gap distance of polyamide-6,6 composite nanofibers reinforced with 4-wt.% of cNCC. The objective is to create a regression model for fiber diameter of PA 6,6 and cNCC nanofibers that can be used to identify critical experimental formulation and performance parameters influencing the final fiber product.

The inclusion of cNCC in the polyamide 6,6 matrix will improve the mechanical properties of the final electrospun mat compared to PA 6,6 alone. This will be explored through the creation of transparent coatings with improved surface properties. The coatings will be comprised of embedded electrospun nanofibers in an epoxy matrix; prepared via rotating drum collection and compression forming methods. Transparency and surface mechanical properties will be tested for PA 6,6, and PA 6,6 reinforced with cNCC, as well as a comparison to the polycarbonate (PC) and PC reinforced with NCC (un-modified) electrospun fibers presented in earlier work. PA 6,6 and PC are choice engineering thermoplastics for applications that require strength, high modulus and

toughness in high-temperature environments, such as light shrouding and engine covers in automotive applications. Weinan et al. has demonstrated a 31% increase in tensile strength and a 27% increase in Young's modulus with a 3 wt.-% addition of CNC within a polycarbonate film [163]. Improving the surface properties of these parts further through the use of electrospinning can increase the products lifetime as well as expand current usage applications, like windows and screens.

5.2 – Materials

Polyamide-6,6

Polyamide-6,6, also commonly referred to as nylon 6,6, is a polyamide containing two monomers each containing 6 carbons: hexamethylenediamine and adipic acid. Over half of PA 6,6's world production is used in the form of fibers while the other half is primarily engineering thermoplastics. PA 6,6 is used for its high mechanical strength, rigidity, chemical and thermal resistance and has primary applications in rope, textiles, carpeting, and molded parts. The repeating unit for polyamide-6,6 can be seen in Figure 5.1.

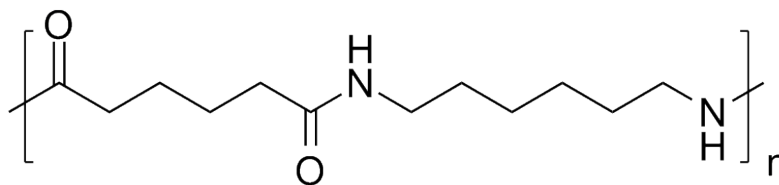


Figure 5.1 - Repeating unit of Polyamide-6,6

The grade of nylon, also referred to as polyamide-6,6 (coded PA 6,6) used for electrospinning, was sourced from a previous graduate student in Leonardo Simon's research group. The nylon was in pellet form with a brownish-translucent color.

StarPlastic PC743R Polycarbonate

See Chapter 4, 4.2 – Materials, StarPlastic PC743R Polycarbonate.

CelluForce DDSA Modified Nanocrystalline Cellulose

See Chapter 4, 4.2 – Materials, CelluForce DDSA Modified Nanocrystalline Cellulose.

CelluForce Ultra Nanocrystalline Cellulose

See Chapter 4, 4.2 – Materials, CelluForce Ultra Nanocrystalline Cellulose.

Formic Acid, 90%

Reagent grade formic acid (coded FA in this study) was used in the electrospinning study and was sourced from Caledon Labs with product code 3841-1 and purity of 89.8 to 90.2% (measured by assay). The specifications noted on the 2.5 L bottle include a density of 1.970 to 1.200 kg/L (at 25 °C), molecular weight of 46.03 g/mol, viscosity of 1.54 to 1.58 cP and a methyl formate concentration of less than 0.2%. The production lot of the FA is 82311. No further modification or purification was made to the solvent; it was used as received.

5.3 – Methods

Polyamide-6,6 and 4 wt.-% cNCC in 90% Formic Acid 2³ Full Factorial Design of Experiments

A 2³ full-factorial DOE was run to explore and model an electrospun composite nanofiber system of polyamide-6,6 (PA-6,6) reinforced with DDSA-modified Nanocrystalline Cellulose (cNCC). PA-6,6 in a formic acid solvent has shown excellent results in literature and through preliminary experimentation. This DOE will determine the effect of different process and formulation factors on the resulting PA-6,6-cNCC fibers synthesized through electrospinning. The factors being analyzed include (a) concentration of PC in solvent solution [PC], (b) voltage applied during electrospinning process (Voltage), as well as (c) the gap distance between needle tip and collector (Gap Distance). Each sample included 4 wt.-% of cNCC incorporated with the PA 6,6.

The different factors tested for the DOE along with their low, high, and center point levels are summarized in Table 5.1 as well as visually presented in 3-dimensional space as a cube plot in Appendix B, Figure B.29. Using the coding scheme, each of the 11 experiments for the first DOE could be represented as shown in Appendix B,

Table B.12.

Table 5.1 - 2³ full factorial DOE including the three different factors tested (coded a, b, and c) with their low (-1), high (+1), and center point (0) values for PA-6,6-cNCC

Factors	Low (-1)	High (+1)	Centre Point (0)
a = [PA] (wt.-%)	10	20	15
b = Voltage (kV)	15	25	20
c = Gap Distance (cm)	15	25	20

Through the course of running this DOE, several experimental parameters were held constant and are summarized in Table 5.2 below.

Table 5.2 - Experimental process and formulation parameter constants for PA-6,6-cNCC electrospinning

Process Constants	Fixed value
Collector	VWR Aluminum Pan
Feed Rate	1.5 mL/hour
Run time	30 s
Formulation Constants	Fixed value
Solvent System	Chloroform
Polymer	PA 6,6
cNCC Concentration	4 wt.-% of solid mass (no solvent)

The different responses to be analyzed through this DOE include turbidity, viscosity, fiber diameter, bead diameter and bead density. The turbidity and viscosity are only a function of the (a) factor of [PC] concentration, whereas each of the other responses are a function of all three factors: a, b, and c.

To run each experiment for the desired time, and to account for any losses through the process, a roughly 30 g solution was prepared for each experimental run. The mass of polyamide-6,6, cNCC, and formic acid for each experiment were calculated as shown in Appendix B,

Table B.12.

Regression will be used to calculate the model parameters and to determine effects of parameters and whether they are statistically significant.

Experimental Setup

The electrospinning equipment and experimental procedures are described in detail in Chapter 4 – Modeling Nanofibers of Polycarbonate Containing Nanocrystalline Cellulose Prepared by Electrospinning in Different Solvent Systems, 4.3 – Methods, 4.3.3 – Experimental Setup.

Surface Properties of Transparent Coatings using Electrospun PA 6,6 and PC Composite Fibers Including NCC

Part of the objective for electrospinning the composite nanofiber mats was to create coatings for transparent abrasion and scratch resistance applications, such as a window, headlight shroud, or screen coating. Various fabrication techniques were explored to create transparent coatings with embedded nanofibers. Larger quantities of PC, PC/NCC, PA-6,6, and PA-6,6/cNCC fibers were collected using the results from the DOE experimentation to achieve desired fiber characteristics. The electrospun PC and PC/NCC fibers were primarily collected using a rotating drum collector, whereas the PA-6,6 and PA-6,6/cNCC nanofibers were collected using a framing technique observed in literature. The rotating drum and frame collectors allow for large uniform collection (over 1 hour) of fibers and easy removal for creating the coatings. Lexan XL10 Polycarbonate sheets were used as the substrate for the coatings application as Lexan is transparent and typically

used in window or barrier applications. SDI Epoxy was used as a binder to adhere the collected fibers to the Lexan sheet.

Preparation of Coatings using Electrospun Fibers

Several processing techniques were explored with the goal of creating a transparent coating that incorporated the electrospun fibers to improve surface characteristics. The progression of these processing techniques is described below.

To test the framing a fiber mat, several experiments were run in progression as small revisions were made each iteration due to observations in the experiment.

- 1) The first attempt was attempted using a small cardboard frame that was placed directly onto the aluminum foil of the collector.
- 2) This was then tested at different angles from the normal to see if by angling the frame it could decrease the effective projected distance across the frame.
- 3) Also explored was increasing the distance between the cardboard frame and the aluminum collector.
- 4) A glass slide with an affixed cardboard frame was then placed upon the collector plate.
- 5) A glass slide with an affixed paper frame was then placed upon the collector plate.
- 6) Spinning directly onto a glass slide.
- 7) Spinning directly onto a polycarbonate slide.
- 8) Spinning directly onto a PLA slide.
- 9) Spinning directly onto PET transparency sheets.
- 10) Spinning directly onto a cardboard slide.

Electrospun Fibers Placed into Spin Coated Epoxy

The first technique that was explored was spin coating of uncured epoxy over the Lexan sheet and then placing the electrospun fibers into the thin wet epoxy film before allowing to cure. This process could create a thin epoxy layer to bind the nanofibers to the Lexan sheet to create the coating, the hypothesis was that the epoxy would wet the fibers completely to create a transparent uniform surface. The epoxy was spin coated onto 4 cm square cutouts of Lexan sheet at 500 RPM for approximately 15 seconds. This process was not immediately successful as the placed fibers did not completely wet with epoxy and significantly decreased the transparency of the sheet. It was also difficult to manually place the fibers in a uniform way.

Direct Electrospinning into Epoxy / Rotating Drum Collector

After learning that it was very difficult to manually lay the fibers flat onto the epoxy layer, directly spinning fibers onto the epoxy was explored. A rotating drum collector was used for the PC and PC/NCC specimens to improve the uniformity of the collected fiber mat.

The rotating drum collector was built in-house for this application and is depicted in Figure 5.2. A hollow aluminum cylinder (6.5 cm diameter and 12.5 cm long) was centered and affixed to a wooden dowel that was spun using a laboratory mixer. The mixer was located outside of the electrospinner enclosure and had the ability to control RPM. The aluminum drum was grounded at one edge using a brush like a commutator in a brushed DC motor.

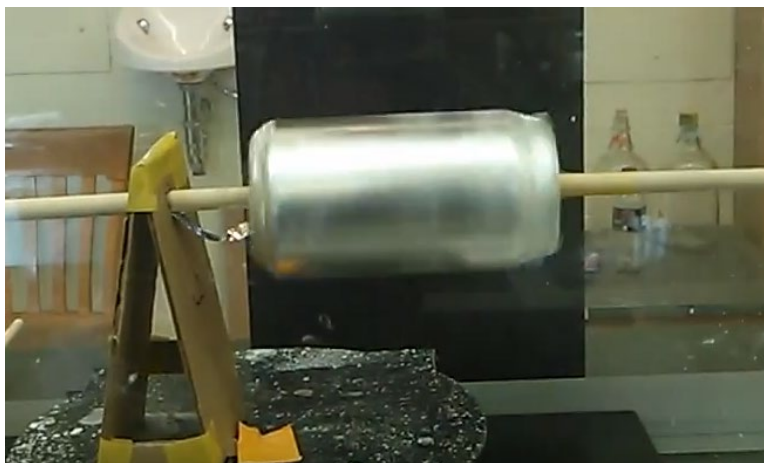


Figure 5.2 - Rotating drum collector built in-house for testing coating applications

Epoxy was spin coated onto the 4 cm Lexan squares at 500 RPM for 15 seconds and the square were then affixed to the surface of the rotating drum. The drum was set to rotate at a speed of 100 RPM for all collections. Fibers were collected on the rotating drum collector for 45, 60 and 90 minutes; all other variables remained constant between the three runs.

Experiments were tested using a rotating drum collector to collect axially oriented polymer nanofibers.

The procedure used to test a low-cost rotating drum collector was as follows.

- 1) A standard 355 mL aluminum can was used as the base of the drum and it was mounted on a 2 cm thick wooden dowel.
- 2) The wooden dowel was mounted to a high-powered lab stirrer, similar to a drill that can apply a consistent set rotation speed.
- 3) The portion of the wooden dowel in contact with the aluminum can had been covered in aluminum tape to create an electrical contact with a small section of the dowel.
- 4) The grounding lead was modified to have a small copper tip that, under spring loading, remained in contact with the aluminum tape on the dowel while rotating.
- 5) The setup could achieve rotation speeds of approximately 900 RPM before some wobble started due to small weight imbalances in the rod and can.

Testing of adding a cardboard frame to the surface of the aluminum can was also explored.

Compression of Electrospun Fibers into Epoxy

One final method was tested for creating transparent composite nanofiber coatings, taking the first method of placing the electrospun fibers into epoxy and adding a compression load at the end. Two low surface energy substrates were tested, PTFE (Teflon) as well as HDPE sheets. Using these sheets, and a load of 1 lb. (0.45 kg), the fibers are compressed into the epoxy and the epoxy permeates the pores of the fiber mat to achieve complete submersion. The load was added for the entirety of the epoxy cure process, approximately 24 hours. Because of the non-stick nature of the compression substrates, they could be easily removed after the curing process to reveal the nanofiber/epoxy coated Lexan PC substrate.

The expected morphology of the coatings prepared via the rotating drum technique and the compression technique are compared to an ideal outcome in Figure 4.13.

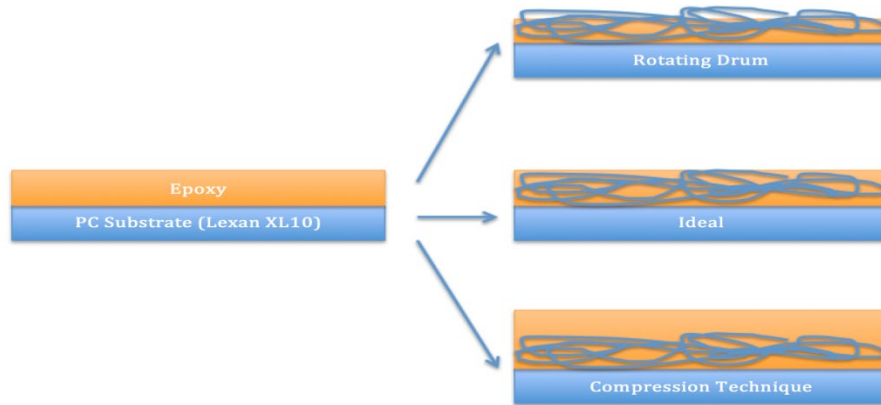


Figure 5.3 - Schematic representation of the cross section profile of fiber deposition of transparent coatings made via rotating drum and compression techniques compared to a desired (ideal) profile

Characterization of Coatings using Electrospun Fibers

Surface Hardness using Vickers Microhardness Testing

Vickers Microhardness testing was used to verify that the addition of nanofibers does in fact increase the surface hardness relative to the epoxy as well as the Lexan PC substrate. This would be a good indication of an increase in surface hardness making the coatings an ideal candidate for abrasion prone applications. This method measures the materials ability to resist plastic deformation from a standard load. Although typically used for metals, the method adapted well to test the surface coatings created here.

Vickers microhardness testing works by depressing a pyramidal diamond indenter tip at a specified load into the surface of the specimen for a loading time of 10 seconds. Figure 4.14 shows a typical Vickers hardness tester, a schematic of the test parameters, and a close-up image of a diamond indenter. Using the applied load and a cross sectional measurement of the indentation left on the surface, the Vickers Pyramid Number (HV) can be calculated using Equation 5.1. Seven indentation measurements were made for each specimen, and the average and standard deviation are reported. The surface coating should be around 2.5 times thicker than the indentation diameter to avoid substrate effects on the HV. [164]

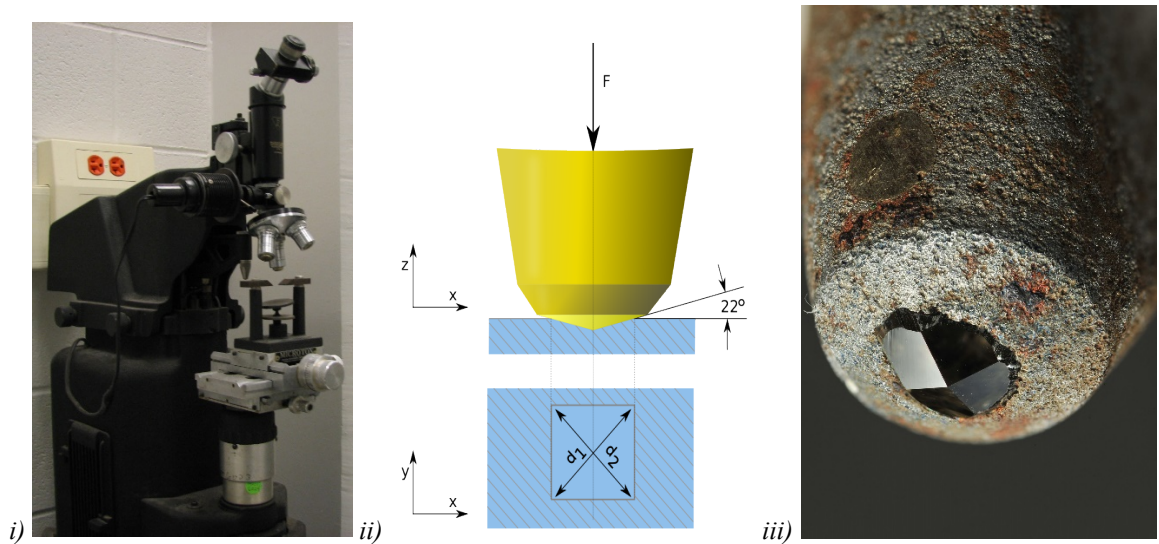


Figure 5.4 - i) A typical Vickers hardness tester, ii) schematic of the test parameters, and iii) a close-up image of the diamond indenter used to indent surface [165]

$$HV \approx 0.1891 F/d^2 \quad (\text{Equation 5.1})$$

The HV value can be compared between samples using the same load, but if different loads are used, the values should be converted to SI units by multiplying by specific gravity, g , to get a surface hardness measurement in MPa.

Optical Transparency using UV-Vis Spectroscopy

Another spectroscopic technique used to characterize the composite nanofiber reinforced coatings is ultraviolet-visible spectroscopy (or UV-Vis for short). This technique probes within the electromagnetic range of ultraviolet and visible light. This technique will help characterize the transparency and any changes to the color of the nanocomposite that may occur due to the addition of the nanofibers and coatings. The visible spectrum is between about 400 to 700 nm wavelengths, and maximum visible transmission in this region is desirable for our transparent nanocomposite.

Each of the prepared specimens was probed by an Ultraviolet-Visible spectrum analyzer or UV-Vis. The UV-Vis used for this study was a Bruker Vector 22 UV-Vis-NIR System. The sample was scanned over a range of 350 to 700 nm to quantify the transparency of the composite materials. A monochromator in the UV-Vis analyzer allows the system to sweep over a range of wavelengths, one at a time, shining the light through the specimen. A detector measures the amount of light passing through the sample and can determine the absorption of light by the sample as well as the percent transmittance of the light passing through the sample and striking the detector. The specimen can be compared to a reference sample (baseline) or no reference (just air) to get the total transmittance of the sample. This process is depicted in a schematic diagram in Figure 4.15.

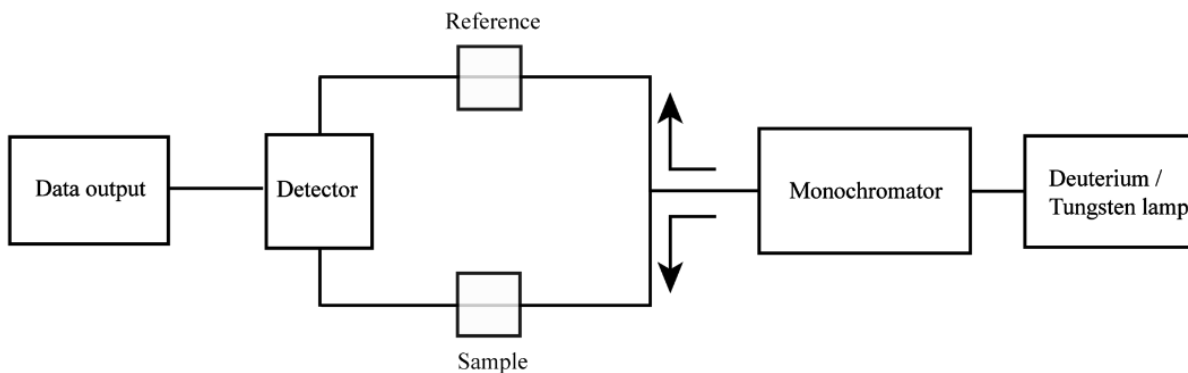


Figure 5.5 - Schematic representation of light path within a UV-Vis spectrometer apparatus [166]

5.4 – Results and Discussion

2³ Full Factorial Design of Experiments for Fiber Diameter

Table 5.3 summarizes the target and actual concentrations for PA 6,6 in solution and cNCC in solid for each experimental run of the DOE based on the recorded masses.

Table 5.3 - Target and actual concentration calculations for PA 6,6 and cNCC in formic acid for each 11 runs

Std. Order	[PA 6,6] Tar. (%TOTAL)	[PA 6,6] Act. (%TOTAL)	[cNCC] Tar. (%SOLID)	[cNCC] Act. (%SOLID)
1 (1)	10	10.1	4	4.0
2 (a)	20	20.0	4	4.0
3 (b)	10	10.0	4	4.1
4 (ab)	20	20.0	4	4.0
5 (c)	10	10.0	4	4.0
6 (ac)	20	20.0	4	4.0
7 (bc)	10	10.0	4	4.0
8 (abc)	20	20.0	4	4.0
9 (0)	15	15.0	4	4.0
10 (0)	15	15.0	4	4.0
11 (0)	15	15.0	4	4.0

(Note: All percentages listed are with respect to weight (w/w) of noted system; total, solid, etc.)

4 wt.-% cNCC/PA 6,6 in Formic Acid Solvent Formulation Performance

The measured turbidity, in Nephelometric Turbidity Units (NTU), and viscosity, in centipoise (cP) with standard deviation, for each run of are summarized in Table 5.4 as well as the actual concentration of PA 6,6 and cNCC.

Table 5.4 - Turbidity and viscosity measurements for PA 6,6 and cNCC in formic acid for each run

Run	[PA 6,6] Act. (%TOTAL)	[cNCC] Act. (%SOLID)	Turbidity (NTU)	Viscosity (cP) [20 RPM]	St. Dev. (cP)
1 (1)	10.1	4.0	264	1002	138
2 (a)	20.0	4.0	2831	16650	2576
3 (b)	10.0	4.1	268	990	138
4 (ab)	20.0	4.0	1202	18720	2576
5 (c)	10.0	4.0	355	1182	138
6 (ac)	20.0	4.0	650	17250	2576
7 (bc)	10.0	4.0	260	846	138
8 (abc)	20.0	4.0	542	12690	2576
9 (0)	15.0	4.0	369	5051	374
10 (0)	15.0	4.0	346	4373	374
11 (0)	15.0	4.0	384	4439	374
Pure Formic Acid	-	-	0.1	0.6	-

Figure 5.6 plots the 11 turbidity measurements of PA 6,6 and 4-wt.-% cNCC in Formic Acid, taken from each run.

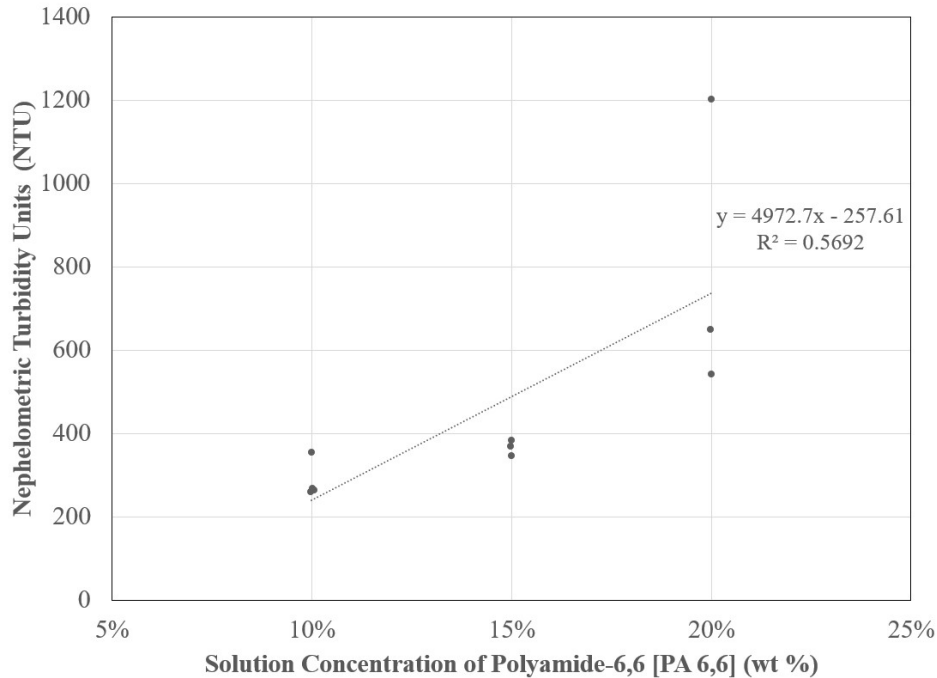


Figure 5.6 - Turbidity versus PA 6,6 concentration in formic acid solvent for each run

The turbidity does appear to increase with the concentration of PA 6,6, following the linear relationship:

$$\text{Turbidity (NTU)} = 4972.7 [\text{PA 6,6}] - 257.61 \quad (\text{Equation 5.2})$$

The linear model for turbidity of PA 6,6 in formic acid in Equation 5.2, has an R^2 value of 56.92% suggesting that the model is poor to ok at explaining the variability present in the system. The measurement for run 2 was removed as it appeared to be an outlier.

The turbidity of 4 wt.-% PA solutions appear to increase about 4972 NTU for each percent addition of PA 6,6 in the overall solution. The intercept at 0% PC has a negative turbidity of about -257.61 NTU which is not close to the measured turbidity of formic acid. There appears to be a large variance in turbidity measured for samples at high loadings of PA 6,6, leading to a poor ability to make a prediction model.

Figure 5.7 plots the 11 viscosity measurements of PA 6,6 and 4-wt.-% cNCC in formic acid, taken from each run.

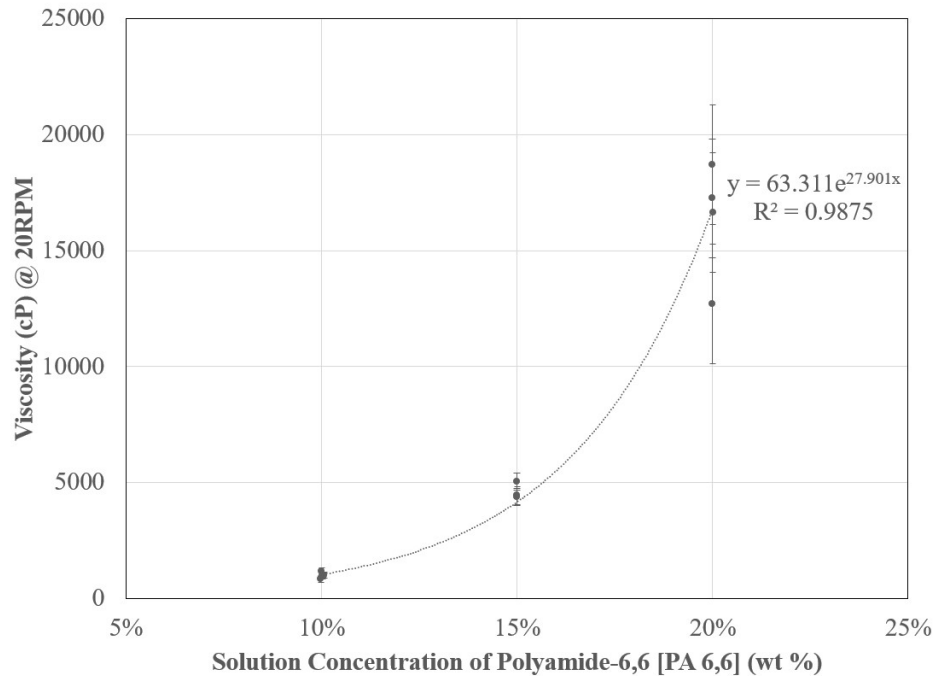


Figure 5.7 - Viscosity versus PA 6,6 concentration in formic acid solvent for each run

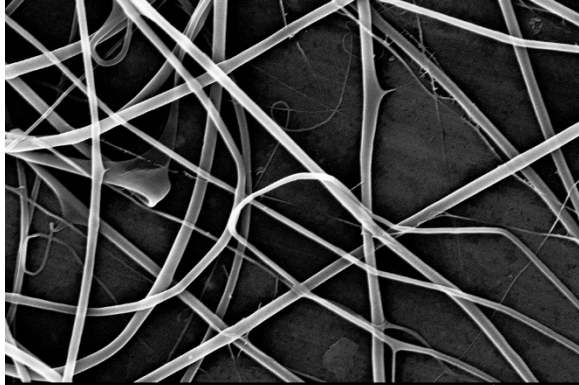
The viscosity does appear to increase with the concentration of PA 6,6, following the exponential relationship:

$$\text{Viscosity (cP)} = 63.311 \exp[27.901 [\text{PA 6,6}](\text{wt.-%})] \quad (\text{Equation 5.3})$$

The exponential model for viscosity of PA 6,6 in chloroform in Equation 5.3, has an R^2 value of only 98.75% suggesting that the model is good at explaining the variability present in the system.

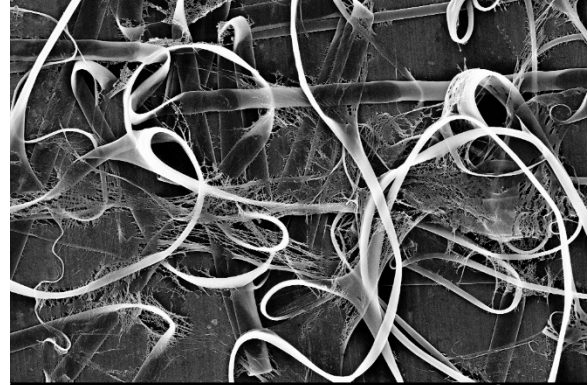
Linear Regression of 4 wt.-% cNCC/PA 6,6 Fiber Diameter

Following the 11 electrospinning runs for the 2^3 full-factorial DOE the collected fiber mats of 4 wt.-% cNCC/PA 6,6 fibers were collected for SEM imaging. The images chosen for ImageJ analysis of fiber diameter, bead density, and bead diameter are included in Figure 5.8 for each run.



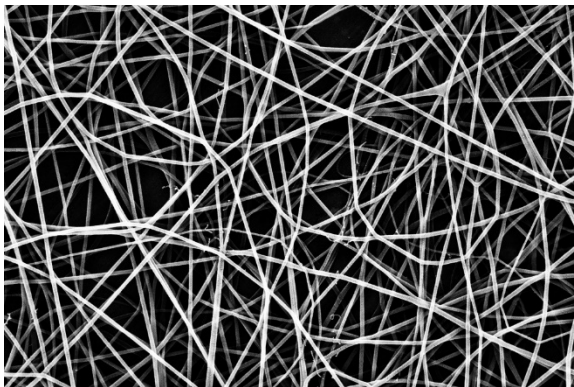
i)

10% | 15 kV | 15 cm



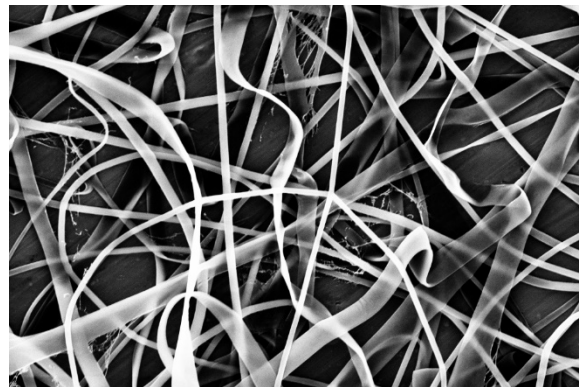
ii)

20% | 15 kV | 15 cm



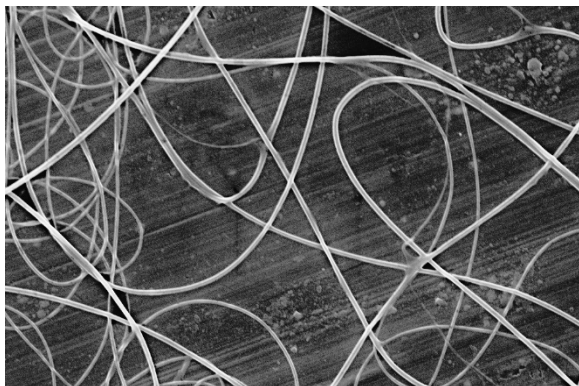
iii)

10% | 25 kV | 15 cm



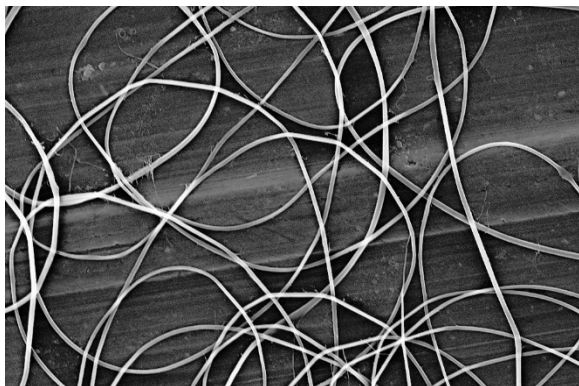
iv)

20% | 25 kV | 15 cm



v)

10% | 15 kV | 25 cm



vi)

20% | 15 kV | 25 cm

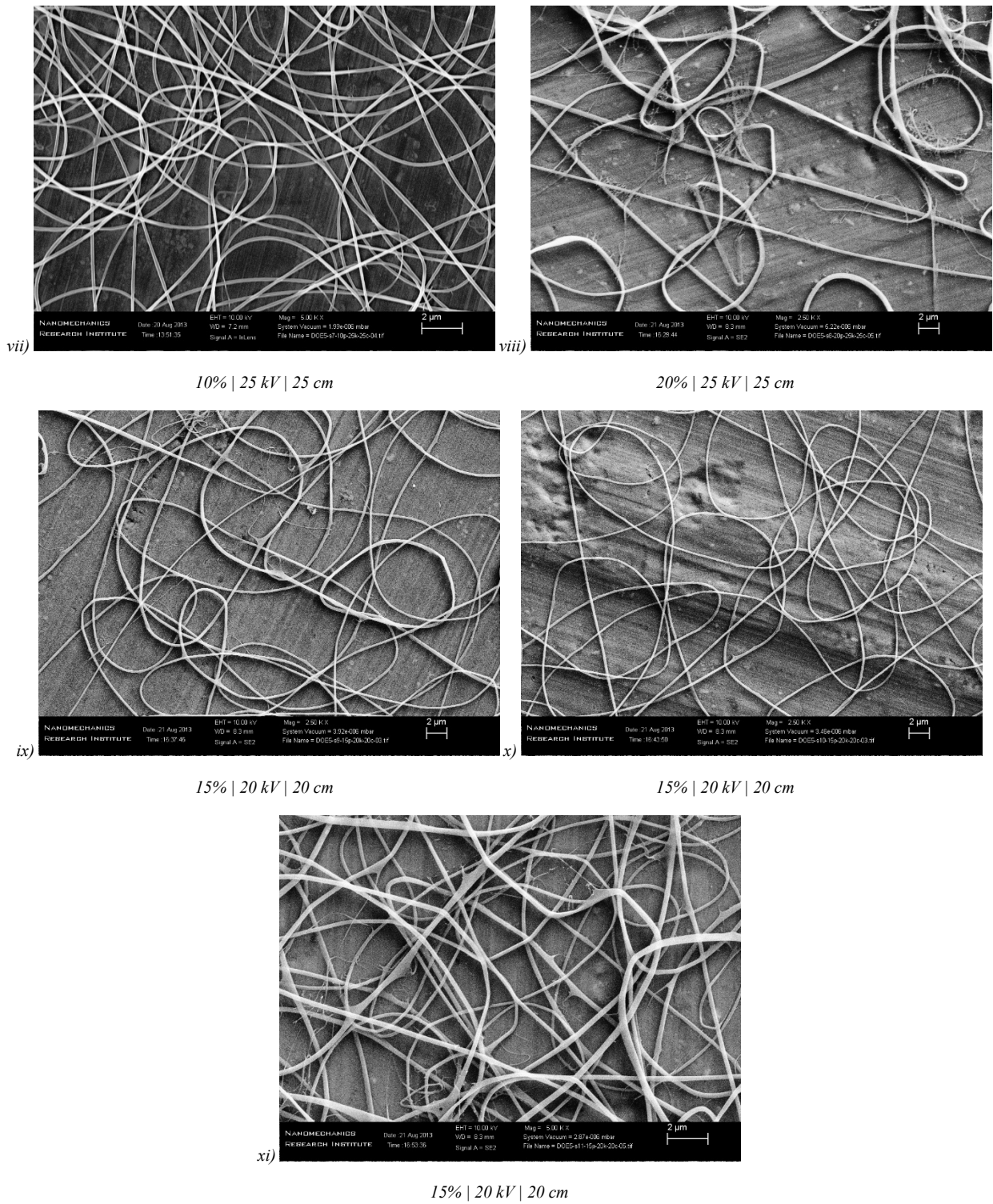


Figure 5.8 - Scanning electron micrographs of PA 6,6 and cNCC electrospun fibers for each DOE run (i-xi)

Table 5.5 lists the measured PA 6,6 and 2 wt.-% cNCC fiber diameter in micrometers (μm) for each run of DOE including the number of measurements (counts) and the standard deviation.

Table 5.5 - Fiber diameter, standard deviation, and measurement counts for PA 6,6 and cNCC electrospun fibers made for each run of DOE

Run	Fiber Diameter (nm)	St. Dev. (nm)	Counts
1 (1)	190	130	162
2 (a)	833	994	108
3 (b)	79	23	96
4 (ab)	1187	663	106
5 (c)	187	46	87
6 (ac)	333	94	173
7 (bc)	166	36	37
8 (abc)	376	164	75
9 (0)	259	88	54
10 (0)	234	43	196
11 (0)	220	81	100

The regression equation in uncoded units for fiber diameter in nanometers of 4% cNCC/PA 6,6 nanofibers, with formic acid solvent, as a function of PA 6,6 concentration ($[PA]$) and gap distance ($Gap\ Distance$) is presented in Equation 5.4.

$$\begin{aligned}
 \text{Fiber Diameter (nm)} = & - 1899 && \text{(Equation 5.4)} \\
 & + 192.1 [PA] \text{ (wt.-%)} \\
 & + 73.9 \text{ Gap Distance (cm)} \\
 & - 6.97 [PA] \text{ (wt.-%)} * \text{Gap Distance (cm)}
 \end{aligned}$$

Backwards elimination of factors was used during regression analysis with $\alpha = 0.1$. This elimination removed some factors and co-factors from the response model. The model has a goodness-of-fit (R^2) value of 87.37%, which suggests a good fit.

The P-values for curvature and lack of fit (LoF) were calculated as 0.049 and 0.022, respectively. This suggests that there may be curvature in the model, but also that the current model does not well represent the relationship between fiber diameter and the factors used.

If the center-point data is included in the model, the regression equation in uncoded units for fiber diameter of 4% cNCC/PA 6,6 nanofibers, with formic acid solvent, as a function of PA 6,6 concentration ($[PA]$) and gap distance ($Gap\ Distance$) is presented in Equation 5.5.

$$\begin{aligned}
 \text{Fiber Diameter (nm)} = & + 774 && \text{(Equation 5.5)} \\
 & - 21.2 [PA] \text{ (wt.\-%)} \\
 & - 131.2 \text{ Voltage (kV)} \\
 & - 24.2 \text{ Gap Distance (cm)} \\
 & + 10.67 [PA] \text{ (wt.\-%)} * \text{Voltage (kV)} \\
 & + 1.05 [PA] \text{ (wt.\-%)} * \text{Gap Distance (cm)} \\
 & + 4.908 \text{ Voltage (kV)} * \text{Gap Distance (cm)} \\
 & - 0.4012 [PA] \text{ (wt.\-%)} * \text{Voltage (kV)} * \text{Gap Distance (cm)} \\
 & - 181.3 \text{ Ct Pt}
 \end{aligned}$$

Backwards elimination of factors was used during regression analysis with $\alpha = 0.1$, no factors were removed. The model has a goodness-of-fit (R^2) value of 99.93%, which suggests a very good fit.

The calculated fitted means for PA 6,6/cNCC fiber diameter are summarized in Appendix B, Figure B.30 for both response models, they are presented in a cube plot which shows the 3-dimensional space that the regression model for this DOE covers.

It can be seen in the cube plots that both models have relatively low residuals, but the model that includes the center-point data fits the measured data nearly perfectly, giving residuals of almost 0 for all measurements. This confirms the excellent power of DOE regression modelling for analyzing electrospun fibers when the fibers are pristine with limited beading and artifacts.

The contour plot for fiber diameter of electrospun fibers of PA 6,6/cNCC in formic acid are included in Figure 5.9. The contour plot shows that the fiber diameter can be fine-tuned for this material system easily by adjusting the $[PA]$ or the gap distance individually of each other. Complete results and outputs from the regression analysis in Minitab are included in Appendix B.

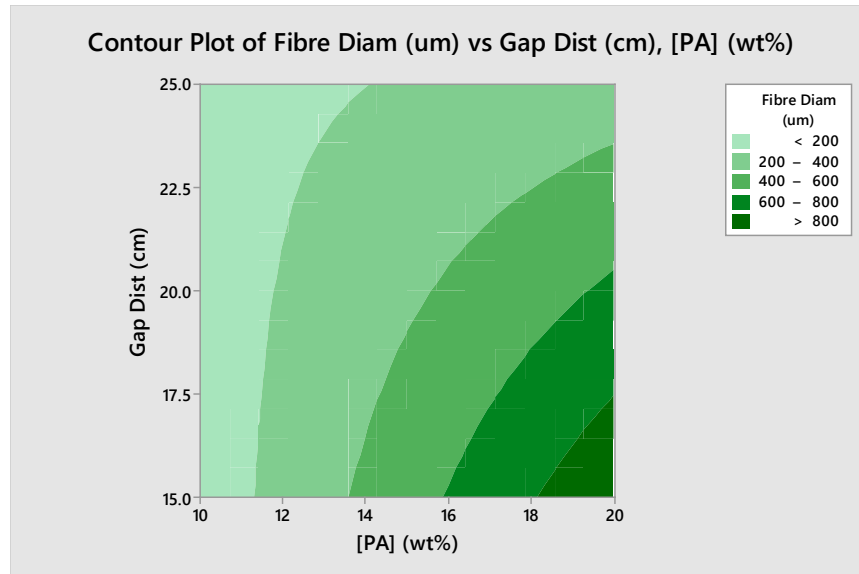


Figure 5.9 - Contour plots for the PA 6,6 and cNCC electrospun fiber diameter response

Surface Properties of Transparent Coatings using Electrospun Composite Fibers

A proof of concept study was completed to test the validity of the fiber systems studied in this thesis in transparent coatings with improved surface properties. If successful, these coatings would offer a lightweight alternative to some glass and shrouding applications. Figure 5.10 shows the typical fiber morphology of each PC, NCC/PC, PA 6,6, and cNCC/PA 6,6 electrospun fibers prepared for the application study using methods outlined in Chapter 3 through 5.

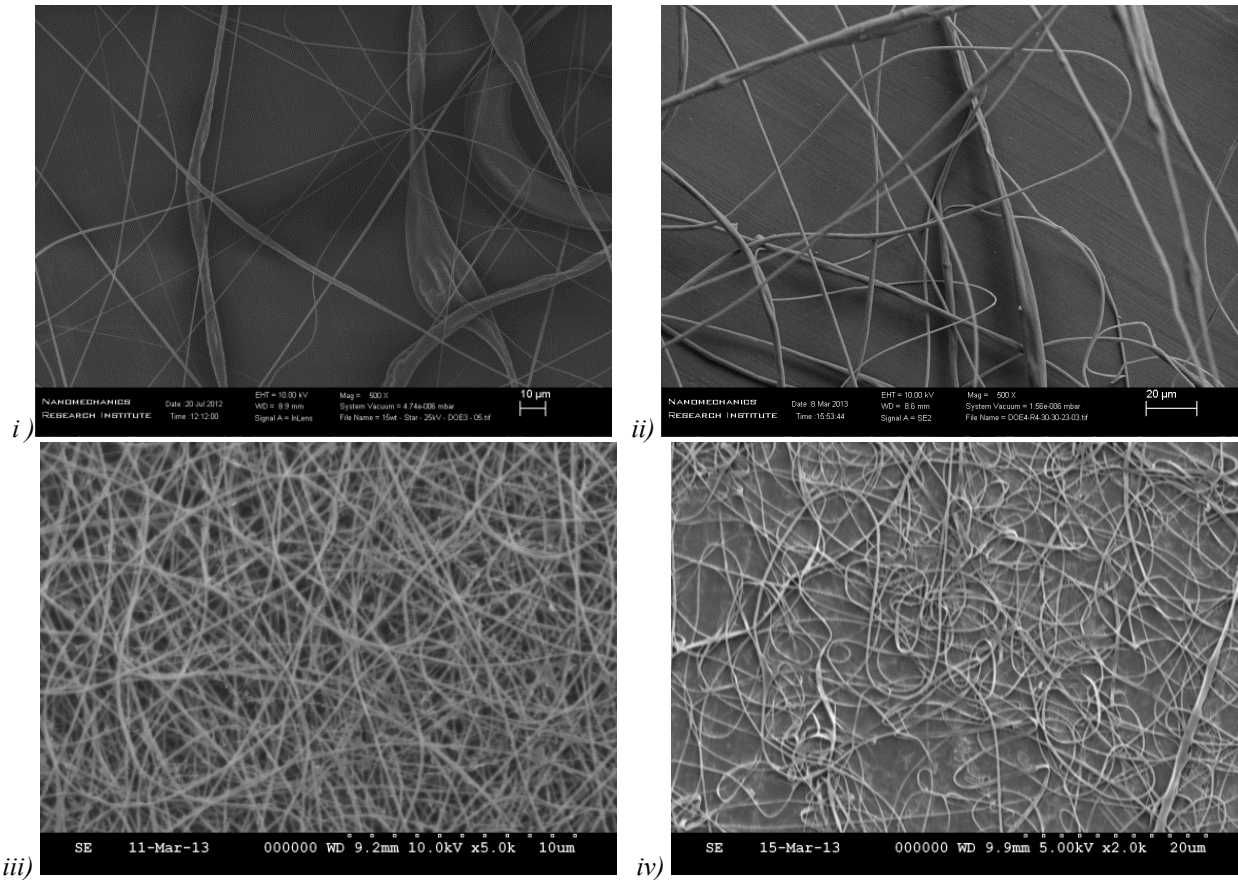


Figure 5.10 - SEM images showing nanofiber morphology of tested material systems: i) PC, ii) NCC/PC, iii) PA 6,6, and iv) cNCC/PA 6,6

The fiber diameters measured for the chosen specimen are listed in Table 5.6 including standard deviation.

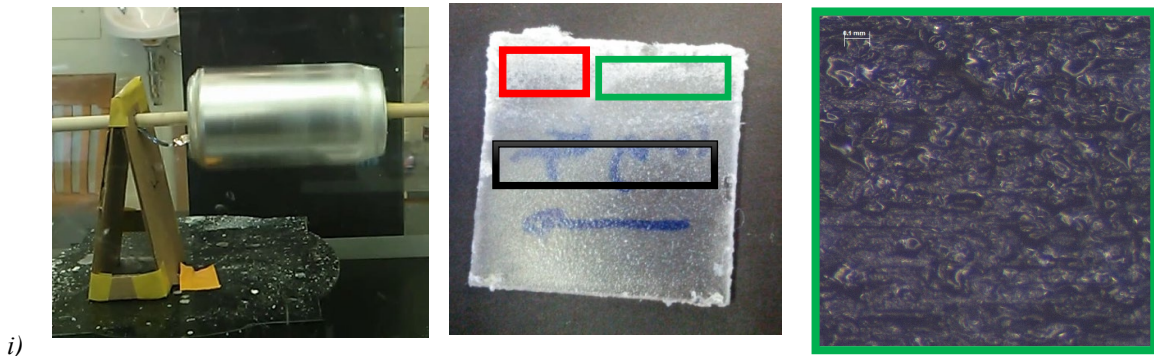
Table 5.6 - Measured fiber diameter for nanofiber material systems tested for coating applications

Sample	Fiber diameter (μm)
PC fibers	0.84 +/- 0.45
PC/NCC fibers	3.54 +/- 2.42
PA 6,6 fibers	0.18 +/- 0.05
NCC/PA 6,6 fibers	0.33 +/- 0.13

Figure 5.11 shows images of the experimental setup for both the rotating drum and compression techniques used. An example of different hardness measuring locations is shown in ii) with green and red representing a “thick” section and the black area representing a “thin” section. The gradient in fiber thickness is a result of the rotating drum technique. The surface morphology of a thin section is presented via an optical micrograph in iii) (scale bar is 0.1 mm). For the

compression technique, fibers are removed from the collection slide and placed on an epoxy coated surface and compressed with HDPE as seen in iv). The surface and transparency of an ideal compressed sample can be seen in v, demonstrating a near transparent sample can be create, and likely improved through process optimization.

Method #1: Rotating Drum



Method #2: Compression Technique

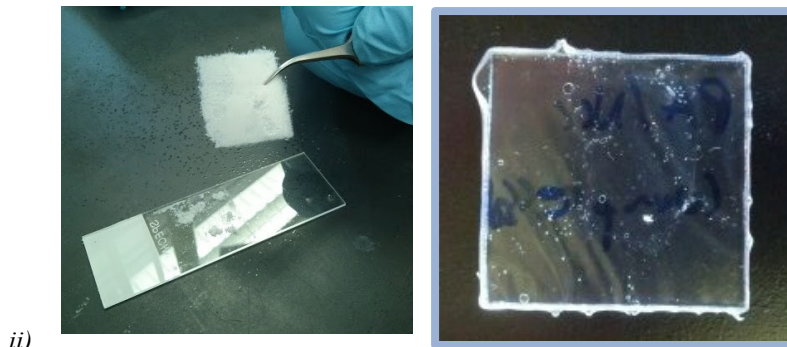


Figure 5.11 - Depiction of the two casting methods used for creating transparent coatings with improved surface properties, 1) Rotating Drum Technique, and 2) Compression Technique

Transmittance

Figure 5.12 shows the UV-Visible spectrum analysis of each of the compression (Method #2) samples made. The transmittance of the Lexan PC sheet used as the substrate has been subtracted from each of the coating samples. It can be seen that the PA 6,6 and cNCC/PA 6,6 samples demonstrate good transparency as the fibers are at or below the size of visible light wavelength (less than 330 nm). The larger PC and NCC/PC samples do not demonstrate the same ideal levels of transparency.

The transmittance measurements are tabulated in Table 5.7 at the 550 nm wavelength, which is approximately the center of the visible spectrum. The results demonstrate the transmittance is inversely proportional to the fiber size, with less than 100-200 nm fiber diameter being ideal.

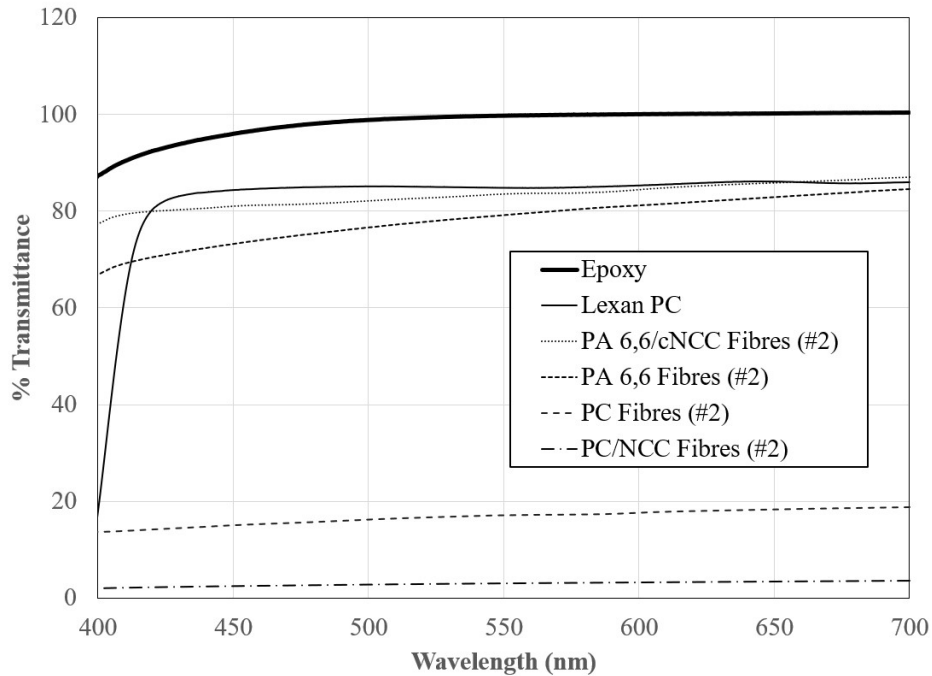


Figure 5.12 - Coating specimen percent transmittance over the visible spectrum of wavelength

Table 5.7 - List of coating specimen percent transmittance at 545 nm wavelength

Sample	Transmittance (% @ 545 nm)
Epoxy	99.6
Lexan PC	84.8
PA 6,6/cNCC Fibres (#2)	83.4
PA 6,6 Fibres (#2)	79.0
StarPlastic PC Fibres (#2)	17.0
StarPlastic PC/NCC Fibres (#2)	3.0

Microhardness

Six coating specimens were tested for surface microhardness, each of the 4 material systems using the compression technique (Method #2) and only PC and NCC/PC for the rotating drum technique (Method #1). Vickers microhardness testing results are presented in Table 5.8 including standard deviation.

Table 5.8 - Vickers Microhardness (HV) measurements for nanofiber coating samples including standard deviation

Sample Measured	Vickers Hardness (HV)	Standard deviation
Epoxy (Bonding Matrix)	12.9	0.1
Lexan PC (Substrate)	12.5	0.1
PA 6,6 Fibers (#2)	11.8	0.2
4% cNCC/PA 6,6 Fibers (#2)	12.0	0.5
PC Fibers (#2)	10.6	0.4
2% NCC/PC Fibers (#2)	11.1	0.2
PC Fibers (#1)	11.7	0.2
2% NCC/PC Fibers (#1)	10.6	0.4

The Vickers Microhardness is also plotted as a bar graph with standard deviation error bars in Figure 5.13.

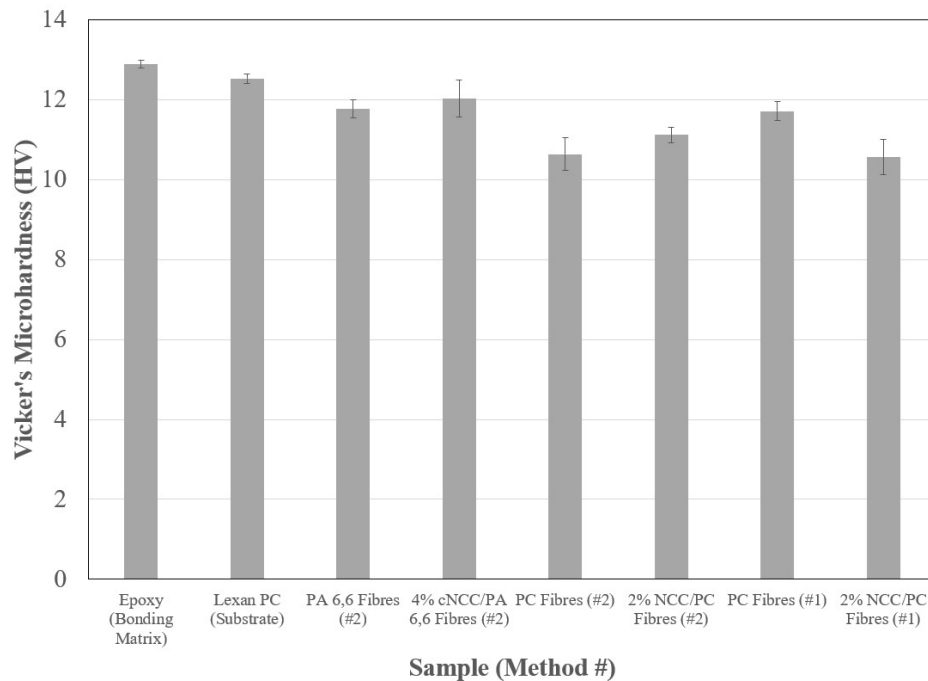


Figure 5.13 - Graph of Vickers Microhardness (HV) measurements for nanofiber coating samples

From the results, it is seen that unfortunately no specimen has the HV levels of either the Lexan PC substrate or epoxy used as the bonding matrix. For the compression technique (#2) we see that the inclusion of NCC tends to increase the surface microhardness, this trend was not seen with the rotating drum technique (#1) for NCC/PC. The NCC/PC were also the largest fiber diameter, so poor embedding could lead to softening of the surface. This may not be completely undesired, as

a self-healing surface could reduce the apparent abrasion on a surface, but more study would need to be completed to confirm this hypothesis.

Finally, the rotating drum technique (Method #1) was employed to create samples with long collection times. This was done to maximize the concentration of nanofibers deposited at the surface of the coating. The results are tabulated in Table 5.9, for run times of 45, 60, and 90 minutes of collection. It is immediately apparent that longer run times lead to harder surfaces, as plotted in Figure 5.14, with the hardest sample valued at double that of Lexan PC or epoxy alone.

Table 5.9 - Vickers Microhardness (HV) measurements for 2% PC/NCC coating samples including standard deviation for extended run rotating drum collection

Sample Measured	Vickers Hardness (HV)	Standard deviation
2% NCC/PC (45 min-thin)	9.2	1.7
2% NCC/PC (45 min-thick)	13.3	2.8
2% NCC/PC (60 min-thin)	10.5	1.8
2% NCC/PC (60 min-thick)	14.6	2.6
2% NCC/PC (90 min-thin)	16.2	5.7
2% NCC/PC (90 min-thick)	26.3	4.9

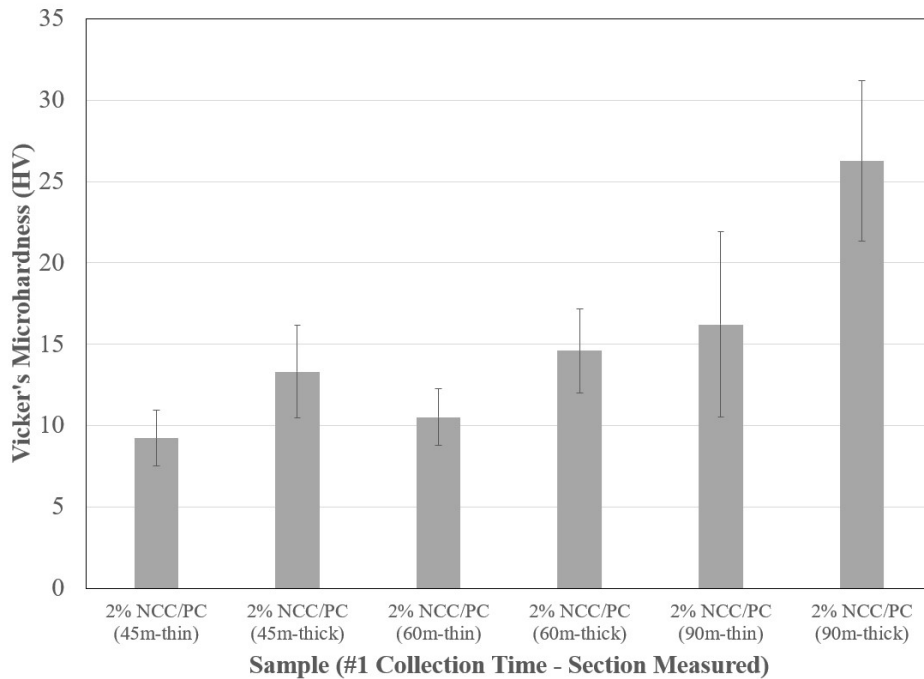


Figure 5.14 - Graph of Vickers Microhardness (HV) measurements for 2% PC/NCC coating samples for extended run rotating drum collection

In summary, it is shown that there is possibility to create transparent coatings that can improve the surface properties (as measured by surface hardness). The compression technique (Method #1) was shown to make transparent (>80% transmittance) coatings with fiber diameters lower than a few hundred nanometers. The rotating drum technique (Method #1) was shown to increase surface hardness over commercial transparent Lexan PC sheeting by over 200%. This summary is visually represented in Figure 5.15. Further exploration into process optimization is encouraged to produce light-weight coatings for applications like automotive and aerospace as well as safety enclosures and shrouds.

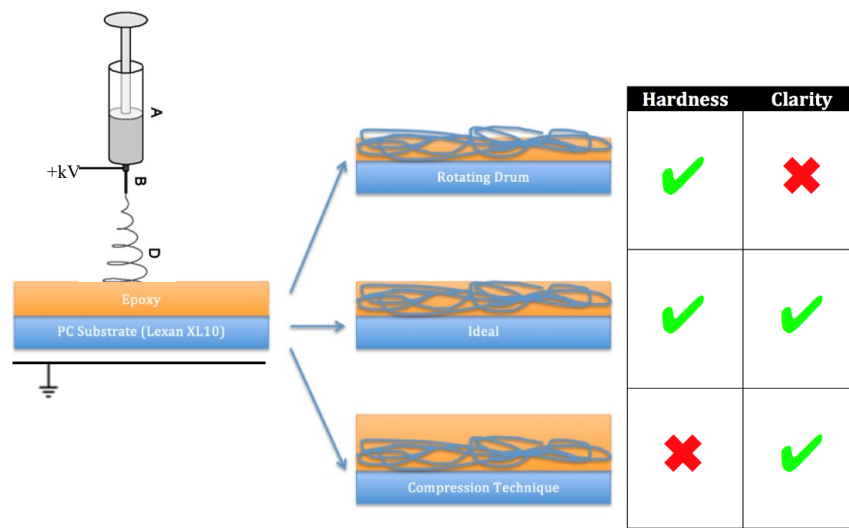


Figure 5.15 - Visual representation of ideal, rotating drum (Method #1) and compression (Method #2) technique strengths (✓) and weaknesses (✗)

5.5 – Conclusions

Novel Contributions

Novel materials based on polyamide-6,6 filled with 4-wt.% DDSA modified Nanocrystalline Cellulose were prepared by electrospinning in a 90% formic acid solution. Fiber diameters ranged from as low as 190 nm to upwards of 1100 nm, but the majority of fibers observed were in the range of 200 to 300 nm. Little to no beading was observed through all electrospinning runs which can improve the overall electrospun mat properties as no defects have been introduced. A 2³ full-factorial design of experiments was explored to model the fiber diameter as a function of the polymer concentration, applied voltage, and gap distance with a goodness-of-fit of 99.9%. Center-point measurements were conducted to test the curvature of the model as well as to account for this curvature in the model. Solution properties were also documented, including the turbidity and viscosity and liner relationships were developed for them. The results of the effects and responses presented here can be used as a basis for any researcher to explore the electrospinning of polyamide-6,6 fibers with DDSA-modified Nanocrystalline Cellulose. As the electrospinning process is complex and can be influenced by many factors, including combined factors, the knowledge from this study provides an excellent groundwork for this material system.

Proof-of-concept transparent surface coatings were also successfully prepared for nanofibers of PA 6,6 and PA 6,6 reinforced with DDSA modified NCC and compared to prepared fibers of polycarbonate and polycarbonate reinforced with NCC. The electrospun composite fibers were embedded in an epoxy matrix via a rotating drum collector and via compression forming. The PA 6,6 and PA 6,6/cNCC coating showed excellent transmittance at 79% and 83% transmittance respectively, much better than the PC and PC/NCC fibers which had transmittances of 17% and 3%, respectively. This demonstrates that the fiber diameter falling below the wavelength of light is critical in transparency and light transmittance, as is the case with our PA 6,6 based coatings, with fibers falling below 330 nm.

Challenges

Improving the surface hardness of the coating specimens proved difficult due to the manufacturing methods. Creating a uniform distribution of fibers on the surface as well as locating the fibers close to the surface of the epoxy matrix is difficult. Due to this issue, many of the measured samples did not show significant improvement. Increasing the electrospinning density through longer collection times on the rotating drum collector did show 282% increase in hardness, although transmittance was sacrificed. Process improvement in the coatings preparation should lead to both desired transmittance and surface hardness.

Chapter 6. Mechanical Characterization of 3D Printed Thermoplastic Starch-Resin Copolymer Nanocomposites Reinforced with Nanocrystalline Cellulose

6.1 – Introduction

Thermoplastic starch-resin copolymer (TPS) is a material developed by Polymer Specialties International Inc. in Ontario and has unique material properties that may be beneficial for 3D printing applications. Starch based materials such as TPS are biodegradable and sustainable over traditional petroleum-based polymers and have applications for short life and disposable applications like packaging and consumer goods. The TPS material is also quite soft and flexible to the touch, properties that are mostly non-existent in 3D printing options. The use of Nanocrystalline Cellulose (NCC) as a natural reinforcing nanoparticle has been explored as an additive in 3D printing studies, but it has not previously been compounded with TPS [167], [168].

An all-green nanocomposite has been created with cellulose nanocrystals (CNX) within a poly(lactic acid) (PLA) matrix [169]–[172], but PLA tends to be a stiffer, more brittle polymer unlike TPS. Poly(vinyl alcohol) (PVA) reinforced with CNX has been explored as another biodegradable nanocomposite for 3D printing [172], [173], the inclusion of 2 wt-% of CNX resulted in an 81% improvement in tensile strength. Other CNX reinforced thermoplastic composites that have been explored in literature include acrylonitrile butadiene styrene (ABS) [174], [175], polypropylene [176], Poly(ϵ -caprolactone) [177], and poly(3-hydroxybutyrate-co-3-hydroxyhexanoate) (PHBH) [172]. Cellulose nanocrystals have also been explored in literature as a 3D printing support material [178] as well as an investigation in alignment of CNX during 3D printing [179].

Objective

This study investigates the application of 3D printing for a new thermoplastic starch-resin copolymer (TPS) developed in Ontario. This new material has unique material properties (like ductility and flexibility as well as being biodegradable) that have strong potential as a consumer 3D printing material. The TPS matrix was also compounded with Nanocrystalline Cellulose (NCC) to aid in processing both the filament feedstock for the 3D printers as well as the fused deposition modeling of a final product. The mechanical properties and trends are compared to literature values for injection molded TPS.

This study will look at:

- the bench scale feasibility of producing TPS composite filaments for 3D printing;
- the effect of 3D printing parameters on mechanical properties;
- the advantages of addition of a biodegradable nano-reinforcement, specifically Nanocrystalline Cellulose (NCC), to create an all-green nanocomposite for 3D printing; and
- the production scale-up of TPS and NCC-TPS composite filaments.

The final section takes the TPS and NCC-TPS systems from the bench scale and tests the scaling up of filament production. It is a preliminary investigation to explore increasing filament production from 1 foot per hour to over 500 feet per hour. This scale up trial tests the ability to take the material to market and what effects it may have on resulting mechanical properties.

The objective is to quantify 3D printing as an alternative to the classic thermoplastic processing methods of injection molding. The experimentation completed includes melt flow indexing (MFI), and mechanical property testing (like impact, tensile, and flexural testing), to draw conclusions and determine the viability of the 3D printing processing method for the all-green nanocomposite. The successful 3D printing of the TPS and NCC material system explored has not previously been published. Also, typical publications of new material systems do not look at the scale up viability for commercial production of filaments as explored in this study.

The goal of this research is to explore the production methodology of 3D printed polymer parts, from the design and manufacture of 3D printer filament (in benchtop and large scale-up processes) to 3D printing mechanical testing specimens and characterizing using ASTM standards for mechanical properties.

The relationship of formulation (material system) and processing (or slicing) parameters to final mechanical properties is explored. Comparisons are also made with respect to traditional processing methods, including injection molding. Benchtop and scaleup methods of 3D printing filament are explored for TPS and TPS/NCC material systems, with the goal of exploring the potential for commercial production.

6.2 – Materials

PSI Inc. Thermoplastic Starch-Resin Copolymer

A single source of a thermoplastic Starch-Resin copolymer (coded TPS) was donated by Bryon Wolff of Polymer Specialties international Incorporated (PSI Inc.) to study the viability and effects of processing via 3D printing. As this is a new starch-polyester copolymer material being tested by the manufacturer to optimize production and material properties, it is best to note the production batch used. The batch was labeled Lot 247 and was produced on January 23rd, 2013. The material, as received, was pelletized and had a yellow-brown opaque color. The starch used by PSI Inc. is amylopectin, one of two components of starch, the other being amylose. The polyester used in this production batch is Ecoflex FB1200 polybutyrate (PBAT). The percentage of functionalized starch to Ecoflex FB1200 is between 40:60 to 60:40. Characterization results and discussion for the TPS material as received is given in detail in Chapter 6 and additional material properties can

be found in the patent US20160017091 [180]. Compositional units of TPS, amylopectin, maleic anhydride (MAH), and polybutyrate are included in Figure 6.1.

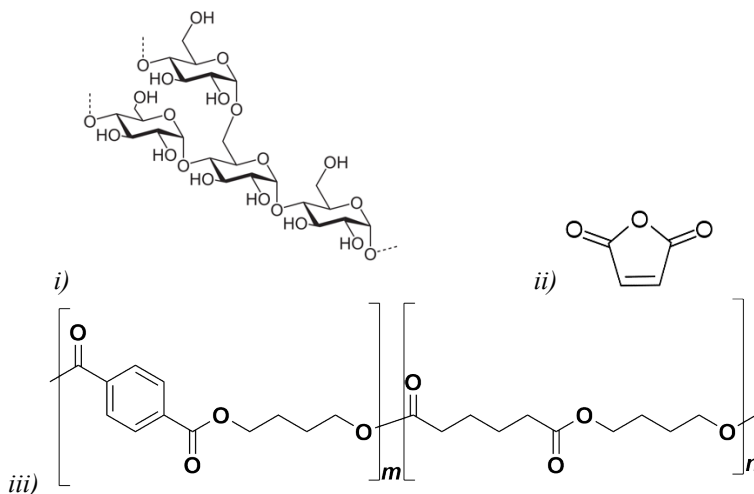


Figure 6.1 - Compositional units of TPS i) amylopectin, ii) maleic anhydride (MAH), and iii) polybutyrate

Thermoplastic starch-resin (TPS) copolymer is formulated by first mixing dicarboxylic acid anhydride, like maleic anhydride (MAH), with starch and tumbled to achieve good coverage. Next, glycerol, water, and peroxide are added to the mixture to initiate esterification of the starch with MAH, functionalizing the starch. The functionalized starch is then dried and mixed with a biodegradable polyester resin. The process can be carried out in batch reaction or a continuous extrusion process. [180]

CelluForce Ultra Nanocrystalline Cellulose

See Chapter 4, 4.2 – Materials, CelluForce Ultra Nanocrystalline Cellulose.

6.3 – Methods

Desktop Melt Compounding of TPS and NCC/TPS 3D Printing Filament

Pure TPS as well as composites loaded with NCC at concentrations of 1, 3, and 5% by weight were melt compounded directly into 3D printing filament using a single screw Filastruder v1.3. Dried TPS and NCC were weighed in correct ratios and added to large containers with excess volume and hand shaken to distribute the NCC powder throughout the TPS beads. The dry mixed material was then loaded into the extruder hopper and covered. The extruder screw consisted of a heated ¾” internal diameter steel cylinder with an 8” length ¾” diameter steel screw attached to a high torque motor. The cylinder was heated to an external nozzle temperature of 185 °C, it is assumed the internal temperature was lower but it could not be measured. The screw rotated at approximately 30 RPM, shearing and mixing the polymer composite, and extruding out of a 1/16” die for 1.75 mm filament. The material was collected on a variable RPM drum spooler adjusted to the output speed of the Filastruder. The Filastruder produced roughly 30 cm of filament per hour. About 10 m of filament were produced for each concentration of NCC. Figure 6.2 shows the Filastruder set up as well as an example of the collected TPS NCC composite filament. [181]

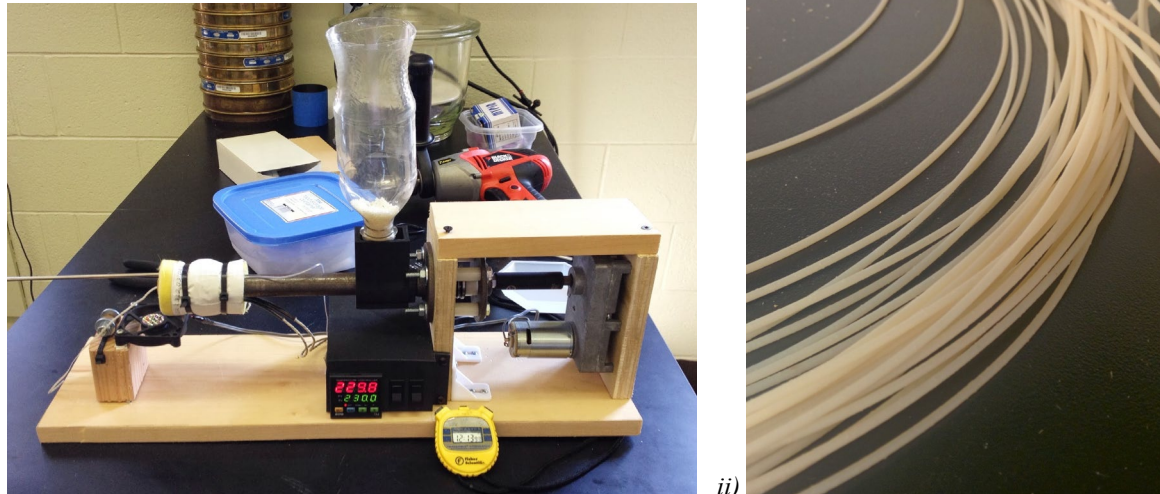


Figure 6.2 - i) The Filastruder 3D printer filament extruder with ii) resulting 1.75 mm NCC-TPS composite filament

3D Printing

Seven specimen bars were 3D printed for each ASTM D256, D790, and D1708 on the Makerbot Replicator 2X 3D printer from Makerbot Industries using the Filastruder TPS and composite NCC-TPS filament [182]–[184]. The Makerbot printer was chosen to continue the 3D printing study attributable to its higher precision. This Makerbot is a popular choice for researchers testing experimental materials as it allows expanded capabilities for bench top 3D printing at a reasonable price.

The bars were printed with a 0.4 mm nozzle with a temperature of 165 °C. The printer head speed was set to 30 mm/s and the bars were printed with 100% linear infill. The linear infill rotated 45° each layer inside of a 2-track perimeter. The specimen bars for each concentration were printed at a layer thickness of 0.3 mm (300 μm) and TPS with no NCC additive was printed at each 100, 200, and 300 μm layer heights to see if there is any effect. Unfortunately, because of low viscosity and web breaks occurring at 100 μm specimens, only enough were collected for flexural testing (ASTM D790) comparisons. There were some 3D print failures at each layer height and NCC concentration, only pristine printed bars were used for mechanical characterization. Figure 6.3 depicts the prepared 3D printed specimen bars for tensile, flexural, and impact testing. Specimens were also dried and conditioned according to ASTM D618 standard before testing [185].

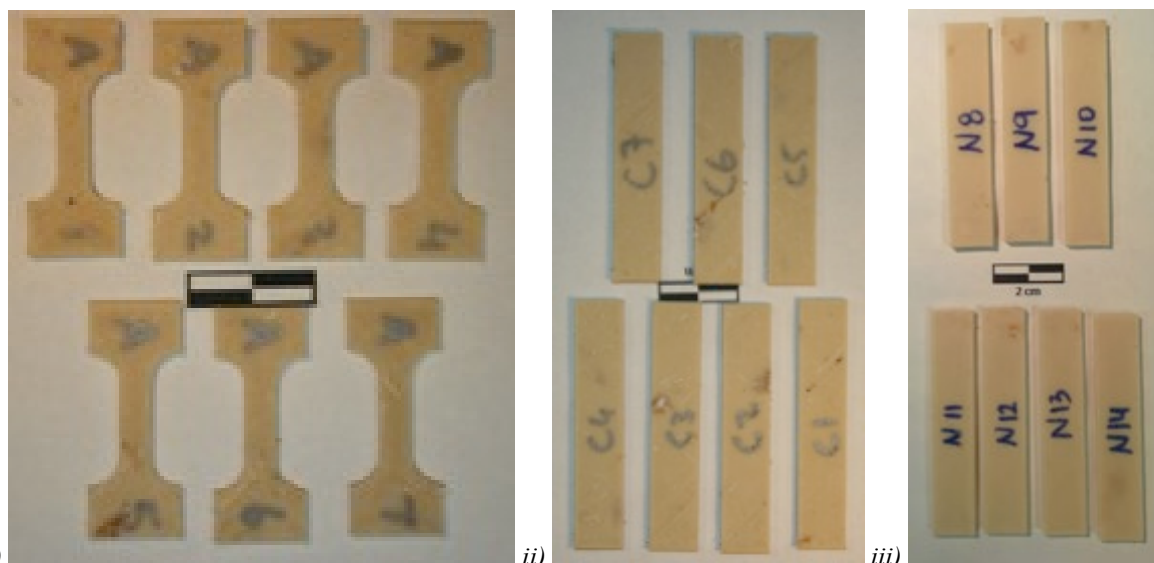


Figure 6.3 - i) ASTM D1708 microtensile testing specimens 3D printed with pure TPS and ASTM D256 (Impact) and ASTM D790 (Flexural) testing specimens 3D printed with ii) pure TPS and iii) 5% NCC-TPS

Scale Up Production of TPS Filament

Following the promising laboratory scale 3D printing study of Thermoplastic Starch Resin Copolymer introduced above with loading of Nanocrystalline Cellulose (NCC), a scale-up of TPS and 2% NCC-TPS samples were conducted. This was a scale-up of the filament production process using a commercial filament extruder at IPEG Conair North America in Pinconning, Michigan, USA. The Conair facility produces filament for Stratasys Inc. as well as other 3D printing filament distributors in North America. A Davis-Standard extruder has been coupled with upstream and downstream equipment developed by Conair. The system was first debuted in March 2015 at NPE in Orlando, FL. [186]

The demonstration line, Figure 6.4(i) is capable of producing 400 to 600 feet per minute of 3D printer filament – three to four times faster than industry capabilities – with better tolerances in the range of 0.0127 mm for diameter and 0.0254 mm for ovality. Upstream, the system uses a Conair mobile drying and conveying system (MDCW100) to control moisture and feed the polymer resin to the extruder hopper. The resin is then extruded using a 2-inch Davis-Standard Super Blue equipped with a Conair GRH-1.0 extrusion die developed specifically for filament production, Figure 6.4(ii). As the polymer exits the die, it is passed through a Conair HTMP multi-pass cooling and sizing tank three times and exits being pulled by a precision belt puller, Figure 6.4(iii). The filament is then spooled using a Conair servo-driven automatic cut-and-transfer coiler first being measured using a Zumbach laser gauge that provides feedback to the system on diameter and ovality, allowing continuous fine tuning and control. [186]

The true innovation of this system comes from the HTMP multi-pass cooling and sizing tank where the filament is not only introduced to the open water bath, as is standard in the industry, it also first passes through a vacuum sizing apparatus. For space saving and compactness of the system, the water bath allows multi pass, shortening the required floor space by 3 times while maintaining high speeds. Overall, with reduced floor space, high speed, continuous feeding and feedback, and

good control of temperature, the Conair system produces high quality filament at a fraction of the time. [186]



Figure 6.4 - i) commercial filament extruder at IPEG Conair North America equipped with a ii) Conair GRH-1.0 filament extrusion die and iii) HTMP multi-pass cooling and sizing tank [186]

The Davis-Standard extruder has seven different heating zones that are individually controllable, named: E1 through E5, Clamp, and Die. Heating zones E1 through E5 control 5 different zones inside the Davis-Standard extruder in sequence from the hopper through to the die end. The Clamp

heating zone is around the collar that secures the die, and the Die heating zone is where the polymer exits the extruder at a specific diameter. The melting temperature of TPS is around 262 °F (127 °C) meaning the processing temperature should be set several degrees higher. Approximately three hours were used initially to find an ideal temperature sequence for the TPS 3D printing filament to be produced. This preliminary trial is summarized in Table 6.1 below; all values are in Fahrenheit.

Table 6.1 - Preliminary scale-up TPS filament extrusion temperature profiles and notes for successive trials to find ideal profile

Prelim Trial No.	E1 (°F)	E2 (°F)	E3 (°F)	E4 (°F)	E5 (°F)	Clamp (°F)	Die (°F)	Notes
1	310	310	310	305	300	280	280	Filament breaking due to unmelted resin.
2	310	310	305	300	290	280	280	Filament breaking due to unmelted resin.
3	320	320	315	310	305	280	280	Filament breaking due to high temp. and low melt strength.
4	330	325	310	280	270	280	280	Filament does not break, some inconsistencies in diameter.
5	340	340	325	280	270	280	280	Main line operator arrives, tunes temp. from experience. Spooling filament begins.

Finding the ideal range in the preliminary trials required creating a larger temperature gradient between the input and output of the extruder. The initial melt region, E1 through E2 was increased by 30 °F to ensure complete melting of the polymer. The temperature then was required to drop at a higher rate through E3 to E5 in order to maintain ideal melt strength of the TPS resin to avoid filament breakage, analogous to a web break in polymer processing. The knowledge and experience of the main line operator helps accelerate this process. After preliminary trial number 4, the spooling of the filament began and focus was given to the feedback loop for diameter, ovality, and tolerance. In total, eight different manufacturing runs were completed, differentiated by a new spool numbered accordingly for each augmentation of the machine parameters, which now includes extruder speed (Ext. RPM) and filament pull speed. These eight manufacturing trials are summarized in Table 6.2.

Table 6.2 - Scale-up TPS and NCC/TPS filament extrusion temperature profiles, extruder RPM, and filament output rate for successive trials (spool number)

Mfg. Run Spool No.	Sample	E1 (°F)	E2 (°F)	E3 (°F)	E4 (°F)	E5 (°F)	Clamp (°F)	Die (°F)	Ext. RPM	Filament Speed (ft./min)
1	TPS	340	340	325	280	270	280	280	8	430
2	TPS	345	340	325	280	280	280	280	8	430
3-A	TPS	345	350	335	290	280	280	280	8	430
(<15k ft.)										
3-B	TPS	360	360	340	295	280	310	280	8	430
(15-30k ft.)										
3-C	TPS	360	360	340	295	280	310	280	8.5	430
(>30k ft.)										
4	TPS	360	360	340	295	280	310	280	14	520
5	TPS	370	380	360	340	340	340	340	14	520
6	2% NCC-TPS	340	320	320	340	340	340	340	10	430
7	2% NCC-TPS	350	350	340	320	310	310	340	14	510
8	2% NCC-TPS	340	310	310	330	350	310	340	15.5	520

For the manufacturing runs 1 and 2, the primary focus was to get the temperature adjusted to allow proper implementation of the feedback system to tune the filament diameter into the ideal point of 1.70 mm (0.0669”). The Conair system monitoring display is shown in Figure 6.5, this is how parameters like temperature, extruder speed, and pulling speed are adjusted. This process was done manually by the lead operator and for our trials there was no logging of the data other than personal notes. This included close monitoring of the different zones of the Conair system, including the extruder, die, vacuum, water bath, puller, sizer, and spooler and ensuring they were all operating in unison. As each spool can contain just over 30 000 ft. of filament, at around 500 ft./min, the spools will completely fill in around 60 minutes. In most cases, the spools were not completely filled, but changed when a new ideal set of parameters were reached. So overall, most manufacturing runs were less than one hour. Manufacturing run 2 was the most successful at good

filament diameter within tolerance and will be used to test the manufacturing properties for the scale-up trial.

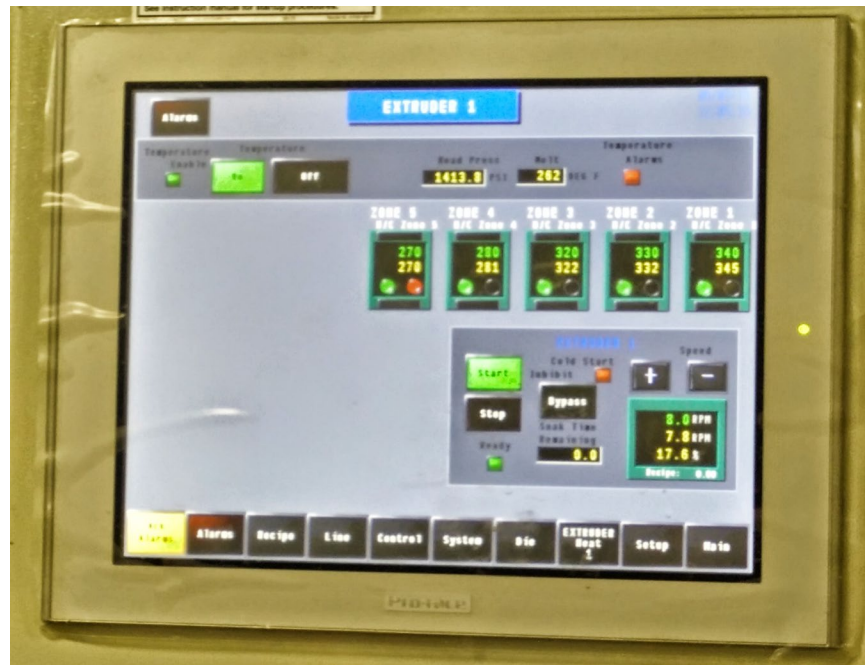


Figure 6.5 - Control unit with measurement settings for Conair Filament Extrusion Line

Manufacturing runs 3 through 5 continued to adjust the temperature to improve the throughput speed from 430 to above 500 ft./min. As stated earlier, the operating speed of the Conair system is between 400 and 600 ft./min, and as we had a nice pristine spool already (#2) it was decided to test increasing the production capacity. By increasing temperature and extruder speed, it allowed the puller to operate at a higher speed while maintaining the ideal diameters. Overall, this was successful as the speed was increased from 430 to 520 ft./min, an increase of 20.9% production capacity. During run 5, some humidity had started to affect the feedstock TPS resin and caused some foaming of the filament making it near impossible to control diameter of TPS any longer.

For the final 3 manufacturing runs (6 through 8), a new sample was used, TPS loaded with 2% by weight of Nanocrystalline Cellulose (2% NCC-TPS) prepared by Bryon Wolff at Polymer Specialties International Inc. in his facility in Newmarket, ON. Similar to the TPS runs, spool 6 focused on getting the equipment parameters tuned, which happened faster from leaning the system in runs 1 through 5. For spool 7, adjustments were made to increase the production speed, this spool had the best diameter, ovality, and tolerances and was used for the scale-up mechanical properties testing study. Spool 8 was run as the day was coming to an end and the objective was to test the limits of the production capabilities. The speed was again able to reach around 520 ft./min which appears to be the limit of the TPS and 2% NCC-TPS systems.

6.4 – Results and Discussion

Melt Flow Index

The melt flow index (MFI) was measured for the thermoplastic starch-resin co-polymer (TPS) as received as well as with 1, 3, 5, and 20 weight % of CelluForce Ultrafine Nanocrystalline Cellulose (NCC). The MFI readings were obtained following ASTM D1238 specification using a 5.0 kg weight at a temperature of 165 °C. As TPS is a new material and is not specifically identified in the ASTM D1238 specification document the weights and temperatures were chosen based on previous research in the lab, otherwise the ASTM process was followed [187]. The MFI results are listed Table 6.3 below.

Table 6.3 - Melt Flow Index values for thermoplastic starch-resin co-polymer with Nanocrystalline Cellulose additives

[NCC](wt.-%)	Total Samples	g/10min	Standard Deviation
0	8	21.06	0.87
1	9	17.68	0.62
3	10	16.61	0.65
5	10	13.67	1.44
20	21	7.93	0.84

The MFI results for the NCC-TPS composites are also plotted in Figure 6.6 with standard deviation error bars. There is a clear trend of decreasing melt flow index with increasing NCC. What this means is that less material will flow through the die in a set period of time as more NCC is added. This is important for 3D printing because as the print head moves and deposits a track of polymer there is stress being applied as the nozzle smears the polymer to the previous layer (or print bed). There is a good correlation between the melt flow index and the materials viscosity. If the print head moves too quickly, or the polymer viscosity is too low, a track break (analogous to a web break) could easily occur, causing a print failure. The NCC acts to immobilize some of the TPS polymer chains giving a more rigid melt strength. This melt strength is also beneficial for maintaining the shape of the FDM part as it is being built, reducing drooping or settling of the deposited polymer tracks.

Through experimentation of printing various materials, a melt flow index of around 10-15 g/10min is ideal for 3D printing at speeds around 90 mm/s. This occurs as the material is not too viscous to pass through the extruder but viscous enough to maintain its melt strength and deposit a nice track. Also, this means that tuning the MFI down slightly can lead to faster printing times. This shows that the addition of a nano-reinforcement can not only act to increase mechanical properties, but the overall processability as well.

The trend of adding NCC to the TPS matrix was modelled as an exponential decay and resulting in Equation 6.1.

$$\text{Melt Flow Index (g/10min)} = 18.997 \exp(-0.045 [\text{NCC}] (\text{wt.-%})) \quad (\text{Equation 6.1})$$

The exponential model has a coefficient of determination, R^2 value, of 0.96 suggesting a good fit of the model. If extrapolated to 100% NCC loading, the melt flow index would be 0.21 g/10min.

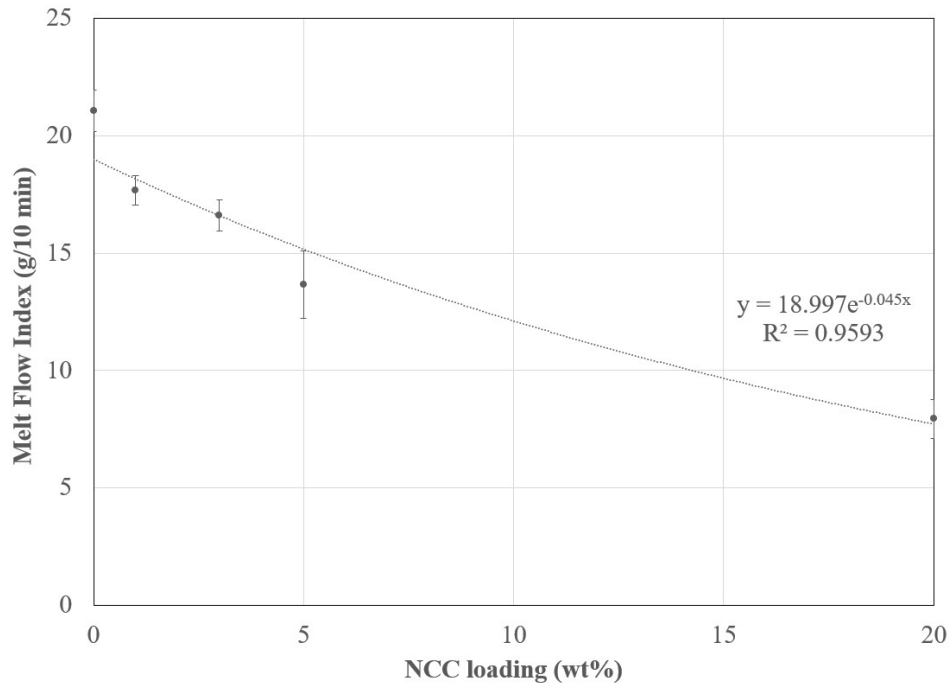


Figure 6.6 - Melt Flow Index values for thermoplastic starch-resin co-polymer composites as a function of Nanocrystalline Cellulose additive

Another observation made with the inclusion of Nanocrystalline Cellulose was that it improved extrusion and bonding between layers and tracks over the pure TPS. The molten form of the TPS-NCC became more homogenous and less imperfections and breaks occurred in the 3D printing. This processing improvement comes from two primary effects, the first outlined above, that the deposited polymer maintains its shape to a higher degree due to the chain immobilization due to NCC and less shrinkage during cooling. The second major factor is the change in surface energy allowing better adhesion and bonding between the layers and tracks because the NCC and TPS chains are freer to entangle between surfaces. It also reduced the amount of material sticking to the 3D printer nozzle and creating a buildup of burnt material that would fall into the print sample causing imperfections structurally and aesthetically.

These effects can be seen in Figure 6.7 displaying 3D printed specimens with no NCC and 5 wt.-% NCC added. The second image (b), shows more pristine flexural testing bars with the incorporation of the NCC. The top right of image (a) also shows where a small buildup of the burnt material was deposited on the corner of the specimen. The bars that incorporated the NCC were clearly more homogeneous and repeatable in production than the pure TPS.

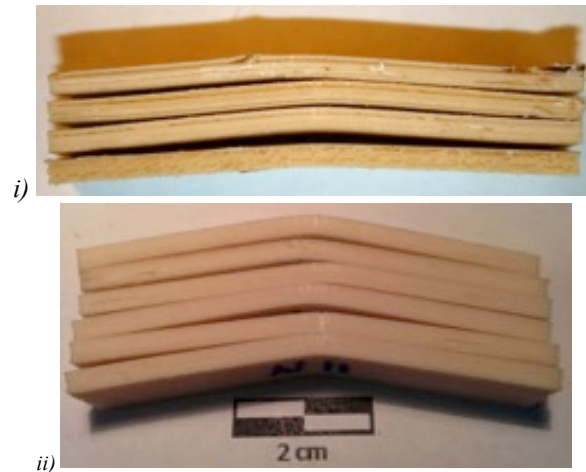


Figure 6.7 - Post-test ASTM D790 3D printed flexural testing specimens for a) pure TPS and b) 5% NCC-TPS

Mechanical Properties

Izod Impact Testing

The impact strength of the pure 3D printed TPS and NCC-TPS specimens with different NCC loading concentrations were tested following ASTM D256 specifications at 3 mm thickness. Each processing method had at least six specimens tested using notched Izod impact testing using the 1 lb. pendulum. For the pure TPS, the impact strength was tested at two different 3D print layer heights, 200 μm and 300 μm . For the NCC-TPS composites, three concentrations of NCC loadings were analyzed: 1, 3, and 5% by weight. Each of the composite samples were printed at 300 μm layer height. The results are displayed in Figure 6.8 and values summarized in Table 6.4. Complete lists of impact strength measurements are included in Appendix C.

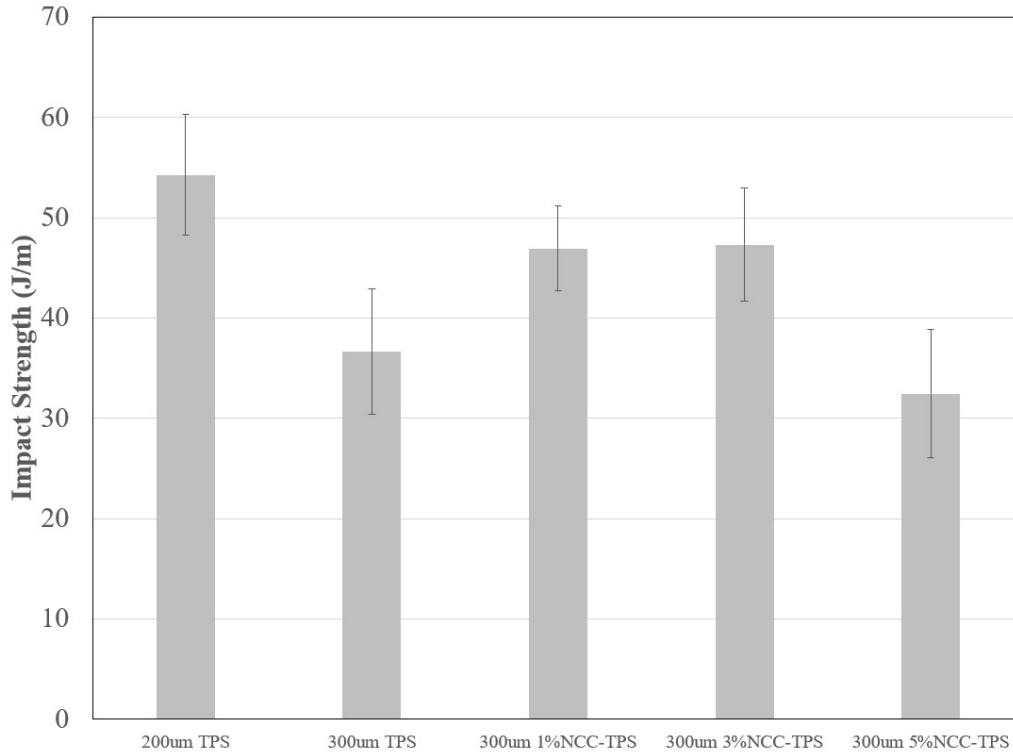


Figure 6.8 - ASTM D256 Izod Impact Strength measurements for TPS printed at varying layer heights and NCC loading

Table 6.4 - Izod Impact Strength measurements for TPS printed at varying layer heights and NCC loading

Sample	Layer Height (μm)	[NCC] (wt.-%)	Impact Strength (J/m)	Standard Deviation (J/m)
a)	200	0	54.296	6.289 (11.6%)
b)	300	0	36.672	4.225 (11.5%)
c)	300	1	46.948	5.647 (12.0%)
d)	300	3	47.320	6.367 (13.5%)
e)	300	5	32.472	3.621 (11.2%)

From the Izod impact strength measurements we can see that layer height and the concentration of NCC additives both have an effect on impact strength. The pure TPS samples (a and b) printed at 200 μm and 300 μm layer heights show that the smaller layer height results in larger impact strength. As the bars had the same dimensions, the specimens printed with the lower layer heights would require more layers, this in turn introduces more micro voids between the 3D printed tracks. Unlike tensile and flexural testing, the voids do not decrease the impact strength, but rather act to resist the instant crack propagation across the bar. The differing layer heights do not seem to affect the deviation of the impact strength significantly.

If we next look at the effect of NCC loading we can see that increasing the NCC concentration increases the impact strength, but to a point. With the discrete values tested in this study we can see that the maximum impact strength occurs somewhere around 3% inclusion by weight. This can be attributable to percolation theory for nanomaterials where nanoparticles with an aspect ratio of 20:1 (as is the case with NCC) will have a complete network of interconnected particles close to a 2-4% loading. This was also observed with the study of polycarbonate and NCC in my master thesis as well as various times in literature [18].

It is also interesting to observe that the standard deviation follows the same trend, increasing from 0% through 3% and then falling back down around 5%. It is hard to deduce a specific reason for this trend; most likely it is a byproduct of the filament thickness (and variation) coming from the Filastruder. Included in Figure 6.9, microscope images of post-break impact specimens are shown for 0, 3, and 5% by weight incorporation of NCC. In the images, the variance of layer defects can be seen with the 3% showing the best fill and inter-layer adhesion.

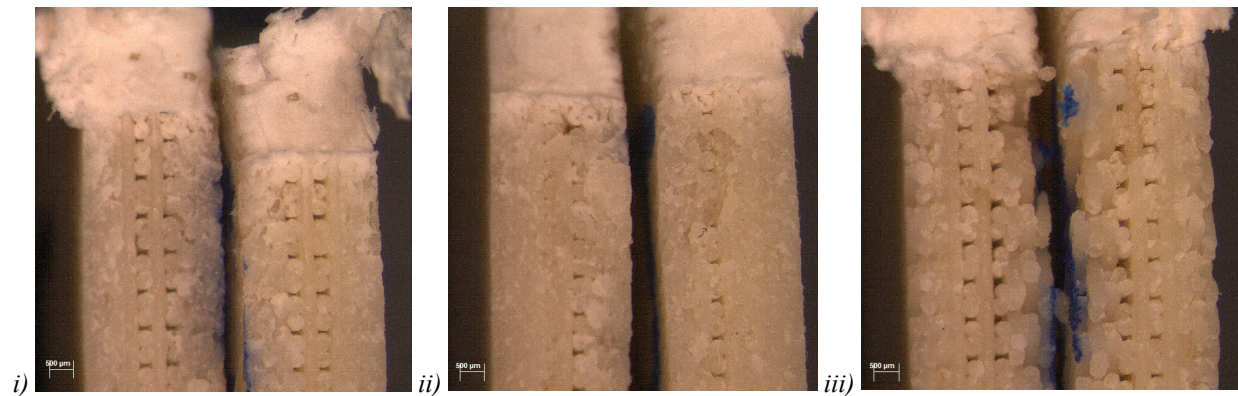


Figure 6.9 - Post break ASTM D256 Izod impact strength specimens for 300 μm i) pure TPS, ii) 3% NCC-TPS, and iii) 5% NCC-TPS

To attempt to quantify this incorporation of processing defects in the 3D printed specimens, the density of the 3D printed bars was compared to pristine injection molded sample of the same dimensions. The data for the injection molded TPS specimens was collected by Ryan S. Park, for his PhD thesis entitled, “Novel Starch Nanocomposites” [188].

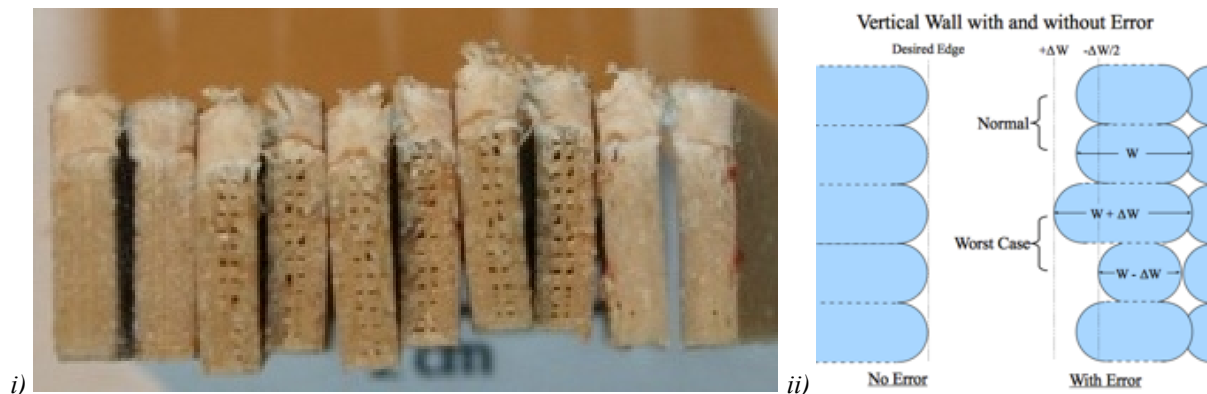


Figure 6.10 - Depiction of air channels that can form inside specimens due to the 3D printing process in i) each TPS and NCC-TPS sample tested and ii) a schematic representation

An average of 14 specimens for each of the 3D printed samples was weighed against the average of six pure TPS injection molded specimens. It is important to note the loading fraction of NCC was not considered but would have a very low relative effect. The measured results are included in Table 6.5. The density for each of the 3D printed samples compared to the ‘full’ injection molded samples were very similar for each, with all samples falling between 80.5% and 83.9%. This is suggesting that for the process used in this study, there is about 20% air within the samples as a direct result of the filament fabrication process using the Filastruder. This phenomenon is depicted in Figure 6.10. Most filament that was produced had a diameter of around 1.60 mm fluctuating 0.05 mm. Producing at this diameter was necessary as the Makerbot could not accept any filaments over 1.70 mm diameter. Although this was accounted for in the slicing algorithm, the variance, and possibly filament slippage in the Makerbot, did lead to defects being incorporated in the specimens. It is also important to note that the mechanical strength results as presented do not factor in this density and assume a ‘full’ bar in cross sectional area calculations.

Table 6.5 - Densities calculated for each 3D printed sample for TPS and NCC-TPS composites relative to injection molded pure TPS

Sample	Layer Height	Density
Pure TPS	100 μm	82.3%
Pure TPS	200 μm	82.9%
Pure TPS	300 μm	80.5%
1% NCC-TPS	300 μm	83.9%
3% NCC-TPS	300 μm	83.9%
5% NCC-TPS	300 μm	82.4%

Tensile Testing

Seven TPS or NCC-TPS specimens from each of the 3D printing methods underwent micro-tensile mechanical testing following ASTM D1708 specifications. Stress-strain curves were plotted and the averages and standard deviations for Young’s modulus, tensile strength, and elongation at break were determined. For the TPS study, each sample was tested on an Instron system with a functional strain-gauge; meaning the calculated modulus values are true and reliable for all TPS and NCC-TPS analyses.

Thermoplastic Starch-Resin Copolymer (TPS) at 200 μm layer height

The ASTM D1708 stress-strain curves for seven 3D printed TPS specimens printed at 200 μm layer height are observed in Figure 6.11. The profile observed shows typical yield behavior of a polymer below its glass transition temperature. The stress rises in a linear fashion to the maximum tensile strength, although there are some discontinuities as seen with the mPLA study indicating some inter layer or inter track breakage before a full break. As this peak is being reached the material begins to observe necking and crazing as polymer chains begins to orient in the direction of the stress. This occurs until the mPLA reaches a failure seen by the drop in stress. For the 200 μm sample, the slope of the linear rise, or the Young’s modulus is 150.1 MPa with a deviation of

28.3 MPa. The tensile strength was observed to be 5.065 MPa with a deviation of 0.273 MPa. Overall, the standard deviations are low suggesting a nice repeatability of the results. The elongation at break was observed to be 16.6% with a standard deviation of 2.46%. A summary of the tensile mechanical properties for 3D printed 200 μm layer height TPS is included in Table 6.6.

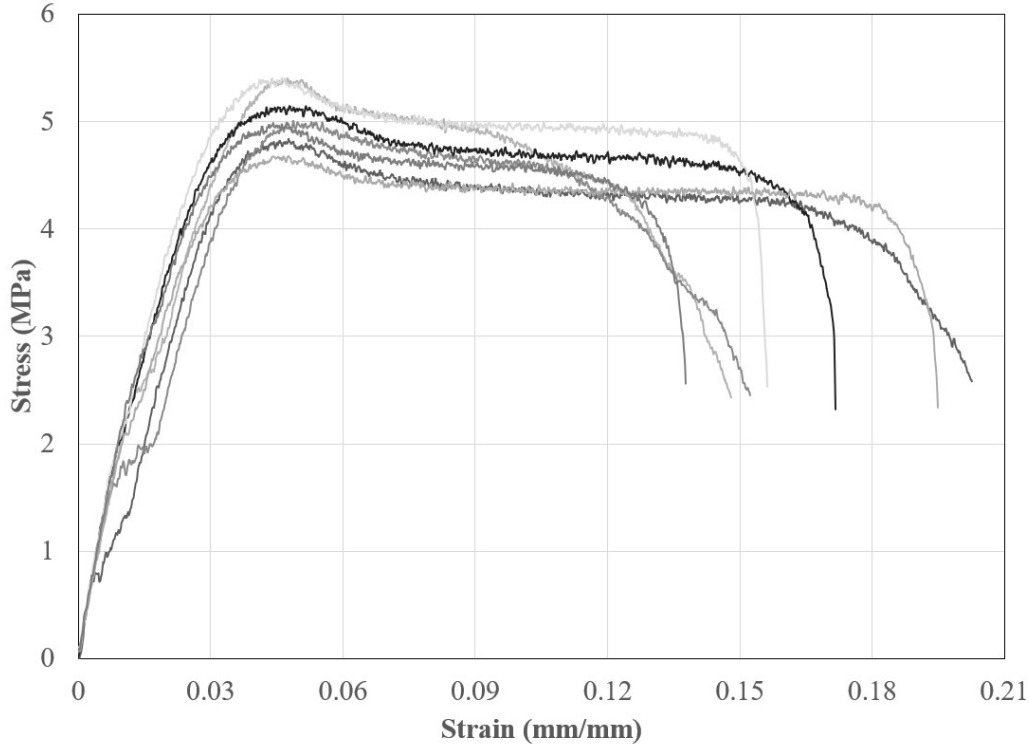


Figure 6.11 - ASTM D1708 micro-tensile mechanical testing stress-strain curves for 3D printed 200 μm TPS specimens

Table 6.6 - ASTM D1708 micro-tensile mechanical testing measurements for 3D printed 200 μm TPS specimens

200 μm TPS	Average	Standard Deviation
Young's Modulus (MPa)	150.146	28.252
Tensile Strength (MPa)	5.065	0.273
Elongation at Break (%)	16.6	2.46

Thermoplastic Starch-Resin Copolymer (TPS) at 300 μm layer height

The ASTM D1708 stress-strain curves for seven 3D printed TPS specimens printed at 300 μm layer height are observed in Figure 6.12. The observed profile is very similar to that observed for the 200 μm layer height. For the 300 μm sample, the slope of the linear rise, or the Young's modulus is 145.4 MPa with a deviation of 26.5 MPa. The tensile strength was observed to be 4.515 MPa with a deviation of 0.232 MPa. The elongation at break was observed to be 11.8% with a standard deviation of 2.34%. Overall, the observed mechanical properties are slightly lower than the 200 μm sample as a result of the fewer but larger inter track defects present. A summary

of the tensile mechanical properties for 3D printed 300 μm layer height TPS is included in Table 6.7.

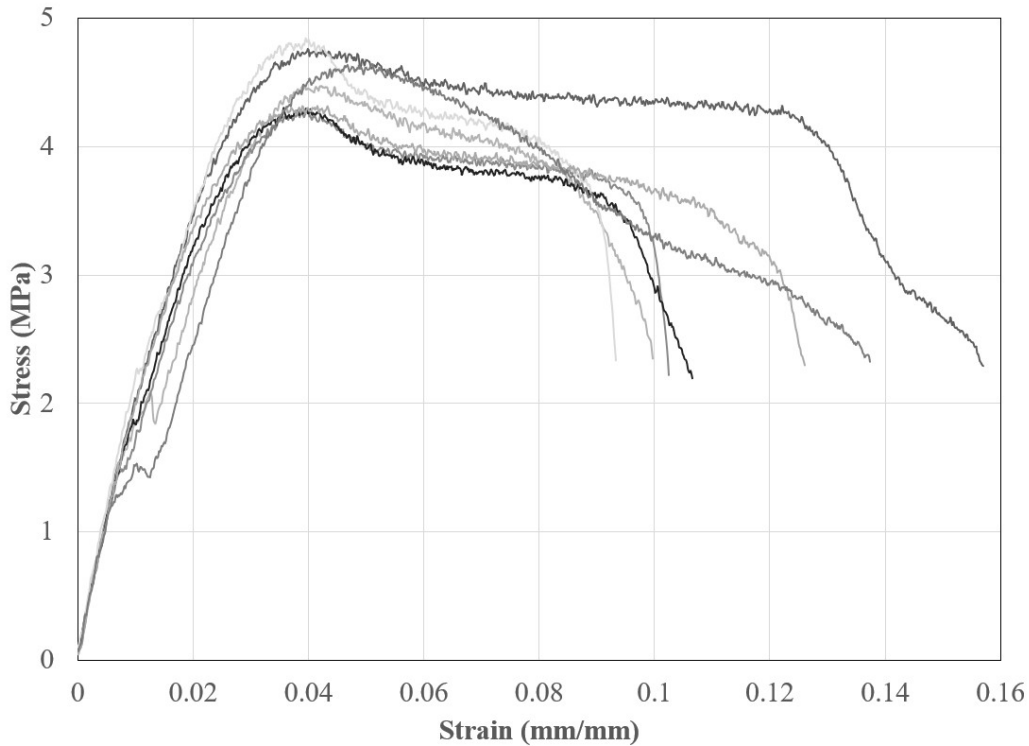


Figure 6.12 - ASTM D1708 micro-tensile mechanical testing stress-strain curves for 3D printed 300 μm TPS specimens

Table 6.7 - ASTM D1708 micro-tensile mechanical testing measurements for 3D printed 300 μm TPS specimens

300 μm TPS	Average	Standard Deviation
Young's Modulus	145.413	26.455
Tensile Strength	4.515	0.232
Percent Elongation at Break	11.8	2.34

1% NCC - Thermoplastic Starch-Resin Copolymer (TPS) at 300 μm layer height

The ASTM D1708 stress-strain curves for seven 3D printed TPS specimens printed at 300 μm layer height with 1% incorporation of NCC are observed in Figure 6.13. The profile observed shows typical yield behavior of a polymer below its glass transition temperature. For the 1% NCC-TPS sample, the slope of the linear rise, or the Young's modulus is 101.5 MPa with a deviation of 32.2 MPa. The tensile strength was observed to be 4.282 MPa with a deviation of 1.478 MPa. The elongation at break was observed to be 31.6% with a standard deviation of 7.63%. Overall, the observed mechanical properties are slightly lower than the pure TPS samples. A summary of the tensile mechanical properties for 3D printed 300 μm layer height 1% NCC-TPS is included in Table 6.8.

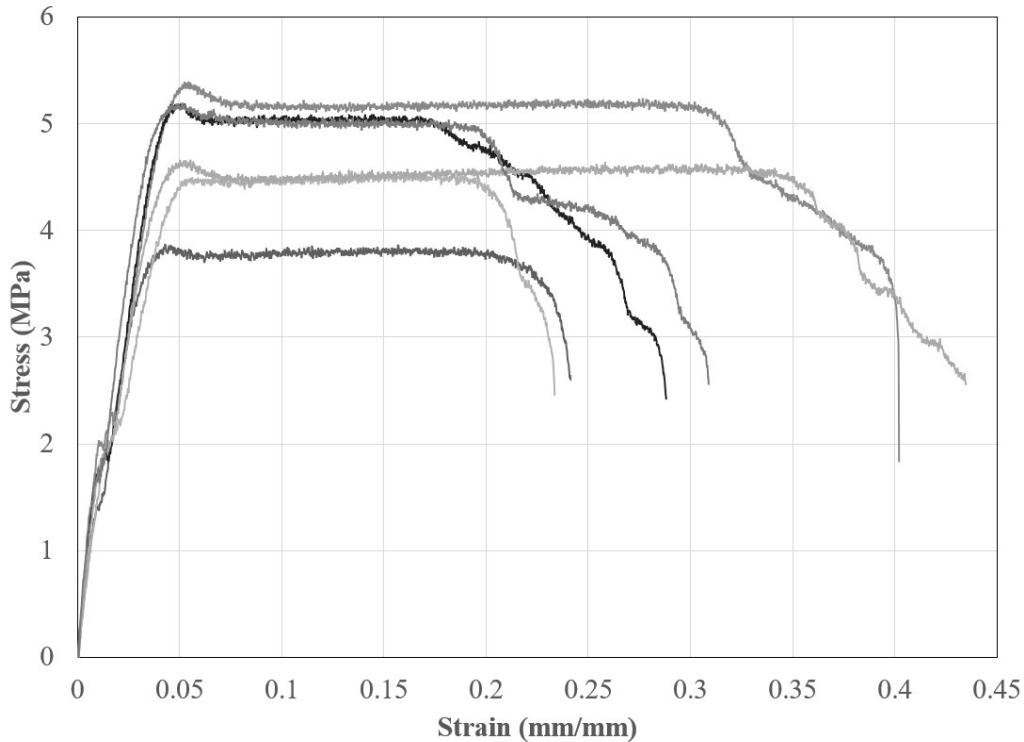


Figure 6.13 - ASTM D1708 micro-tensile mechanical testing stress-strain curves for 3D printed 300 μm 1% NCC-TPS specimens

Table 6.8 - ASTM D1708 micro-tensile mechanical testing measurements for 3D printed 300 μm 1% NCC-TPS specimens

300 μm 1% NCC-TPS	Average	Standard Deviation
Young's Modulus	101.495	32.158
Tensile Strength	4.282	1.478
Percent Elongation at Break	31.6	7.63

3% NCC - Thermoplastic Starch-Resin Copolymer (TPS) at 300 μm layer height

The ASTM D1708 stress-strain curves for seven 3D printed TPS specimens printed at 300 μm layer height with 3% incorporation of NCC are observed in Figure 6.14. The profile observed shows typical yield behavior of a polymer below its glass transition temperature. For the 3% NCC-TPS sample the Young's modulus is 108.8 MPa with a deviation of 18.4 MPa. The tensile strength was observed to be 5.165 MPa with a deviation of 0.625 MPa. The elongation at break was observed to be 46.9% with a standard deviation of 16.7%. This is a slight increase in the modulus and strength and a large increase in elongation at break over the 1% NCC-TPS sample. Although the modulus is about 35% below the pure TPS sample, the tensile strength is the highest of all TPS and NCC-TPS samples tested with a 15% increase over pure TPS at 300 μm . A summary of the tensile mechanical properties for 3D printed 300 μm layer height 3% NCC-TPS is included in Table 6.9.

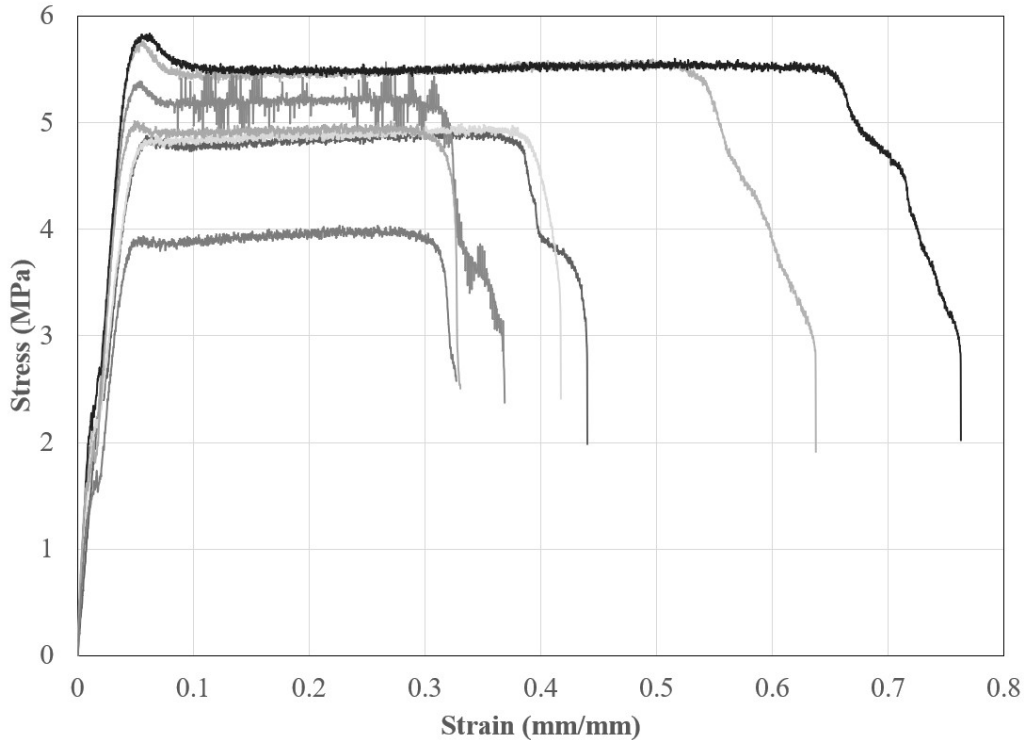


Figure 6.14 - ASTM D1708 micro-tensile mechanical testing stress-strain curves for 3D printed 300 μm 3% NCC-TPS specimens

Table 6.9 - ASTM D1708 micro-tensile mechanical testing measurements for 3D printed 300 μm 3% NCC-TPS specimens

300 μm 3% NCC-TPS	Average	Standard Deviation
Young's Modulus	108.823	18.350
Tensile Strength	5.165	0.625
Percent Elongation at Break	46.9	16.71

5% NCC - Thermoplastic Starch-Resin Copolymer (TPS) at 300 μm layer height

The ASTM D1708 stress-strain curves for seven 3D printed TPS specimens printed at 300 μm layer height with 5% incorporation of NCC are observed in Figure 6.15. The profile observed shows typical yield behavior of a polymer below its glass transition temperature. For the 5% NCC-TPS sample, the Young's modulus is 141.7 MPa with a deviation of 25.8 MPa. The tensile strength was observed to be 5.054 MPa with a deviation of 0.627 MPa. The elongation at break was observed to be 23.5% with a standard deviation of 5.71%. The 5% NCC-TPS sample is showing a large increase in the modulus compared to the 1 and 3% NCC-TPS samples while the tensile strength is improved from the pure TPS by 11.9%. A summary of the tensile mechanical properties for 3D printed 300 μm layer height 3% NCC-TPS is included in Table 6.10.

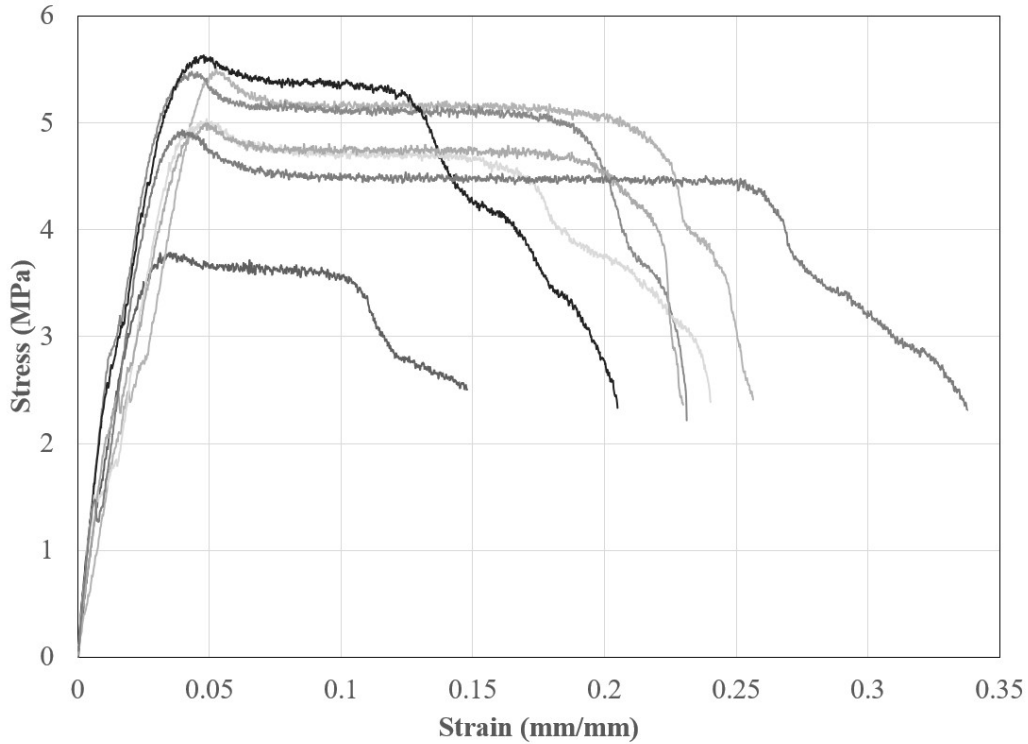


Figure 6.15 - ASTM D1708 micro-tensile mechanical testing stress-strain curves for 3D printed 300 μm 5% NCC-TPS specimens

Table 6.10 - ASTM D1708 micro-tensile mechanical testing measurements for 3D printed 300 μm 5% NCC-TPS specimens

300 μm 5% NCC-TPS	Average	Standard Deviation
Young's Modulus	141.706	25.832
Tensile Strength	5.054	0.627
Percent Elongation at Break	23.5	5.71

Figure 6.16 shows the post break microtensile test specimens for the 5% NCC-TPS sample. These samples had only a 3% decrease in modulus relative to the pure TPS samples and an increase in strength by 11.9%. The overall elongation at break was 23.5% which is about double the 300 μm TPS sample. It can be seen in the image of the specimens that there are several cracks along the length corresponding to the small discontinuities in the elastic linear region. This is a byproduct of the layer by layer 3D printing process. As the layers are deposited, they rotate 45° per layer resulting in many tracks being deposited orthogonally to the direction of the stress. This is where these breaks initiate due to inter track gaps and defects. Because not all layers through the cross section of the specimens are perpendicular to the stress, the crack does not necessarily propagate all the way through. Figure 6.16 also displays a magnified image of the cross section of one of the broken specimens. The cross section appears to have more thinning and drawing of the polymer relative to the impact specimens shown previously. Nearly all of the elongation occurs at these crack locations and there is relatively low strain on the other sections of the bars.

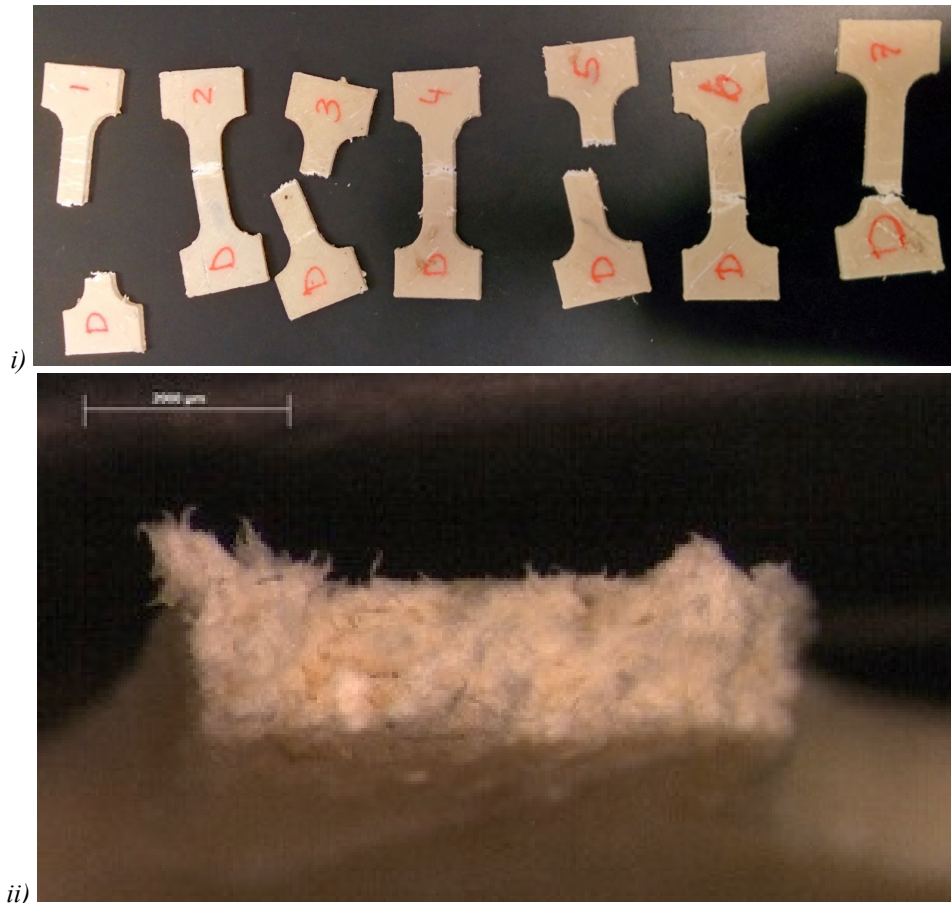


Figure 6.16 - i) Post break ASTM D1708 micro-tensile testing specimens for 5% NCC-TPS including ii) close-up of cross-section

Thermoplastic Starch-Resin Copolymer (TPS) at 300 μm layer height – Filament Scale-Up

The ASTM D1708 micro-tensile stress-strain curves for eleven 3D printed scale-up TPS specimens printed at 300 μm layer height are observed in Figure 6.17. The observed profile appears different from the curves obtained with the Filastruder samples and represents a soft and weak polymer, breaking each time at its maximum tensile strength. It is also important to note that the tensile testing machine used was missing a strain gauge and only the tensile strength should be accepted as accurate. For the scale up TPS sample, the tensile strength was observed to be 3.598 MPa with a deviation of 0.334 MPa. Overall, the observed tensile strength is lower than the 300 μm bench-scale pure TPS sample by about 47.8%. A summary of the tensile mechanical properties for 3D printed 300 μm layer height scale-up of TPS is included in Table 6.11.

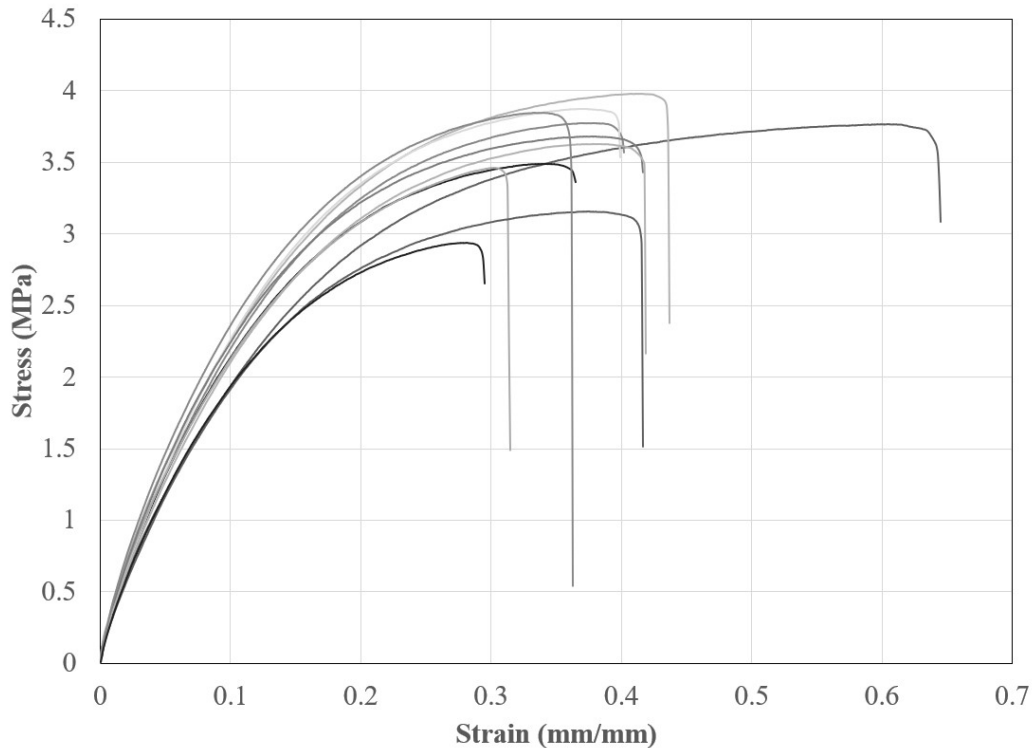


Figure 6.17 - ASTM D1708 micro-tensile mechanical testing stress-strain curves for 3D printed 300 μm TPS specimens from scale up trial

Table 6.11 - ASTM D1708 micro-tensile mechanical testing measurements for 3D printed 300 μm TPS specimens from scale up trial

	Average	Standard Deviation
Tensile Strength (MPa)	3.598	0.334

Flexural Testing

Seven TPS or NCC-TPS specimens from each of the 3D printing methods underwent flexural mechanical testing following ASTM D790 specifications. Stress-strain curves were plotted and the averages and standard deviations for flexural modulus and strength were determined.

Thermoplastic Starch-Resin Copolymer (TPS) at 100 μm layer height

The ASTM D790 stress-strain curves for seven 3D printed TPS specimens printed at 100 μm layer height are observed in Figure 6.18. The flexural profile follows a ductile material that does not break before the maximum strain. The flexural modulus observed was 188.2 MPa with a deviation of 28.8 MPa. The flexural strength was 7.429 MPa with a deviation of 1.019 MPa. These values are significantly higher than the tensile testing as in flexural testing the layers of rotating tracks are deposited in a plane perpendicular to the applied force, with force acting in tension and compression. The inter track voids are much less significant in compression than in tension. A summary of the flexural mechanical properties for 3D printed 100 μm layer height TPS is included in Table 6.12.

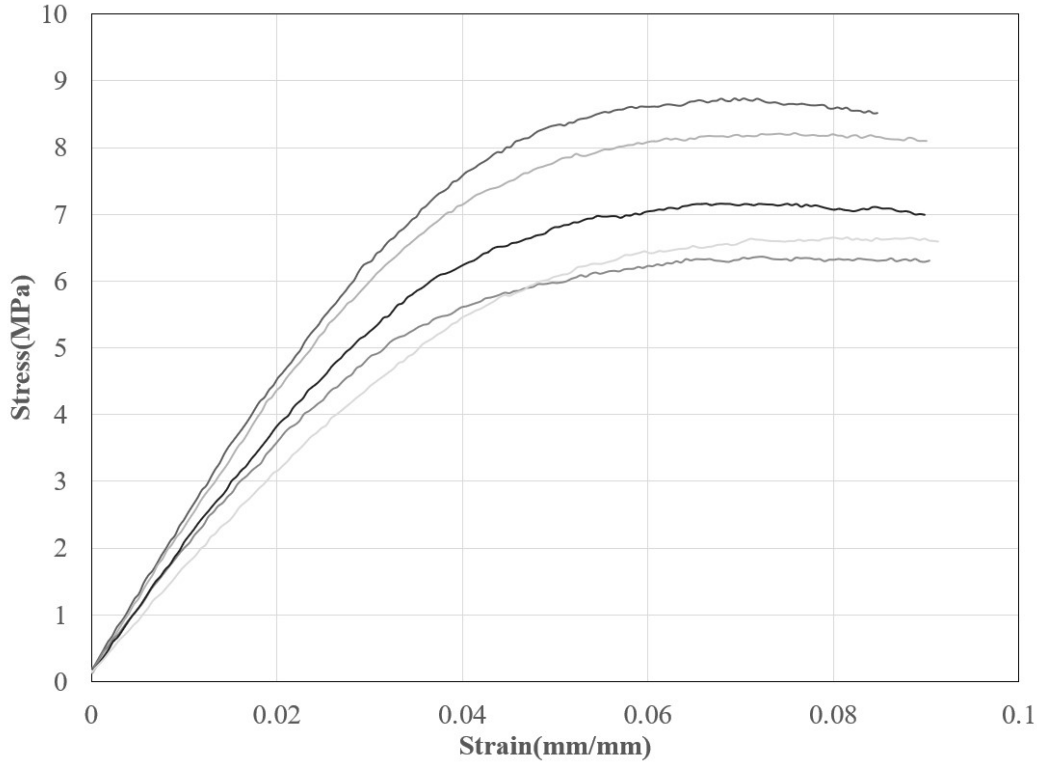


Figure 6.18 - ASTM D790 flexural mechanical testing stress-strain curves for 3D printed 100 μm TPS specimens

Table 6.12 - ASTM D790 flexural mechanical testing measurements for 3D printed 100 μm TPS specimens

100 μm TPS	Average	Standard Deviation
Flexural Strength (MPa)	7.429	1.019
Flexural Modulus (MPa) sec @ 1%	188.181	28.781

Thermoplastic Starch-Resin Copolymer (TPS) at 200 μm layer height

The ASTM D790 stress-strain curves for seven 3D printed TPS specimens printed at 200 μm layer height are observed in Figure 6.19. The flexural profile follows a ductile material that does not break before the maximum strain. The flexural modulus observed was 197.1 MPa with a deviation of 9.5 MPa. The flexural strength was 8.191 MPa with a deviation of 0.235 MPa. Overall, the 200 μm layer height shows slight improvement over the 100 μm TPS sample, about 4.7% increase in modulus and 10.2% in strength. All of the mechanical properties at 200 μm have much less deviation than 100 μm , this can be attributed to the more unreliable and unrepeatable printing process for the very thin layer heights, in this case the nozzle to layer height ratio is around 4:1 (below the good threshold). A summary of the flexural mechanical properties for 3D printed 200 μm layer height TPS is included in Table 6.13.

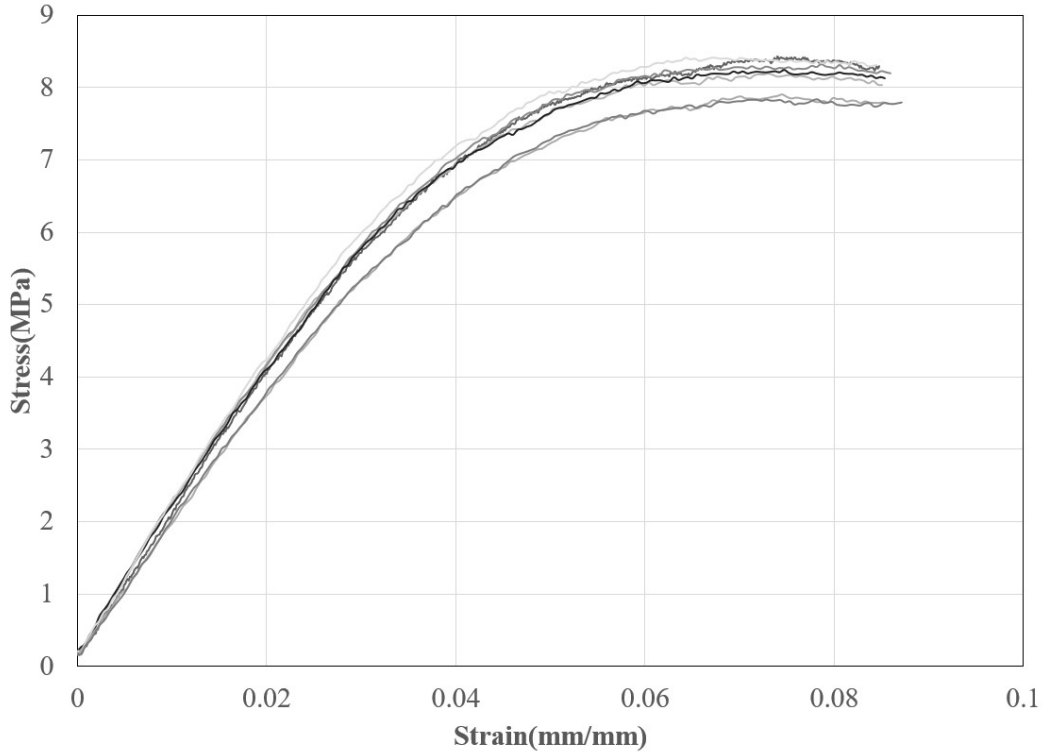


Figure 6.19 - ASTM D790 flexural mechanical testing stress-strain curves for 3D printed 200 μm TPS specimens

Table 6.13 - ASTM D790 flexural mechanical testing measurements for 3D printed 200 μm TPS specimens

200 μm TPS	Average	Standard Deviation
Flexural Strength (MPa)	8.191	0.235
Flexural Modulus (MPa) sec @ 1%	197.055	9.524

Thermoplastic Starch-Resin Copolymer (TPS) at 300 μm layer height

The ASTM D790 stress-strain curves for four 3D printed TPS specimens printed at 300 μm layer height are observed in Figure 6.20. The flexural profile follows a ductile material that does not break before the maximum strain. The flexural modulus observed was 183.95 MPa with a deviation of 17.487 MPa. The flexural strength was 6.890 MPa with a deviation of 0.676 MPa. The flexural strength and modulus for the 300 μm samples are slightly lower than both the 100 μm and 200 μm TPS samples. A summary of the flexural mechanical properties for 3D printed 300 μm layer height TPS is included in Table 6.14.

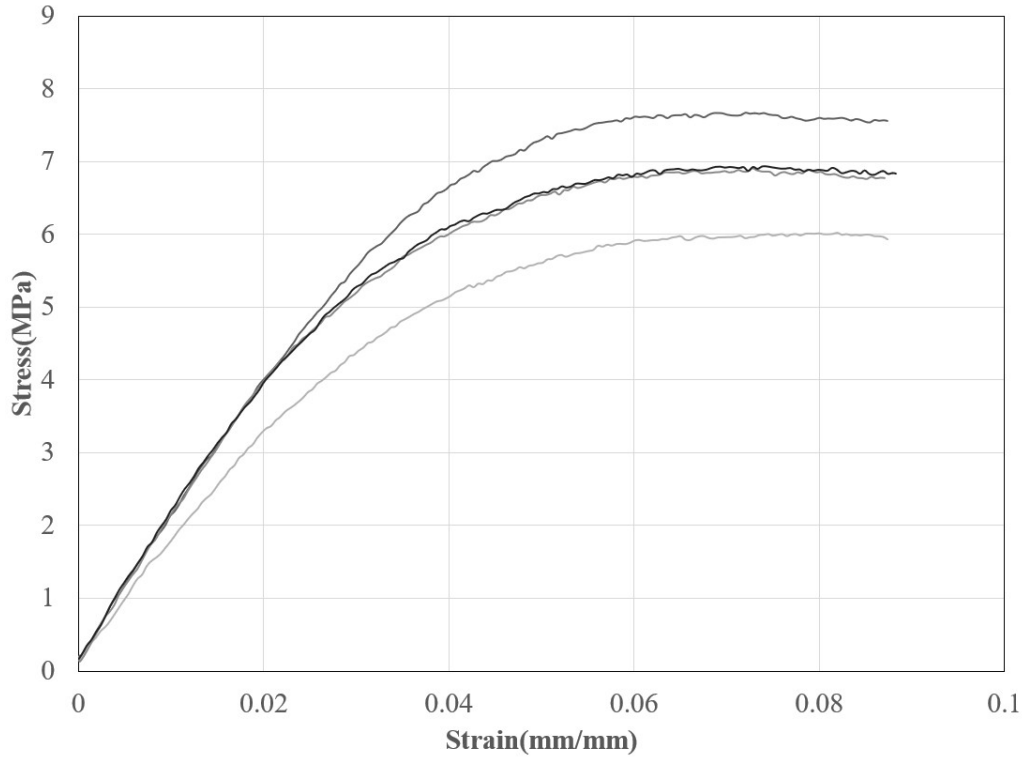


Figure 6.20 - ASTM D790 flexural mechanical testing stress-strain curves for 3D printed 300 μm TPS specimens

Table 6.14 - ASTM D790 flexural mechanical testing measurements for 3D printed 300 μm TPS specimens

300 μm TPS	Average	Standard Deviation
Flexural Strength (MPa)	6.890	0.676
Flexural Modulus (MPa) sec @ 1%	183.950	17.487

1% NCC - Thermoplastic Starch-Resin Copolymer (TPS) at 300 μm layer height

The ASTM D790 stress-strain curves for four 3D printed TPS specimens printed at 300 μm layer height with 1% incorporation of NCC by weight are observed in Figure 6.21. The flexural profile follows a ductile material that does not break before the maximum strain. The flexural modulus observed was 155.0 MPa with a deviation of 15.1 MPa. The flexural strength was 6.619 MPa with a deviation of 0.533 MPa. With the addition of 1% NCC the flexural modulus observed a decrease of 15.7% with only 3.9% decrease in flexural strength. A summary of the flexural mechanical properties for 3D printed 1% NCC-TPS layer height TPS is included in Table 6.15.

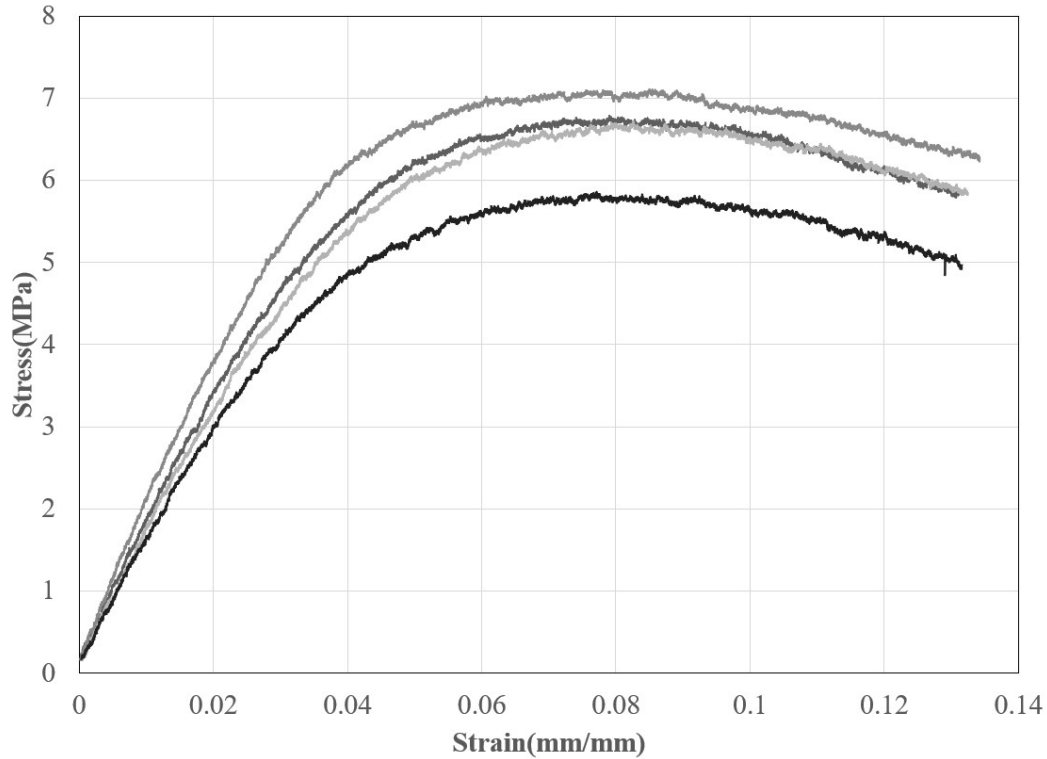


Figure 6.21 - ASTM D790 flexural mechanical testing stress-strain curves for 3D printed 300 μm 1% NCC-TPS specimens

Table 6.15 - ASTM D790 flexural mechanical testing measurements for 3D printed 300 μm 1% NCC-TPS specimens

300 μm 1% NCC-TPS	Average	Standard Deviation
Flexural Strength (MPa)	6.619	0.533
Flexural Modulus (MPa) sec @ 1%	155.043	15.082

3% NCC - Thermoplastic Starch-Resin Copolymer (TPS) at 300 μm layer height

The ASTM D790 stress-strain curves for seven 3D printed TPS specimens printed at 300 μm layer height with 3% incorporation of NCC by weight are observed in Figure 6.22. The flexural profile follows a ductile material that does not break before the maximum strain. The flexural modulus observed was 176.6 MPa with a deviation of 15.4 MPa. The flexural strength was 7.547 MPa with a deviation of 0.601 MPa, showing an increase in both properties compared to the 1% NCC-TPS sample. Compared to the 300 μm pure TPS sample the flexural modulus observed a decrease of only 4.0% while the flexural strength increased by 9.5%. This is very similar to the same 3% NCC-TPS sample in tensile, but with a significantly smaller drop in modulus. A summary of the flexural mechanical properties for 3D printed 3% NCC-TPS layer height TPS is included in Table 6.16.

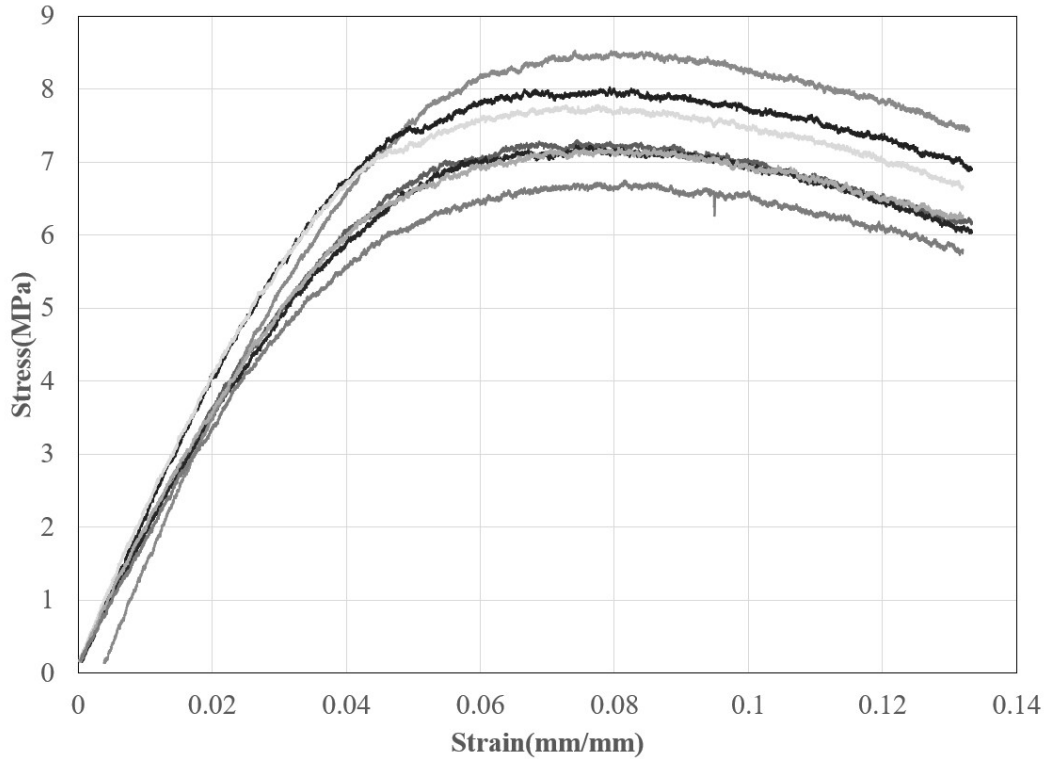


Figure 6.22 - ASTM D790 flexural mechanical testing stress-strain curves for 3D printed 300 μm 3% NCC-TPS specimens

Table 6.16 - ASTM D790 flexural mechanical testing measurements for 3D printed 300 μm 3% NCC-TPS specimens

300 μm 3% NCC-TPS	Average	Standard Deviation
Flexural Strength (MPa)	7.547	0.601
Flexural Modulus (MPa) sec @ 1%	176.625	15.421

5% NCC - Thermoplastic Starch-Resin Copolymer (TPS) at 300 μm layer height

The ASTM D790 stress-strain curves for seven 3D printed TPS specimens printed at 300 μm layer height with 5% incorporation of NCC by weight are observed in Figure 6.23. The flexural profile follows a ductile material that does not break before the maximum strain. The flexural modulus observed was 178.0 MPa with a deviation of 28.9 MPa. The flexural strength was 6.869 MPa with a deviation of 0.883 MPa, again showing a slight increase in flexural modulus over the 1% and 3%-NCC-TPS samples, although the flexural strength dropped slightly below that of the 3% NCC-TPS. Compared to the 300 μm pure TPS sample the flexural modulus observed a decrease of only 3.2% while the flexural strength was nearly identical. A summary of the flexural mechanical properties for 3D printed 3% NCC-TPS layer height TPS is included in Table 6.17.

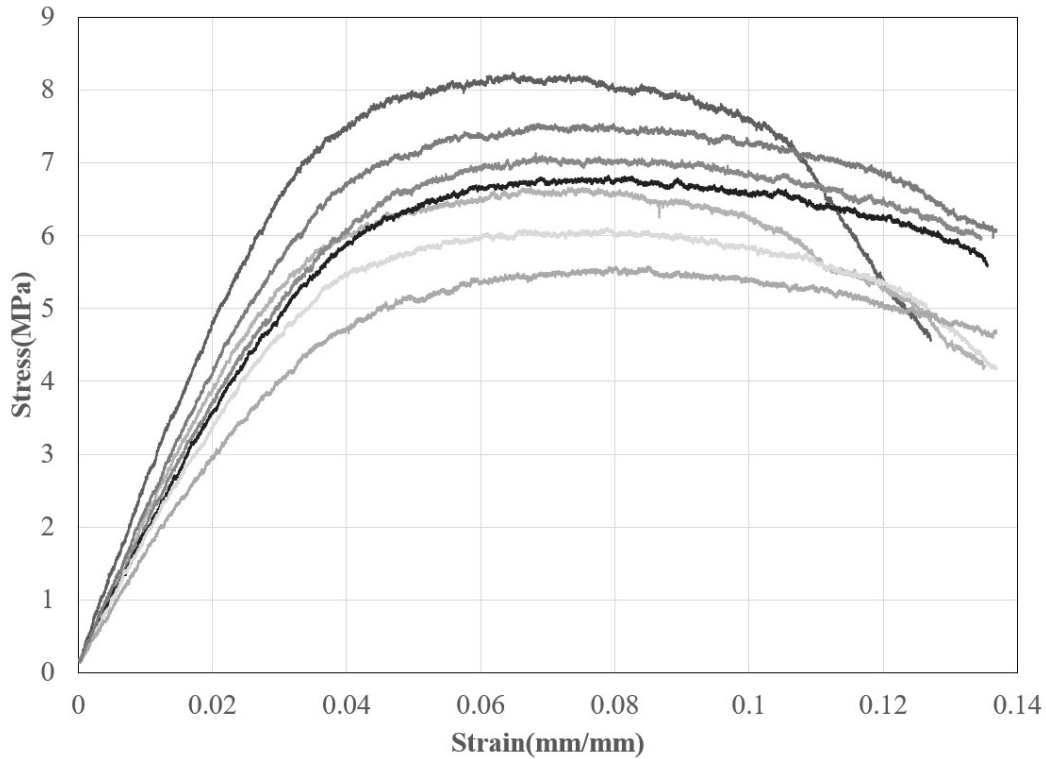


Figure 6.23 - ASTM D790 flexural mechanical testing stress-strain curves for 3D printed 300 μm 5% NCC-TPS specimens

Table 6.17 - ASTM D790 flexural mechanical testing measurements for 3D printed 300 μm 5% NCC-TPS specimens

300 μm 5% NCC-TPS	Average	Standard Deviation
Flexural Strength (MPa)	6.869	0.883
Flexural Modulus (MPa) sec @ 1%	178.041	28.858

20% NCC - Thermoplastic Starch-Resin Copolymer (TPS) at 300 μm layer height

The ASTM D790 stress-strain curves for a single 3D printed TPS specimens printed at 300 μm layer height with 20% incorporation of NCC by weight are observed in Figure 6.24. The flexural profile follows a ductile material that does not break but begins to deform before the maximum strain. The flexural modulus observed was 179.376 MPa. The flexural strength was 6.445 MPa. The 20% NCC-TPS sample showed the highest modulus of all the NCC modified samples but the lowest flexural strength, both properties are still below the 300 μm pure TPS standard. This comparison should be taken loosely as only one specimen was tested due to limited filament supply and difficulty of 3D printing. A summary of the flexural mechanical properties for 3D printed 3% NCC-TPS layer height TPS is included in Table 6.18.

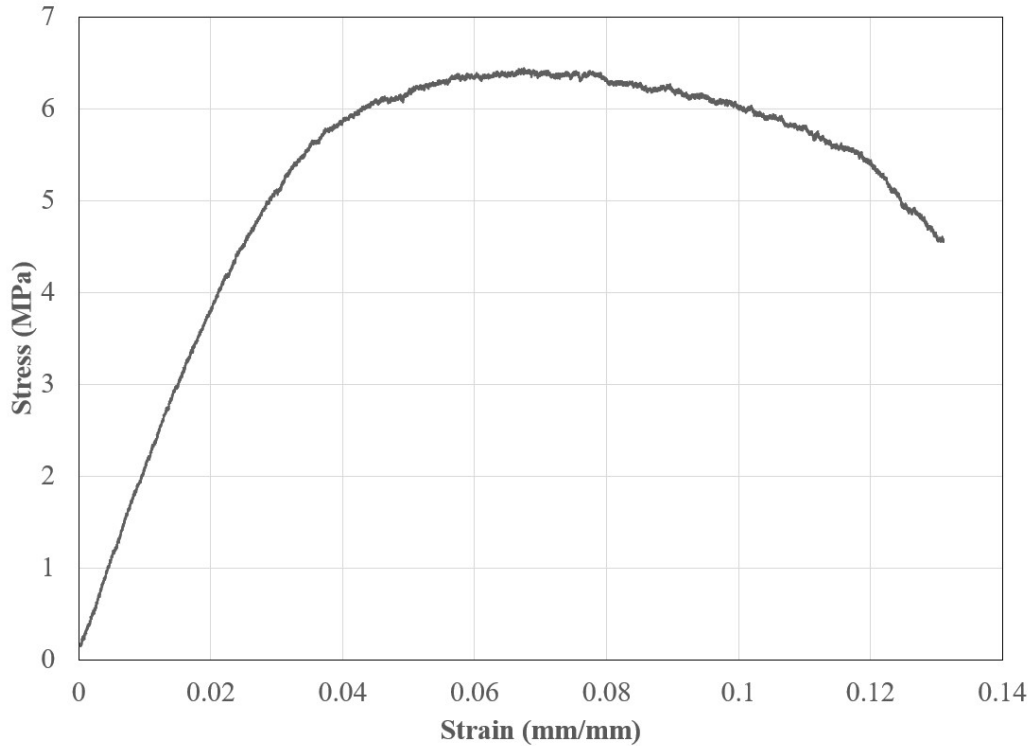


Figure 6.24 - ASTM D790 flexural mechanical testing stress-strain curves for single 3D printed 300 μm 20% NCC-TPS specimen

Table 6.18 - ASTM D790 flexural mechanical testing measurements for single 3D printed 300 μm 20% NCC-TPS specimens

300 μm 20% NCC-TPS	Value
Flexural Strength (MPa)	6.445
Flexural Modulus (MPa) sec @ 1%	179.376

2% NCC - Thermoplastic Starch-Resin Copolymer (TPS) at 300 μm layer height (Scale-up)

The ASTM D790 stress-strain curves for seven 3D printed scale-up TPS specimens printed at 300 μm layer height with 2% incorporation of NCC by weight are observed in Figure 6.25. The flexural profile follows a ductile material that does not break before the maximum strain. The results for the flexural testing of the 2% NCC-TPS scale-up are more reliable for comparison with the lab scale Filastruder study. The flexural modulus observed was 124.7 MPa with a deviation of 12.4 MPa. The flexural strength was 4.605 MPa with a deviation of 0.369 MPa. Although the NCC loading does not match exactly with the lab scale study, we can see it falls below each the 1, 3, and 5% NCC-TPS results. If a linear relationship is considered between 1 and 3% NCC-TPS and the mechanical properties, this suggests a drop of 24.8% for the modulus and 35.0% for the strength. A summary of the flexural mechanical properties for 3D printed scale-up of 2% NCC-TPS layer height TPS is included in Table 6.19.

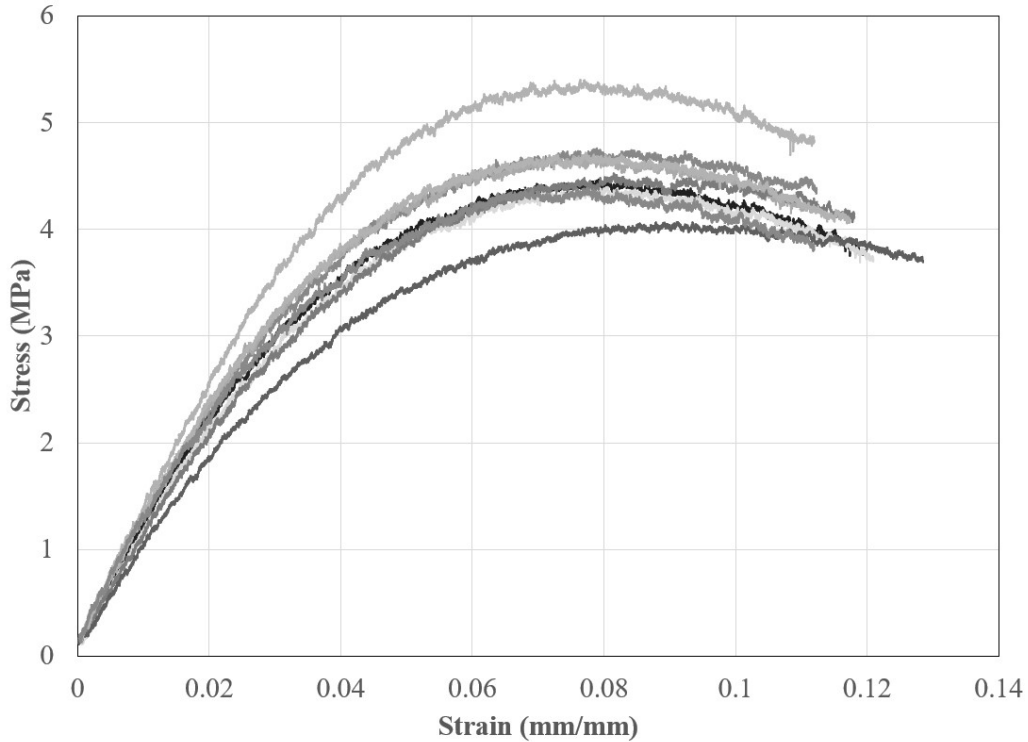


Figure 6.25 - ASTM D790 flexural mechanical testing stress-strain curves for 3D printed 300 μm 2% NCC-TPS specimens from scale up trial

Table 6.19 - ASTM D790 flexural mechanical testing measurements for 3D printed 300 μm 2% NCC-TPS specimens from scale up trial

Results	Average	Standard Deviation
Flexural Modulus (MPa) - Secant @ 1%	124.676	12.428
Flexural Strength (MPa)	4.605	0.369

Comparison of TPS and NCC-TPS Bench and Scale-up Mechanical Properties

Figure 6.26 combines the collected tensile moduli and flexural moduli for each of the TPS samples produced and tested. The primary variables that were explored include: i) the 3D printing layer height for pure TPS (100, 200, and 300 μm TPS represented with solid bars); ii) incorporation of NCC reinforcements at different loadings (300 μm 1, 3 and 5% NCC-TPS represented with diagonal and horizontal lines); iii) maximum incorporation of NCC at 20% loading (300 μm 20% NCC-TPS represented as white); and iv) scale-up trials of 2% NCC-TPS (represented with diamonds). The results for injection molded samples are presented for comparison [188].

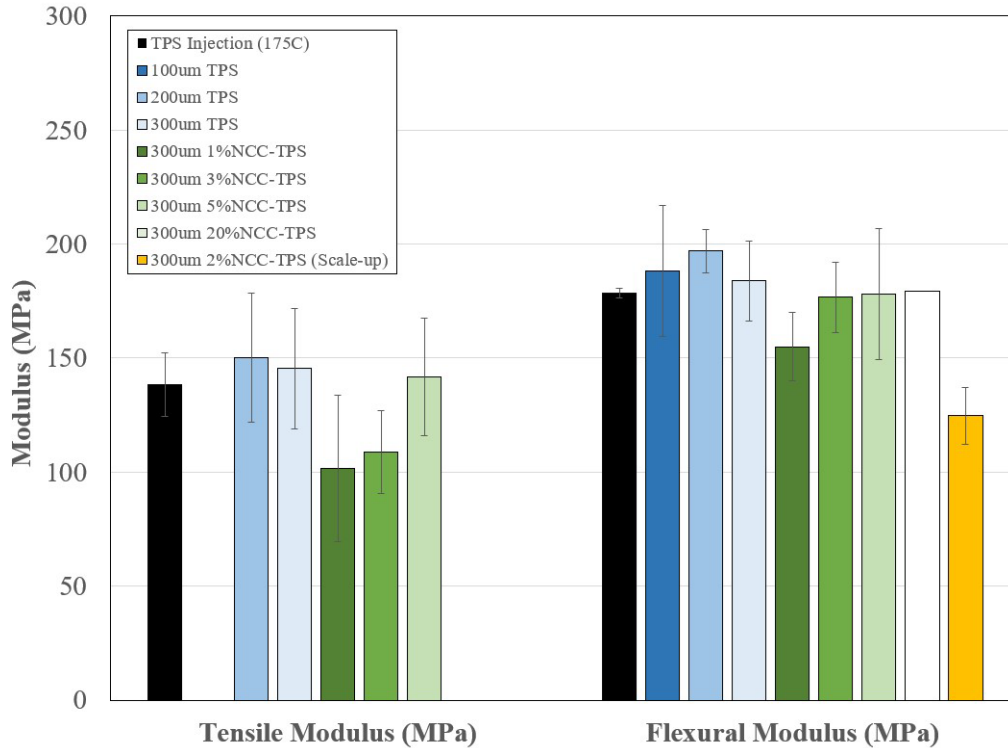


Figure 6.26 - ASTM Tensile Modulus and Flexural Modulus measurements for TPS with varying 3D printed layer heights and NCC loading, as well as scale-up trials

The pure TPS samples had the largest tensile and flexural moduli recorded at 300 μm . In each of the other composite NCC-TPS samples, the modulus was below that of the pure TPS.

Between the three different 3D printed layer heights (100, 200, & 300 μm) for pure TPS, the 200 μm samples show the highest moduli. This can be explained by a balance between less repeatable 3D printing at lower layer heights (due to nozzle geometry) and larger inter track and layer defects at larger layer heights. Printing at a 200 μm layer height provides a great balance of properties as well as overall printing time, as the 100 μm specimens would take twice as long to print.

Another trend that is observed with both the tensile and flexural moduli for the NCC loaded samples is that an increase in NCC loading increases the modulus, with 1% NCC being lowest and 5% highest. The single 20% NCC-TPS sample that was tested also hints that this may have a ceiling as a 400% increase in NCC moved the modulus up only slightly. The flexural modulus for the scale-up trial of 2% NCC-TPS resulted with the lowest modulus of all tests. The elongation at break for the NCC loaded samples showed a significant increase over the pure TPS with 3% NCC loading having the largest elongation. This can be explained by better inter layer and inter track bonding and overall improved homogeneity with the incorporated NCC.

It is important to note that due to the high number of human and machine factors that influence the entire process from filament manufacture, storage and conditioning, 3D printing, scale-up, and mechanical testing there may be other factors that influence some of the results. Although, important to say that caution was paid to hold these factors constant to the best abilities possible.

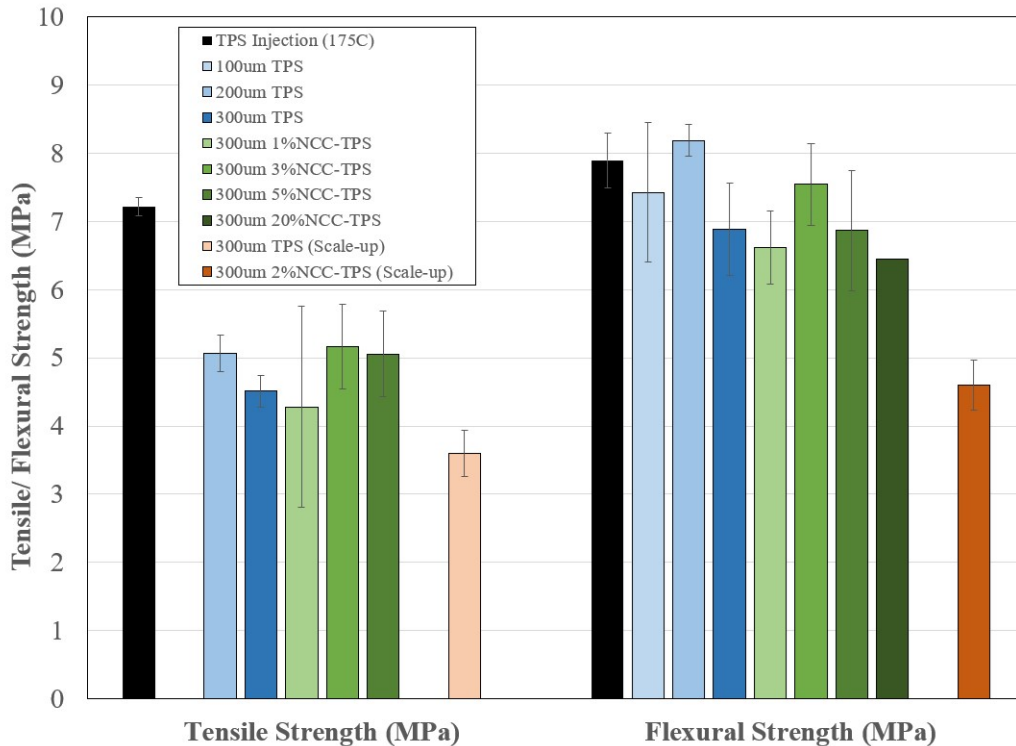


Figure 6.27 - ASTM Tensile Strength and Flexural Strength measurements for TPS with varying 3D printed layer heights and NCC loading, as well as scale-up trials

Figure 6.27 combines the collected tensile and flexural strengths for each of the TPS samples produced and tested. The primary variables that were explored are the same as i) through iv) noted above for the moduli (iv. Also including a pure TPS scale-up). Similar to the trend observed for the moduli, the 200 μm layer height TPS sample showed the best strength for both tensile and flexural testing when compared to the 100 and 300 μm TPS samples – due to the improved homogeneity. Two of the three NCC-TPS samples – 3 and 5 weight % – had an improved tensile and flexural strength compared to the pure TPS, with 3% NCC-TPS having the highest overall tensile and flexural strength (at 300 μm). This occurs because the percolation threshold occurs around 2-3% loading of nanofibers allowing a percolated network of NCC for stress to transfer and diffuse through the composite. The lack of percolation for the 1% NCC-TPS sample explains why there is a decrease compared to pure TPS. As the loading surpasses the percolation threshold, the strength begins to decrease again due to introduction of more defects; this is confirmed with the 20% NCC-TPS sample. The scale-up trials for pure TPS (box pattern in tensile) and 2% NCC-TPS (diamond pattern in flexural) both had a smaller strength to the bench-scale samples. The results for injection molded samples are presented for comparison [188].

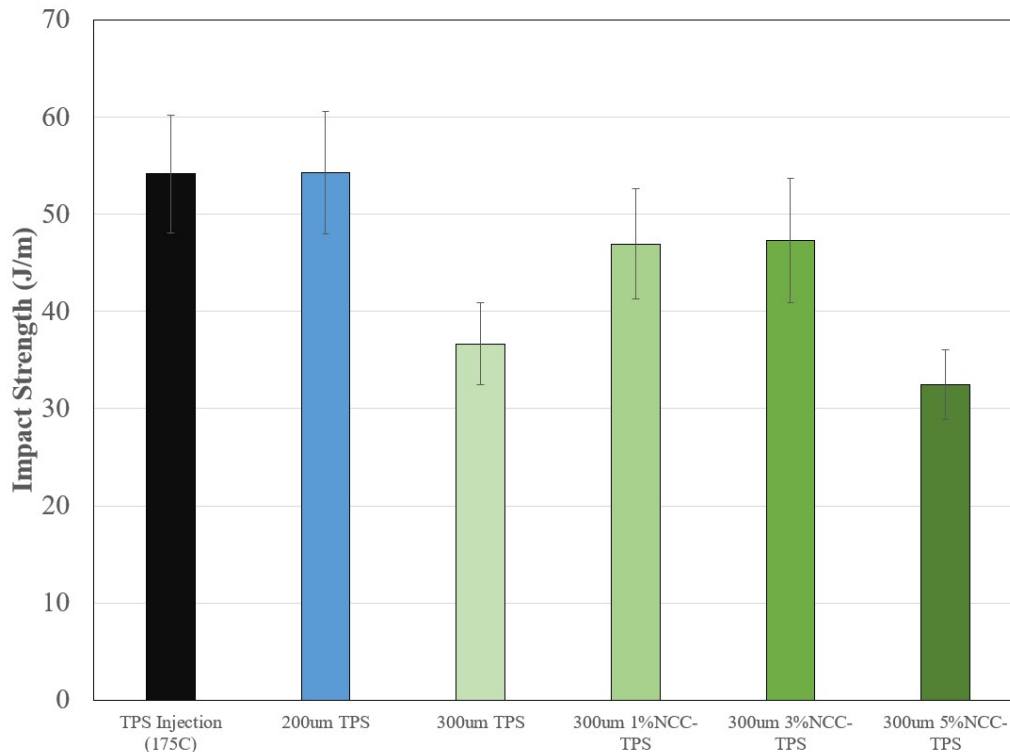


Figure 6.28 - ASTM Impact Strength measurements for TPS with varying 3D printed layer heights and NCC loading, as well as scale-up trial

Figure 6.28 combines the collected impact strengths for each of the TPS and NCC/TPS samples produced and tested. A full comparison has been explored previously in this Section; this chart simply includes the addition of a single scale up trial measurement for the impact strength of 300 μm . This sample with filament produced using the large-scale production equipment has an impact strength of 22.85 J/m with a standard deviation of 3.56 J/m. This is about 63.3% of the benchtop sample of identical 3D printing parameters like layer height. This reduction is similar to the reduction in tensile strength of the same sample, 300 μm TPS, and can be attributed to large increase in moisture present in the scale up production, whereas the benchtop process did not incorporate any water for quenching the filament. This is not needed with the slower benchtop production. The results for injection molded samples are presented for comparison [188].

6.5 – Conclusions

Novel Contributions

Successful thermoplastic starch resin co-polymer (TPS) 3D printing filaments were prepared on the desktop Filastruder filament extruder as well as Nanocrystalline Cellulose (NCC) composite filaments with 1, 3, 5, and 20 wt.-% inclusion. The melt flow index (MFI) was also measured and showed that increasing NCC weight content of the composite resulted in a lower MFI value. The MFI influenced the overall success of a composite blend. Mechanical testing of pure TPS showed that 3D printed specimens could achieve improved mechanical properties over injection molded samples in tensile and flexural modulus, flexural strength, and impact testing, with approximately 8-10% improvements. Tensile strength fell by approximately 30% as a result of the increased

defects and poor interlayer adhesion of 3D printed parts in tension. A layer height of 0.2 mm displayed the best performance of the parts tested.

The inclusion of NCC reinforcements demonstrated an increase in mechanical properties at the 0.3 mm layer height in comparison to the pure TPS at the same print resolution. An inclusion of 3 wt.-% of NCC showed the best performance in tensile, flexural and impact strength, whereas for tensile and flexural modulus, increasing NCC concentration increased modulus. The impact strength, tensile strength, and flexural strength of the 0.3 mm layer height and 3 wt.-% 3D printed specimens increased by 29%, 14%, and 10% over no NCC inclusion.

Scale up trials were successful at producing kilograms of TPS and 2 wt.-% NCC-TPS composite filament. Mechanical properties were lower than the benchtop Filastruder specimens for all formulations tested. Challenges such as moisture and dispersion differences in the filament production techniques could explain the decreases and should be further explored for hydrophilic materials such as NCC and TPS.

Challenges

The primary challenges encountered within the present study included successful filament production, successful 3D printed specimen production, and successful scale-up filament production. For the successful filament production with the desktop Filastruder, special attention was given to ensuring consistent filament diameter. Any section of filament that did not meet 0.05 mm tolerance in each direction would not be used for experimentation. Many hours were spent monitoring the filament production as the throughput was approximately 1 foot per hour. 3D printing requires many conditions to be met for successful part production. The print speed, nozzle temperatures and geometry, and bed temperature, among others, were chosen to ensure the highest chances of a successful print. This is especially time consuming when using a new material that has no set guidelines for success. Overall this was overcome, except for the printing of 0.1 mm specimens as the nozzle tended to be too large and the high shear on the extruded polymer tended to break the web. This could be overcome for lower layer heights by using a smaller diameter nozzle. Finally, the scale-up manufacturing of the TPS and NCC-TPS filament took some trial and error to achieve successful filament on the commercial equipment. Optimal speeds needed to be identified to optimize throughput versus the melt strength of the polymer. If there was a web break in production, the system was required to be re-fed with the length of filament reaching about 200 m. This was a time-consuming task, that was made easier with the assistance of the operating technicians and Bryon Wolff from PSI Inc., the producer of the TPS polymer material.

Chapter 7. Conclusions

Through the completion of literature review, experimentation, and analysis and discussion of results this study hopes to express the advantages of using polymer nanocomposites for applications in advanced manufacturing techniques. Specifically, effects of formulation and processing of thermoplastics and composites containing Nanocrystalline Cellulose (NCC) were explored and characterized for electrospinning and fused deposition modeling 3D printing manufacturing techniques. Applicability of the developed formulations and processes were validated through real-world uses for both techniques.

Using electrospinning, desirable responses were optimized through 6 DOEs for electrospun fibers of 3 material systems by controlling up to four formulation and processing factors. Regression models were developed for fiber diameter, beading density, and bead diameter for each material system and improved with center point measurements where applicable. The three material systems include: NCC and PC in THF:DMF, NCC and PC in chloroform, and NCC and PA 6,6 in formic acid.

For NCC and PC in THF:DMF, the inclusion of NCC tended to improve the spinnability of the system. Less beading, smaller fibers, and more pristine fibers were observed with the incorporation of 2-wt% of NCC with PC. Modified NCC (cNCC) and PC in chloroform was the least ideal system tested, as it had a very narrow window of parameters to achieve desirable fibers. Concentrations of PC are required to be greater than 15-wt% to achieve some fibers and this was improved through the addition of cNCC, but the resulting uniformity and repeatability of the chloroform solvent was not ideal for the current benchtop experimental setup.

Modified NCC and PA 6,6 lead to the most desirable fibers, with sub-micron fiber diameters that can lead to desired nanoscale effects, like extremely high surface area and slip-flow filtration benefits. The cNCC and PA 6,6 system did not include any beading and produced a regression model for fiber diameter that has an R-squared fit of 0.999, making it excellent for producing desired fiber diameters. The results are consistent with literature for PC and PA 6,6 and add upon this through the inclusion of NCC and modified NCC. Proof of concept application of electrospun fibers in transparent coatings with improved surface properties were presented and validated through microhardness and light transmittance testing.

To further refine the methods presented and build more confidence in the experimental results, moving this project forward suggested research would include the following: confirmation of inclusion and dispersion and axial arrangement of NCC in electrospun composite fibers via TEM, the degree of crystallization of the fiber mats, explore new methodologies for improved pristine fibers as well as addressing scale-up and environmental concerns through reduction of solvent, identify degree of branching of fibers as well as porosity of the mat, and finally, how each of the responses may affect the final mechanical properties of the mat. Some ideas and preliminary exploration of these concepts are presented later in this chapter in – Inspiration for Continued Work.

Using 3D printing, several thermoplastics and composites were explored including thermoplastic starch (TPS) and NCC reinforced TPS. 3D printer filaments were designed and manufactured on a benchtop scale as well as in a scale-up facility used for industrial production. ASTM specimens were 3D printed on the Makerbot Replicator 2X printer with Gcode and slicing parameters optimized for the new formulation. Mechanical Properties were measured for impact, tensile, and flexural testing and layer bonding artifacts were explored. 3D Printing slightly increased tensile and flexural modulus relative to injection molding techniques, while only slightly decreasing impact, flexural and tensile strength, suggesting that 3D printing may be a suitable replacement process for certain applications. The addition of NCC to TPS increased tensile and flexural modulus at all loadings while the addition of NCC increased impact, tensile and flexural strength to a maximum at ~3% loading. This 3% loading corresponds with literature and percolation theory. Scale-Up trials were successful at preparing NCC/TPS filaments for 3D printing, but in general, mechanical properties were at about 65-80% of the desktop filament extrusion.

Moving forward with research in NCC reinforced TPS composites for 3D printing, the following research is suggested to improve or corroborate the presented research: confirmation and control of arrangement of NCC dispersions within a feedstock filament as well as in a 3D printed track of a part, optimization of slicing parameters/algorithms to optimize strength through toolpath movement, improve scale-up processing conditions to maintain mechanical properties for hygroscopic polymers like TPS and NCC, experiment with possible NCC/TPS filament compatibility with different printers and part geometries as it is a softer material, assess challenges for industrial application (scale-up).

Further benefit comes from biologically inspired engineering also commonly known as biomimicry. Inspiration for designing a material formulation with medium and high concentrations is in part to attempt to achieve what nature has, mimicking the composition of a plant cell wall. If 50% incorporation is successful, the crystalline cellulose composition of the electrospun mat will be similar to that of plant cell wall, which is a very strong naturally occurring material. Pushing this NCC concentration up to 90%, if successful, could push the mechanical properties of a single spun fiber close to the theoretical values for NCC. The fundamental idea is that it through NCC alignment in the jetting of the electrospun fiber, crystalline grains within the cellulose will align with some grains in an adjacent fiber, leading to some extension of the crystalline regions throughout the fiber, reducing grain boundaries. This crystalline bridging, or pseudo co-crystallinity, will hypothetically push the strength of the spun fiber closer to that of a single NCC fiber.

The material developed for this project has made several steps towards the idea of 3D printing a tree layer-by-layer, in a fashion similar to nature. Self-assembly is a driving force in nature and in can be used as inspiration for biomimicry in engineering. It is not a stretch to imagine an additive manufacturing system that uses artificial intelligence and machine learning to develop and manufacture new products in real time, that learn from their own and others shared history. This is already beginning to happen with generative design, where designers specify constraints and allow machine learning to design new parts that constrain strength, cost, weight, performance, material, heat deflection, and much more. Companies like Stanley Black and Decker and Ford

Motor Company are exploring these methods and implementing them in internal jigs and fixtures for manufacturing as well as to reduce weight of industrial hand tools that are used for many hours per day [189]. Many of these parts have a very organic appearance to them, not far from a tree or plant, with complex geometries that can only be realized through composites and additive manufacturing.



Figure 7.1 – Stanley hydraulic crimping attachment reduced by 3 lb. through generative design [189]

Upon completion of this research, the data and analysis generated has contributed to the areas of exploration in electrospinning and 3D printing of nanocomposites containing Nanocrystalline Cellulose. The results were the first of their kind in many areas including the incorporation of NCC within an electrospun PC fiber as well as compounding with TPS for an all-green nanocomposite for 3D printing.

As electrospinning and 3D printing are complex processes, the reported literature from any new system is extremely beneficial to not only those studying similar material systems, but also those looking to design universal models. Most parameter effects and especially the combined effects are very typical to the specific material and process system and being able to find correlations between different polymer/solvent/additive systems will help advance innovation in electrospinning and additive manufacturing.

This research also has great potential impact on the Nanocrystalline Cellulose industry, especially manufacturers CelluForce in Canada. Generation of new materials and intellectual property with the goal of a commercial product gives feasibility and justification for this new nanoparticle. The NCC has the potential to be incorporated into various polymer composite applications and proving feasibility of the electrospinning process is of benefit to the NCC and composites industry.

7.1 – Summary of Electrospinning Results

The DOE results of the systems explored through Chapters 3 through 5 are presented in Table 7.1 for fiber diameter, bead density, and bead diameter. The goodness-of-fit (R^2) value and lack of fit (LoF) P-values are presented for each model presented.

Table 7.1 - Summary of each of the responses of the six design of experiments including goodness-of-fit (R^2) and Lack of Fit (LoF) P-Values, $\alpha = 0.1$

DOE	System	Fiber Diameter	Bead Density	Bead Diameter
DOE#1	PC in THF/DMF	$R^2 = 97.8\%$	$R^2 = 42.7\%$ LoF = 0.020	$R^2 = 96.2\%$
DOE#2	NCC/PC in THF/DMF	$R^2 = 80.6\%$ LoF = 0.174 CtPt Model $R^2 = 95.4\%$ LoF = 0.174	$R^2 = 90.9\%$ LoF = 0.032	All factors removed and considered insignificant.
DOE#0	PC and NCC/PC in THF/DMF	$R^2 = 87.4\%$ (Saturated)	$R^2 = 51.9\%$	All factors removed and considered insignificant.
DOE#3	PC in Chloroform	$R^2 = 88.2\%$ LoF = 0.035 CtPt Model $R^2 = 95.5\%$ LoF = 0.035	$R^2 = 66.0\%$ LoF = 0.540	All factors removed and considered insignificant.
DOE#4	cNCC/PC in Chloroform	$R^2 = 36.5\%$ LoF = 0.452	All factors removed and considered insignificant.	All factors removed and considered insignificant.
DOE#5	cNCC/PA 6,6 in Formic Acid	$R^2 = 87.4\%$ LoF = 0.022 CtPt Model $R^2 = 99.9\%$	No beads present.	No beads present.

For DOE#1, PC in THF/DMF, the regression model generated for the fiber diameter response had a good fit with only a few outliers in the residuals between the fitted means and measured responses. The model is adequate at predicting measurements at different levels within the ranges explored for PC concentration, voltage, and gap distance. The model for bead density was less adequate at fitting the relationship with the factors but did identify low PC concentration as a leading factor to bead formation and density. It is recommended to use concentrations of greater than 23.9% StarPlastic PC when using a THF/DMF mix solvent for fiber production and reduce

gap distance and voltage when using a lower concentration. The model for bead diameter presented a very similar result.

For DOE#2, 2 wt.-% NCC/PC in THF/DMF, the regression model generated for the fiber diameter response had a good fit but was improved through the incorporation of center-point data to account for curvature in the data. The model is adequate at predicting measurements at different levels within the ranges explored for PC concentration, voltage, and gap distance. The model for bead density was less adequate at fitting the relationship with the factors but did identify low PC concentration as a leading factor to bead formation and density. Similar to DOE#1, higher PC concentration will give better fibers, but to reduce diameter as well all three factors tested should be reduced simultaneously (i.e. use of a smaller electrospinning set-up with low [PC]). No model for bead diameter was successful due to no significant factors.

For DOE#0, PC in chloroform, the regression model generated for the fiber diameter response (up to 2nd level co-factors due to saturation) has a good fit with only a few outliers in the residuals between the fitted means and measured responses. The DOE also confirmed the addition of NCC also increases fiber diameter, but also reduced beading and increased branching. The model for bead density was less adequate at fitting the relationship with the factors but did identify higher PC and NCC concentrations will reduce beading.

For DOE#3, PC in chloroform, the regression model generated for the fiber diameter response had a poor fit with many outliers in the residuals between the fitted means and measured responses. The model was not adequate at predicting measurements due to limited fiber production. The model for bead density was more adequate at fitting the relationship with the factors as many beads were present and identified low PC concentration and Lexan PC as leading factors to bead formation and density. It is recommended to use higher concentrations of StarPlastic PC when using a chloroform mix solvent for fiber production and reduce gap distance and voltage when using a lower concentration. The model for bead diameter presented a very similar result.

For DOE#4, 2 wt.-% cNCC/PC in chloroform, the regression model generated for the fiber diameter response had an adequate fit with many outliers in the residuals between the fitted means and measured responses. The model did reiterate the significance of PC concentration on fiber diameter. No model for bead density or bead diameter were successfully generated due to no significant factors.

For DOE#5, 4 wt.-% NCC/PA 6,6 in formic acid, the regression model generated for the fiber diameter response had a good fit but was improved through the incorporation of center-point data to account for curvature in the data. The model is very adequate at predicting measurements at different levels within the ranges explored for PA 6,6 concentration, voltage, and gap distance as many of the residuals are near zero.

Moving forward, experimental recommendations for improving and expanding upon the results of this section include:

- Confirmation and arrangement of NCC and cNCC dispersion via TEM analysis,

- Study interaction of materials via FTIR,
- Reperform DOE#0 with improved factor levels for NCC/PC in THF/DMF,
- Perform a similar 2^4 DOE for cNCC/PC in chloroform and cNCC/PA 6,6 in formic acid.

In conclusion, many significant results can be taken from the analysis performed herein for the different material systems explored. Due to the complexity and subtle differences between every formulation and processing factor considered, special attention should be made to the process developed for analyzing a system in general and can be applied to any new desired system of study, as different applications of the fibers may demand different formulation and processing specifics.

7.2 – Inspiration for Continued Work

7.2.1 – Controlling Electrospinning Temperature

Some possible routes for controlling the temperature would be the inclusion of a heat gun or high-powered lamp to aid in the evaporation of the less volatile solvents like DMF. Incorporation of liquid nitrogen within the vicinity of the electrospinning apparatus will cool the surrounding area and prolong the rate of drying of the more volatile solvents like chloroform or THF. There is also consideration for the construction of a heating element for the syringe to allow for the ability of solvent free electrospinning, advantageous for scale up and environmental factors. Controlling the pressure of the system will also give added benefits to the system. Application of a vacuum will aid in the evaporation of the solvent potentially allowing the ability to fine tune the pressure and thus the evaporation rate of the polymer solution. Figure 7.2 below depicts the schematic designs for some proposed melt-vacuum electrospinnners for the synthesis of composite nanofibers. [2]

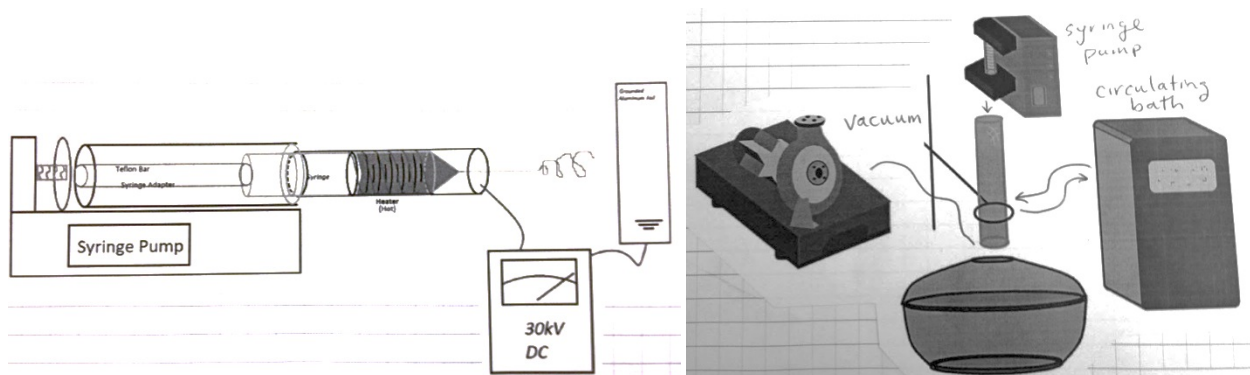


Figure 7.2 - Schematic designs for proposed melt-vacuum electrospinner

Understanding the mechanical properties of a single nanofiber is important, as it is these properties that govern those of the overall mat. As the nanofibers are typically on the order of 100 to 500 nm, they are difficult to isolate and manipulate for testing. At the moment there is no single desirable technique but many new and innovative techniques. Some development has been made in the area of AFM to complete a flexural bending test as well as tensile techniques for testing single or several aligned fibers. In this study the implementation of nanoindentation will be used to find mechanical properties of the single fibers. [2]

In nanoindentation a very fine tip is brought into contact with a single nanofiber and a force is applied to indent the fiber. The tip diameter must be much smaller than the diameter of the nanofiber and the same strain rate must be employed for all data generated to get reliable and comparable data. The nanoindentation is force-controlled and the indentation depth, Z , will increase linearly with the applied load, P . The slope (Equation 7.1) of the curve at the maximum applied load is proportional to the Young's modulus of the material via Equation 4.2, where A is the contact area of the tip. [2]

$$\text{Slope} = [dP/dZ]_{P_{max}} = 2 E^* (A/\pi)^{1/2} \quad (\text{Equation 7.1})$$

Because of uncertainties typically related to A , a reference sample can be used to find the Young's modulus. This technique only requires comparison of the slope, through the above technique, of the nanofiber and the reference sample, R , with the radius of the indentation area, r or r_R . The calculation for the Young's Modulus of the nanofiber, E^* , is then Equation 7.2.

$$\frac{[dP/dZ]_{P_{max}}}{[dP/dZ]_{R_{max}}} = \frac{r}{r_R} \frac{E^*}{E_R^*} \quad (\text{Equation 7.2})$$

$$[dP/dZ]_{R_{max}} \quad r_R E_R^*$$

The processing through electrospinning will have a great effect on the individual nanofiber mechanical properties as well as the mat. Using a different solvent, for example, can affect the fiber morphology due to the change in surface tension and volatility. This could lead to more beading and branching and thus significant differences in the strengths.

7.2.2 – Measuring Branching Density

The branching density is the number of times a fiber will split from one into many fibers without breakage. This may occur during the jetting of the polymer solution or through fusion of wet fibers after striking the collector. In literature the branching density is usually reported as a counts per area metric [34]. This should be normalized to determine a more relative metric, as the density of fibers is not necessarily uniform across a sample mat on the collector and a single or even a few micrographs may not be typical of the entire system. Determining the number of branching vertices per length of fiber is a better option. This can be determined using image analysis software. Figure 7.3 depicts micrographs of low and high concentration examples of branching density within electrospun mats.

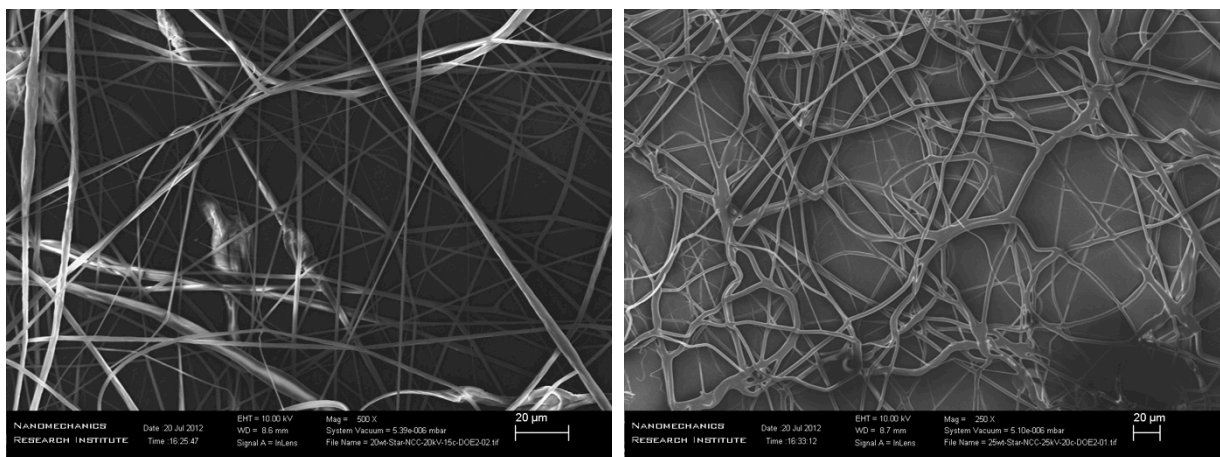


Figure 7.3 - Examples of low (left) and high (right) concentration of branching density electrospun mats

7.2.3 – Measuring Porosity

The porosity is the percentage of average areal coverage of the interstitial areas between the polymer fibers in the mat. Determining the porosity via microscopy is also a very difficult technique as a random area of the mat must be sampled and assumed characteristic of the entire mat. The grey-scale micrograph is turned into a binary image, black or white pixels, through a global threshold. This will turn the fiber areas white and the pores black. Image analysis is completed determining the concentration of the different pixels, or the percent porosity. A lower magnification image is usually easier to analyze and will give a value closer to the true pore size distribution as the sample population will be much larger.

7.2.4 – Mechanical Properties of Electrospun Fibers and Mats

Of most importance in the characterization of the electrospun nanofibers is the mechanical properties not only of the mat but also the individual fibers. Also, as the goal is to fabricate a composite material it would be of great significance to determine the improvement of mechanical properties as a function of the NCC incorporation. For the testing of the mat, dynamical mechanical thermal analysis (DMTA) can be implemented. For the testing of the individual nanofibers, more advanced techniques must be employed such as nano-indentation or flexural tests via atomic force microscopy.

Testing of the nanofiber mats is usually completed using traditional tensile testing methods often with some minor modifications to avoid some issues. The random mat of the electrospun fibers are cut into tiny strips on the order of 1 cm gauge length with a cross section of about 0.6 cm by 0.01-0.02 cm. In order to achieve these thicker nanofiber mats, the electrospinning must be carried out for a prolonged period of time. Extreme caution must be given during the sample preparation as the samples are very fragile and the structural integrity and geometric arrangement of the fibers must be maintained. A process to make this easier has been developed by Ramakrishna and group [2]. This sample preparation technique involves a paper template with parallel strips of double-sided tape onto which a large section of the nanofiber mat is placed and secured with another strip of tape. This framed sample is then cut to the desired width before testing. The mechanical testing is typically carried out on a DMTA apparatus because of the small sample size.

Due to the porosity of the mat, and the fact that much of the test specimen is air, determination of a reliable tensile strength is difficult. Data is usually normalized through a constant volume density of the fibers in the specimen through an areal density of the fibers in the mat [2]. The areal density is the mass of the test piece divided by its area, similar to resistivity in electrical calculations. This will give a stress value in g/tex, where tex is a unit familiar to the textiles industry that is mg per meter of fiber. The equation for stress is then calculated as Equation 7.3.

$$\text{Stress (g/tex)} = \text{Force (g)} / [\text{Width (mm)} \cdot \text{Areal Density (g/m}^2\text{)}] \quad (\text{Equation 7.3})$$

It is also very important to consider the uniformity and homogeneity of the electrospun mat, as it may not be the same across the entire specimen length. Areas of higher bead density or areas of low fiber density will impact the measured mechanical properties of the specimen. Visual inspection via light microscopy is necessary before testing and perhaps a defect threshold criterion should be maintained for all samples.

7.2.5 – Measuring Nanofiber Crystallinity

It is advantageous to determine the degree of crystallinity in the electrospun nanofibers as it will not only show the effect of introducing the NCC into the polymer but also any crystallinity that may have been induced by strain hardening and chain alignment of the polycarbonate. This expected higher crystallinity would likely have a direct effect on the mechanical properties of the individual nanofibers as well as the overall mat.

Using differential scanning calorimetry (DSC) techniques an estimate of the crystallinity in the mat can be found. The technique uses the crystalline melting transition where an exothermic peak is observed. The location of this peak (melting temperature) is indicative of the crystallite size. The area under this curve is proportional to the amount of crystallinity. DSC cannot be used to estimate the crystallinity of cellulose because it goes through thermal decomposition before melting. [2]

X-ray diffraction techniques can also be used to determine an estimate for the crystalline content in a semi-crystalline polymer sample. Similar to the technique introduced for the crystallinity index of cellulose, the crystalline peaks and broad amorphous peak can be deconvoluted and by dividing the area under the crystalline region by the entire area under the curve, an estimate of percent crystallinity can be found. X-ray diffraction can also be used to determine the type of crystalline phases and the relative size of the phases. [2]

References

- [1] J. Lyons, C. Li, and F. Ko, "Melt-electrospinning part I: processing parameters and geometric properties," *Polymer (Guildf)*, vol. 45, no. 22, pp. 7597–7603, Oct. 2004.
- [2] A. Andrady, *Science and Technology of Polymer Nanofibres*, 1st ed. Hoboken, NJ: Wiley-Interscience, 2008.
- [3] W. E. Teo and S. Ramakrishna, "A review on electrospinning design and nanofibre assemblies," *Nanotechnology*, vol. 17, no. 14, 2006.
- [4] P. Heikkilä and A. Harlin, "Parameter study of electrospinning of polyamide-6," *Eur. Polym. J.*, vol. 44, no. 10, pp. 3067–3079, Oct. 2008.
- [5] P. Lu and B. Ding, "Applications of electrospun fibers," *Recent Pat. Nanotechnol.*, vol. 2, no. 3, pp. 169–182, 2008.
- [6] GrandView Research, "Nanofibers Market Analysis By Product, End-Use, and Segment: Forecasts To 2024," 2016. [Online]. Available: <https://www.grandviewresearch.com/industry-analysis/nanofibers-market>. [Accessed: 03-Jun-2019].
- [7] S. Ramkumar, "Nanofiber market to reach \$4 billion by 2020," *Textile News United States Of America*, 2011. [Online]. Available: http://www.fibre2fashion.com/news/textile-news/newsdetails.aspx?news_id=99282. [Accessed: 31-Jul-2012].
- [8] S. Crump, "Apparatus and method for creating three-dimensional objects," US5121329, 1992.
- [9] Protolabs, "Rapid Prototyping and On-Demand Production," 2019. [Online]. Available: <https://www.protolabs.com/>. [Accessed: 25-Aug-2017].
- [10] EY, "EY Global 3D Printing Report 2016," 2016. [Online]. Available: <https://www.ey.com/de/de/services/advisory/performance-improvement/supply-chain/ey-global-3d-printing-report-2016-experience-and-expectations>. [Accessed: 25-Aug-2019].
- [11] T. T. Wohlers, I. Campbell, O. Diegel, and J. Kowen, "Wohlers Report 2018," 2018.
- [12] T. C. Sottek, "Inside Microsoft's model shop, where prototypes are printed in 3D," *The Verge*, 2011. [Online]. Available: <http://www.theverge.com/2011/12/20/2650157/microsoft-model-lab-3d-printing-video>. [Accessed: 27-Mar-2013].
- [13] L. Y. Yeo and J. R. Friend, "Electrospinning carbon nanotube polymer composite nanofibers," *J. Exp. Nanosci.*, vol. 1, no. 2, pp. 177–209, Jun. 2006.
- [14] R. Sahay *et al.*, "Electrospun composite nanofibers and their multifaceted applications," *J. Mater. Chem.*, vol. 22, no. 26, p. 12953, 2012.
- [15] R. Berry and R. Crostogino, "Nanocrystalline Cellulose - 'Green' Nanoparticles," 2008. [Online]. Available: http://www.fpinnovations.ca/pdfs/NCC-flyer_EN.pdf. [Accessed: 22-Feb-2019].

- [16] R. V. N. N. Krishnappa, K. Desai, and C. Sung, "Morphological study of electrospun polycarbonates as a function of the solvent and processing voltage," *J. Mater. Sci.*, vol. 38, no. 11, pp. 2357–2365, Jun. 2003.
- [17] A. C. Finkle, C. R. Reddy, and L. C. Simon, "Thermal stability of nanocrystalline cellulose," in *Biocomp 2010: 10th Pacific Rim Bio-Based Composites Symposium*, 2010.
- [18] A. C. Finkle, "Cellulose-Polycarbonate Nanocomposites: A novel window alternative," University of Waterloo, 2011.
- [19] M. A. Hubbe, O. J. Rojas, L. A. Lucia, and M. Sain, "Cellulosic nanocomposites: A Review," *BioResources*, vol. 3, no. 3, pp. 929–980, 2008.
- [20] G. Taylor, "Electrically Driven Jets," *Proc. R. Soc. A Math. Phys. Eng. Sci.*, vol. 313, no. 1515, pp. 453–475, Dec. 1969.
- [21] P. K. Baumgarten, "Electrostatic spinning of acrylic microfibers," *J. Colloid Interface Sci.*, vol. 36, no. 1, pp. 71–79, May 1971.
- [22] D. H. Reneker and I. Chun, "Nanometre diameter fibres of polymer, produced by electrospinning," *Nanotechnology*, vol. 7, no. 3, pp. 216–223, Sep. 1996.
- [23] A. F. Spivak and Y. A. Dzenis, "A condition of the existence of a conductive liquid meniscus in an external electric field," *J. Appl. Mech. Trans. ASME*, vol. 66, no. 4, pp. 1026–1028, 1999.
- [24] M. M. Hohman, Y. M. Shin, M. P. Brenner, and G. C. Rutledge, "Experimental characterization of electrospinning: the electrically forced jet and instabilities," *Polymer (Guildf.)*, vol. 42, no. 25, pp. 09955–09967, Dec. 2001.
- [25] Y. M. Shin, M. M. Hohman, M. P. Brenner, and G. C. Rutledge, "Electrospinning: A whipping fluid jet generates submicron polymer fibers," *Appl. Phys. Lett.*, vol. 78, no. 8, pp. 1149–1151, Feb. 2001.
- [26] J. Deitzel, "Controlled deposition of electrospun poly(ethylene oxide) fibers," *Polymer (Guildf.)*, vol. 42, no. 19, pp. 8163–8170, Sep. 2001.
- [27] J. Doshi and D. H. Reneker, "Electrospinning process and applications of electrospun fibers," *J. Electrostat.*, vol. 35, no. 2–3, pp. 151–160, Aug. 1995.
- [28] C. Zhang, X. Yuan, L. Wu, Y. Han, and J. Sheng, "Study on morphology of electrospun poly(vinyl alcohol) mats," *Eur. Polym. J.*, vol. 41, no. 3, pp. 423–432, Mar. 2005.
- [29] D. Wang, G. Sun, B.-S. Chiou, and J. P. Hinestroza, "Controllable fabrication and properties of polypropylene nanofibers," *Polym. Eng. Sci.*, vol. 47, no. 11, pp. 1865–1872, Nov. 2007.
- [30] K.-H. Lee *et al.*, "Electrospinning of Syndiotactic Polypropylene from a Polymer Solution at Ambient Temperatures," *Macromolecules*, vol. 42, no. 14, pp. 5215–5218, Jul. 2009.
- [31] S. R. Givens, K. H. Gardner, J. F. Rabolt, and B. Chase, "High-Temperature Electrospinning of Polyethylene Microfibers from Solution," *Macromolecules*, vol. 40, no. 3, pp. 608–610, Feb. 2007.

- [32] G.-M. Kim, G. H. Michler, and P. Pötschke, “Deformation processes of ultrahigh porous multiwalled carbon nanotubes/polycarbonate composite fibers prepared by electrospinning,” *Polymer (Guildf)*, vol. 46, no. 18, pp. 7346–7351, Aug. 2005.
- [33] N. Kattamuri and C. Sung, “Uniform Polycarbonate Nanofibers Produced By Electrospinning,” in *NSTI-Nanotech*, 2004, vol. 3.
- [34] J. Shawon and C. Sung, “Electrospinning of polycarbonate nanofibers with solvent mixtures THF and DMF,” *J. Mater. Sci.*, vol. 39, no. 14, pp. 4605–4613, Jul. 2004.
- [35] C. Meechaisue, R. Dubin, P. Supaphol, V. P. Hoven, and J. Kohn, “Electrospun mat of tyrosine-derived polycarbonate fibers for potential use as tissue scaffolding material,” *J. Biomater. Sci. Polym. Ed.*, vol. 17, no. 9, pp. 1039–1056, 2006.
- [36] A. Welle, M. Kröger, M. Döring, K. Niederer, E. Pindel, and I. S. Chronakis, “Electrospun aliphatic polycarbonates as tailored tissue scaffold materials,” *Biomaterials*, vol. 28, no. 13, pp. 2211–2219, Apr. 2007.
- [37] S. Warner, A. Buer, and S. Ugbohue, “A Fundamental Investigation of the Formation and Properties of Electrospun Fibers,” National Textile Center, 1998.
- [38] R. Jaeger, M. M. Bergshoef, C. M. I. Battle, H. Schönherr, and G. Julius Vancso, “Electrospinning of ultra-thin polymer fibers,” *Macromol. Symp.*, vol. 127, no. 1, pp. 141–150, Feb. 1998.
- [39] R. Baba and S. H. Jayaram, “An IGBT-Based Pulsed Power Supply in the Fabrication of Non-Contiguous Nanofibres Using Electrospinning,” in *2010 IEEE Industry Applications Society Annual Meeting*, 2010, pp. 1–4.
- [40] Elmarco Inc., “NS 8S1600U.” [Online]. Available: <https://www.elmarco.com/production-lines/ns-8s1600u>. [Accessed: 15-Aug-2019].
- [41] FibeRio Technology Corp., “FibeRio Announces Release of Cyclone L-1000: Enables Forcespinning Nanofibers,” *PRWeb Press Release*, 2010. [Online]. Available: <https://www.prweb.com/releases/2010/11/prweb4740564.htm>. [Accessed: 18-Jun-2015].
- [42] Y. Li, “Emulsion-Electrospinning of Nanocrystalline Cellulose Reinforced Nanocomposite Fibres,” University of British Columbia, 2010.
- [43] Y. Dror, W. Salalha, R. L. Khalfin, Y. Cohen, A. L. Yarin, and E. Zussman, “Carbon Nanotubes Embedded in Oriented Polymer Nanofibers by Electrospinning,” *Langmuir*, vol. 19, no. 17, pp. 7012–7020, Aug. 2003.
- [44] A. Hivechi, S. H. Bahrami, and R. A. Siegel, “Drug release and biodegradability of electrospun cellulose nanocrystal reinforced polycaprolactone,” *Mater. Sci. Eng. C*, vol. 94, no. September 2018, pp. 929–937, 2019.
- [45] S. Huan, L. Bai, W. Cheng, and G. Han, “Manufacture of electrospun all-aqueous poly(vinyl alcohol)/cellulose nanocrystal composite nanofibrous mats with enhanced properties through controlling fibers arrangement and microstructure,” *Polymer (Guildf)*, vol. 92, pp. 25–35, 2016.

- [46] J. O. Zoppe, M. S. Peresin, Y. Habibi, R. A. Venditti, and O. J. Rojas, “Reinforcing poly(epsilon-caprolactone) nanofibers with cellulose nanocrystals,,” *ACS Appl. Mater. Interfaces*, vol. 1, no. 9, pp. 1996–2004, Sep. 2009.
- [47] M. Wang, H.-J. Jin, D. L. Kaplan, and G. C. Rutledge, “Mechanical Properties of Electrospun Silk Fibers,” *Macromolecules*, vol. 37, no. 18, pp. 6856–6864, Sep. 2004.
- [48] I. W. Baek, J. Y. Jaung, S. H. Kim, and H. Ahn, “Electrospinning of Polycarbonate/Tetrapyrzinoindoloporphyrazine Composite Fibers,” *Mol. Cryst. Liq. Cryst.*, vol. 472, no. 1, pp. 181–191, Aug. 2007.
- [49] T. D. Fornes, J. W. Baur, Y. Sabba, and E. L. Thomas, “Morphology and properties of melt-spun polycarbonate fibers containing single- and multi-wall carbon nanotubes,” *Polymer (Guildf)*, vol. 47, no. 5, pp. 1704–1714, Feb. 2006.
- [50] X. Xie, Y. Mai, and X. Zhou, “Dispersion and alignment of carbon nanotubes in polymer matrix: A review,” *Mater. Sci. Eng. Reports*, vol. 49, no. 4, pp. 89–112, May 2005.
- [51] M. Moniruzzaman and K. I. Winey, “Polymer Nanocomposites Containing Carbon Nanotubes,” *Macromolecules*, vol. 39, no. 16, pp. 5194–5205, Aug. 2006.
- [52] Hach, “Stablcal Turbidity Standards Calibration Kit,” 2017. [Online]. Available: <https://www.hach.com/stablcal-turbidity-standards-calibration-kit-0-4000-ntu-sealed-vials/product?id=7640202647&callback=qs#>. [Accessed: 13-Aug-2019].
- [53] Hach, “Turbidity,” 2018. [Online]. Available: <https://www.hach.com/industries/drinking-water/turbidity>. [Accessed: 13-Aug-2019].
- [54] Brookfield, “What is Viscosity?,” 2019. [Online]. Available: <https://www.brookfieldengineering.com/learning-center/learn-about-viscosity/what-is-viscosity>. [Accessed: 20-Sep-2019].
- [55] Z.-M. Huang, Y.-Z. Zhang, M. Kotaki, and S. Ramakrishna, “A review on polymer nanofibers by electrospinning and their applications in nanocomposites,” *Compos. Sci. Technol.*, vol. 63, no. 15, pp. 2223–2253, Nov. 2003.
- [56] G. E. Wnek *et al.*, “Electroprocessing of materials useful in drug delivery and cell encapsulation,” US20040018226A1, 2003.
- [57] Z. Han, J. Li, S. Xu, and A. He, “Biopolymer nano tunica fibrosa material capable of being biological degraded and absorbed, preparing method and uses of the same,” CN101172164A, 03-Nov-2006.
- [58] K. Ramachandran and P.-I. Gouma, “Electrospinning for bone tissue engineering,,” *Recent Pat. Nanotechnol.*, vol. 2, no. 1, pp. 1–7, Jan. 2008.
- [59] W.-J. Li and R. S. Tuan, “Tissue engineered cartilage, method of making same, therapeutic and cosmetic surgical applications using same,” WO2006138552A2, 2006.
- [60] H. Wang, “Innovative bottom-up cell assembly approach to three-dimensional tissue formation using nano-or micro-fibers,” US20080112998A1, 2008.
- [61] A. Greiner and J. Hehl, “Microbicidal nano- and meso-polymer fibers produced from

- polymers and honey, for textile applications,” WO2008049251A1, 2008.
- [62] D. Groitzsch and E. Fahrbach, “Mikroporoerer multilayer nonwoven for medical application purposes and process for its manufacture,” DE3437183A1, 1986.
- [63] S. Shiratori, B. Ding, and H. Li, “JP154336,” JP154336, 2007.
- [64] M. Guo, “Novel environmental protection fiber film material and its preparation method,” CN101077473A, 2007.
- [65] Y.-J. Hu, H.-Y. Chen, and W.-C. Hwang, “Method for treating wastewater containing active sludge,” vol. 1, no. 19, 2008.
- [66] S. J. Kim, Y. S. Nam, D. M. Rhee, H.-S. Park, and W. H. Park, “Preparation and characterization of antimicrobial polycarbonate nanofibrous membrane,” *Eur. Polym. J.*, vol. 43, no. 8, pp. 3146–3152, Aug. 2007.
- [67] K. Onozuka *et al.*, “Electrospinning processed nanofibrous TiO₂ membranes for photovoltaic applications,” *Nanotechnology*, vol. 17, no. 4, pp. 1026–31, Mar. 2006.
- [68] B. Ding, J. Kim, Y. Miyazaki, and S. Shiratori, “Electrospun nanofibrous membranes coated quartz crystal microbalance as gas sensor for NH₃ detection,” *Sensors actuators B Chem.*, vol. 101, no. 3, pp. 373–380, Jul. 2004.
- [69] S. Shiratori and D. Bin, “JP264386,” JP264386, 2005.
- [70] FundingUniverse, “History of Stratasys Inc.,” 2003. [Online]. Available: <http://www.fundinguniverse.com/company-histories/stratasys-inc-history/>. [Accessed: 27-Mar-2013].
- [71] S. Crump, “3D Printer Cost,” *Stratasys Blog*, 2012. [Online]. Available: <http://blog.stratasys.com/blog/3d-printer-cost>. [Accessed: 27-Mar-2013].
- [72] R. Jones *et al.*, “RepRap – the replicating rapid prototyper,” *Robotica*, vol. 29, no. 01, pp. 177–191, Jan. 2011.
- [73] J. Flynt, “A Detailed History of 3D Printing,” *3DInsiders.com*. [Online]. Available: <https://3dinsider.com/3d-printing-history/>. [Accessed: 14-Nov-2013].
- [74] RepRap, “RepRapWiki,” 2013. [Online]. Available: http://www.reprap.org/wiki/Main_Page. [Accessed: 27-Mar-2013].
- [75] B. Pettis, “All-Star Lineup Invests in MakerBot,” *Makerbot News*, 2011. [Online]. Available: <http://www.makerbot.com/blog/2011/08/23/all-star-lineup-invests-in-makerbot/>. [Accessed: 27-Mar-2013].
- [76] G. D. Goh, Y. L. Yap, H. K. J. Tan, S. L. Sing, G. L. Goh, and W. Y. Yeong, “Process–Structure–Properties in Polymer Additive Manufacturing via Material Extrusion: A Review,” *Crit. Rev. Solid State Mater. Sci.*, pp. 1–21, Jan. 2019.
- [77] Cimetrix Solutions, “Materials,” 2013. [Online]. Available: <http://www.cimetrixsolutions.com/materials/fdm>. [Accessed: 27-Mar-2013].
- [78] UltiMachine, “Print Materials,” 2013. [Online]. Available:

- <https://ultimachine.com/catalog/print-materials>. [Accessed: 27-Mar-2013].
- [79] Aniwaa Pte. Ltd., “Filastruder Kit,” 2013. [Online]. Available: <https://www.aniwaa.com/product/3d-printers/filastruder-filastruder-kit/>. [Accessed: 13-Apr-2013].
- [80] Makerbot Inc., “MAKERBOT REPLICATOR 2X.” [Online]. Available: <https://pages.makerbot.com/ap-replicator-2x.html>. [Accessed: 22-May-2017].
- [81] SeeMeCNC Inc., “ROSTOCKMAX V3.2 DIY KIT.” [Online]. Available: <https://www.seemecnc.com/products/rostockmax-v3-2-diy-kit-black>. [Accessed: 03-Oct-2019].
- [82] Kaipa, “LAYWOO-D3 - Print wood now-with tree rings,” *Thingiverse*, 2012. [Online]. Available: <http://www.thingiverse.com/thing:30552>. [Accessed: 27-Mar-2013].
- [83] M. R. Skorski, J. M. Esenther, Z. Ahmed, A. E. Miller, and M. R. Hartings, “The chemical, mechanical, and physical properties of 3D printed materials composed of TiO₂-ABS nanocomposites,” *Sci. Technol. Adv. Mater.*, vol. 17, no. 1, pp. 89–97, 2016.
- [84] K. V. Niaza, F. S. Senatov, S. D. Kaloshkin, A. V. Maksimkin, and D. I. Chukov, “3D-printed scaffolds based on PLA/HA nanocomposites for trabecular bone reconstruction,” *J. Phys. Conf. Ser.*, vol. 741, no. 1, 2016.
- [85] S. Hwang, E. I. Reyes, K. sik Moon, R. C. Rumpf, and N. S. Kim, “Thermo-mechanical Characterization of Metal/Polymer Composite Filaments and Printing Parameter Study for Fused Deposition Modeling in the 3D Printing Process,” *J. Electron. Mater.*, vol. 44, no. 3, pp. 771–777, 2015.
- [86] M. Nikzad, S. H. Masood, and I. Sbarski, “Thermo-mechanical properties of a highly filled polymeric composites for Fused Deposition Modeling,” *Mater. Des.*, vol. 32, no. 6, pp. 3448–3456, Jun. 2011.
- [87] M. Kurimoto, H. Ozaki, Y. Yamashita, T. Funabashi, T. Kato, and Y. Suzuoki, “Dielectric properties and 3D printing of UV-cured acrylic composite with alumina microfiller,” *IEEE Trans. Dielectr. Electr. Insul.*, vol. 23, no. 5, pp. 2985–2992, Oct. 2016.
- [88] A. Bowyer, “Conducting Plastic Experiments,” *RepRapPro Blog*, 2013. [Online]. Available: http://reprappro.com/Special_Blog?cmd=post&id=19. [Accessed: 27-Mar-2013].
- [89] C. M. Shemelya *et al.*, “Mechanical, Electromagnetic, and X-ray Shielding Characterization of a 3D Printable Tungsten–Polycarbonate Polymer Matrix Composite for Space-Based Applications,” *J. Electron. Mater.*, vol. 44, no. 8, pp. 2598–2607, Aug. 2015.
- [90] I. Peterson, “Trickling Sand: How an Hourglass Ticks,” *Sci. News*, vol. 144, no. 11, p. 167, 1993.
- [91] K. Gnanasekaran *et al.*, “3D printing of CNT- and graphene-based conductive polymer nanocomposites by fused deposition modeling,” *Appl. Mater. Today*, vol. 9, pp. 21–28, 2017.

- [92] S. Meng, H. He, Y. Jia, P. Yu, B. Huang, and J. Chen, “Effect of nanoparticles on the mechanical properties of acrylonitrile-butadiene-styrene specimens fabricated by fused deposition modeling,” *J. Appl. Polym. Sci.*, vol. 134, no. 7, Feb. 2017.
- [93] J. Torres, M. Cole, A. Owji, Z. DeMastry, and A. P. Gordon, “An approach for mechanical property optimization of fused deposition modeling with polylactic acid via design of experiments,” *Rapid Prototyp. J.*, vol. 22, no. 2, pp. 387–404, 2016.
- [94] S. J. Leigh, R. J. Bradley, C. P. Purssell, D. R. Billson, and D. A. Hutchins, “A simple, low-cost conductive composite material for 3D printing of electronic sensors.,” *PLoS One*, vol. 7, no. 11, p. e49365, Jan. 2012.
- [95] M. L. Shofner, K. Lozano, F. J. Rodriguez-Macias, and E. V. Barrera, “Nanofiber-reinforced polymers prepared by fused deposition modeling,” *J. Appl. Polym. Sci.*, vol. 89, no. 11, pp. 3081–3090, Sep. 2003.
- [96] A. R. T. Perez, D. A. Roberson, and R. B. Wicker, “Fracture surface analysis of 3D-printed tensile specimens of novel ABS-based materials,” *J. Fail. Anal. Prev.*, vol. 14, no. 3, pp. 343–353, 2014.
- [97] Z. Weng, J. Wang, T. Senthil, and L. Wu, “Mechanical and thermal properties of ABS/montmorillonite nanocomposites for fused deposition modeling 3D printing,” *Mater. Des.*, vol. 102, pp. 276–283, 2016.
- [98] G. Li, J. Aspler, A. Kingsland, L. Cormier, and X. Zou, “3D printing - A review of technologies, market and opportunities for the forestry industry,” *Fibre Value Chain Conf. Expo 2015 Pulp Pap. Bioenergy Bioprod.*, vol. 5, no. 2, pp. 55–63, 2015.
- [99] T. Halterman, “New Research Says That a New BioEconomy May Be Driven By 3D Printed Cellulose Materials,” *3DPrint.com*, 2015. [Online]. Available: <https://3dprint.com/70827/3d-printed-cellulose-materials/>. [Accessed: 13-Aug-2019].
- [100] C. A. Murphy and M. N. Collins, “Microcrystalline cellulose reinforced polylactic acid biocomposite filaments for 3D printing,” *Polym. Compos.*, vol. 39, no. 4, pp. 1311–1320, Apr. 2018.
- [101] J. S. Park, T. Kim, and W. S. Kim, “Conductive Cellulose Composites with Low Percolation Threshold for 3D Printed Electronics,” *Sci. Rep.*, vol. 7, no. 1, p. 3246, Dec. 2017.
- [102] G. Siqueira *et al.*, “Cellulose Nanocrystal Inks for 3D Printing of Textured Cellular Architectures,” *Adv. Funct. Mater.*, vol. 27, no. 12, p. 1604619, 2017.
- [103] T. R. Kramer, F. M. Proctor, and E. Messina, “The NIST RS274NGC Interpreter,” 2000.
- [104] G. Hodgson, A. Ranellucci, and J. Moe, “Slic3r Manual,” 2013. [Online]. Available: <https://manual.slic3r.org/intro/overview>. [Accessed: 26-Aug-2019].
- [105] J. F. Shackelford, *Introduction to Materials Science for Engineers*, 8th ed. Upper Saddle River, NJ: Pearson Higher Ed., 2015.
- [106] A. A. Berlin, S. A. Volfson, N. S. Enikolopian, and S. S. Negmatov, *Principles of polymer composites*, 1st ed. Springer-Verlag Berlin Heidelberg, 1986.

- [107] D. J. Gardner, G. S. Oporto, R. Mills, and M. A. S. Azizi Samir, "Adhesion and surface issues in cellulose and nanocellulose," *J. Adhes. Sci. Technol.*, vol. 22, pp. 545–56, 2008.
- [108] V. Mittal, *Polymer Nanotubes Nanocomposites: Synthesis, Properties and Applications: Second Edition*. Wiley Blackwell, 2014.
- [109] M. A. S. Azizi Samir, F. Alloin, and A. Dufresne, "Review of recent research into cellulosic whiskers, their properties and their application in nanocomposite field," *Biomacromolecules*, vol. 6, no. 2, pp. 612–26, Jan. 2005.
- [110] M. K. Tam, "Nanotechnology NE335 Macromolecular Science 2 Class Notes." Waterloo, Canada, 2008.
- [111] A. Rai and C. N. Jha, "Natural fibre composites and its potential as building materials," New Delhi, 2010.
- [112] A. Leão, M. Bernstein, and M. Woods, "'Green' cars could be made from pineapples and bananas," *American Chemical Society News Releases*, 2011. [Online]. Available: <https://www.acs.org/content/acs/en/pressroom/newsreleases/2011/march/green-cars-could-be-made-from-pineapples-and-bananas.html>. [Accessed: 01-Apr-2011].
- [113] E. Small and D. Marcus, "Hemp: A New Crop with New Uses for North America," *J. Janick A. Whipkey (eds.), Trends new Crop. new uses.*, pp. 284–326, 2002.
- [114] A. P. Mathew, A. Chakraborty, K. Oksman, and M. Sain, "The Structure and Mechanical Properties of Cellulose Nanocomposites Prepared by Twin Screw Extrusion," in *Cellulose Nanocomposites*, 1st ed., K. Oksman and M. Sain, Eds. American Chemical Society, 2006, pp. 114–131.
- [115] L. Petersson and K. Oksman, "Preparation and Properties of Biopolymer-Based Nanocomposite Films Using Microcrystalline Cellulose," in *Cellulose Nanocomposites*, K. Oksman and M. Sain, Eds. American Chemical Society, 2006, pp. 132–150.
- [116] H. Yano *et al.*, "Optically Transparent Composites Reinforced with Networks of Bacterial Nanofibers," *Adv. Mater.*, vol. 17, no. 2, pp. 153–155, Jan. 2005.
- [117] W. J. Orts, J. Shey, S. H. Imam, G. M. Glenn, M. E. Guttman, and J.-F. F. Revol, "Application of Cellulose Microfibrils in Polymer Nanocomposites," *J. Polym. Environ.*, vol. 13, no. 4, pp. 301–306, Oct. 2005.
- [118] P. Zadorecki and A. J. Michell, "Future prospects for wood cellulose as reinforcement in organic polymer composites," *Polym. Compos.*, vol. 10, no. 2, pp. 69–77, Apr. 1989.
- [119] A. N. Nakagaito and H. Yano, "The effect of morphological changes from pulp fiber towards nano-scale fibrillated cellulose on the mechanical properties of high-strength plant fiber based composites," *Appl. Phys. A*, vol. 78, no. 4, pp. 547–552, Mar. 2004.
- [120] A. N. N. Nakagaito, S. Iwamoto, and H. Yano, "Bacterial cellulose: the ultimate nano-scalar cellulose morphology for the production of high-strength composites," *Appl. Phys. A*, vol. 80, no. 1, pp. 93–97, Jul. 2004.
- [121] A. N. Nakagaito and H. Yano, "Novel high-strength biocomposites based on

- microfibrillated cellulose having nano-order-unit web-like network structure,” *Appl. Phys. A Mater. Sci. Process.*, vol. 80, no. 1, pp. 155–159, Jan. 2005.
- [122] K. Oksman, A. P. Mathew, D. Bondeson, and I. Kvien, “Manufacturing process of cellulose whiskers/poly(lactic acid) nanocomposites,” *Compos. Sci. Technol.*, vol. 66, no. 15, pp. 2776–2784, Dec. 2006.
- [123] I. Kvien and K. Oksman, “Orientation of cellulose nanowhiskers in poly(vinyl alcohol),” *Appl. Phys. A*, vol. 87, no. 4, pp. 641–643, Feb. 2007.
- [124] A. Iwatake, M. Nogi, and H. Yano, “Cellulose nanofiber-reinforced poly(lactic acid),” *Compos. Sci. Technol.*, vol. 68, no. 9, pp. 2103–2106, Jul. 2008.
- [125] Q. Ping, Z. LiPing, D. JiuFang, and C. Yu, “Study on micro-nano cellulose/poly (lactic acid) composite,” in *Symposium on Chemistry and Engineering of Forestry Biomass, Nanjing, China.*, 2009, vol. 29, no. Supplement, pp. 179–182, 186.
- [126] M. Ozgurseydibeyoglu, K. Oksman, M. Ö. Seydibeyoğlu, and K. Oksman, “Novel nanocomposites based on polyurethane and micro fibrillated cellulose,” *Compos. Sci. Technol.*, vol. 68, no. 3–4, pp. 908–914, Mar. 2008.
- [127] T. Pullawan, A. N. Wilkinson, and S. J. Eichhorn, “Discrimination of matrix-fibre interactions in all-cellulose nanocomposites,” *Compos. Sci. Technol.*, vol. 70, no. 16, pp. 2325–2330, Dec. 2010.
- [128] T. Nishino, I. Matsuda, and K. Hirao, “All-Cellulose Composite,” *Macromolecules*, vol. 37, no. 20, pp. 7683–7687, Oct. 2004.
- [129] A. C. Finkle and L. C. Simon, “Preparation of polycarbonate nanofibres containing nanocrystalline cellulose,” *J-FOR*, vol. 2, no. 6, 2012.
- [130] R. Ramasubramaniam, J. Chen, and H. Liu, “Homogeneous carbon nanotube/polymer composites for electrical applications,” *Appl. Phys. Lett.*, vol. 83, no. 14, p. 2928, 2003.
- [131] MatWeb, “Star Plastics PC743 Molding Grade PC Specification Sheet,” *MatWeb: Material Property Data*. [Online]. Available: <http://www.matweb.com/search/datasheettext.aspx?matguid=0def137a1ecf4015af5ec05fc43b5bd1>. [Accessed: 24-Feb-2011].
- [132] S. R. Dhakate, B. Singla, M. Uppal, and R. B. Mathur, “Effect of processing parameters on morphology and thermal properties of electrospun polycarbonate nanofibers,” *Adv. Mater. Lett.*, vol. 1, no. 3, pp. 200–204, 2010.
- [133] H.-Y. Hsiao, C.-M. Huang, Y.-Y. Liu, Y.-C. Kuo, and H. Chen, “Effect of Air Blowing on the Morphology and Nanofiber Properties of Blowing-Assisted Electrospun Polycarbonates,” *J. Appl. Polym. Sci.*, vol. 124, pp. 4904–4914, 2012.
- [134] T. Baby, T. Jose E, G. George, V. Varkey, and S. K. Cherian, “A new approach for the shaping up of very fine and beadless UV light absorbing polycarbonate fibers by electrospinning,” *Polym. Test.*, vol. 80, no. August, 2019.
- [135] M. S. Peresin, Y. Habibi, J. O. Zoppe, J. J. Pawlak, and O. J. Rojas, “Nanofiber composites

- of polyvinyl alcohol and cellulose nanocrystals: manufacture and characterization.,” *Biomacromolecules*, vol. 11, no. 3, pp. 674–81, Mar. 2010.
- [136] M. S. Peresin *et al.*, “Effect of moisture on electrospun nanofiber composites of poly(vinyl alcohol) and cellulose nanocrystals,” *Biomacromolecules*, vol. 11, no. 9, pp. 2471–2477, 2010.
- [137] N. D. Wanasekara, R. P. O. Santos, C. Douch, E. Frollini, and S. J. Eichhorn, “Orientation of cellulose nanocrystals in electrospun polymer fibres,” *J. Mater. Sci.*, vol. 51, no. 1, pp. 218–227, 2016.
- [138] C. Zhou *et al.*, “Electrospun bio-nanocomposite scaffolds for bone tissue engineering by cellulose nanocrystals reinforcing maleic anhydride grafted PLA,” *ACS Appl. Mater. Interfaces*, vol. 5, no. 9, pp. 3847–3854, 2013.
- [139] H. Dong, K. E. Strawhecker, J. F. Snyder, J. A. Orlicki, R. S. Reiner, and A. W. Rudie, “Cellulose nanocrystals as a reinforcing material for electrospun poly(methyl methacrylate) fibers: Formation, properties and nanomechanical characterization,” *Carbohydr. Polym.*, vol. 87, no. 4, pp. 2488–2495, 2012.
- [140] O. J. Rojas, G. A. Montero, and Y. Habibi, “Electrospun nanocomposites from polystyrene loaded with cellulose nanowhiskers,” *J. Appl. Polym. Sci.*, vol. 113, no. 2, pp. 927–935, Jul. 2009.
- [141] C. Zhou, R. Chu, R. Wu, and Q. Wu, “Electrospun polyethylene oxide/cellulose nanocrystal composite nanofibrous mats with homogeneous and heterogeneous microstructures,” *Biomacromolecules*, vol. 12, no. 7, pp. 2617–2625, 2011.
- [142] N. Naseri, A. P. Mathew, L. Girandon, M. Fröhlich, and K. Oksman, “Porous electrospun nanocomposite mats based on chitosan–cellulose nanocrystals for wound dressing: effect of surface characteristics of nanocrystals,” *Cellulose*, vol. 22, no. 1, pp. 521–534, 2015.
- [143] M. Ago, K. Okajima, J. E. Jakes, S. Park, and O. J. Rojas, “Lignin-based electrospun nanofibers reinforced with cellulose nanocrystals,” *Biomacromolecules*, vol. 13, no. 3, pp. 918–926, Mar. 2012.
- [144] S. Huang, L. Zhou, M. C. Li, Q. Wu, Y. Kojima, and D. Zhou, “Preparation and properties of electrospun poly (vinyl pyrrolidone)/cellulose nanocrystal/silver nanoparticle composite fibers,” *Materials (Basel)*, vol. 9, no. 7, 2016.
- [145] X. He *et al.*, “Uniaxially aligned electrospun all-cellulose nanocomposite nanofibers reinforced with cellulose nanocrystals: Scaffold for tissue engineering,” *Biomacromolecules*, vol. 15, no. 2, pp. 618–627, 2014.
- [146] SABIC Innovative Plastics, “Lexan XL10 Product Data Sheet,” 2008. [Online]. Available: http://www.sabic-ip.com/resins/DataSheet/Internet/PDF/1002002131_1002003959_1002038469_SI.pdf. [Accessed: 03-May-2017].
- [147] C. Miao and W. Y. Hamad, “Alkenylation of cellulose nanocrystals (CNC) and their applications,” *Polym. (United Kingdom)*, vol. 101, pp. 338–346, 2016.

- [148] ChemStores, “Bulk solvents - Chloroform,” *University of Waterloo*, 2017. [Online]. Available: <https://uwaterloo.ca/chemstores/stock/bulk-solvents#chloroform>. [Accessed: 03-May-2017].
- [149] Minitab, “Interpret the key results for Multiple Regression,” 2017. [Online]. Available: <https://support.minitab.com/en-us/minitab-express/1/help-and-how-to/modeling-statistics/regression/how-to/multiple-regression/interpret-the-results/key-results/>. [Accessed: 13-Aug-2019].
- [150] Minitab, “Regression Analysis: How to Interpret S, the Standard Error of the Regression,” 2014. [Online]. Available: <https://blog.minitab.com/blog/adventures-in-statistics-2/regression-analysis-how-to-interpret-s-the-standard-error-of-the-regression>. [Accessed: 13-Aug-2019].
- [151] Minitab, “Coefficients table for Analyze Factorial Design,” 2017. [Online]. Available: <https://support.minitab.com/en-us/minitab/18/help-and-how-to/modeling-statistics/doe/how-to/factorial/analyze-factorial-design/interpret-the-results/all-statistics-and-graphs/coefficients-table/>. [Accessed: 13-Aug-2019].
- [152] Minitab, “Residual plots in Minitab,” 2017. [Online]. Available: <https://support.minitab.com/en-us/minitab/18/help-and-how-to/modeling-statistics/regression/supporting-topics/residuals-and-residual-plots/residual-plots-in-minitab/>. [Accessed: 13-Aug-2019].
- [153] C. Mit-Uppatham, M. Nithitanakul, and P. Supaphol, “Ultrafine electrospun polyamide-6 fibers: Effect of solution conditions on morphology and average fiber diameter,” *Macromol. Chem. Phys.*, vol. 205, no. 17, pp. 2327–2338, 2004.
- [154] P. Heikkilä, A. Taipale, M. Lehtimäki, and A. Harlin, “Electrospinning of Polyamides With Different Chain Compositions for Filtration Application,” *Polym. Eng. Sci.*, vol. 48, pp. 1168–1176, 2008.
- [155] R. Dersch, T. Liu, A. K. Schaper, A. Greiner, and J. H. Wendorff, “Electrospun nanofibers: Internal structure and intrinsic orientation,” *J. Polym. Sci. Part A Polym. Chem.*, vol. 41, no. 4, pp. 545–553, 2003.
- [156] P. Supaphol, C. Mit-uppatham, and M. Nithitanakul, “Ultrafine electrospun polyamide-6 fibers: Effects of solvent system and emitting electrode polarity on morphology and average fiber diameter,” *Macromol. Mater. Eng.*, vol. 290, no. 9, pp. 933–942, 2005.
- [157] P. Supaphol, C. Mit-Uppatham, and M. Nithitanakul, “Ultrafine electrospun polyamide-6 fibers: Effect of emitting electrode polarity on morphology and average fiber diameter,” *J. Polym. Sci. Part B Polym. Phys.*, vol. 43, no. 24, pp. 3699–3712, 2005.
- [158] N. Ristolainen, P. Heikkilä, A. Harlin, and J. Seppälä, “Poly(vinyl alcohol) and polyamide-66 nanocomposites prepared by electrospinning,” *Macromol. Mater. Eng.*, vol. 291, no. 2, pp. 114–122, 2006.
- [159] R. Nirmala, R. Navamathavan, M. H. El-Newehy, and H. Y. Kim, “Preparation and electrical characterization of polyamide-6/chitosan composite nanofibers via electrospinning,” *Mater. Lett.*, vol. 65, no. 3, pp. 493–496, 2011.

- [160] R. Nirmala, R. Navamathavan, H. S. Kang, M. H. El-Newehy, and H. Y. Kim, "Preparation of polyamide-6/chitosan composite nanofibers by a single solvent system via electrospinning for biomedical applications," *Colloids Surfaces B Biointerfaces*, vol. 83, no. 1, pp. 173–178, 2011.
- [161] M. K. Joshi *et al.*, "Cellulose reinforced nylon-6 nanofibrous membrane: Fabrication strategies, physicochemical characterizations, wicking properties and biomimetic mineralization," *Carbohydr. Polym.*, vol. 147, pp. 104–113, 2016.
- [162] P. Sobolčiak, A. Tanvir, A. Popelka, J. Moffat, K. A. Mahmoud, and I. Krupa, "The preparation, properties and applications of electrospun co-polyamide 6,12 membranes modified by cellulose nanocrystals," *Mater. Des.*, vol. 132, pp. 314–323, 2017.
- [163] W. Xu *et al.*, "Cellulose nanocrystals as organic nanofillers for transparent polycarbonate films," *J. Nanoparticle Res.*, vol. 15, no. 4, 2013.
- [164] American Society for Testing and Materials, "ASTM E92 -Standard Test Methods for Vickers Hardness and Knoop Hardness of Metallic Materials," 2017.
- [165] R. Tanaka, "Vickers hardness test," 2012. [Online]. Available: https://en.wikipedia.org/wiki/Vickers_hardness_test. [Accessed: 26-Aug-2019].
- [166] Sobarwiki, "Simplified UV-vis Diagram," 2016. [Online]. Available: https://commons.wikimedia.org/wiki/File:Simplified_UV-vis_diagram.png. [Accessed: 26-Aug-2019].
- [167] Q. Wang, J. Sun, Q. Yao, C. Ji, J. Liu, and Q. Zhu, "3D printing with cellulose materials," *Cellulose*, vol. 25, no. 8, pp. 4275–4301, 2018.
- [168] J. Liu, L. Sun, W. Xu, Q. Wang, S. Yu, and J. Sun, "Current advances and future perspectives of 3D printing natural-derived biopolymers," *Carbohydr. Polym.*, vol. 207, no. November 2018, pp. 297–316, 2019.
- [169] R. Daniele, V. Nguyen, A. Cataldi, and A. Pegoretti, "Polyvinyl alcohol reinforced crystalline nanocellulose in 3d printing application," in *The 21st International conference on composites materials*, 2017, pp. 1–8.
- [170] Z. Wang *et al.*, "Preparation of 3D printable micro/nanocellulose-poly(lactic acid) (MNC/PLA) composite wire rods with high MNC constitution," *Ind. Crops Prod.*, vol. 109, no. January 2019, pp. 889–896, 2017.
- [171] J. Dong, C. Mei, J. Han, S. Lee, and Q. Wu, "3D printed poly(lactic acid) composites with grafted cellulose nanofibers: Effect of nanofiber and post-fabrication annealing treatment on composite flexural properties," *Addit. Manuf.*, vol. 28, no. June, pp. 621–628, 2019.
- [172] R. Daniele, "Polymer composites for sustainable 3D printing materials," University of Trento, 2019.
- [173] A. Cataldi, D. Rigotti, V. D. H. Nguyen, and A. Pegoretti, "Polyvinyl alcohol reinforced with crystalline nanocellulose for 3D printing application," *Mater. Today Commun.*, vol. 15, no. March, pp. 236–244, 2018.


- [174] S. Shariatnia, A. Veldanda, S. Obeidat, D. Jarrahbashi, and A. Asadi, "Atomization of cellulose nanocrystals aqueous suspensions in fused deposition modeling: A scalable technique to improve the strength of 3D printed polymers," *Compos. Part B Eng.*, vol. 177, no. June, p. 107291, 2019.
- [175] B. Huang, H. He, S. Meng, and Y. Jia, "Optimizing 3D printing performance of acrylonitrile-butadiene-styrene composites with cellulose nanocrystals/silica nanohybrids," *Polym. Int.*, vol. 68, no. 7, pp. 1351–1360, 2019.
- [176] L. Wang and D. J. Gardner, "Enhanced cellulose nanofibril / polypropylene composites for 3D printing," *Plast. Res. Online*, no. June, 2017.
- [177] J. K. Hong, "Bioactive Cellulose Nanocrystal Reinforced 3D Printable Poly(ϵ -caprolactone) Nanocomposite for Bone Tissue Engineering," Virginia Polytechnic Institute and State University, 2015.
- [178] V. C. F. Li, X. Kuang, C. M. Hamel, D. Roach, Y. Deng, and H. J. Qi, "Cellulose nanocrystals support material for 3D printing complexly shaped structures via multi-materials-multi-methods printing," *Addit. Manuf.*, vol. 28, no. March, pp. 14–22, 2019.
- [179] M. K. Hausmann *et al.*, "Dynamics of Cellulose Nanocrystal Alignment during 3D Printing," *ACS Nano*, vol. 12, no. 7, pp. 6926–6937, 2018.
- [180] B. Wolfe and G. M. Chapman, "Process for making starch resin copolymer," US20160017091A1, 2016.
- [181] T. Elmore, "Filastruder Manual," 2013. [Online]. Available: <http://www.soliform.com/topic/2036/filastruder-documentation-and-cadstl-files/>. [Accessed: 12-Jan-2014].
- [182] American Society for Testing and Materials, "ASTM D256 - Standard Test Methods for Determining the Izod Pendulum Impact Resistance of Plastics," 2010.
- [183] American Society for Testing and Materials, "ASTM D790 - Standard test methods for flexural properties of unreinforced and reinforced plastics and electrical insulating materials," 2010.
- [184] American Society for Testing and Materials, "ASTM D1708 - Standard Test Method for Tensile Properties of Plastics by Use of Microtensile Specimens," 2013.
- [185] American Society for Testing and Materials, "ASTM D618 - Standard practice for conditioning plastics for testing," 2008.
- [186] Conair Group, "Extrusion Line Optimized for 3D Printing Filament Demonstrates Precision, Productivity Potential," *Press Release*, 2015. [Online]. Available: <http://www.conairgroup.com/about-us/news-press/3d-printing-filament-/>. [Accessed: 24-Aug-2017].
- [187] American Society for Testing and Materials, "ASTM D1238 - Standard Test Method for Melt Flow Rates of Thermoplastics by Extrusion Plastometer," 2013.
- [188] R. S. Park, "Novel Starch Nanocomposites," University of Waterloo, 2019.

[189] G. Fallon, “Stanley Black & Decker commit to generative design,” *Autodesk*. [Online]. Available: <https://customersuccess.autodesk.com/articles/stanley-black-decker-seized-on-generative-design>. [Accessed: 19-Aug-2019].

Appendix A. Material Specification Sheets

STAR PRIME™ Resins

Grade: PC743, PC743R
Molding Grade PC w/ UV, w/ UV and Release



starplastics.com

Typical Material Properties

326 Jack Burlingame Dr, Millwood, WV 25262 USA
 Phone: 304.273.0352, Fax: 304.273.0355

Physical	Nominal Values	ASTM Test
Specific Gravity	1.20	D792
Melt Flow (300 °C/ 1.2 kg)	11.0 g/ 10 min	D1238
Mechanical		
Tensile Modulus	350,000 psi	D638
Tensile Strength at Yield	9,000 psi	D638
Flexural Modulus	350,000 psi	D790
Flexural Strength at Yield	13,000 psi	D790
Impact		
Notched Izod Impact (73 °F, 0.125 in)	15 ft-lb/ in	D256
Thermal		
DTUL @264 psi-unannealed (0.125 in)	265 °F	D648
Mold Shrinkage		
Linear Flow	.005 - .007 in/in	D955
UL Rating	HB (1.15 mm) V2 (1.5 mm)	UL 94

The information provided above is based upon typical values, and are intended only as guides. Star Plastics, Inc/ SDR Inc assumes no obligation or liability for any advice furnished or for any results obtained with respect to this information. No guarantees or warranties are expressed or implied.

* STARPRIME™ is a registered trademark of Star Plastics Inc; SDR Plastics Inc, its subsidiaries or affiliates.

Recommended Processing Guidelines

	Nominal Values
Drying Time and Temperature	4.0 hrs at 250 °F
Suggested Max Moisture	0.020%
Rear Temperature	500 – 530 °F
Middle Temperature	500 – 530 °F
Front Temperature	500 – 550 °F
Nozzle Temperature	500 – 550 °F
Processing (melt) Temperature	500 - 550 °F
Mold Temperature	170 - 220 °F
Back Pressure	50 - 100 psi
Screw Speed	40 - 75 rpm

The conditions listed above are only guidelines. You may want to adjust conditions to meet your requirements.

Your Competitive Advantage in an Ever Changing Market!

REV: 9/01/13
Technical Data Sheet
Access: 10/16/13

Figure A.1 - Specification Sheet for StarPlastic Polycarbonate PC743R [131]

Certificate Of Analysis

Star Plastics Inc
Jackson County Industrial Center
Millwood WV 25282
Phone: (304) 273-0352
Fax: (304) 273-3326

Customer Name : POLYONE
Product : PC743R-CLS112
Lot : 62896
Date : 6/18/2009

Izod Impact, Notched 73F .125"	ASTM D256A
Melt Flow 300C/1.2kg	ASTM D1238
UL Vertical Burn @ 0.060"	UL Standard 94

17.1	9125/m	Ft-Lb/In
12.0		Grams/10Min.
94V2		Pass

Certified By: Mickey Ballard
Quality Assurance Rep.

An ISO 9001:2000 Registered Company

Figure A.2 - Certificate of Analysis for Polycarbonate PC743R Batch 62896

Description

Lexan XL10 sheet combines the impact strength of Lexan polycarbonate sheet with a proprietary UV-resistant surface treatment on one side that protects it from weathering. Lexan XL10 sheet is the only polycarbonate glazing material backed by a ten-year limited warranty against yellowing, loss of light transmission and breakage*. Providing long-lasting clarity over a wide range of weather conditions and environments, Lexan XL10 sheet improves service life and reduces life-cycle material costs. Lexan XL10 sheet is well suited for all types of vertical glazing and overhead applications such as skylights, covered walkways and barrel vaults.

Typical Property Values ♦

Property	Test Method	Unit	Value
Physical			
Specific Gravity	ASTM D792	-	1.20
Sound Transmission, STC Rating (36" x 84")	ASTM E9070	-	
@ 0.118"			25
@ 0.177"			29
@ 0.236"			31
@ 0.375"			34
@ 0.500"			34
Light Transmission (Average)	ASTM D1003	%	88
Rockwell Hardness	ASTM D785	-	M70, R118
Chemical Resistance	ANSI Z26.1		Passes
Mechanical			
Tensile Strength, Ultimate	ASTM D638	psi	9,500
Tensile Modulus	ASTM D638	psi	340,000
Flexural Strength	ASTM D790	psi	13,500
Flexural Modulus	ASTM D790	psi	340,000
Flexural Endurance @ 1,800 Cycles/Min, 73°F, 50% RH	ASTM D671	psi	1,000
Compressive Strength	ASTM D695	psi	12,500
Elongation	ASTM D638	%	110
Izod Impact Strength, up to 125 mils, Notched Drop	ASTM D256A	ft-lbs-in	12-16
Dart Impact Strength, 1" dia. Dart @ 73°F @ 0°F	SABIC Test [£]	ft-lbs	>200 >200
Thermal			
Coefficient of Thermal Expansion	ASTM D696	in/in/°F	3.75 x10 ⁻⁵
Thermal Shrinkage	SABIC Test	%	1
Heat Deflection Temperature @ 264 psi @ 66 psi	ASTM D648	°F	270 280
Shading Coefficient	ASHRAE	-	1.02 .79
Clear			1.02
Grey/Bronze			.79
Flammability			
Horizontal Burn (Flame Spread), AEB	ASTM D635	in	<1
Ignition Temperature Flash Self	ASTM D1929	°F	873 1,076

Request details of limited warranty and maintenance instructions

♦ These typical values are not intended for specification purposes. If minimum certifiable properties are required please contact your local SABIC Innovative Plastics, Specialty Film & Sheet representative.

£ Measured by dropping a 5-pound dart (1" dia. tip) from a height of 40 feet. These are typical properties and are not intended for specification purposes. If minimum certifiable properties are required, please contact your local SABIC Innovative Plastics representative or the SABIC Innovative Plastics Quality Services Department.

* Lexan is a trademark of SABIC Innovative Plastics IP BV

Lexan*

Figure A.3 - Specification Sheet for Sabic Lexan XL10 Polycarbonate [146]

Appendix B. Supplementary Electrospinning Results

B.1 – PC Electrospun Nanofibers in 60:40 (w/w) THF/DMF Solvent (DOE#1)

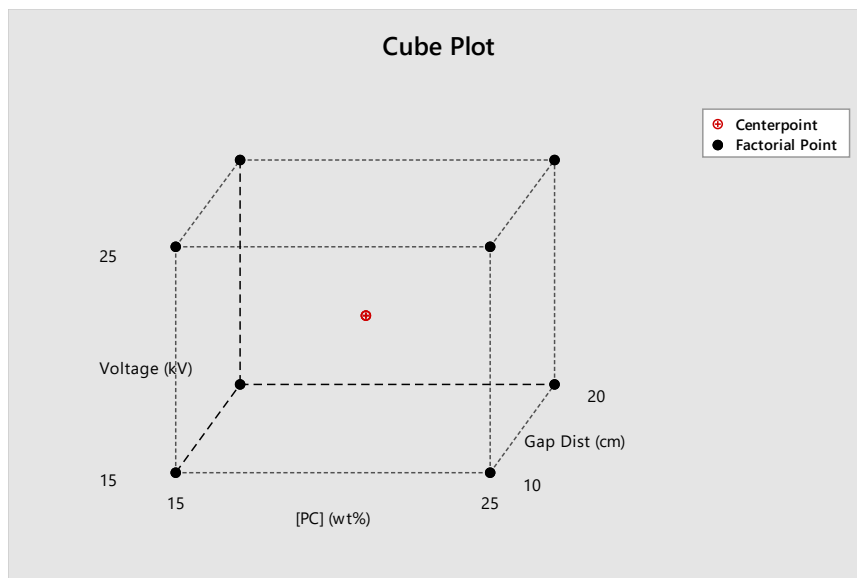


Figure B.1 - Cube plot representation of the 3D space of DOE#1 defined by high and low factor levels

Table B.1 - Target solution formulation masses for each run of DOE#1

Std. Order	Mass PC (g)	Mass 60:40 THF/DMF (g)	Total Mass (g)
1 (1)	7.5	42.5	50
2 (a)	12.5	37.5	50
3 (b)	7.5	42.5	50
4 (ab)	12.5	37.5	50
5 (c)	7.5	42.5	50
6 (ac)	12.5	37.5	50
7 (bc)	7.5	42.5	50
8 (abc)	12.5	37.5	50
9 (0)	10	40	50

10 (0)	10	40	50
11 (0)	10	40	50
Total Required	110	440	550

Table B.2 - DOE#1 target and actual mass (m) measurements for StarPlastic PC in 60:40 (w/w) THF/DMF for each 11 runs

Std.	mPC	mPC	mTHF	mTHF	mDMF	mDMF
Order	Target (g)	Actual (g)	Target (g)	Actual (g)	Target (g)	Actual (g)
1 (1)	7.5	7.51	25.5	24.90	17	17.66
2 (a)	12.5	12.50	22.5	21.84	15	15.69
3 (b)	7.5	7.55	25.5	24.83	17	17.70
4 (ab)	12.5	12.50	22.5	21.86	15	15.69
5 (c)	7.5	7.50	25.5	24.84	17	17.70
6 (ac)	12.5	12.50	22.5	22.00	15	15.57
7 (bc)	7.5	7.53	25.5	24.77	17	17.66
8 (abc)	12.5	12.52	22.5	22.01	15	15.58
9 (0)	10	10.07	24	23.37	16	16.73
10 (0)	10	9.99	24	23.37	16	16.63
11 (0)	10	10.09	24	23.36	16	16.73

B.1.1 – DOE#1 – Bead Density

Backward Elimination of Terms (α to remove = 0.1)

Analysis of Variance

Source	DF	Adj SS	Adj MS	F-Value	P-Value
Model	1	33945638	33945638	6.72	0.029
Linear	1	33945638	33945638	6.72	0.029
[PC] (wt%)	1	33945638	33945638	6.72	0.029
Error	9	45467145	5051905		
Curvature	1	6241305	6241305	1.27	0.292
Lack-of-Fit	6	38961346	6493558	49.10	0.020
Pure Error	2	264494	132247		
Total	10	79412782			

Model Summary

S	R-sq	R-sq(adj)	R-sq(pred)
2247.64	42.75%	36.38%	9.39%

Coded Coefficients

Term	Effect	Coef	SE Coef	T-Value	P-Value	VIF
Constant		1599	678	2.36	0.043	

[PC] (wt%) -4120 -2060 795 -2.59 0.029 1.00

Regression Equation in Uncoded Units

Bead Dens (beads/mm²) = 9838 - 412 [PC] (wt%)

Alias Structure

Factor Name

A [PC] (wt%)
B Voltage (kV)
C Gap Dist (cm)

Aliases

I
A

Fits and Diagnostics for Unusual Observations

	<u>Bead Dens</u>			<u>Std</u>	
<u>Obs</u>	<u>(beads/mm²)</u>	<u>Fit</u>	<u>Resid</u>		
3	9437	3659	5778	2.90	R

R Large residual

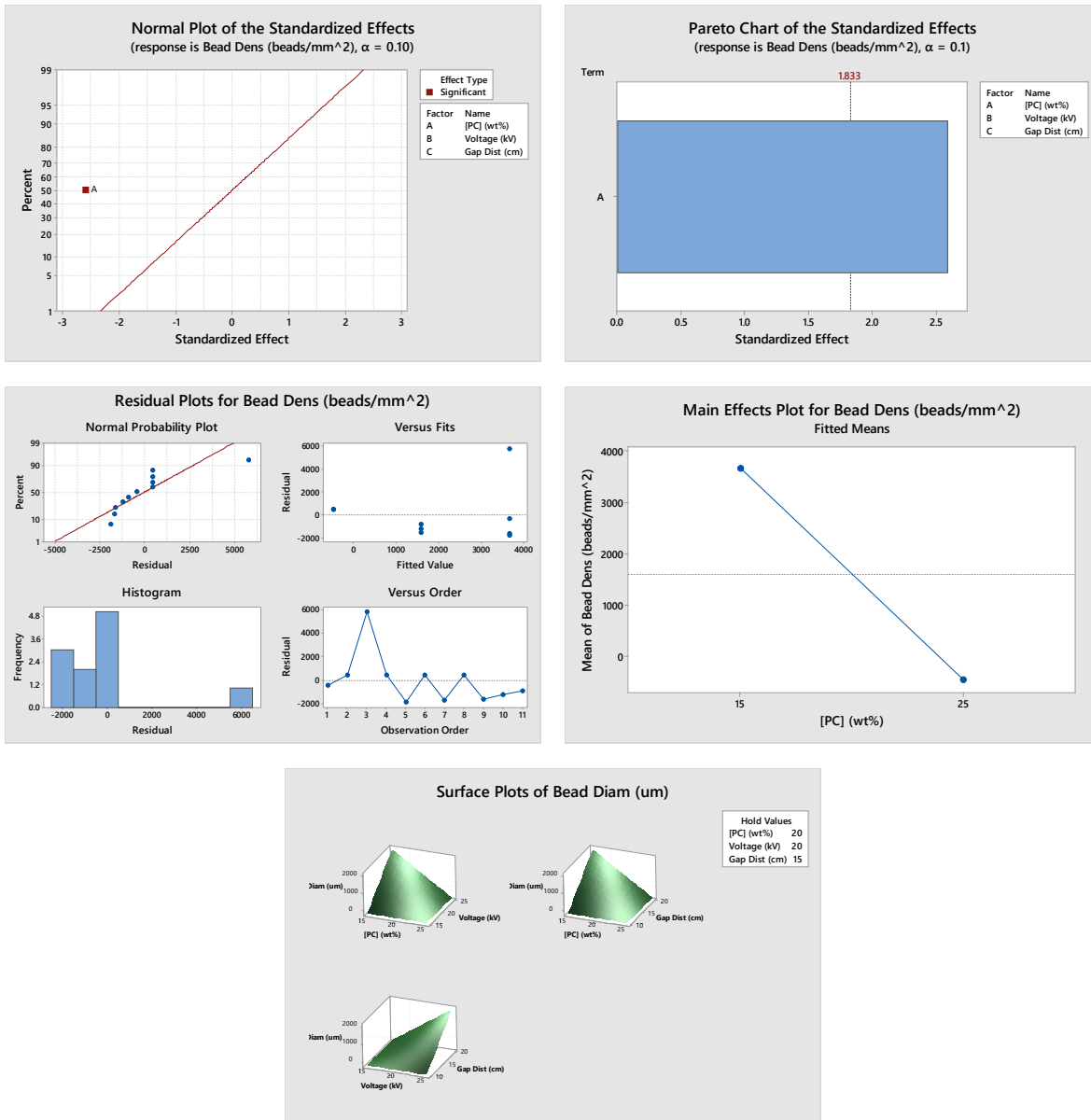


Figure B.2 - Minitab plot and chart outputs for DOE#1 – Bead Density

* NOTE * There are no valid interactions to plot.

B.1.2 – DOE#1 – Bead Diameter

Backward Elimination of Terms (α to remove = 0.1)

Analysis of Variance

Source	DF	Adj SS	Adj MS	F-Value	P-Value
Model	7	16616285	2373755	10.95	0.037
Linear	3	7138882	2379627	10.98	0.040
[PC] (wt%)	1	2393409	2393409	11.05	0.045
Voltage (kV)	1	2376281	2376281	10.97	0.045
Gap Dist (cm)	1	2369192	2369192	10.93	0.046
2-Way Interactions	3	7111438	2370479	10.94	0.040
[PC] (wt%)*Voltage (kV)	1	2376281	2376281	10.97	0.045
[PC] (wt%)*Gap Dist (cm)	1	2369192	2369192	10.93	0.046

Voltage (kV)*Gap Dist (cm)	1	2365965	2365965	10.92	0.046
3-Way Interactions	1	2365965	2365965	10.92	0.046
[PC] (wt%)*Voltage (kV)*Gap Dist (cm)	1	2365965	2365965	10.92	0.046
Error	3	650067	216689		
Curvature	1	650059	650059	170400.26	0.000
Pure Error	2	8	4		
Total	10	17266352			

Model Summary

S	R-sq	R-sq(adj)	R-sq(pred)
465.499	96.24%	87.45%	0.00%

Coded Coefficients

Term	Effect	Coef	SE Coef	T-Value	P-Value	VIF
Constant		398	140	2.84	0.066	
[PC] (wt%)	-1094	-547	165	-3.32	0.045	1.00
Voltage (kV)	1090	545	165	3.31	0.045	1.00
Gap Dist (cm)	1088	544	165	3.31	0.046	1.00
[PC] (wt%)*Voltage (kV)	-1090	-545	165	-3.31	0.045	1.00
[PC] (wt%)*Gap Dist (cm)	-1088	-544	165	-3.31	0.046	1.00
Voltage (kV)*Gap Dist (cm)	1088	544	165	3.30	0.046	1.00
[PC] (wt%)*Voltage (kV)*Gap Dist (cm)	-1088	-544	165	-3.30	0.046	1.00

Regression Equation in Uncoded Units

Bead Diam (um) = 16152 - 652 [PC] (wt%) - 1086 Voltage (kV) - 1631 Gap Dist (cm)
+ 43.5 [PC] (wt%)*Voltage (kV) + 65.2 [PC] (wt%)*Gap Dist (cm)
+ 108.8 Voltage (kV)*Gap Dist (cm)
- 4.35 [PC] (wt%)*Voltage (kV)*Gap Dist (cm)

Alias Structure

Factor	Name
A	[PC] (wt%)
B	Voltage (kV)
C	Gap Dist (cm)

Aliases

I
A
B
C
AB
AC
BC
ABC

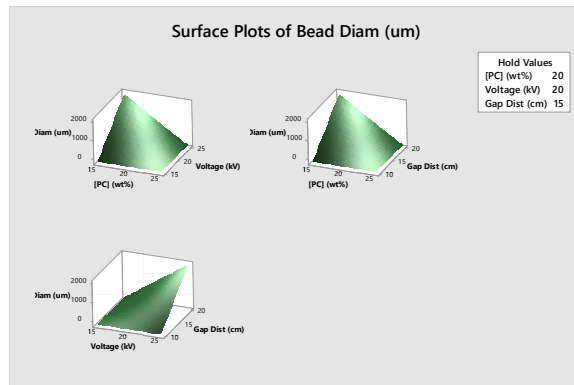
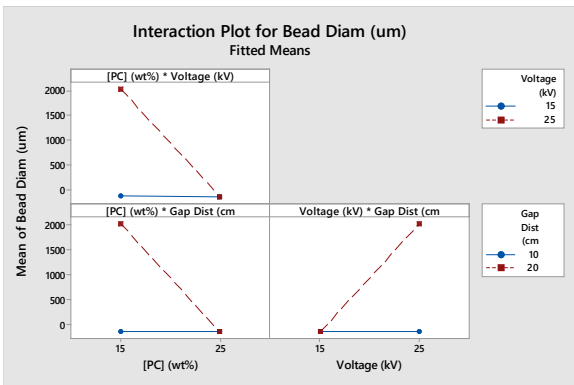
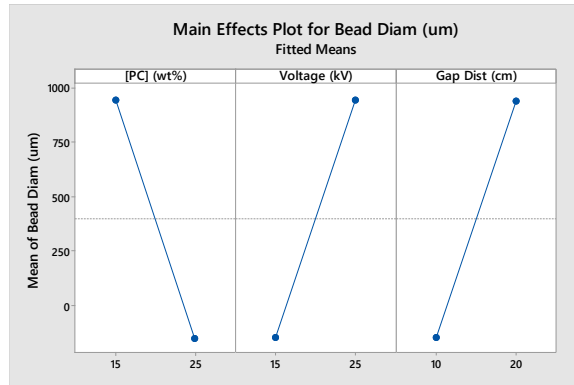
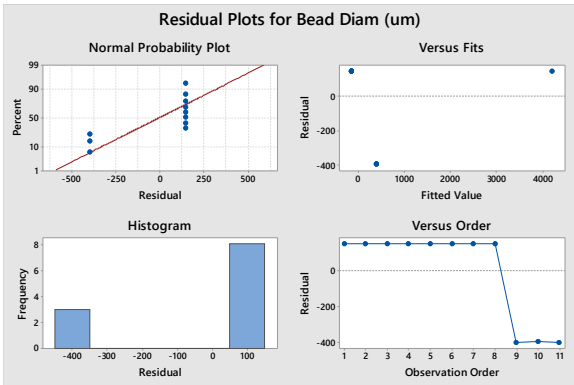
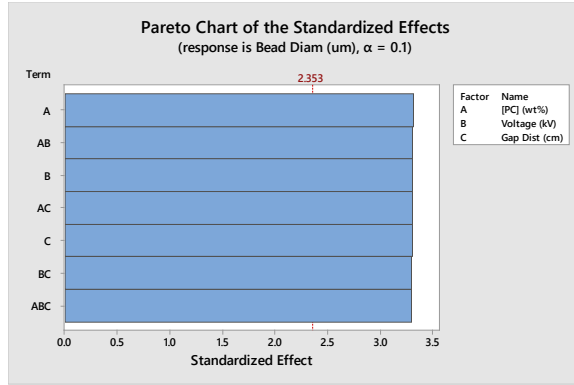


Figure B.3 - Minitab plot and chart outputs for DOE#1 - Bead Diameter

B.2 – 2 wt.-% NCC/PC Electrospun Nanofibers in 60:40 (w/w) THF/DMF Solvent (DOE#2)

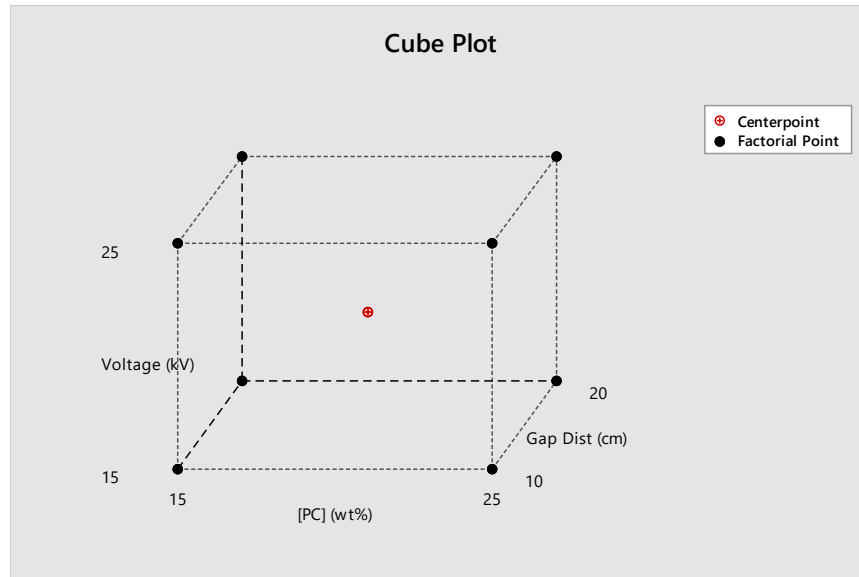


Figure B.4 - Cube plot representation of the 3D space of DOE#2 defined by high and low factor levels

Table B.3 - Target solution formulation masses for each run of DOE#1

Std. Order	Mass PC (g)	Mass NCC (g)	Mass 60:40 THF/DMF (g)	Total Mass (g)
1	7.5	0.1531	42.5	50.1531
2	12.5	0.2551	37.5	50.2551
3	7.5	0.1531	42.5	50.1531
4	12.5	0.2551	37.5	50.2551
5	7.5	0.1531	42.5	50.1531
6	12.5	0.2551	37.5	50.2551
7	7.5	0.1531	42.5	50.1531
8	12.5	0.2551	37.5	50.2551
9	10	0.2041	40	50.2041
10	10	0.2041	40	50.2041
11	10	0.2041	40	50.2041
Total Required	110	2.2449	440	552.2449

Table B.4 - DOE#2 target and actual mass measurements for StarPlastic PC and NCC in 60:40 (w/w) THF/DMF for each 11 runs

Std.	mPC	mPC	mNCC	mNCC	mTHF/DMF	mTHF/DMF
Order	Target (g)	Actual (g)	Target (g)	Actual (g)	Target (g)	Actual (g)
1 (1)	7.5	7.51	0.1531	0.15	42.5	42.52
2 (a)	12.5	12.51	0.2551	0.26	37.5	37.51
3 (b)	7.5	7.52	0.1531	0.16	42.5	42.00
4 (ab)	12.5	12.56	0.2551	0.26	37.5	37.51
5 (c)	7.5	7.50	0.1531	0.16	42.5	42.50
6 (ac)	12.5	12.52	0.2551	0.26	37.5	37.52
7 (bc)	7.5	7.51	0.1531	0.16	42.5	42.52
8 (abc)	12.5	12.53	0.2551	0.26	37.5	37.50
9 (0)	10	10.02	0.2041	0.20	40.0	39.99
10 (0)	10	10.02	0.2041	0.21	40.0	40.07
11 (0)	10	10.02	0.2041	0.20	40.0	40.03

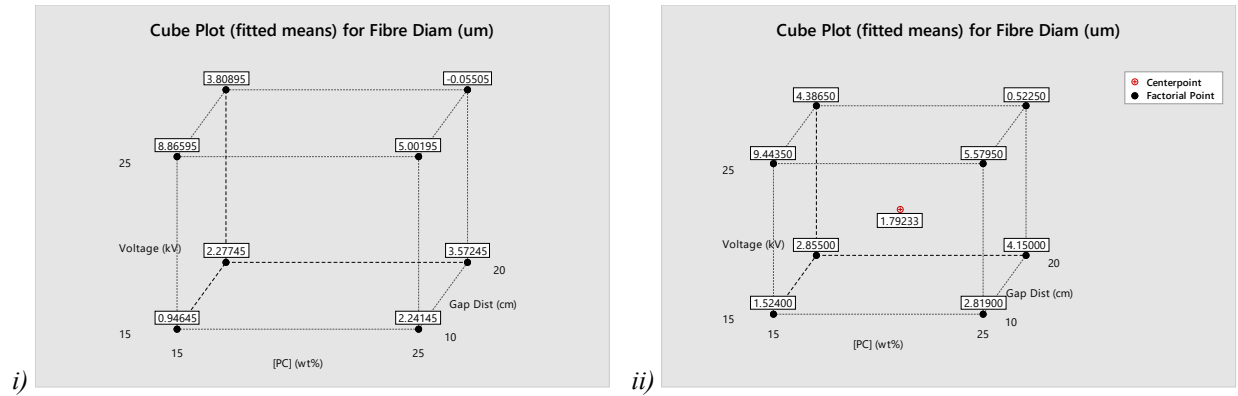


Figure B.5 - Cube plot of fitted means for the fiber diameter regression model for StarPlastic PC and NCC electrospun fibers in DOE#2; i) without CtPt and ii) with CtPt inclusion

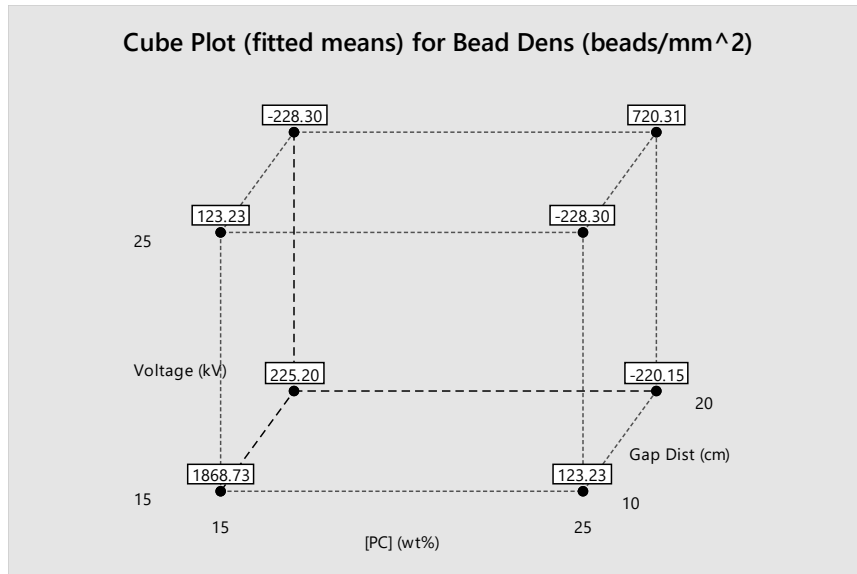


Figure B.6 - Cube plot of fitted means for the bead density regression model for StarPlastic PC and NCC electrospun fibers in DOE#2

B.2.1 – DOE#2 – Fiber Diameter

Backward Elimination of Terms (α to remove = 0.1)

Analysis of Variance

Source	DF	Adj SS	Adj MS	F-Value	P-Value
Model	5	53.1630	10.6326	4.15	0.072
Linear	3	19.4521	6.4840	2.53	0.171
[PC] (wt%)	1	3.2999	3.2999	1.29	0.308
Voltage (kV)	1	9.2106	9.2106	3.60	0.116
Gap Dist (cm)	1	6.9415	6.9415	2.71	0.161
2-Way Interactions	2	33.7109	16.8555	6.58	0.040
[PC] (wt%)*Voltage (kV)	1	13.3076	13.3076	5.20	0.072
Voltage (kV)*Gap Dist (cm)	1	20.4033	20.4033	7.97	0.037
Error	5	12.8051	2.5610		
Curvature	1	9.7844	9.7844	12.96	0.023
Lack-of-Fit	2	2.4941	1.2471	4.74	0.174
Pure Error	2	0.5266	0.2633		
Total	10	65.9681			

Model Summary

S	R-sq	R-sq(adj)	R-sq(pred)
1.60032	80.59%	61.18%	0.00%

Coded Coefficients

Term	Effect	Coef	SE Coef	T-Value	P-Value	VIF
Constant		3.332	0.483	6.91	0.001	
[PC] (wt%)	-1.285	-0.642	0.566	-1.14	0.308	1.00
Voltage (kV)	2.146	1.073	0.566	1.90	0.116	1.00
Gap Dist (cm)	-1.863	-0.931	0.566	-1.65	0.161	1.00
[PC] (wt%)*Voltage (kV)	-2.579	-1.290	0.566	-2.28	0.072	1.00
Voltage (kV)*Gap Dist (cm)	-3.194	-1.597	0.566	-2.82	0.037	1.00

Regression Equation in Uncoded Units

$$\text{Fibre Diam (um)} = -35.4 + 0.903 [\text{PC}] (\text{wt}\%) + 2.205 \text{ Voltage (kV)} + 1.091 \text{ Gap Dist (cm)} - 0.0516 [\text{PC}] (\text{wt}\%) * \text{Voltage (kV)} - 0.0639 \text{ Voltage (kV)} * \text{Gap Dist (cm)}$$

Alias Structure

Factor Name

A [PC] (wt%)
 B Voltage (kV)
 C Gap Dist (cm)

Aliases

I
 A
 B
 C
 AB
 BC

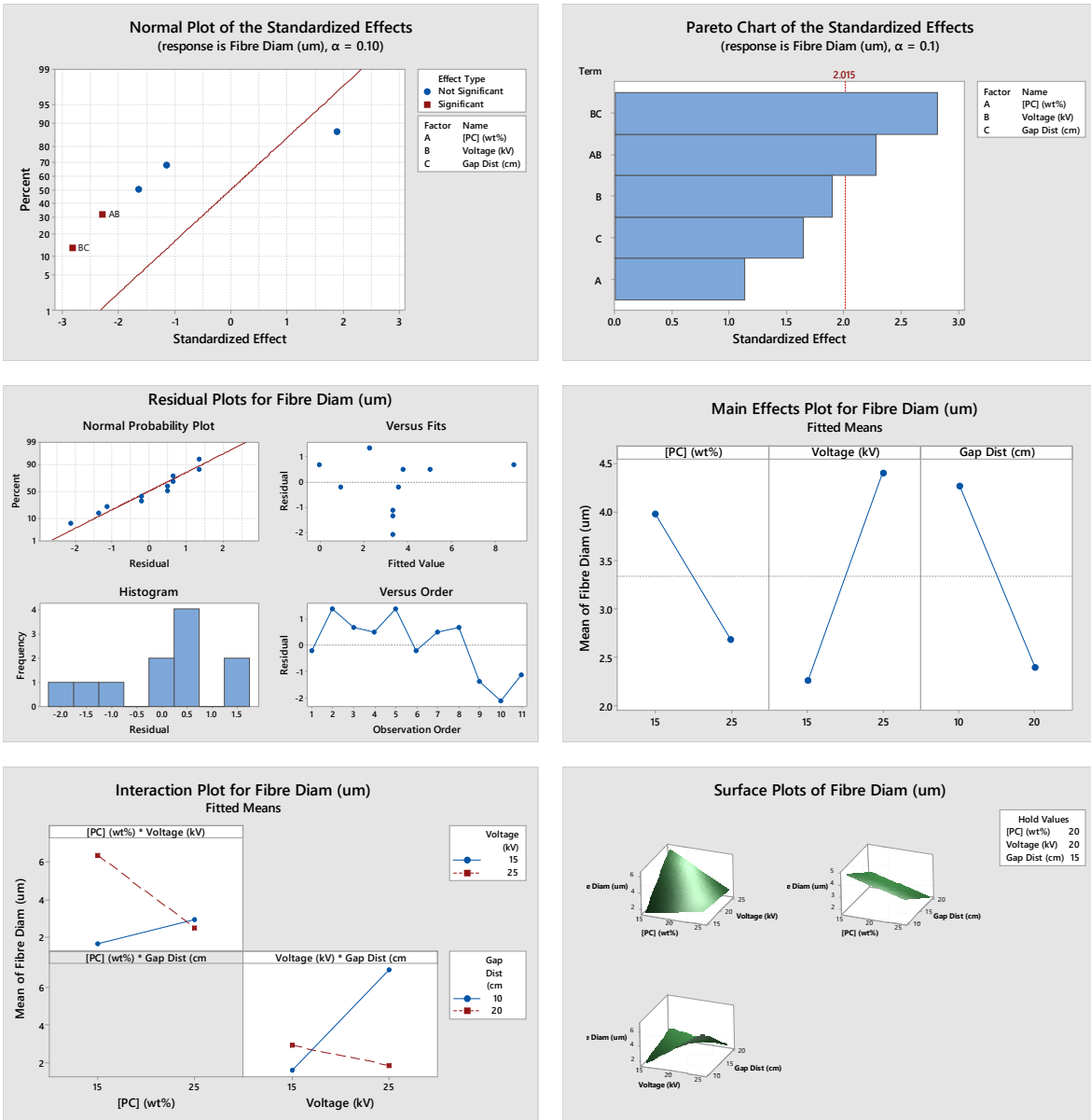


Figure B.7 - Minitab plot and chart outputs for DOE#2 – Fiber Diameter

B.2.2 – DOE#2 – Fiber Diameter (including CtPt)

Backward Elimination of Terms (α to remove = 0.1)

Analysis of Variance

Source	DF	Adj SS	Adj MS	F-Value	P-Value
Model	6	62.9474	10.4912	13.89	0.012
Linear	3	19.4521	6.4840	8.59	0.032
[PC] (wt%)	1	3.2999	3.2999	4.37	0.105
Voltage (kV)	1	9.2106	9.2106	12.20	0.025
Gap Dist (cm)	1	6.9415	6.9415	9.19	0.039
2-Way Interactions	2	33.7109	16.8555	22.32	0.007
[PC] (wt%)*Voltage (kV)	1	13.3076	13.3076	17.62	0.014
Voltage (kV)*Gap Dist (cm)	1	20.4033	20.4033	27.02	0.007
Curvature	1	9.7844	9.7844	12.96	0.023
Error	4	3.0207	0.7552		
Lack-of-Fit	2	2.4941	1.2471	4.74	0.174
Pure Error	2	0.5266	0.2633		
Total	10	65.9681			

Model Summary

S	R-sq	R-sq(adj)	R-sq(pred)
0.869009	95.42%	88.55%	37.71%

Coded Coefficients

Term	Effect	Coef	SE Coef	T-Value	P-Value	VIF
Constant		3.910	0.307	12.73	0.000	
[PC] (wt%)	-1.285	-0.642	0.307	-2.09	0.105	1.00
Voltage (kV)	2.146	1.073	0.307	3.49	0.025	1.00
Gap Dist (cm)	-1.863	-0.932	0.307	-3.03	0.039	1.00
[PC] (wt%)*Voltage (kV)	-2.579	-1.290	0.307	-4.20	0.014	1.00
Voltage (kV)*Gap Dist (cm)	-3.194	-1.597	0.307	-5.20	0.007	1.00
Ct Pt		-2.118	0.588	-3.60	0.023	1.00

Regression Equation in Uncoded Units

Fiber Diam (um) = -34.82 + 0.903 [PC] (wt%) + 2.205 Voltage (kV) + 1.091 Gap Dist (cm)
 - 0.0516 [PC] (wt%)*Voltage (kV) - 0.0639 Voltage (kV)*Gap Dist (cm)
 - 2.118 Ct Pt

Alias Structure

Factor	Name
A	[PC] (wt%)
B	Voltage (kV)
C	Gap Dist (cm)

Aliases

I
 A
 B
 C
 AB
 BC

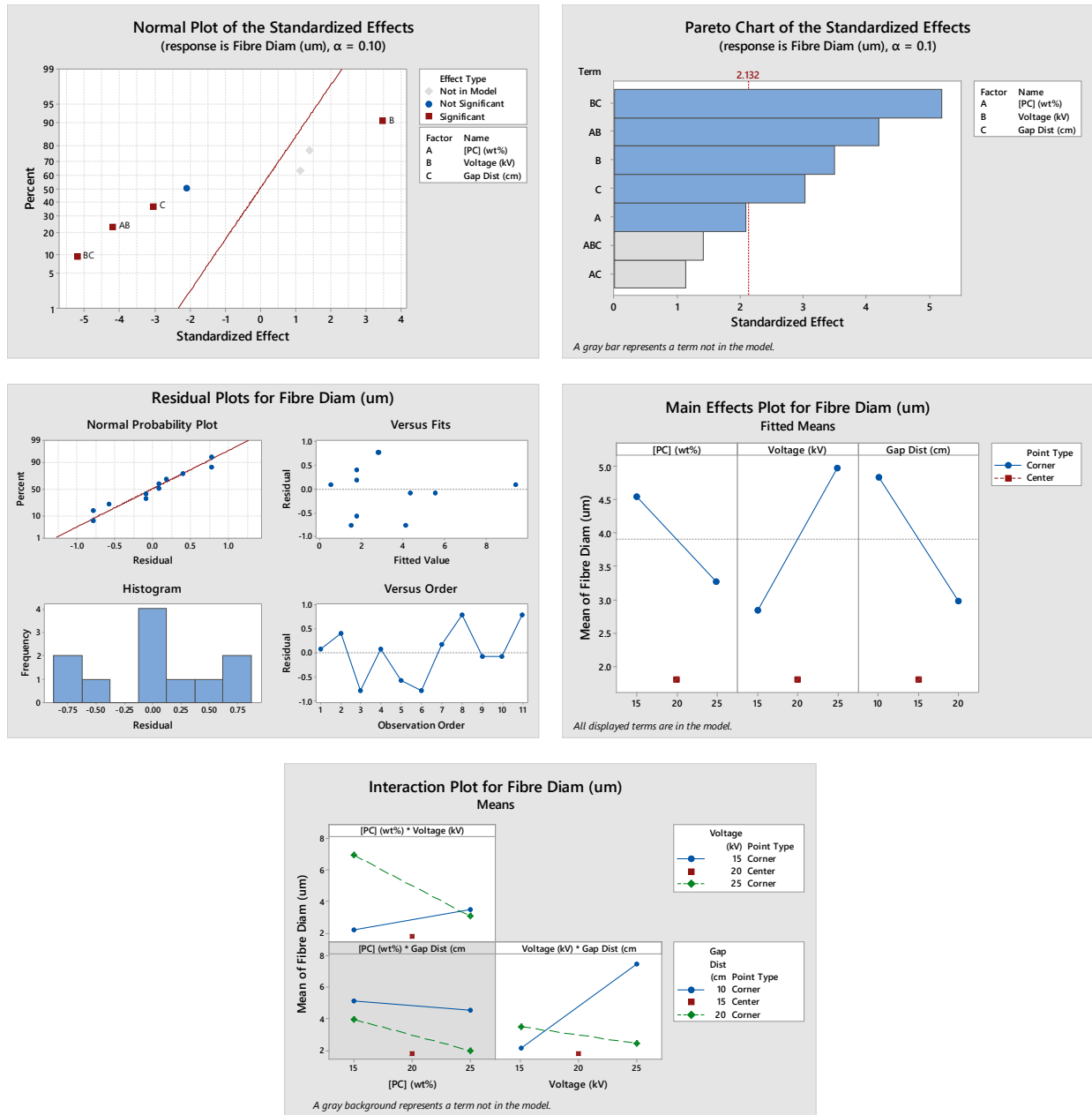


Figure B.8 - Minitab plot and chart outputs for DOE#2 – Fiber Diameter (including CtPt)

B.2.3 – DOE#2 – Bead Density

Backward Elimination of Terms (α to remove = 0.1)

Analysis of Variance

Source	DF	Adj SS	Adj MS	F-Value	P-Value
Model	6	3534395	589066	6.66	0.044
Linear	3	883001	294334	3.33	0.138
[PC] (wt%)	1	317511	317511	3.59	0.131
Voltage (kV)	1	324043	324043	3.66	0.128
Gap Dist (cm)	1	241447	241447	2.73	0.174
2-Way Interactions	3	2651394	883798	9.99	0.025

[PC] (wt%)*Voltage (kV)	1	971578	971578	10.99	0.030
[PC] (wt%)*Gap Dist (cm)	1	845193	845193	9.56	0.037
Voltage (kV)*Gap Dist (cm)	1	834623	834623	9.44	0.037
Error	4	353772	88443		
Curvature	1	131989	131989	1.79	0.274
Lack-of-Fit	1	207947	207947	30.06	0.032
Pure Error	2	13836	6918		
Total	10	3888167			

Model Summary

S	R-sq	R-sq(adj)	R-sq(pred)
297.394	90.90%	77.25%	0.00%

Coded Coefficients

Term	Effect	Coef	SE Coef	T-Value	P-Value	VIF
Constant		298.0	89.7	3.32	0.029	
[PC] (wt%)	-398	-199	105	-1.89	0.131	1.00
Voltage (kV)	-403	-201	105	-1.91	0.128	1.00
Gap Dist (cm)	-347	-174	105	-1.65	0.174	1.00
[PC] (wt%)*Voltage (kV)	697	348	105	3.31	0.030	1.00
[PC] (wt%)*Gap Dist (cm)	650	325	105	3.09	0.037	1.00
Voltage (kV)*Gap Dist (cm)	646	323	105	3.07	0.037	1.00

Regression Equation in Uncoded Units

Bead Dens (beads/mm²) = 15773 - 514 [PC] (wt%) - 513 Voltage (kV) - 553 Gap Dist (cm)
+ 13.94 [PC] (wt%)*Voltage (kV)
+ 13.00 [PC] (wt%)*Gap Dist (cm)
+ 12.92 Voltage (kV)*Gap Dist (cm)

Alias Structure

Factor	Name
A	[PC] (wt%)
B	Voltage (kV)
C	Gap Dist (cm)

Aliases

I
A
B
C
AB
AC
BC

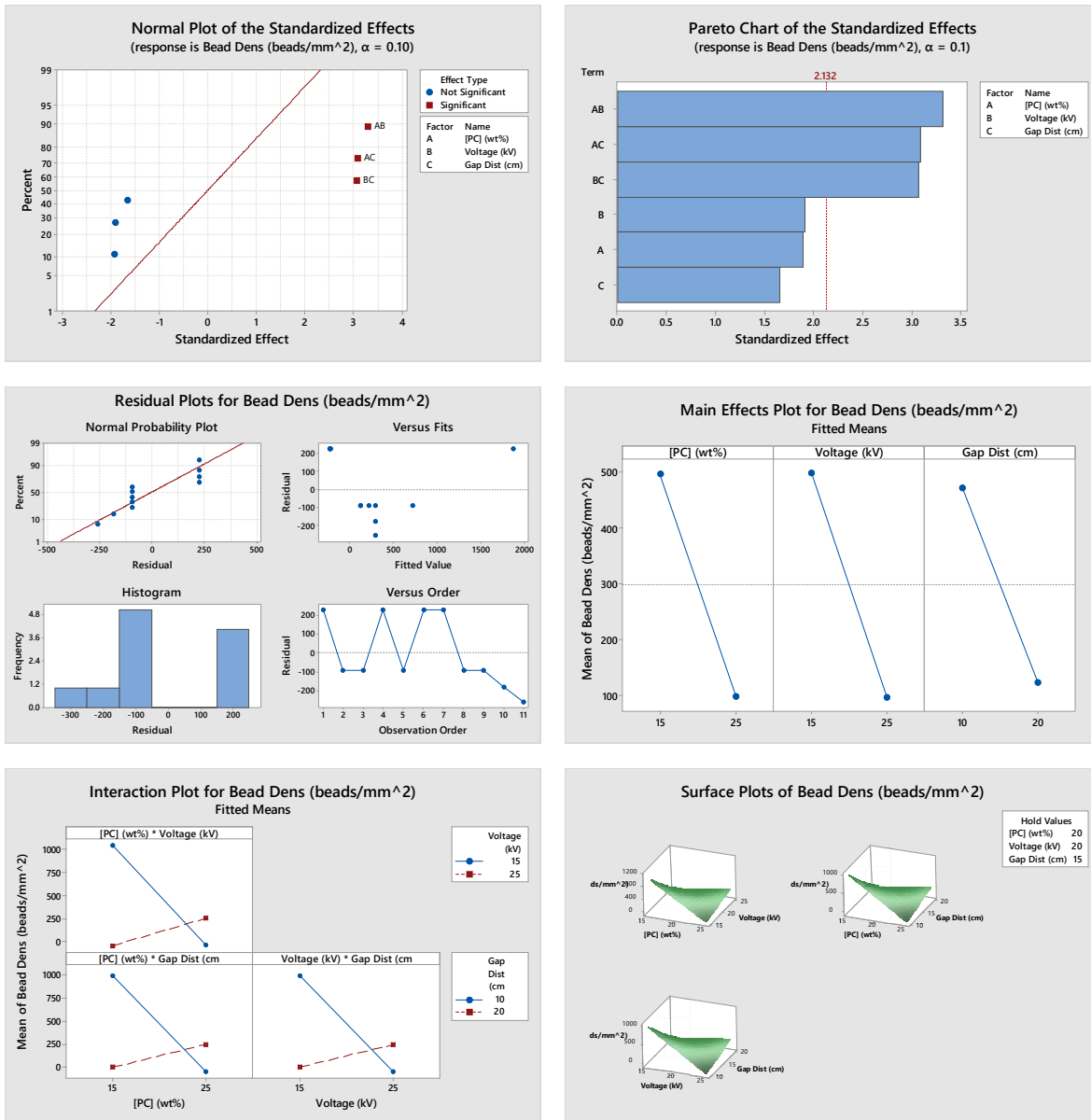


Figure B.9 - Minitab plot and chart outputs for DOE#2 – Bead Density

B.2.4 – DOE#2 – Bead Diameter

* NOTE * There are no terms in the model.

Backward Elimination of Terms (α to remove = 0.1)

Backward elimination removed all terms from the model.

Analysis of Variance

Source	DF	Adj SS	Adj MS	F-Value	P-Value
Model	7	1909.74	272.820	0.44	0.834
Linear	3	1334.35	444.782	0.71	0.606
[PC] (wt%)	1	8.84	8.837	0.01	0.913
Voltage (kV)	1	799.56	799.560	1.28	0.340
Gap Dist (cm)	1	525.95	525.950	0.84	0.426
2-Way Interactions	3	506.25	168.749	0.27	0.844

[PC] (wt%)*Voltage (kV)	1	2.38	2.378	0.00	0.955
[PC] (wt%)*Gap Dist (cm)	1	164.62	164.621	0.26	0.643
Voltage (kV)*Gap Dist (cm)	1	339.25	339.249	0.54	0.514
3-Way Interactions	1	69.15	69.149	0.11	0.761
[PC] (wt%)*Voltage (kV)*Gap Dist (cm)	1	69.15	69.149	0.11	0.761
Error	3	1872.68	624.228		
Curvature	1	71.68	71.681	0.08	0.804
Pure Error	2	1801.00	900.502		
Total	10	3782.43			

Model Summary

S	R-sq	R-sq(adj)	R-sq(pred)
24.9846	50.49%	0.00%	0.00%

Coded Coefficients

Term	Effect	Coef	SE Coef	T-Value	P-Value	VIF
Constant		13.16	7.53	1.75	0.179	
[PC] (wt%)	2.10	1.05	8.83	0.12	0.913	1.00
Voltage (kV)	-19.99	-10.00	8.83	-1.13	0.340	1.00
Gap Dist (cm)	16.22	8.11	8.83	0.92	0.426	1.00
[PC] (wt%)*Voltage (kV)	1.09	0.55	8.83	0.06	0.955	1.00
[PC] (wt%)*Gap Dist (cm)	9.07	4.54	8.83	0.51	0.643	1.00
Voltage (kV)*Gap Dist (cm)	-13.02	-6.51	8.83	-0.74	0.514	1.00
[PC] (wt%)*Voltage (kV)*Gap Dist (cm)	-5.88	-2.94	8.83	-0.33	0.761	1.00

Regression Equation in Uncoded Units

Bead Diam (um) = 151 - 10.0 [PC] (wt%) - 5.6 Voltage (kV) - 6.2 Gap Dist (cm)
+ 0.37 [PC] (wt%)*Voltage (kV) + 0.65 [PC] (wt%)*Gap Dist (cm)
+ 0.21 Voltage (kV)*Gap Dist (cm)
- 0.0235 [PC] (wt%)*Voltage (kV)*Gap Dist (cm)

Alias Structure

Factor	Name
A	[PC] (wt%)
B	Voltage (kV)
C	Gap Dist (cm)

Aliases

I
A
B
C
AB
AC
BC
ABC

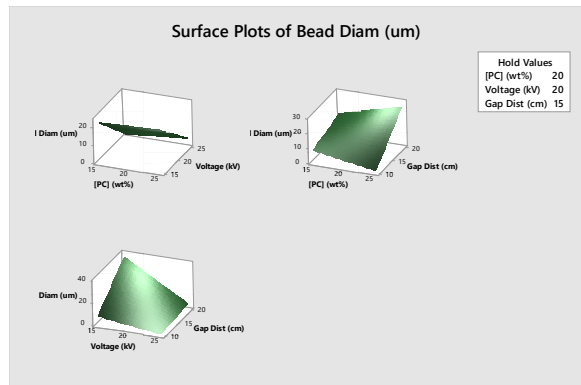
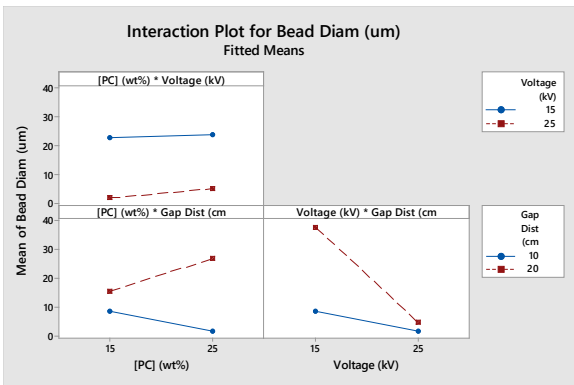
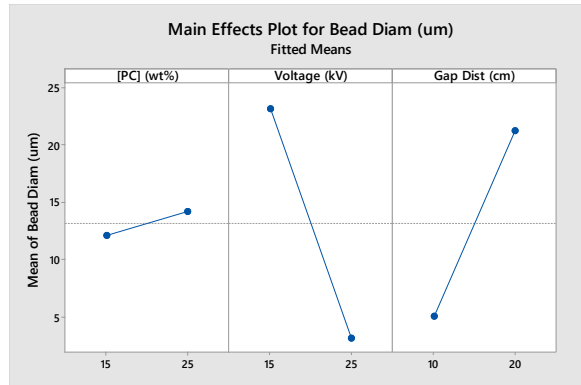
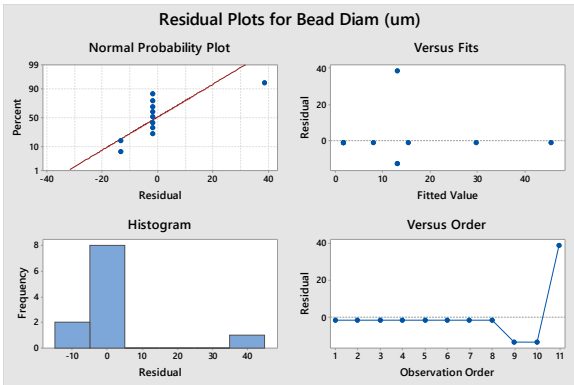
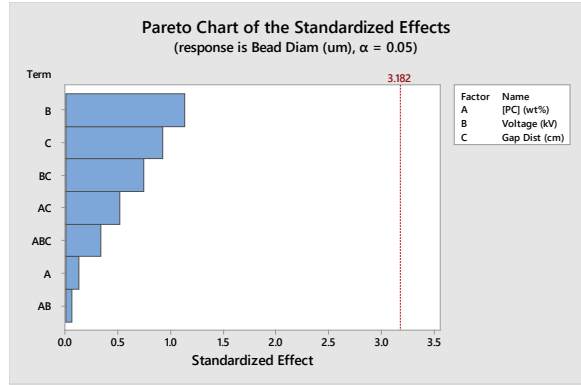


Figure B.10 - Minitab plot and chart outputs for DOE#2 – Bead Diameter

B.3 – PC and 2 wt.-% NCC/PC Electrospun Nanofibers in 60:40 (w/w) THF/DMF Solvent (DOE#0)

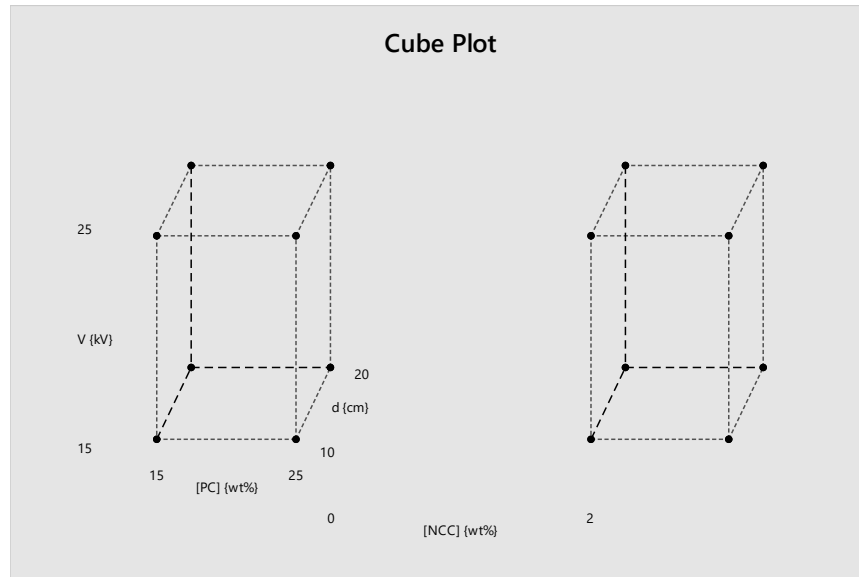


Figure B.11 - Cube plot representation of the 3D space of DOE#0 defined by high and low factor levels

Table B.5 - Standard order of experiments for a 2^4 full factorial DOE including the treatment shorthand notation and coded factor levels; high (1) and low (-1)

Standard Order	Treatment	a=[PC]	b=V	c=d	d=[NCC]
1	(1)	-1	-1	-1	-1
2	a	1	-1	-1	-1
3	b	-1	1	-1	-1
4	ab	1	1	-1	-1
5	c	-1	-1	1	-1
6	ac	1	-1	1	-1
7	bc	-1	1	1	-1
8	abc	1	1	1	-1
9	d	-1	-1	-1	1
10	ad	1	-1	-1	1
11	bd	-1	1	-1	1
12	abd	1	1	-1	1
13	cd	-1	-1	1	1

14	acd	1	-1	1	1
15	bcd	-1	1	1	1
16	abcd	1	1	1	1

Table B.6 - Target solution formulation masses for each run of DOE#0

Std. Order	Mass PC (g)	Mass 60:40 THF/DMF (g)	Mass NCC (g)	Total Mass (g)
1	7.5	42.5	0	50
2	12.5	37.5	0	50
3	7.5	42.5	0	50
4	12.5	37.5	0	50
5	7.5	42.5	0	50
6	12.5	37.5	0	50
7	7.5	42.5	0	50
8	12.5	37.5	0	50
9	7.5	42.5	0.1531	50.1531
10	12.5	37.5	0.2551	50.2551
11	7.5	42.5	0.1531	50.1531
12	12.5	37.5	0.2551	50.2551
13	7.5	42.5	0.1531	50.1531
14	12.5	37.5	0.2551	50.2551
15	7.5	42.5	0.1531	50.1531
16	12.5	37.5	0.2551	50.2551
Total Required	160	640	1.6328	801.6328

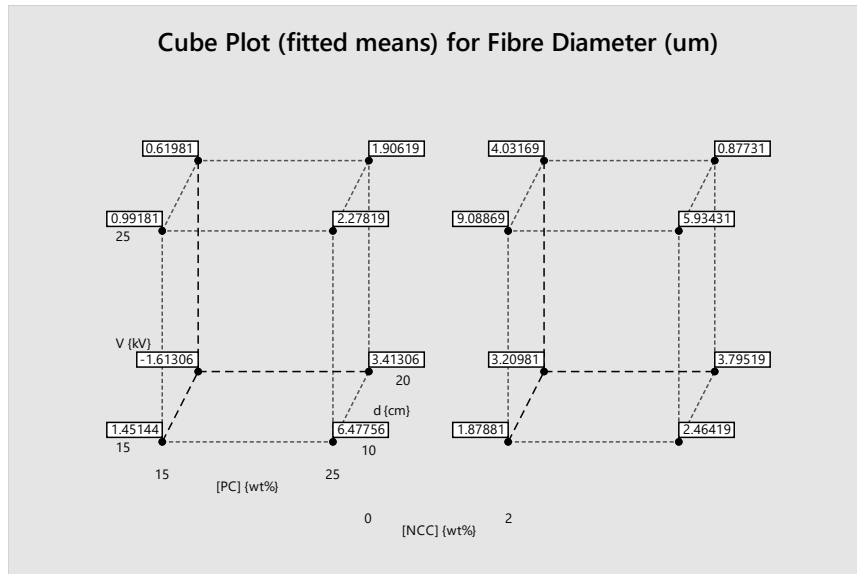


Figure B.12 - Cube plot of fitted means for the fiber diameter regression model for StarPlastic PC and PC/NCC electrospun fibers in DOE#0

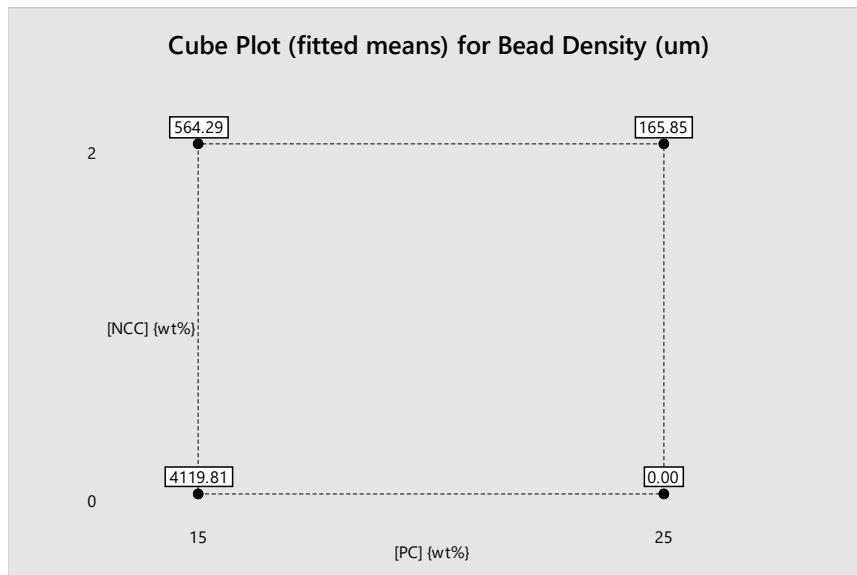


Figure B.13 - Cube plot of fitted means for the bead density regression model for StarPlastic PC and PC/NCC electrospun fibers in DOE#0

B.3.1 – DOE#0 – Fiber Diameter

Backward Elimination of Terms (α to remove = 0.1)

The initial model was saturated. The stepwise procedure removed the following terms in order to obtain sufficient degrees of freedom to begin: [PC] (wt%)*V (kV)*d (cm), [PC] (wt%)*V (kV)*[NCC] (wt%), [PC] (wt%)*d (cm)*[NCC] (wt%), [PC] (wt%)*V (kV)*d (cm)*[NCC] (wt%)

Analysis of Variance

Source	DF	Adj SS	Adj MS	F-Value	P-Value
Model	10	100.742	10.0742	3.48	0.091

Linear	4	33.195	8.2986	2.86	0.139
[PC] (wt%)	1	3.503	3.5034	1.21	0.322
V (kV)	1	1.352	1.3520	0.47	0.525
d (cm)	1	12.825	12.8254	4.43	0.089
[NCC] (wt%)	1	15.514	15.5138	5.35	0.069
2-Way Interactions	5	46.933	9.3867	3.24	0.111
[PC] (wt%)*V (kV)	1	13.986	13.9857	4.83	0.079
[PC] (wt%)*[NCC] (wt%)	1	19.720	19.7203	6.81	0.048
V (kV)*d (cm)	1	3.414	3.4142	1.18	0.327
V (kV)*[NCC] (wt%)	1	9.792	9.7922	3.38	0.125
d (cm)*[NCC] (wt%)	1	0.021	0.0210	0.01	0.936
3-Way Interactions	1	20.614	20.6139	7.11	0.044
V (kV)*d (cm)*[NCC] (wt%)	1	20.614	20.6139	7.11	0.044
Error	5	14.487	2.8975		
Total	15	115.229			

Model Summary

S	R-sq	R-sq(adj)	R-sq(pred)
1.70219	87.43%	62.28%	0.00%

Coded Coefficients

Term	Effect	Coef	SE Coef	T-Value	P-Value	VIF
Constant		2.925	0.426	6.87	0.001	
[PC] (wt%)	0.936	0.468	0.426	1.10	0.322	1.00
V (kV)	0.581	0.291	0.426	0.68	0.525	1.00
d (cm)	-1.791	-0.895	0.426	-2.10	0.089	1.00
[NCC] (wt%)	1.969	0.985	0.426	2.31	0.069	1.00
[PC] (wt%)*V (kV)	-1.870	-0.935	0.426	-2.20	0.079	1.00
[PC] (wt%)*[NCC] (wt%)	-2.220	-1.110	0.426	-2.61	0.048	1.00
V (kV)*d (cm)	-0.924	-0.462	0.426	-1.09	0.327	1.00
V (kV)*[NCC] (wt%)	1.565	0.782	0.426	1.84	0.125	1.00
d (cm)*[NCC] (wt%)	-0.072	-0.036	0.426	-0.09	0.936	1.00
V (kV)*d (cm)*[NCC] (wt%)	-2.270	-1.135	0.426	-2.67	0.044	1.00

Regression Equation in Uncoded Units

Fiber Diam (um) = -6.7 + 1.064 [PC] (wt%) + 0.246 V (kV) - 0.710 d (cm)
 - 11.22 [NCC] (wt%) - 0.0374 [PC] (wt%)*V (kV) - 0.2220 [PC] (wt%)*
 [NCC] (wt%) + 0.0269 V (kV)*d (cm) + 0.837 V (kV)*[NCC] (wt%)
 + 0.901 d (cm)*[NCC] (wt%) - 0.0454 V (kV)*d (cm)*[NCC] (wt%)

Alias Structure

Factor	Name
A	[PC] (wt%)
B	V (kV)
C	d (cm)
D	[NCC] (wt%)

Aliases

I
 A
 B
 C
 D
 AB
 AD
 BC
 BD
 CD
 BCD

Fits and Diagnostics for Unusual Observations

Fibre Diameter

Obs	(um)	Fit	Resid	Std Resid	R
5	0.30	-1.61	1.91	2.01	R
6	1.50	3.41	-1.91	-2.01	R

R Large residual

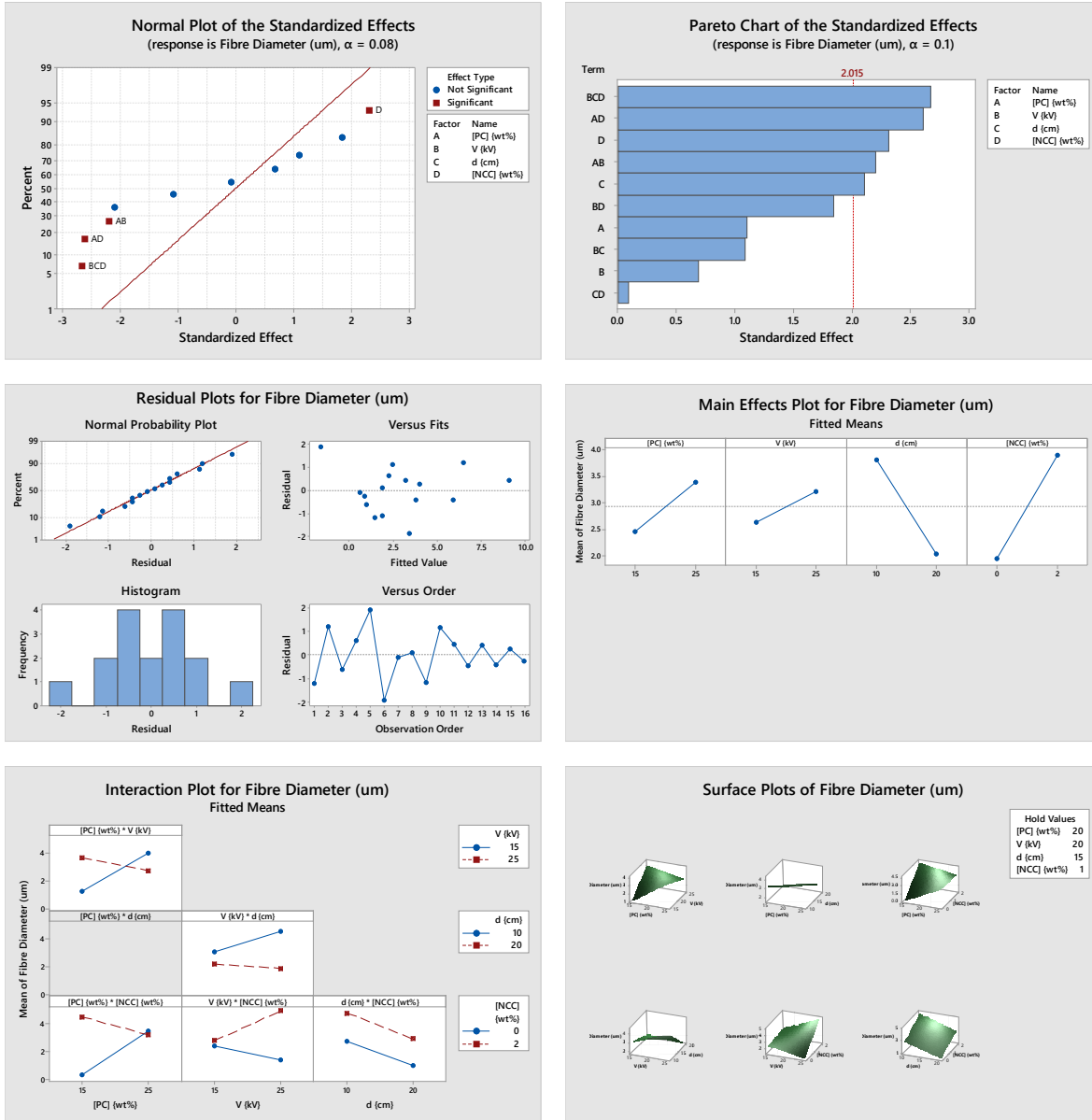


Figure B.14 - Minitab plot and chart outputs for DOE#0 – Fiber Diameter

B.3.2 – DOE#0 – Bead Density

Backward Elimination of Terms (α to remove = 0.1)

The initial model was saturated. The stepwise procedure removed the following terms in order to obtain sufficient degrees of freedom to begin: [PC] (wt%)*V (kV)*d (cm), [PC]

(wt%)*d (cm)*[NCC] (wt%), V (kV)*d (cm)*[NCC] (wt%), [PC] (wt%)*V (kV)*d (cm)*[NCC] (wt%)

Analysis of Variance

Source	DF	Adj SS	Adj MS	F-Value	P-Value
Model	3	45752971	15250990	4.32	0.028
Linear	2	31904402	15952201	4.52	0.034
[PC] (wt%)	1	20414579	20414579	5.78	0.033
[NCC] (wt%)	1	11489823	11489823	3.25	0.096
2-Way Interactions	1	13848569	13848569	3.92	0.071
[PC] (wt%)*[NCC] (wt%)	1	13848569	13848569	3.92	0.071
Error	12	42386176	3532181		
Total	15	88139148			

Model Summary

S	R-sq	R-sq(adj)	R-sq(pred)
1879.41	51.91%	39.89%	14.51%

Coded Coefficients

Term	Effect	Coef	SE Coef	T-Value	P-Value	VIF
Constant		1212	470	2.58	0.024	
[PC] (wt%)	-2259	-1130	470	-2.40	0.033	1.00
[NCC] (wt%)	-1695	-847	470	-1.80	0.096	1.00
[PC] (wt%)*[NCC] (wt%)	1861	930	470	1.98	0.071	1.00

Regression Equation in Uncoded Units

Bead Density (um) = 10300 - 412 [PC] (wt%) - 4569 [NCC] (wt%)
 + 186.1 [PC] (wt%)*[NCC] (wt%)

Alias Structure

Factor	Name
A	[PC] (wt%)
B	V (kV)
C	d (cm)
D	[NCC] (wt%)

Aliases

I
 A
 D
 AD

Fits and Diagnostics for Unusual Observations

Obs	Bead		Fit	Resid	Std
	Density (um)				
3	9437		4120	5317	3.27 R

R Large residual

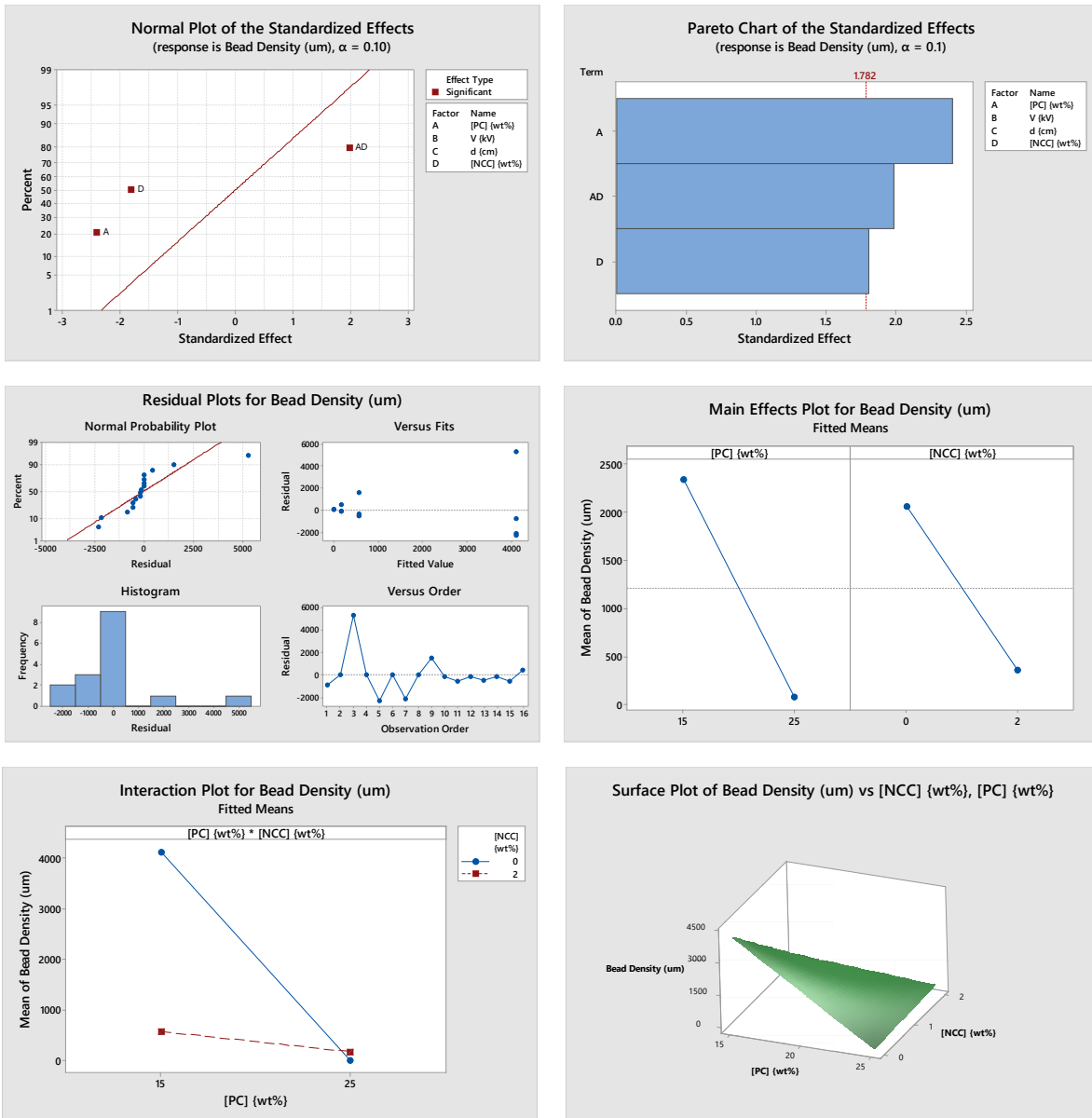


Figure B.15 - Minitab plot and chart outputs for DOE#0 – Bead Density

B.3.3 – DOE#0 – Bead Diameter

* NOTE * There are no terms in the model.

Backward Elimination of Terms (α to remove = 0.1)

Backward elimination removed all terms from the model. The initial model was saturated. The stepwise procedure removed the following terms in order to obtain sufficient degrees of freedom to begin: [PC] (wt%)*V (kV), [PC] (wt%)*V (kV)*d (cm), [PC] (wt%)*V (kV)*[NCC] (wt%), [PC] (wt%)*V (kV)*d (cm)*[NCC] (wt%)

Analysis of Variance

Source	DF	Adj SS	Adj MS	F-Value	P-Value
Model	15	17764707	1184314	*	*
Linear	4	4703732	1175933	*	*
[PC] (wt%)	1	1192110	1192110	*	*

V (kV)	1	1144951	1144951	*	*
d (cm)	1	1220159	1220159	*	*
[NCC] (wt%)	1	1146512	1146512	*	*
2-Way Interactions	6	7088511	1181418	*	*
[PC] (wt%)*V (kV)	1	1185764	1185764	*	*
[PC] (wt%)*d (cm)	1	1164930	1164930	*	*
[PC] (wt%)*[NCC] (wt%)	1	1201308	1201308	*	*
V (kV)*d (cm)	1	1154821	1154821	*	*
V (kV)*[NCC] (wt%)	1	1232129	1232129	*	*
d (cm)*[NCC] (wt%)	1	1149559	1149559	*	*
3-Way Interactions	4	4802237	1200559	*	*
[PC] (wt%)*V (kV)*d (cm)	1	1195808	1195808	*	*
[PC] (wt%)*V (kV)*[NCC] (wt%)	1	1190519	1190519	*	*
[PC] (wt%)*d (cm)*[NCC] (wt%)	1	1204427	1204427	*	*
V (kV)*d (cm)*[NCC] (wt%)	1	1211483	1211483	*	*
4-Way Interactions	1	1170226	1170226	*	*
[PC] (wt%)*V (kV)*d (cm)*[NCC] (wt%)	1	1170226	1170226	*	*
Error	0	*	*		
Total	15	17764707			

Model Summary

S	R-sq	R-sq(adj)	R-sq(pred)
*	100.00%	*	*

Coded Coefficients

Term	Effect	Coef	SE	T-Value	P-Value	VIF
Constant		279.3	*	*	*	
[PC] (wt%)	-545.9	-273.0	*	*	* 1.00	
V (kV)	535.0	267.5	*	*	* 1.00	
d (cm)	552.3	276.2	*	*	* 1.00	
[NCC] (wt%)	-535.4	-267.7	*	*	* 1.00	
[PC] (wt%)*V (kV)	-544.5	-272.2	*	*	* 1.00	
[PC] (wt%)*d (cm)	-539.7	-269.8	*	*	* 1.00	
[PC] (wt%)*[NCC] (wt%)	548.0	274.0	*	*	* 1.00	
V (kV)*d (cm)	537.3	268.7	*	*	* 1.00	
V (kV)*[NCC] (wt%)	-555.0	-277.5	*	*	* 1.00	
d (cm)*[NCC] (wt%)	-536.1	-268.0	*	*	* 1.00	
[PC] (wt%)*V (kV)*d (cm)	-546.8	-273.4	*	*	* 1.00	
[PC] (wt%)*V (kV)*[NCC] (wt%)	545.6	272.8	*	*	* 1.00	
[PC] (wt%)*d (cm)*[NCC] (wt%)	548.7	274.4	*	*	* 1.00	
V (kV)*d (cm)*[NCC] (wt%)	-550.3	-275.2	*	*	* 1.00	
[PC] (wt%)*V (kV)*d (cm)*[NCC] (wt%)	540.9	270.4	*	*	* 1.00	

Regression Equation in Uncoded Units

Bead Diam (um) = 16301 - 652.0 [PC] (wt%) - 1086 V (kV) - 1631 d (cm) - 8076 [NCC] (wt%)
+ 43.46 [PC] (wt%)*V (kV) + 65.24 [PC] (wt%)*d (cm) + 321.0 [PC] (wt%)*
[NCC] (wt%) + 108.8 V (kV)*d (cm) + 540.4 V (kV)*[NCC] (wt%) + 812.4 d (cm)*
[NCC] (wt%) - 4.351 [PC] (wt%)*V (kV)*d (cm) - 21.54 [PC] (wt%)*V (kV)*
[NCC] (wt%) - 32.30 [PC] (wt%)*d (cm)*[NCC] (wt%) - 54.28 V (kV)*d (cm)*
[NCC] (wt%) + 2.164 [PC] (wt%)*V (kV)*d (cm)*[NCC] (wt%)

Alias Structure

Factor	Name
A	[PC] (wt%)
B	V (kV)
C	d (cm)
D	[NCC] (wt%)

Aliases

- I
- A
- B
- C
- D
- AB
- AC
- AD
- BC
- BD
- CD
- ABC
- ABD
- ACD
- BCD
- ABCD

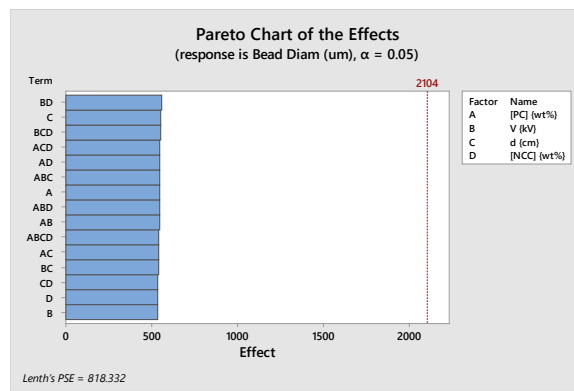


Figure B.16 - Minitab plot and chart output for DOE#0 – Bead Diameter

* NOTE * Could not graph the specified residual type because MSE = 0 or the degrees of freedom for error = 0.

B.4 – PC Electrospun Nanofibers in Chloroform Solvent (DOE#3)

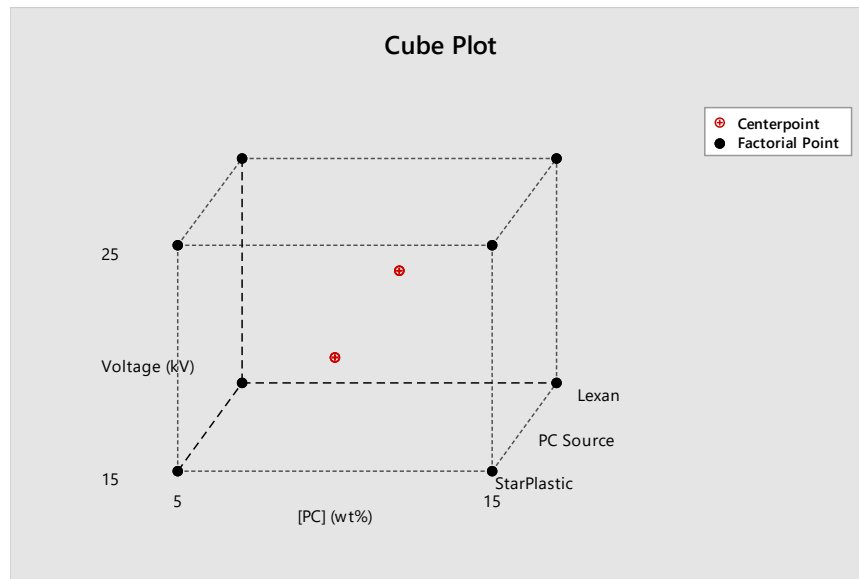


Figure B.17 - Cube plot representation of the 3D space of DOE#3 defined by high and low factor levels

Table B.7 - Standard order of experiments for a 2^3 full factorial DOE including the treatment shorthand notation and coded factor levels; high (1), center (0), and low (-1) with one non-numeric (discrete) factor

Run	Treatment	A=[PC]	B=V	C=d
1	(1)	-1	-1	-1
2	a	1	-1	-1
3	b	-1	1	-1
4	ab	1	1	-1
5	c	-1	-1	1
6	ac	1	-1	1
7	bc	-1	1	1
8	abc	1	1	1
Replicates				
9	Centre	0	0	1
10	Point	0	0	1
11	Replicates	0	0	1
12		0	0	-1

13	0	0	-1
14	0	0	-1

Table B.8 - Target solution formulation masses for each run of DOE#3

Std. Order	Mass PC (g)	Mass Chloroform (g)	Total Mass (g)
1	2.5	47.5	50
2	7.5	42.5	50
3	2.5	47.5	50
4	7.5	42.5	50
5	2.5	47.5	50
6	7.5	42.5	50
7	2.5	47.5	50
8	7.5	42.5	50
9	5	45	50
10	5	45	50
11	5	45	50
12	5	45	50
13	5	45	50
14	5	45	50
Total Required	70	630	700

Table B.9 - DOE#3 target and actual mass measurements for StarPlastic and Lexan PC in chloroform for each 14 runs

Std. Order	mPC Target (g)	mPC Actual (g)	mCHLORO Target (g)	mCHLORO Actual (g)
1 (1)	2.5	2.50	47.5	47.54
2 (a)	7.5	7.50	42.5	42.48
3 (b)	2.5	2.50	47.5	47.58
4 (ab)	7.5	7.51	42.5	42.53

5 (c)	2.5	2.54	47.5	47.49
6 (ac)	7.5	7.52	42.5	43.58
7 (bc)	2.5	2.52	47.5	47.59
8 (abc)	7.5	7.52	42.5	42.65
9 (0)	5	4.95	45	45.05
10 (0)	5	5.08	45	45.05
11 (0)	5	4.51	45	42.65
12 (0)	5	5.07	45	45.05
13 (0)	5	5.01	45	44.98
14 (0)	5	5.04	45	45.08

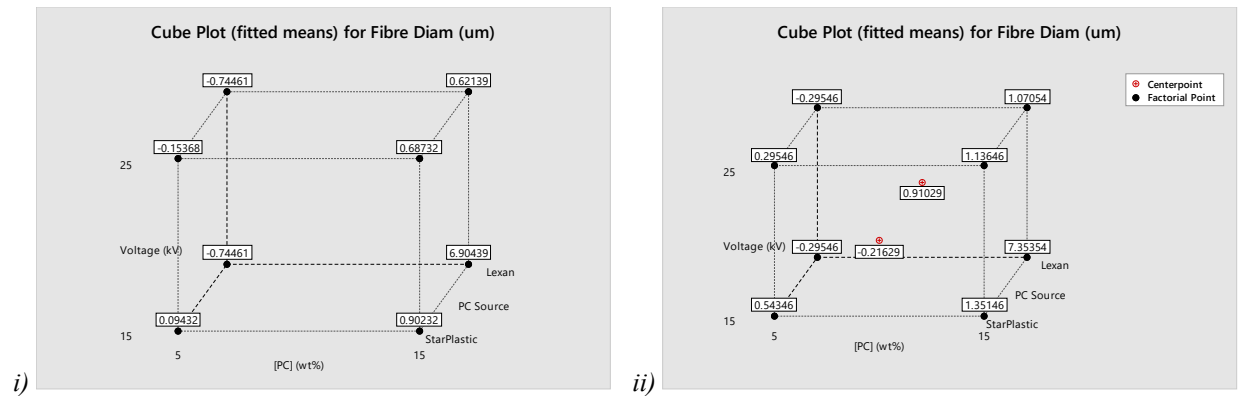


Figure B.18 - Cube plot of fitted means for the fiber diameter regression model for StarPlastic and Lexan PC electrospun fibers in DOE#3; i) without CtPt and ii) with CtPt inclusion

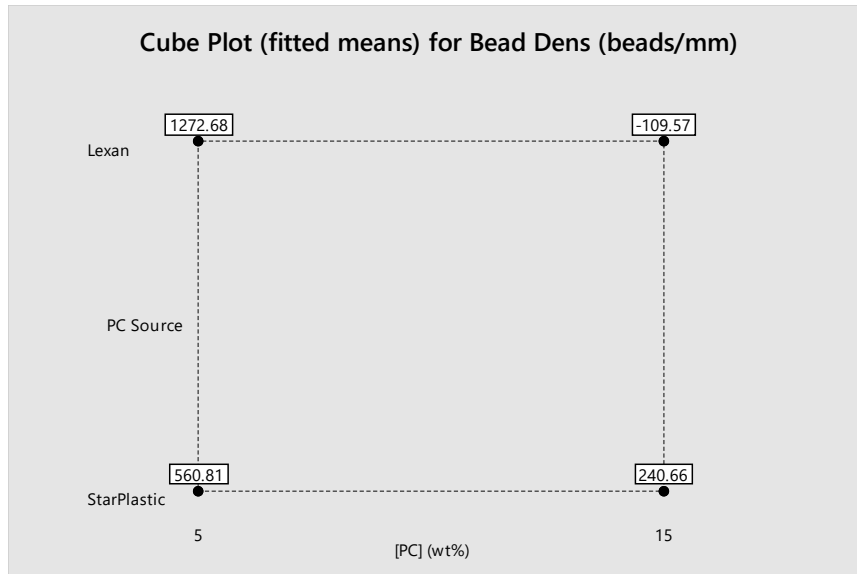


Figure B.19 - Cube plot of fitted means for the bead density regression model for StarPlastic and Lexan PC electrospun fibers in DOE#3

B.4.1 – DOE#3 – Fiber Diameter

Backward Elimination of Terms (α to remove = 0.1)

Analysis of Variance

Source	DF	Adj SS	Adj MS	F-Value	P-Value
Model	7	45.2313	6.4616	6.40	0.019
Linear	3	24.3457	8.1152	8.04	0.016
[PC] (wt%)	1	14.2151	14.2151	14.08	0.009
Voltage (kV)	1	5.6886	5.6886	5.63	0.055
PC Source	1	4.4421	4.4421	4.40	0.081
2-Way Interactions	3	15.8991	5.2997	5.25	0.041
[PC] (wt%)*Voltage (kV)	1	4.8828	4.8828	4.84	0.070
[PC] (wt%)*PC Source	1	6.7822	6.7822	6.72	0.041
Voltage (kV)*PC Source	1	4.2340	4.2340	4.19	0.086
3-Way Interactions	1	4.9865	4.9865	4.94	0.068
[PC] (wt%)*Voltage (kV)*PC Source	1	4.9865	4.9865	4.94	0.068
Error	6	6.0571	1.0095		
Curvature	1	3.7656	3.7656	8.22	0.035
Lack-of-Fit	1	1.6296	1.6296	9.85	0.035
Pure Error	4	0.6619	0.1655		
Total	13	51.2884			

Model Summary

S	R-sq	R-sq(adj)	R-sq(pred)
1.00474	88.19%	74.41%	0.00%

Coded Coefficients

Term	Effect	Coef	SE Coef	T-Value	P-Value	VIF
Constant		0.946	0.269	3.52	0.012	
[PC] (wt%)	2.666	1.333	0.355	3.75	0.009	1.00
Voltage (kV)	-1.686	-0.843	0.355	-2.37	0.055	1.00
PC Source	1.127	0.563	0.269	2.10	0.081	1.00
[PC] (wt%)*Voltage (kV)	-1.562	-0.781	0.355	-2.20	0.070	1.00
[PC] (wt%)*PC Source	1.841	0.921	0.355	2.59	0.041	1.00
Voltage (kV)*PC Source	-1.455	-0.727	0.355	-2.05	0.086	1.00
[PC] (wt%)*Voltage (kV)*PC Source	-1.579	-0.789	0.355	-2.22	0.068	1.00

Regression Equation in Uncoded Units

Fibre Diam (um) = -4.60 + 0.892 [PC] (wt%) + 0.144 Voltage (kV) - 4.68 PC Source
- 0.0313 [PC] (wt%)*Voltage (kV) + 0.816 [PC] (wt%)*PC Source
+ 0.170 Voltage (kV)*PC Source - 0.0316 [PC] (wt%)*Voltage (kV)*PC Source

Alias Structure

Factor	Name
A	[PC] (wt%)
B	Voltage (kV)
C	PC Source

Aliases

I
A
B
C
AB
AC
BC
ABC

Fits and Diagnostics for Unusual Observations

Obs	Fibre Diam (um)	Fit	Resid	Std	
5	0.000	-0.745	0.745	2.26	R
6	7.649	6.904	0.745	2.26	R
7	0.000	-0.745	0.745	2.26	R
8	1.366	0.621	0.745	2.26	R

R Large residual

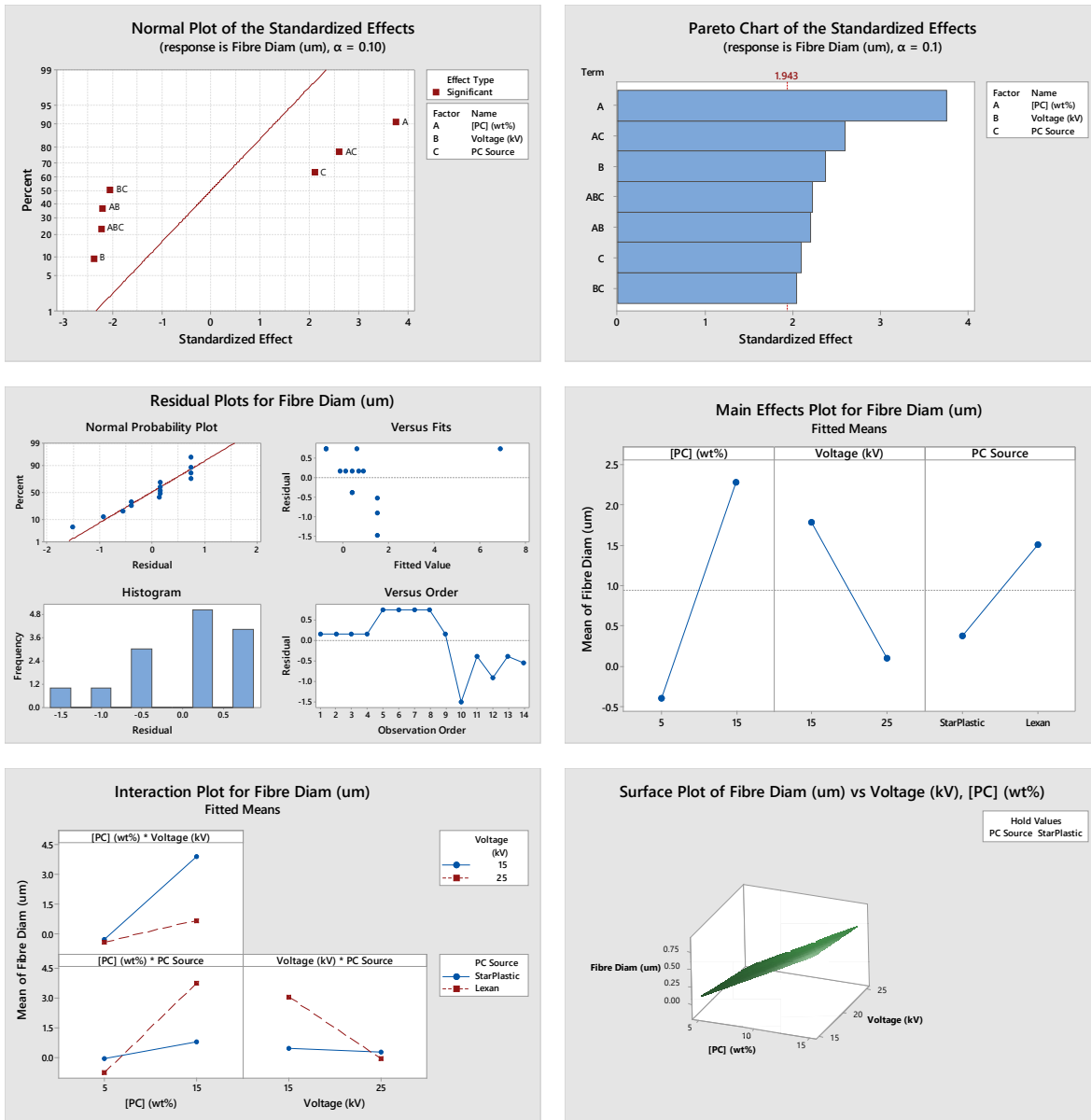


Figure B.20 - Minitab plot and chart outputs for DOE#3 – Fiber Diameter

B.4.2 – DOE#3 – Fiber Diameter (including CtPt)

Backward Elimination of Terms (α to remove = 0.1)

Analysis of Variance

Source	DF	Adj SS	Adj MS	F-Value	P-Value
Model	8	48.9970	6.1246	13.36	0.006
Linear	3	24.3457	8.1152	17.71	0.004
[PC] (wt%)	1	14.2151	14.2151	31.02	0.003
Voltage (kV)	1	5.6886	5.6886	12.41	0.017
PC Source	1	4.4421	4.4421	9.69	0.026
2-Way Interactions	3	15.8991	5.2997	11.56	0.011
[PC] (wt%)*Voltage (kV)	1	4.8828	4.8828	10.65	0.022
[PC] (wt%)*PC Source	1	6.7822	6.7822	14.80	0.012

Voltage (kV)*PC Source	1	4.2340	4.2340	9.24	0.029
3-Way Interactions	1	4.9865	4.9865	10.88	0.022
[PC] (wt%)*Voltage (kV)*PC Source	1	4.9865	4.9865	10.88	0.022
Curvature	1	3.7656	3.7656	8.22	0.035
Error	5	2.2915	0.4583		
Lack-of-Fit	1	1.6296	1.6296	9.85	0.035
Pure Error	4	0.6619	0.1655		
Total	13	51.2884			

Model Summary

S	R-sq	R-sq(adj)	R-sq(pred)
0.676972	95.53%	88.38%	0.00%

Coded Coefficients

Term	Effect	Coef	SE Coef	T-Value	P-Value	VIF
Constant		1.395	0.239	5.83	0.002	
[PC] (wt%)	2.666	1.333	0.239	5.57	0.003	1.00
Voltage (kV)	-1.686	-0.843	0.239	-3.52	0.017	1.00
PC Source	1.127	0.563	0.181	3.11	0.026	1.00
[PC] (wt%)*Voltage (kV)	-1.563	-0.781	0.239	-3.26	0.022	1.00
[PC] (wt%)*PC Source	1.841	0.921	0.239	3.85	0.012	1.00
Voltage (kV)*PC Source	-1.455	-0.727	0.239	-3.04	0.029	1.00
[PC] (wt%)*Voltage (kV)*PC Source	-1.579	-0.789	0.239	-3.30	0.022	1.00
Ct Pt		-1.048	0.366	-2.87	0.035	1.00

Regression Equation in Uncoded Units

Fiber Diam (um) = -4.15 + 0.892 [PC] (wt%) + 0.144 Voltage (kV) - 4.68 PC Source
- 0.03125 [PC] (wt%)*Voltage (kV) + 0.816 [PC] (wt%)*PC Source
+ 0.170 Voltage (kV)*PC Source - 0.03158 [PC] (wt%)*Voltage (kV)*PC Source
- 1.048 Ct Pt

Alias Structure

Factor	Name
A	[PC] (wt%)
B	Voltage (kV)
C	PC Source

Aliases

I
A
B
C
AB
AC
BC
ABC

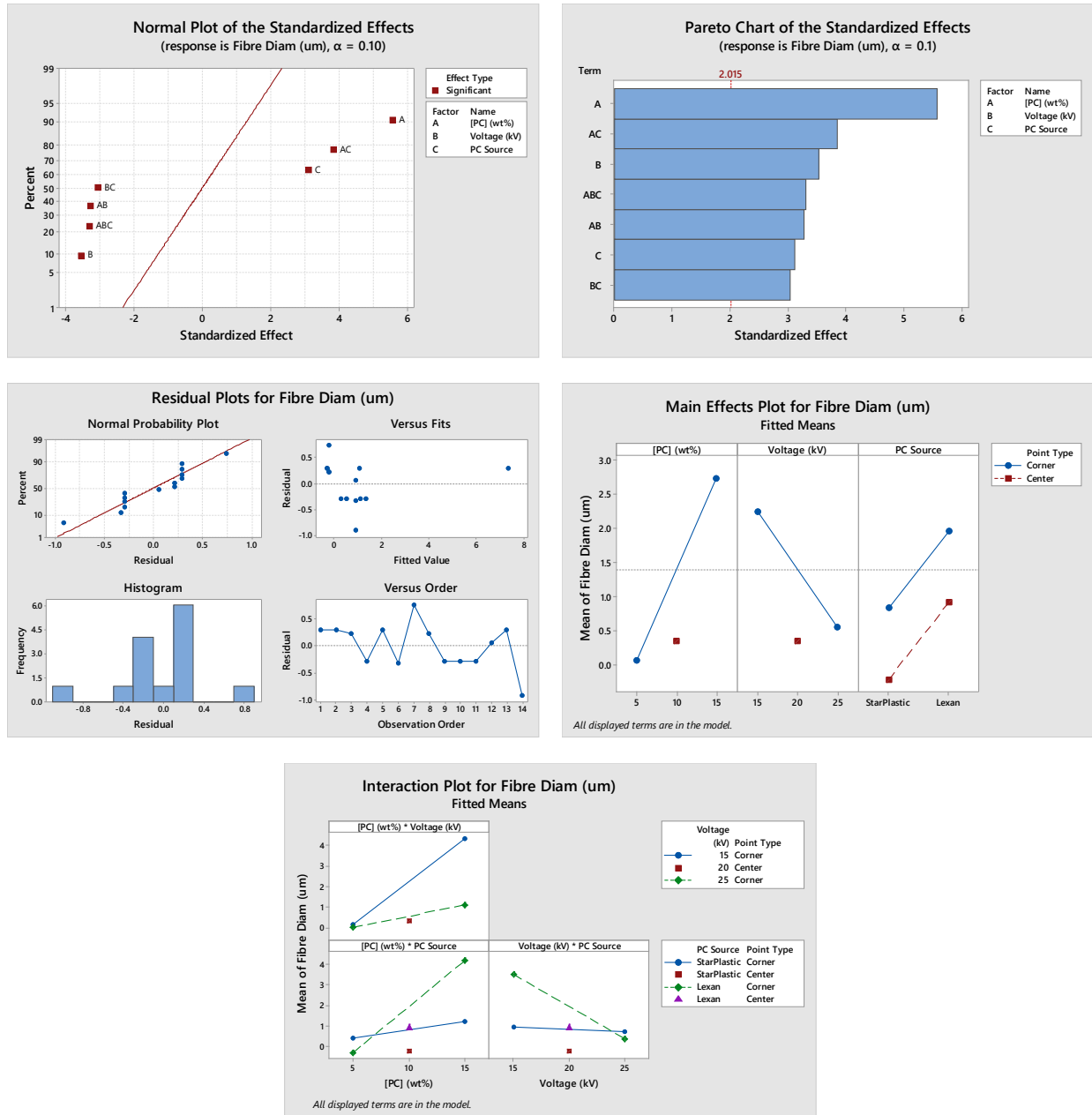


Figure B.21 - Minitab plot and chart outputs for DOE#3 – Fiber Diameter (including CtPt)

B.4.3 – DOE#3 – Bead Density

Backward Elimination of Terms (α to remove = 0.1)

Analysis of Variance

Source	DF	Adj SS	Adj MS	F-Value	P-Value
Model	3	2127548	709183	6.48	0.010
Linear	2	1563523	781762	7.14	0.012
[PC] (wt%)	1	1449079	1449079	13.24	0.005
PC Source	1	114444	114444	1.05	0.331
2-Way Interactions	1	564025	564025	5.15	0.047

[PC] (wt%)*PC Source	1	564025	564025	5.15	0.047
Error	10	1094349	109435		
Curvature	1	2009	2009	0.02	0.900
Lack-of-Fit	5	589494	117899	0.94	0.540
Pure Error	4	502846	125711		
Total	13	3221897			

Model Summary

S	R-sq	R-sq(adj)	R-sq(pred)
330.809	66.03%	55.84%	37.24%

Coded Coefficients

Term	Effect	Coef	SE Coef	T-Value	P-Value	VIF
Constant		491.1	88.4	5.56	0.000	
[PC] (wt%)	-851	-426	117	-3.64	0.005	1.00
PC Source	180.8	90.4	88.4	1.02	0.331	1.00
[PC] (wt%)*PC Source	-531	-266	117	-2.27	0.047	1.00

Regression Equation in Uncoded Units

Bead Dens (beads/mm) = 1342 - 85.1 [PC] (wt%) + 621 PC Source - 53.1 [PC] (wt%)*PC Source

Alias Structure

Factor	Name
A	[PC] (wt%)
B	Voltage (kV)
C	PC Source

Aliases

I
A
C
AC

Fits and Diagnostics for Unusual Observations

Obs	Bead Dens (beads/mm)	Fit	Resid	Std
13	1134	401	733	2.39 R

R Large residual

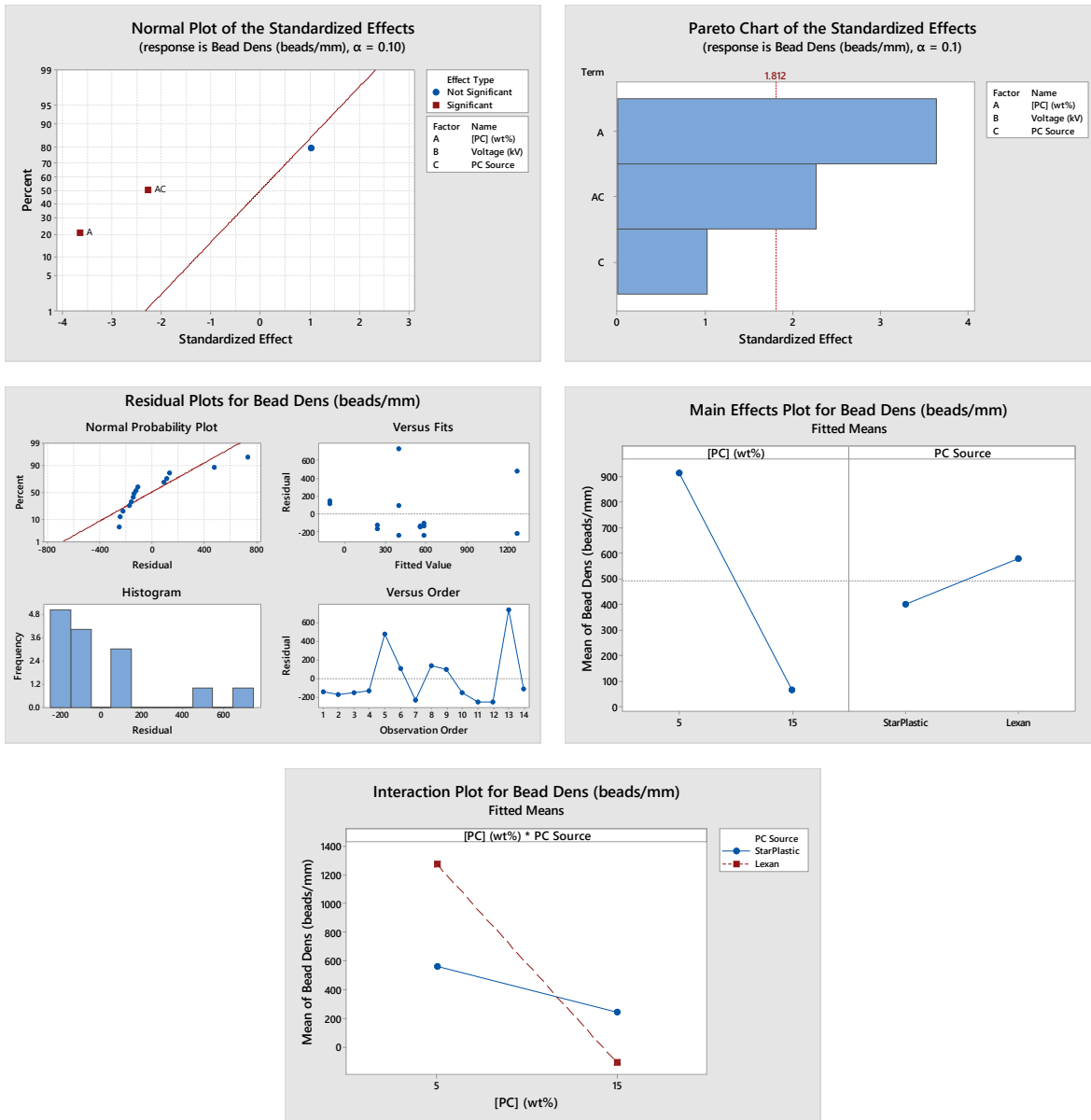


Figure B.22 - Minitab plot and chart outputs for DOE#3 – Bead Density

B.4.4 – DOE#3 – Bead Diameter

* NOTE * There are no terms in the model.

Backward Elimination of Terms (α to remove = 0.1)

Backward elimination removed all terms from the model.

Analysis of Variance

Source	DF	Adj SS	Adj MS	F-Value	P-Value
Model	7	369.71	52.815	0.19	0.978
Linear	3	205.88	68.625	0.24	0.864
[PC] (wt%)	1	145.82	145.821	0.52	0.500
Voltage (kV)	1	58.11	58.110	0.21	0.666
PC Source	1	1.95	1.946	0.01	0.937
2-Way Interactions	3	163.76	54.587	0.19	0.897

[PC] (wt%)*Voltage (kV)	1	12.64	12.643	0.04	0.839
[PC] (wt%)*PC Source	1	21.55	21.553	0.08	0.792
Voltage (kV)*PC Source	1	129.56	129.565	0.46	0.524
3-Way Interactions	1	0.07	0.070	0.00	0.988
[PC] (wt%)*Voltage (kV)*PC Source	1	0.07	0.070	0.00	0.988
Error	6	1695.82	282.636		
Curvature	1	356.27	356.269	1.33	0.301
Lack-of-Fit	1	378.67	378.669	1.58	0.278
Pure Error	4	960.88	240.220		
Total	13	2065.52			

Model Summary

S	R-sq	R-sq(adj)	R-sq(pred)
16.8118	17.90%	0.00%	0.00%

Coded Coefficients

Term	Effect	Coef	SE Coef	T-Value	P-Value	VIF
Constant		19.01	4.49	4.23	0.005	
[PC] (wt%)	-8.54	-4.27	5.94	-0.72	0.500	1.00
Voltage (kV)	5.39	2.70	5.94	0.45	0.666	1.00
PC Source	0.75	0.37	4.49	0.08	0.937	1.00
[PC] (wt%)*Voltage (kV)	2.51	1.26	5.94	0.21	0.839	1.00
[PC] (wt%)*PC Source	3.28	1.64	5.94	0.28	0.792	1.00
Voltage (kV)*PC Source	8.05	4.02	5.94	0.68	0.524	1.00
[PC] (wt%)*Voltage (kV)*PC Source	-0.19	-0.09	5.94	-0.02	0.988	1.00

Regression Equation in Uncoded Units

Bead Diam (um) = 26.8 - 1.86 [PC] (wt%) + 0.04 Voltage (kV) - 19.8 PC Source
+ 0.050 [PC] (wt%)*Voltage (kV) + 0.40 [PC] (wt%)*PC Source
+ 0.84 Voltage (kV)*PC Source - 0.004 [PC] (wt%)*Voltage (kV)*PC Source

Alias Structure

Factor	Name
A	[PC] (wt%)
B	Voltage (kV)
C	PC Source

Aliases

I
A
B
C
AB
AC
BC
ABC

Fits and Diagnostics for Unusual Observations

Obs	Bead Diam (um)	Fit	Resid	Std Resid	
12	52.6	19.4	33.2	2.13	R

R Large residual

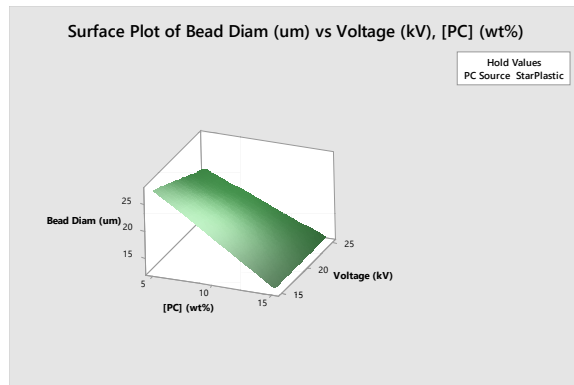
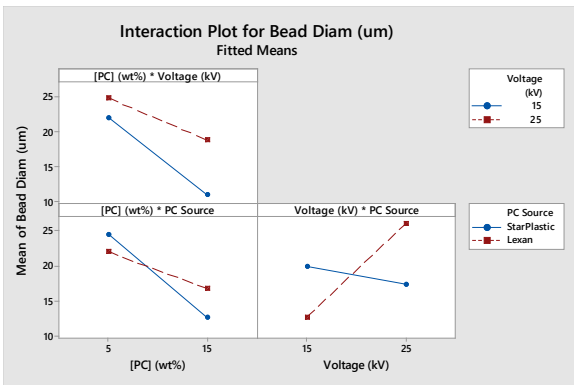
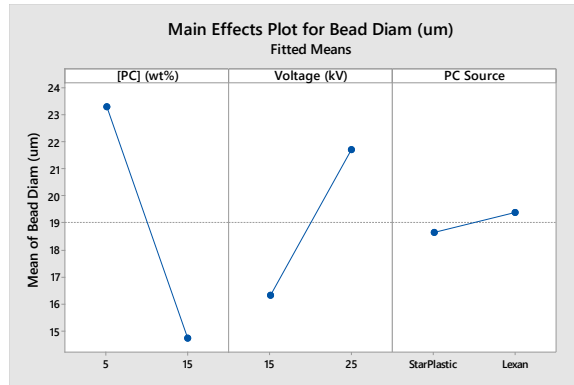
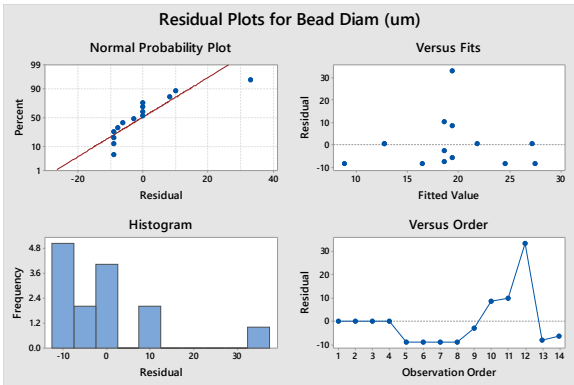
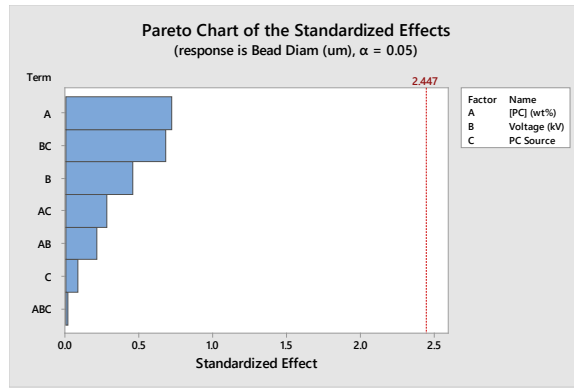
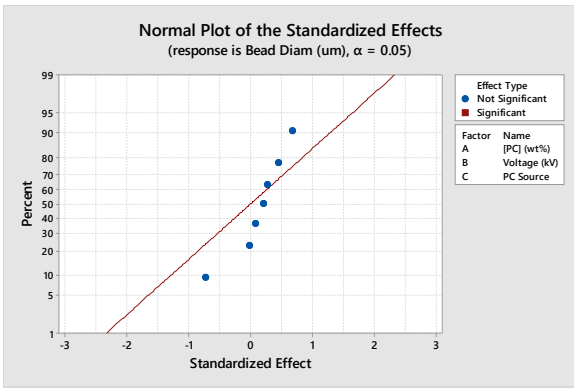


Figure B.23 - Minitab plot and chart outputs for DOE#3 – Bead Diameter

B.5 – 2 wt.-% cNCC/PC Electrospun Nanofibers in Chloroform Solvent (DOE#4)

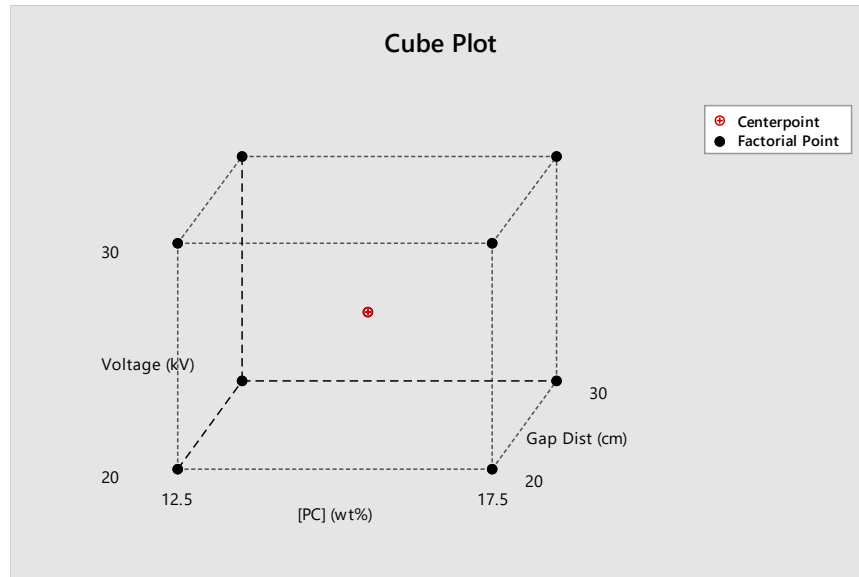


Figure B.24 - Cube plot representation of the 3D space of DOE#4 defined by high and low factor levels

Table B.10 - Target solution formulation masses for each run of DOE#4

Std. Order	Mass PC (g)	Mass cNCC (g)	Mass Chloroform (g)	Total Mass (g)
1	9.375	0.1910	65.434	75
2	13.125	0.2680	61.607	75
3	9.375	0.1910	65.434	75
4	13.125	0.2680	61.607	75
5	9.375	0.1910	65.434	75
6	13.125	0.2680	61.607	75
7	9.375	0.1910	65.434	75
8	13.125	0.2680	61.607	75
9	10	0.2295	63.521	75
10	10	0.2295	63.521	75
11	10	0.2295	63.521	75
Total Required	123.8	2.5245	698.7255	825

Table B.11 - DOE#4 target and actual mass measurements for StarPlastic PC and cNCC in chloroform for each 11 runs

Std. Order	mPC Target (g)	mPC Actual (g)	m _c NCC Target (g)	m _c NCC Actual (g)	mCHLORO Target (g)	mCHLORO Actual (g)
1 (1)	9.375	9.37	0.191	0.19	65.434	65.41
2 (a)	13.125	13.12	0.268	0.27	61.607	61.60
3 (b)	9.375	9.37	0.191	0.19	65.434	65.45
4 (ab)	13.125	13.12	0.268	0.27	61.607	61.62
5 (c)	9.375	9.37	0.191	0.20	65.434	65.53
6 (ac)	13.125	13.13	0.268	0.27	61.607	61.60
7 (bc)	9.375	9.37	0.191	0.20	65.434	65.46
8 (abc)	13.125	13.13	0.268	0.27	61.607	61.63
9 (0)	11.25	11.25	0.2295	0.23	63.5205	63.59
10 (0)	11.25	11.24	0.2295	0.23	63.5205	63.53
11 (0)	11.25	11.25	0.2295	0.22	63.5205	63.54

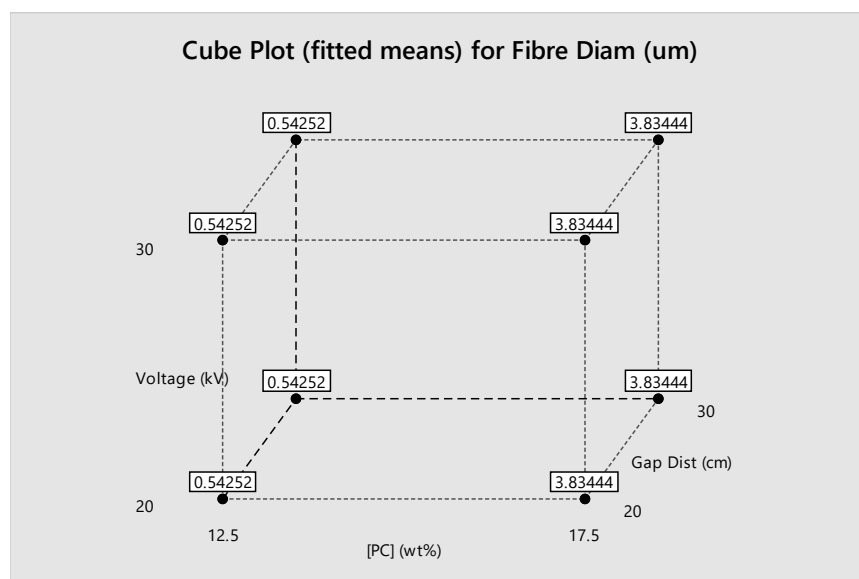


Figure B.25 - Cube plot of fitted means for the fiber diameter regression model for StarPlastic PC and cNCC electrospun fibers in DOE#4

B.5.1 – DOE#4 – Fiber Diameter

Backward Elimination of Terms (α to remove = 0.1)

Analysis of Variance

Source	DF	Adj SS	Adj MS	F-Value	P-Value
Model	1	21.674	21.674	5.17	0.049
Linear	1	21.674	21.674	5.17	0.049
[PC] (wt%)	1	21.674	21.674	5.17	0.049
Error	9	37.706	4.190		
Curvature	1	2.143	2.143	0.48	0.507
Lack-of-Fit	6	29.104	4.851	1.50	0.452
Pure Error	2	6.459	3.229		
Total	10	59.380			

Model Summary

S	R-sq	R-sq(adj)	R-sq(pred)
2.04685	36.50%	29.44%	2.34%

Coded Coefficients

Term	Effect	Coef	SE Coef	T-Value	P-Value	VIF
Constant		2.188	0.617	3.55	0.006	
[PC] (wt%)	3.292	1.646	0.724	2.27	0.049	1.00

Regression Equation in Uncoded Units

Fiber Diam (um) = -7.69 + 0.658 [PC] (wt%)

Alias Structure

Factor	Name
A	[PC] (wt%)
B	Voltage (kV)
C	Gap Dist (cm)

Aliases

I
A

Fits and Diagnostics for Unusual Observations

Obs	Fibre Diam (um)	Fit	Resid	Std	
6	8.264	3.834	4.430	2.44	R

R Large residual

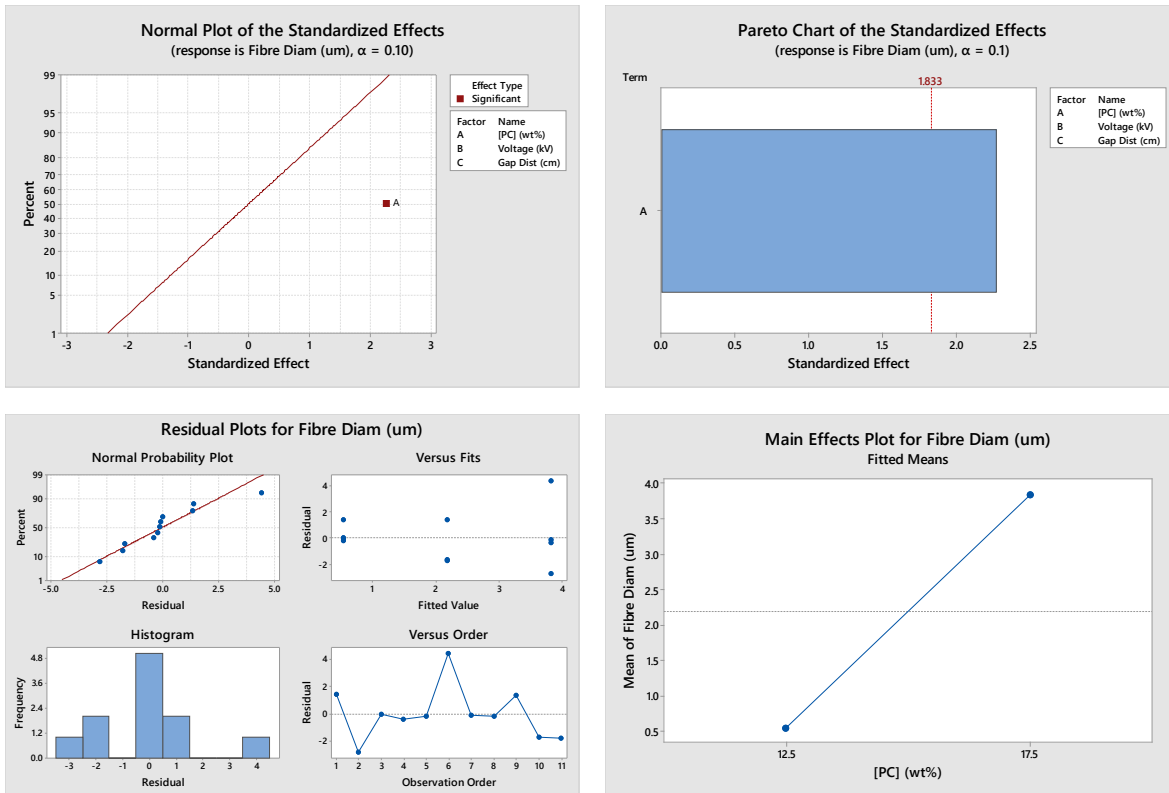


Figure B.26 - Minitab plot and chart outputs for DOE#4 – Fiber Diameter

* NOTE * There are no valid interactions to plot.

B.5.2 – DOE#4 – Bead Density

* NOTE * There are no terms in the model.

Backward Elimination of Terms (α to remove = 0.1)

Backward elimination removed all terms from the model.

Analysis of Variance

Source	DF	Adj SS	Adj MS	F-Value	P-Value
Model	7	119258	17037	0.13	0.986
Linear	3	81232	27077	0.21	0.882
[PC] (wt%)	1	30645	30645	0.24	0.657
Voltage (kV)	1	6027	6027	0.05	0.841
Gap Dist (cm)	1	44561	44561	0.35	0.595
2-Way Interactions	3	37585	12528	0.10	0.956
[PC] (wt%)*Voltage (kV)	1	3206	3206	0.03	0.884
[PC] (wt%)*Gap Dist (cm)	1	23	23	0.00	0.990
Voltage (kV)*Gap Dist (cm)	1	34356	34356	0.27	0.639
3-Way Interactions	1	441	441	0.00	0.957
[PC] (wt%)*Voltage (kV)*Gap Dist (cm)	1	441	441	0.00	0.957
Error	3	380706	126902		
Curvature	1	44070	44070	0.26	0.660
Pure Error	2	336636	168318		
Total	10	499964			

Model Summary

S	R-sq	R-sq(adj)	R-sq(pred)
356.233	23.85%	0.00%	0.00%

Coded Coefficients

Term	Effect	Coef	SE Coef	T-Value	P-Value	VIF
Constant		268	107	2.49	0.088	
[PC] (wt%)	-124	-62	126	-0.49	0.657	1.00
Voltage (kV)	55	27	126	0.22	0.841	1.00
Gap Dist (cm)	-149	-75	126	-0.59	0.595	1.00
[PC] (wt%)*Voltage (kV)	-40	-20	126	-0.16	0.884	1.00
[PC] (wt%)*Gap Dist (cm)	3	2	126	0.01	0.990	1.00
Voltage (kV)*Gap Dist (cm)	131	66	126	0.52	0.639	1.00
[PC] (wt%)*Voltage (kV)*Gap Dist (cm)	15	7	126	0.06	0.957	1.00

Regression Equation in Uncoded Units

Bead Dens (beads/mm²) = 850 + 86 [PC] (wt%) + 9 Voltage (kV) - 38 Gap Dist (cm)
- 4.6 [PC] (wt%)*Voltage (kV) - 2.8 [PC] (wt%)*Gap Dist (cm)
+ 0.8 Voltage (kV)*Gap Dist (cm)
+ 0.12 [PC] (wt%)*Voltage (kV)*Gap Dist (cm)

Alias Structure

Factor	Name
A	[PC] (wt%)
B	Voltage (kV)
C	Gap Dist (cm)

Aliases

I
A
B
C
AB
AC
BC
ABC

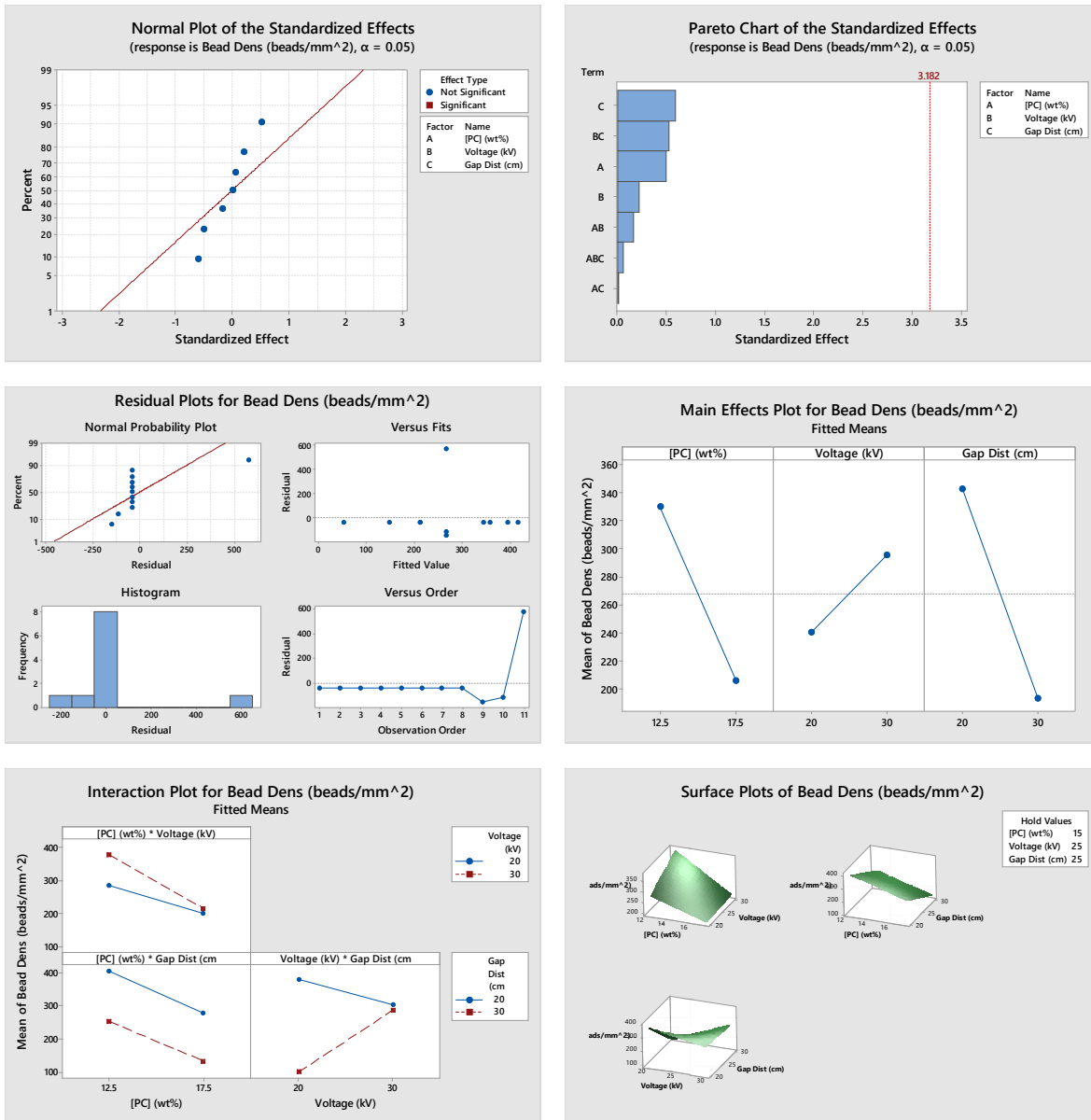


Figure B.27 - Minitab plot and chart outputs for DOE#4 – Bead Density

B.5.3 – DOE#4 – Bead Diameter

* NOTE * There are no terms in the model.

Backward Elimination of Terms (α to remove = 0.1)

Backward elimination removed all terms from the model.

Analysis of Variance

Source	DF	Adj SS	Adj MS	F-Value	P-Value
Model	7	1273.97	181.996	1.92	0.318
Linear	3	475.89	158.630	1.67	0.341
[PC] (wt%)	1	256.21	256.206	2.70	0.199
Voltage (kV)	1	142.48	142.476	1.50	0.308
Gap Dist (cm)	1	77.21	77.209	0.82	0.433
2-Way Interactions	3	431.13	143.712	1.52	0.370

[PC] (wt%)*Voltage (kV)	1	6.99	6.992	0.07	0.803
[PC] (wt%)*Gap Dist (cm)	1	326.85	326.849	3.45	0.160
Voltage (kV)*Gap Dist (cm)	1	97.29	97.294	1.03	0.385
3-Way Interactions	1	366.95	366.948	3.87	0.144
[PC] (wt%)*Voltage (kV)*Gap Dist (cm)	1	366.95	366.948	3.87	0.144
Error	3	284.17	94.723		
Curvature	1	33.50	33.503	0.27	0.657
Pure Error	2	250.66	125.332		
Total	10	1558.14			

Model Summary

S	R-sq	R-sq(adj)	R-sq(pred)
9.73256	81.76%	39.21%	0.00%

Coded Coefficients

Term	Effect	Coef	SE Coef	T-Value	P-Value	VIF
Constant		10.01	2.93	3.41	0.042	
[PC] (wt%)	-11.32	-5.66	3.44	-1.64	0.199	1.00
Voltage (kV)	-8.44	-4.22	3.44	-1.23	0.308	1.00
Gap Dist (cm)	6.21	3.11	3.44	0.90	0.433	1.00
[PC] (wt%)*Voltage (kV)	1.87	0.93	3.44	0.27	0.803	1.00
[PC] (wt%)*Gap Dist (cm)	-12.78	-6.39	3.44	-1.86	0.160	1.00
Voltage (kV)*Gap Dist (cm)	-6.97	-3.49	3.44	-1.01	0.385	1.00
[PC] (wt%)*Voltage (kV)*Gap Dist (cm)	13.55	6.77	3.44	1.97	0.144	1.00

Regression Equation in Uncoded Units

Bead Diam (um) = -1217 + 76.4 [PC] (wt%) + 42.2 Voltage (kV) + 52.4 Gap Dist (cm)
- 2.63 [PC] (wt%)*Voltage (kV) - 3.22 [PC] (wt%)*Gap Dist (cm)
- 1.765 Voltage (kV)*Gap Dist (cm)
+ 0.1084 [PC] (wt%)*Voltage (kV)*Gap Dist (cm)

Alias Structure

Factor	Name
A	[PC] (wt%)
B	Voltage (kV)
C	Gap Dist (cm)

Aliases

I
A
B
C
AB
AC
BC
ABC

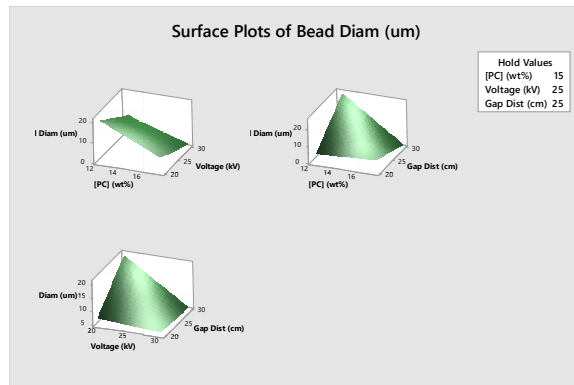
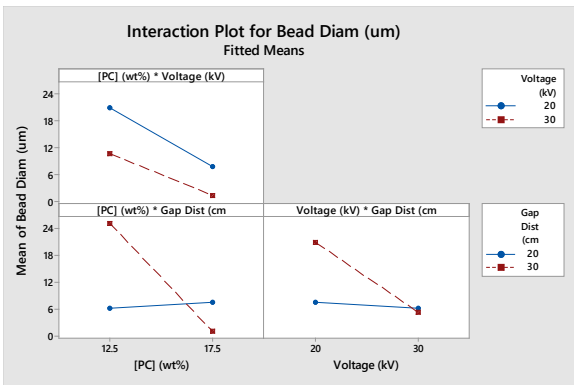
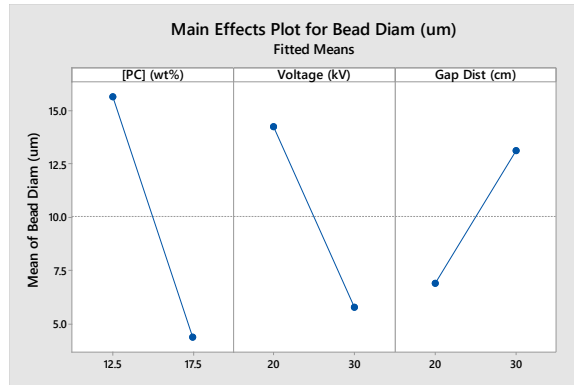
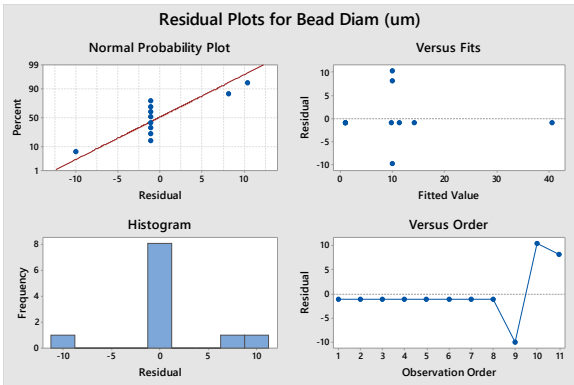
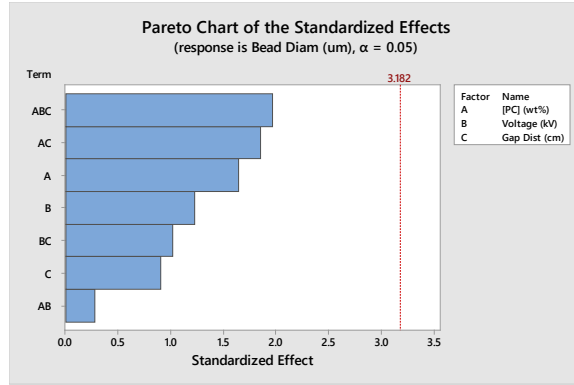


Figure B.28 - Minitab plot and chart outputs for DOE#4 – Bead Diameter

B.6 – 4 wt.-% cNCC/PA 6,6 Electrospun Nanofibers in Formic Acid Solvent (DOE#5)

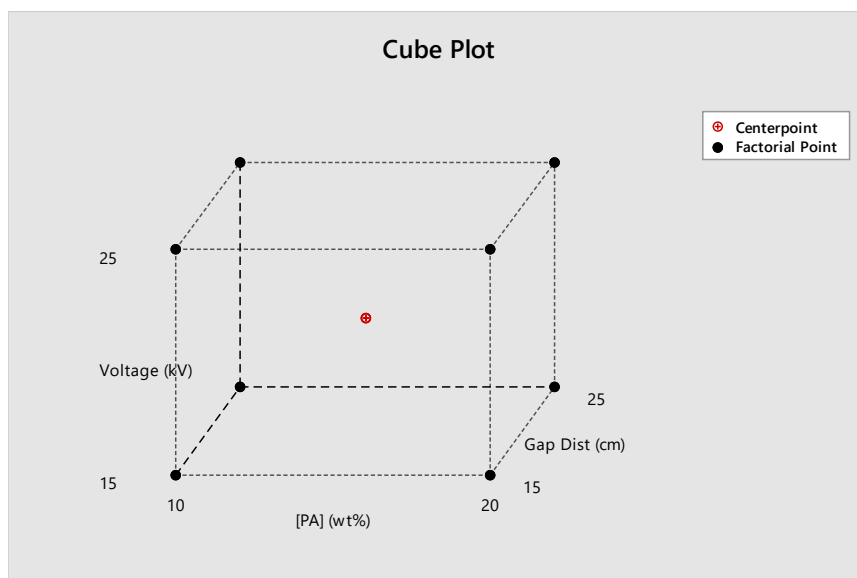


Figure B.29 - Cube plot representation of the 3D space of DOE#5 defined by high and low factor levels

Table B.12 - DOE#5 target and actual mass measurements for PA 6,6 and cNCC in formic acid for each 11 runs

Std.	mPA6,6	mPA6,6	m _c NCC	m _c NCC	m _{FORMIC}	m _{FORMIC}
Order	Target (g)	Actual (g)	Target (g)	Actual (g)	Target (g)	Actual (g)
1 (1)	3	3.01	0.125	0.13	27	26.88
2 (a)	6	6.01	0.25	0.25	24	23.76
3 (b)	3	3.01	0.125	0.13	27	26.88
4 (ab)	6	6.00	0.25	0.25	24	23.76
5 (c)	3	3.00	0.125	0.13	27	26.88
6 (ac)	6	6.00	0.25	0.25	24	23.77
7 (bc)	3	3.00	0.125	0.13	27	26.88
8 (abc)	6	6.01	0.25	0.25	24	23.77
9 (0)	4.5	4.50	0.1875	0.1875	25.5	25.31
10 (0)	4.5	4.50	0.1875	0.1887	25.5	25.33
11 (0)	4.5	4.51	0.1875	0.1883	25.5	25.33

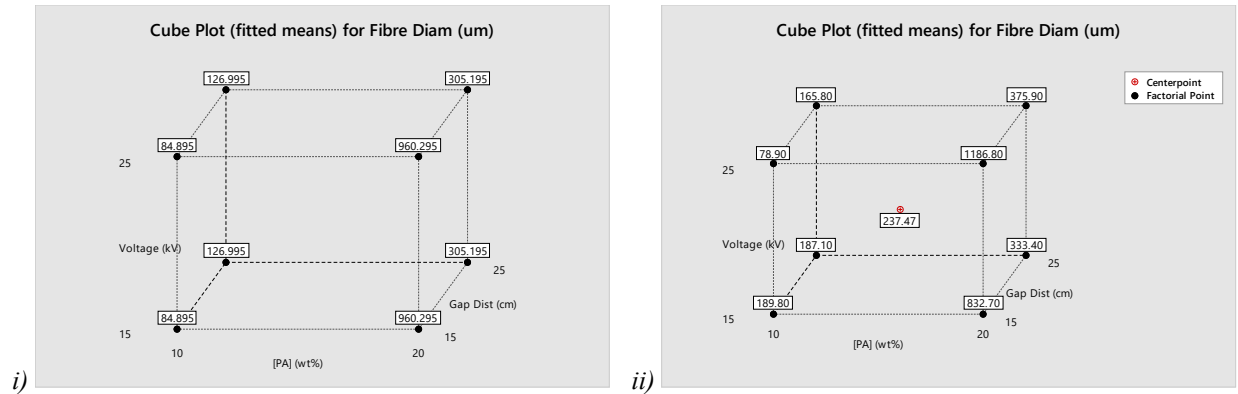


Figure B.30 - Cube plot of fitted means for the fiber diameter regression model for PA 6,6 and cNCC electrospun fibers in DOE#5; i) without CtPt and ii) with CtPt inclusion

B.6.1 – DOE#5 – Fiber Diameter

Backward Elimination of Terms (α to remove = 0.1)

Analysis of Variance

Source	DF	Adj SS	Adj MS	F-Value	P-Value
Model	3	985965	328655	16.14	0.002
Linear	2	742921	371460	18.25	0.002
[PA] (wt%)	1	555036	555036	27.26	0.001
Gap Dist (cm)	1	187884	187884	9.23	0.019
2-Way Interactions	1	243044	243044	11.94	0.011
[PA] (wt%)*Gap Dist (cm)	1	243044	243044	11.94	0.011
Error	7	142511	20359		
Curvature	1	71742	71742	6.08	0.049
Lack-of-Fit	4	69973	17493	43.93	0.022
Pure Error	2	796	398		
Total	10	1128476			

Model Summary

S	R-sq	R-sq(adj)	R-sq(pred)
142.684	87.37%	81.96%	66.50%

Coded Coefficients

Term	Effect	Coef	SE Coef	T-Value	P-Value	VIF
Constant		369.3	43.0	8.59	0.000	
[PA] (wt%)	526.8	263.4	50.4	5.22	0.001	1.00
Gap Dist (cm)	-306.5	-153.3	50.4	-3.04	0.019	1.00
[PA] (wt%)*Gap Dist (cm)	-348.6	-174.3	50.4	-3.46	0.011	1.00

Regression Equation in Uncoded Units

$$\text{Fibre Diam (um)} = -1899 + 192.1 [\text{PA}] (\text{wt}\%) + 73.9 \text{ Gap Dist (cm)} - 6.97 [\text{PA}] (\text{wt}\%) * \text{Gap Dist (cm)}$$

Alias Structure

Factor	Name
A	[PA] (wt%)
B	Voltage (kV)
C	Gap Dist (cm)

Aliases

I
A
C
AC

Fits and Diagnostics for Unusual Observations

Obs	Diam (um)	Fit	Resid	Std Resid	
4	1186.8	960.3	226.5	2.17	R

R Large residual

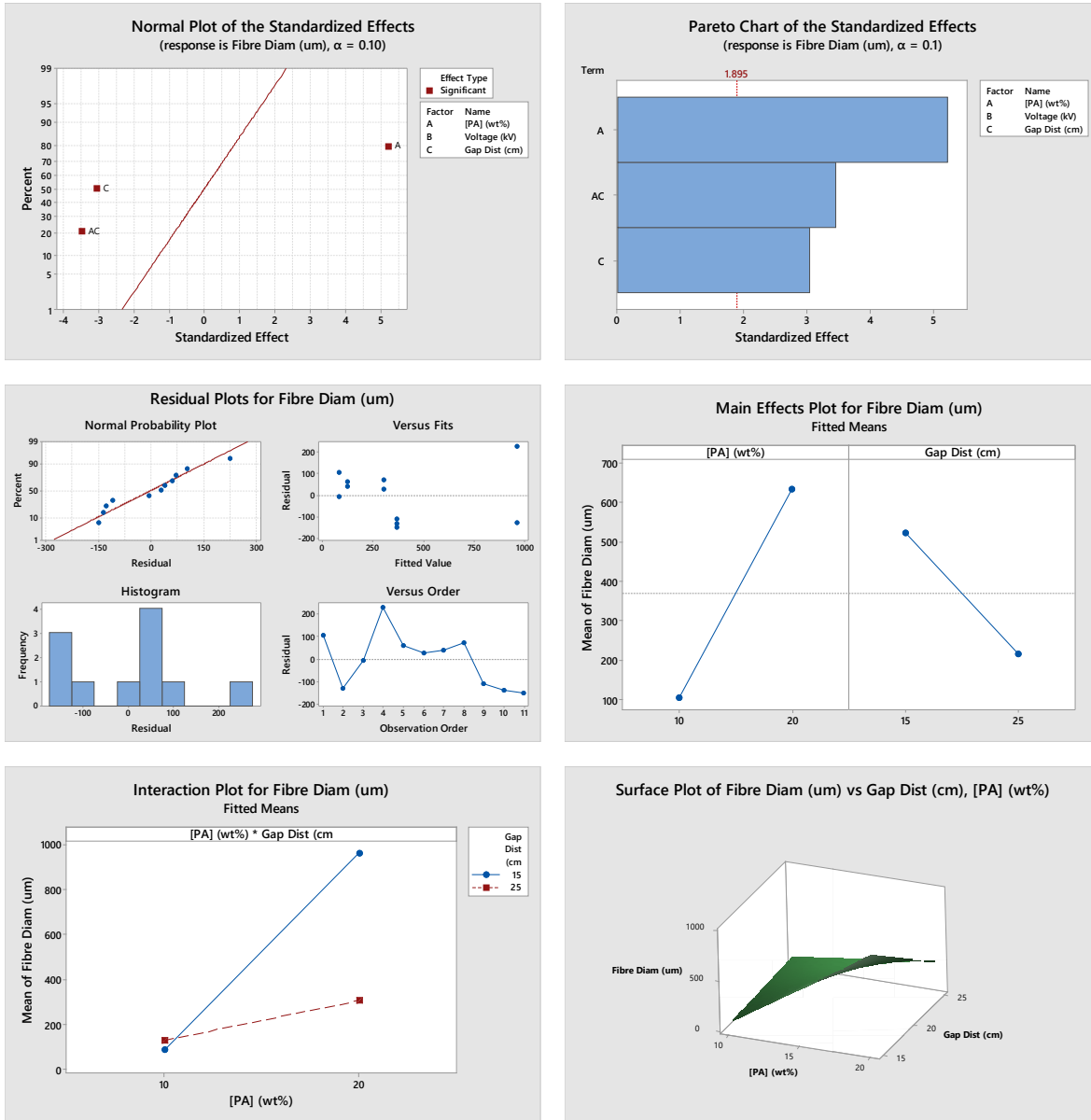


Figure B.31 - Minitab plot and chart outputs for DOE#5 – Fiber Diameter

B.6.2 – DOE#5 – Fiber Diameter (including CtPt)

Backward Elimination of Terms (α to remove = 0.1)

Analysis of Variance

Source	DF	Adj SS	Adj MS	F-Value	P-Value
Model	8	1127680	140960	354.02	0.003
Linear	3	751659	250553	629.26	0.002
[PA] (wt%)	1	555036	555036	1393.96	0.001

Voltage (kV)	1	8738	8738	21.95	0.043
Gap Dist (cm)	1	187884	187884	471.87	0.002
2-Way Interactions	3	284158	94719	237.88	0.004
[PA] (wt%)*Voltage (kV)	1	34954	34954	87.79	0.011
[PA] (wt%)*Gap Dist (cm)	1	243044	243044	610.40	0.002
Voltage (kV)*Gap Dist (cm)	1	6160	6160	15.47	0.059
3-Way Interactions	1	20120	20120	50.53	0.019
[PA] (wt%)*Voltage (kV)*Gap Dist (cm)	1	20120	20120	50.53	0.019
Curvature	1	71742	71742	180.18	0.006
Error	2	796	398		
Total	10	1128476			

Model Summary

S	R-sq	R-sq(adj)	R-sq(pred)
19.9543	99.93%	99.65%	*

Coded Coefficients

Term	Effect	Coef	SE Coef	T-Value	P-Value	VIF
Constant		418.80	7.05	59.36	0.000	
[PA] (wt%)	526.80	263.40	7.05	37.34	0.001	1.00
Voltage (kV)	66.10	33.05	7.05	4.68	0.043	1.00
Gap Dist (cm)	-306.50	-153.25	7.05	-21.72	0.002	1.00
[PA] (wt%)*Voltage (kV)	132.20	66.10	7.05	9.37	0.011	1.00
[PA] (wt%)*Gap Dist (cm)	-348.60	-174.30	7.05	-24.71	0.002	1.00
Voltage (kV)*Gap Dist (cm)	-55.50	-27.75	7.05	-3.93	0.059	1.00
[PA] (wt%)*Voltage (kV)*Gap Dist (cm)	-100.30	-50.15	7.05	-7.11	0.019	1.00
Ct Pt		-181.3	13.5	-13.42	0.006	1.00

Regression Equation in Uncoded Units

Fibre Diam (um) = 774 - 21.2 [PA] (wt%) - 131.2 Voltage (kV) - 24.2 Gap Dist (cm)
+ 10.67 [PA] (wt%)*Voltage (kV) + 1.05 [PA] (wt%)*Gap Dist (cm)
+ 4.908 Voltage (kV)*Gap Dist (cm)
- 0.4012 [PA] (wt%)*Voltage (kV)*Gap Dist (cm) - 181.3 Ct Pt

Alias Structure

Factor	Name
A	[PA] (wt%)
B	Voltage (kV)
C	Gap Dist (cm)

Aliases

I
A
B
C
AB
AC
BC
ABC

Fits and Diagnostics for Unusual Observations

Obs	Fibre Diam (um)	Fit	Resid	Std Resid
1	189.8	189.8	-0.0	* X
2	832.7	832.7	-0.0	* X
3	78.9	78.9	0.0	* X
4	1186.8	1186.8	-0.0	* X
5	187.1	187.1	0.0	* X
6	333.4	333.4	0.0	* X
7	165.8	165.8	-0.0	* X
8	375.9	375.9	0.0	* X

X Unusual X

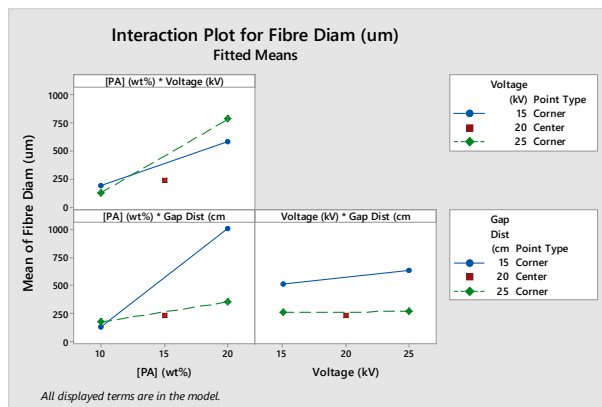
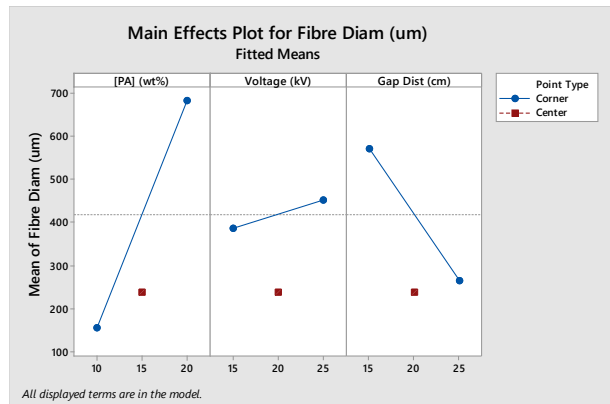
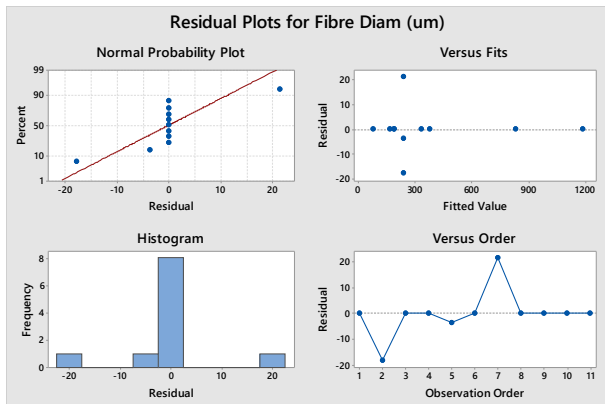
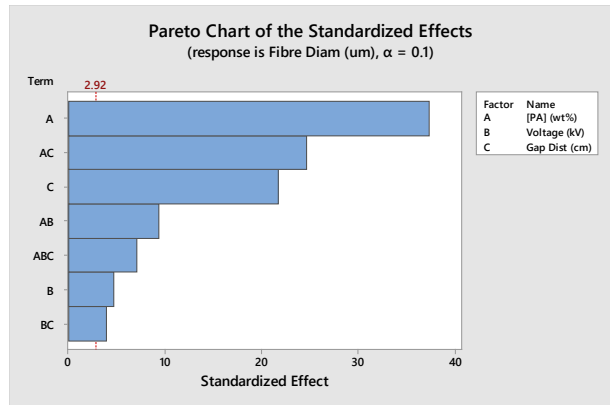
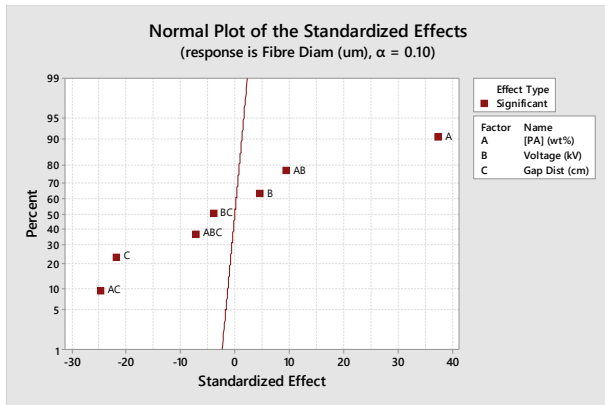


Figure B.32 - Minitab plot and chart outputs for DOE#5 – Fiber Diameter (including CtPt)

Appendix C. Supplementary 3D Printing Data

Table C.1 - ASTM D256 Izod Impact results for 3D printed a) 200 μm TPS, b) 300 μm TPS, c) 300 μm 1% NCC-TPS, d) 300 μm 3% NCC-TPS, e) 300 μm 5% NCC-TPS

a)	200 μm TPS	Method name:	3D PRINTING
Specimen No.	Thickness (mm)	Impact Strength (J/m)	post-Condition
C1		49.703	Broke
C2		47.462	Broke
C3		55.955	Broke
C4		62.780	Broke
C5		62.596	Broke
C6		49.976	Broke
C7		51.601	Broke
Average		54.296	All Broke
St. Dev.		6.289	
b)	TPS 300 μm	Method name:	3D PRINTING
Specimen No.	Thickness (mm)	Impact Strength (J/m)	post-Condition
E2		42.988	Broke
M4		37.062	Broke
M5		36.676	Broke
M6		35.066	Broke
M7		39.451	Broke
G2		36.313	Broke
G3		29.146	Broke
Average		36.672	All Broke
St. Dev.		4.225	

c)	300 μm 1% NCC-TPS	Method name:	3D PRINTING
Specimen No.	Thickness (mm)	Impact Strength (J/m)	post-Condition
I1		39.490	Broke
I3		53.097	Broke
I5		46.770	Broke
I7		48.434	Broke
Average		46.948	All Broke
St. Dev.		5.647	
d)	300 μm 3% NCC-TPS	Method name:	3D PRINTING
Specimen No.	Thickness (mm)	Impact Strength (J/m)	post-Condition
j8		37.230	Broke
j9		41.758	Broke
j10		47.255	Broke
j11		46.931	Broke
j12		53.839	Broke
j13		55.418	Broke
j14		48.811	Broke
Average		47.320	All Broke
St. Dev.		6.367	
e)	300 μm 5% NCC-TPS	Method name:	3D PRINTING
Specimen No.	Thickness (mm)	Impact Strength (J/m)	post-Condition
n1		39.059	Broke
n2		30.014	Broke
n3		33.917	Broke
n4		31.317	Broke
n5		34.367	Broke
n6		28.244	Broke
n7		30.387	Broke
Average		32.472	All Broke
St. Dev.		3.621	